

ABSTRACT

ZHOU, YING. Printing of Barium Titanate Nanoparticles for Smart Textile Applications. (Under the direction of Dr. Jesse S. Jur).

Smart textiles have shown tremendous growth over the past decades. Antennas and capacitors are two essential components of electronic textiles. Antennas serve as a communication platform to transmit data between sensors, actuators, and processors wirelessly. Capacitors function as energy storage devices and sensors. One thing in common for these two devices is the need for high-dielectric materials in order to achieve good device performance and size reduction. In this research, barium titanate (BT) nanoparticles (NPs) were explored due to the high dielectric constant and low dielectric loss. Printing is a promising method for fabricating wearable electronics. Various printing methods (e.g., spray coating, screen printing, inkjet printing) were also investigated to fabricate antenna and capacitors with high-dielectric BT NPs inks.

Next-generation wearable devices demand lightweight, flexible, and breathable antenna designs. Ultraviolet (UV)-curable BT NPs dielectric ink was prepared and printed on a textile substrate with spray coating. By optimization of the printing process, the dielectric constant of the textile substrate was enhanced. The patch and ground layer fabrication relied on traditional screen printing methods. The final textile antenna can operate in a full-duplex mode while presenting a relatively high gain of 9.12 dB at 2.3 GHz and a bandwidth of 79 MHz for each port. The performance of the textile antenna was improved by using inkjet printing method as the prior design required dense screen-printed ground and path layer, impairing breathability and flexibility. An all inkjet printed antenna was realized by printing reactive MOD (metal-organic-decomposition) silver ink and the UV curable BT NPs dielectric ink. The fabricated patch antenna

showed a low return loss of 24.98 dB in free space and preserved its performance even when bent to $>300^\circ$.

The potential of using inkjet printing of BT NPs for textile electronics was further demonstrated by preparing a flexible capacitor array pressure sensor. The UV curable BT NPs ink was printed on a textile substrate to improve the dielectric constant, and Ag MOD ink was printed for electrode layers. The resultant flexible capacitor array pressure sensor is highly sensitive (11.4 kPa^{-1}) with a low detection limit (50 Pa).

The above works provide an innovative strategy for flexible and breathable textile electronics through various printing methods. In addition to using flexible textile substrates, devices that are lightweight and miniature in size are also preferred for wearable applications, such as miniature capacitors.

A fully inkjet-printed silver capacitor was prepared by printing a newly developed high-concentration large-size BT/polymer ink and commercial silver MOD ink. After optimization of drying temperature and printing settings, uniformly printed layers were achieved. The printed nanocomposite dielectric layer with a thickness of $5 \mu\text{m}$ showed a high dielectric constant of 100 at 100 Hz. A high-temperature sintered inkjet-printed nickel capacitor was also prepared. The inkjet-printed capacitor contained printed Nickel (Ni) NPs electrodes and a dielectric layer consisting of 200 nm BT NPs. The sintering temperature and partial oxygen pressure were optimized. The resultant capacitor ($1.5 \text{ mm} \times 2.5 \text{ mm}$) showed capacitance of 1.15 nF at 100 Hz with a $7 \mu\text{m}$ BTO layer.

The success of this project was built on the development of various BT nanoparticles ink. In the end, the fabrication of ceramic ink containing high concentration BT NPs was explored systematically, including the selection of surfactants, solvents, and processes. The prepared stable BT NP ink with high nanoparticle concentration (20 wt.%) was inkjet printable, and the printed layer shows good uniformity.

The research covered the whole process of printing both an antenna and capacitors, including fabricating of inks, substrate selection, optimization of printing parameters, and device fabrication.

© Copyright 2021 by Ying Zhou

All Rights Reserved

Printing of Barium Titanate Nanoparticles for Smart Textile Applications

by
Ying Zhou

A dissertation submitted to the Graduate Faculty of
North Carolina State University
in partial fulfillment of the
requirements for the degree of
Doctor of Philosophy

Fiber and Polymer Science

Raleigh, North Carolina
2021

APPROVED BY:

Dr. Jesse S. Jur
Committee Chair

Dr. Minyoung Suh

Dr. Philip D. Bradford

Dr. Jacob Adams

DEDICATION

To my lovely parents and inspiring husband for their unconditional love and support

BIOGRAPHY

Born in China, Ying Zhou received a BS in Textile Engineering from Wuhan Textile University in 2009. With a strong interest in Textile, she began her master's degree in Textile Materials at Donghua University in 2013. After graduation, she joined the Fiber and Polymer Science Ph. D. program at Wilson College of Textiles, North Carolina State University. From 2017-2018 July, she worked in the Physics department in nanofabrication and biophysics. In 2018, she was fortunate to join the NEXT research group and work under the direction of Dr. Jesse. S. Jur, with a focus on smart textiles. In the NEXT research group, she developed a strong interest in making functional electronic textile by printing nanomaterials. The collaborative work with the team members supports her academy progress. It is a precious and happy time for both learning and playing.

ACKNOWLEDGMENTS

Sincerest and deepest thanks to my advisor, Dr. Jesse. S. Jur, who always supported, advised, mentored, and inspired me to fill my interests into research work. He introduced me to a new multidisciplinary research field: printing technology, ceramic nanomaterials, and conductive materials to develop smart textiles. Without his endurance, support, and patient instruction, I would not have arrived at this moment.

I also offer special thanks to all my committee members, Dr. Philip D. Bradford, Dr. Jacob Adams and Dr. Minyoung Suh, for guiding me with their expertise. Their valuable insights contributed immensely to my dissertation.

I would like to express my appreciation to my research group members. I am grateful to Dr. Amanda C. Mills for her support and guidance. I appreciate Dr. Wade Ingram, Dr. Inhwan Kim, Dr. Braden M. Li, Zoe Rosenberg, Caitlin Knowles, Beomjun Ju, Henry Soewardiman and Isabel Hines, who contributed to my research through my Ph. D. program.

I must also thank Shoei, AVX, Knowles, Xaar, Center for Dielectrics and Piezoelectrics (CDP), and Advanced Self-Powered Systems for Integrated Sensors and Technologies (ASSIS), for their sponsorship and support in conducting this research project.

Finally, I would love to thank my family, in particular my parents and my husband, for their love and support.

TABLE OF CONTENTS

LIST OF TABLES	xi
LIST OF FIGURES	xii
1 INTRODUCTION	1
1.1 Research Objectives	2
2 LITERATURE REVIEW	6
2.1 Barium Titanate (BT).....	6
2.2 Printing Method	9
2.2.1 Inkjet Printing	11
2.2.1.1 Voltage and waveform.....	14
2.2.1.2 Printing speed and frequency	15
2.2.1.3 Height.....	16
2.2.1.4 Drop space	17
2.2.1.5 Ink printability	18
2.2.1.6 Ink drying.....	21
2.2.2 Screen Printing.....	23
2.2.3 Spray Coating.....	24
2.3 Wearable Antenna.....	25
2.4 Capacitor	29
2.5 Summary of Critical Gaps in Current Knowledge.....	33
3 DIRECT-WRITE SPRAY COATING OF A FULL-DUPLEX ANTENNA FOR E-TEXTILE APPLICATIONS	35
3.1 Introduction.....	36

3.2	Materials and Methods.....	39
3.2.1	Preparation and Characterization of the Barium Titanate Ultraviolet (UV) Curing Ink	39
3.2.2	Configuration of Antenna	40
3.2.3	Dielectric Constant Test.....	41
3.2.4	Antenna Fabrication.....	42
3.2.5	Characterization of the Antenna	45
3.3	Results and Discussion	45
3.3.1	Characterization of BT Dielectric Ink.....	45
3.3.2	Dielectric Properties of the Printed Textile-Based Antenna.....	47
3.3.3	Characterization of the Printed Textile-Based Antenna	48
3.3.4	Simulated and Measured S-Parameter Results for the Printed Textile-Based Antenna	50
3.3.5	Radiation Pattern and Far-Field Results for the Printed Textile-Based Antenna ..	51
3.4	Related Work	53
3.5	Conclusions.....	54
4	ALL-INKJET-PRINTED BARIUM TITANATE NANOPARTICLES ULTRAVIOLET INK AND SILVER METAL-ORGANIC- DECOMPOSITION INK LARGE-AREA TEXTILE PRESSURE SENSORS ...	56
4.1	Introduction.....	56
4.2	Experiments	60
4.2.1	Material	60
4.2.2	Inkjet Printing BT Ink on Woven/ Knit/ Nonwoven Structures	60

4.2.3	Inkjet Printing Ag MOD Ink on Nonwoven Structures	61
4.2.4	Optical Photothermal Infrared (O-PTIR) Spectroscopy	62
4.2.5	Characterizations.....	62
4.3	Results and Discussion	63
4.3.1	Ink Characterization.....	63
4.3.2	Barium Titanate UV Ink Wetting, Absorption and Diffusion on Different Textiles.....	64
4.3.3	Characteristics of Barium Titanate UV Inks.....	69
4.3.4	Characteristics of Ag MOD ink	74
4.3.5	Layer-by-Layer BT UV Cured Nonwoven Fabric Dielectric Properties.....	76
4.3.6	Textile Capacitor Array	77
4.3.7	Microscopic Analysis of the Inkjet Printed E-Textiles.....	78
4.3.8	Smart Sensor of the Textile Capacitor Array.....	80
4.4	Conclusion	80
5	ALL-INKJET-PRINTED WEARABLE AND BREATHABLE TEXTILE	
	ANTENNA	83
5.1	Introduction.....	84
5.2	Experimental Section/Methods.....	89
5.2.1	Conductive and Dielectric Inks.....	89
5.2.2	Fabric Selection	89
5.2.3	Morphology of the Antenna.....	90
5.2.4	Dielectric Constant Test.....	90
5.2.5	Inkjet Printing Antenna Process.....	90

5.2.6	Antenna Fabrication.....	90
5.2.7	Antenna Measurement	91
5.2.8	Air Permeability.....	92
5.3	Results and Discussion	92
5.3.1	Inkjet Printing Process on Textiles	92
5.3.2	Morphology of Inkjet-Printed Textile.....	96
5.3.3	Electrical Properties of the Inkjet-Printed Textile	98
5.3.4	Dielectric Properties of the Inkjet-Printed Textile.....	99
5.3.5	Antenna Simulation and Return Loss	100
5.3.6	Antenna Bending Test.....	102
5.3.7	Antenna Body Test	103
5.4	Conclusion	105
6	FABRICATION OF BARIUM TITANATE NANOCOMPOSITE FILM WITH HIGH PERMITTIVITY USING INKJET PRINTING FOR METAL- INSULATOR-METAL CAPACITOR APPLICATION	106
6.1	Introduction.....	106
6.2	Experimental Section	108
6.2.1	Materials	108
6.2.2	Fabrication of BT-PVP Composite Ink.....	109
6.2.3	Deposition System	109
6.2.4	Characterization	109
6.3	Results and Discussion	110
6.3.1	Inkjet Ink Characterization	110

6.3.2	Inkjet Setting Influence on Printed Ag Layer Roughness.	115
6.3.3	Fabrication of All-inkjet-Printed MIM Capacitor.....	122
6.4	Conclusion	125
7	ALL-INKJET-PRINTED HIGH-TEMPERATURE NICKEL CAPACITOR BY ONE STEP CO-FIRING PROCESS	127
7.1	Introduction.....	127
7.2	Experimental Section	131
7.2.1	Ink Formulation	131
7.2.2	Characterization	131
7.2.3	Inkjet Printing and Annealing Process.....	132
7.2.4	Drying Process Optimization.....	133
7.2.5	High Temperature Sintering	134
7.3	Results and Discussion	135
7.3.1	Ink Characterization.....	135
7.3.2	Sintering Effects on Inkjet-Printed Capacitor.....	137
7.3.3	Substrate Effects on Inkjet-Printed Capacitor.....	139
7.3.4	XRD of the Inkjet-Printed Capacitor Before and After Sintering.	140
7.3.5	Structure of the Inkjet-Printed Capacitor	141
7.3.6	Ni Capacitor	142
7.4	Conclusion	143
8	HIGH-CONCENTRATION BARIUM TITANATE NANO-INKS FOR INKJET PRINTING AND REDUCED COFFEE RING EFFECT	144
8.1	Introduction.....	144

8.2	Experimental Section	148
8.2.1	BT Ink Fabrication	148
8.2.2	Deposition System	148
8.2.3	Characterization	149
8.3	Results and Discussion	150
8.3.1	Ink Stability.....	150
8.3.2	Characterization of the BT Surface Modification.....	152
8.3.3	Ink Jettability and Liquid Properties.....	153
8.4	Conclusion	161
9	CONCLUSION AND FUTURE WORK	162
9.1	Summary and Conclusion	162
9.2	Future Work	165
9.2.1	Ceramic-Metal-Polymer nanocomposites.....	165
9.2.2	Nickel Inkjet Printing Ink	165
9.2.3	Barium Titanate Nanoparticles Doping	165
10	REFERENCE.....	167
	APPENDICES	211
	Appendix-1: Supporting Information for Chapter 4	212
	Appendix-2: Supporting Information for Chapter 5	220
	Appendix-3: Supporting Information for Chapter 6	224
	Appendix-4: Supporting Information for Chapter 7	227
	Appendix-5: Supporting Information for Chapter 8	232

LIST OF TABLES

Table 2.1.	Dielectric permittivity of commonly used ceramics and polymer for capacitors. ²³	8
Table 2.2.	Comparison of various common printing techniques	11
Table 3.1.	Specification of the fabric for antenna design.	42
Table 3.2.	Fabric dielectric properties.	48
Table 3.3.	Comparison of the antennas proposed in previous works.	54
Table 4.1.	Specification of fabrics for inkjet printing e-textiles.	66
Table 5.1.	Comparison of Flexible Antenna Reported in the Literature.....	88
Table 5.2.	Dielectric Property Data Archived for Different Fabric Assembly with SPDR Test.....	100
Table 6.1.	Ag NPs ink and BT NPs ink properties.	112
Table 6.2.	Characteristics of PMC (ceramic filler with polymer), published in the literature.	125
Table 7.1.	Ni NPs and BTO NPs inks properties.....	135

LIST OF FIGURES

Figure 1-1.	Research approach	5
Figure 2-1.	The crystal structure of BaTiO ₃ at cubic phase (left) and tetragonal phase (right). Displacements of the Ba ²⁺ (white), Ti ⁴⁺ (black), ions relative to the O ²⁻ (red) ions are indicated by the arrows. ²¹	7
Figure 2-2.	Conventional unit cell of BT in polymorphs. ²²	7
Figure 2-3.	The classification of common printing technologies.	9
Figure 2-4.	Schematic of (a) gravure processes, ³⁶ (b) roll offset printing process, ³⁷ (c) microcontact printing process, ³⁸ (d) flexographic ink splitting process, ³⁹ (e) spray coating process, ⁴⁰ (f) screen printing, ⁴¹ (g) inkjet printing process ⁴² , and (h) slot-die process. ⁴³	10
Figure 2-5.	The two operation modes of inkjet-printing: (a) continuous inkjet-printing (CIJ) and (b) drop-on-demand (DOD) system. ⁸³	12
Figure 2-6.	Schematic diagram showing the principles of DOD inkjet printing system. (a) a vapor pocket or bubble generated by a thin-film heater (thermal inkjet), (b) a mechanical actuation by a piezoelectric transducer (piezoelectric inkjet). ⁸⁴	12
Figure 2-7.	Waveform of the piezoelectric printing.	14
Figure 2-8.	Time sequence photographs for the ejection of a 60 μm diameter drop from a nozzle, showing the tail that eventually releases and merges with the main drop. ⁸⁸	15
Figure 2-9.	Inkjet printing process.....	16

Figure 2-10.	Schematic illustration of the single droplet impinges on glass substrate. (a) Spreading process, D_{\max} is the maximum diameter of the droplet; (b) Equilibrium state of a droplet, D_e is the diameter of the droplet. ⁶⁶	17
Figure 2-11.	(a)Contact phenomenon of two droplets, three droplets, four droplets and five droplets; (b) the least number of droplets for the forming of larger droplet. ⁶⁶	18
Figure 2-12.	Representative photo sequence of drop formation for fluids with values of Z ranging from 2 to 17 at a constant driving voltage of 25 V: (a) $Z = 2.17$, (b) $Z = 3.57$, (c) $Z = 4.08$, (d) $Z = 6.57$, (e) $Z = 7.32$, (f) $Z = 13.68$, and (g) $Z = 17.32$. ⁹⁴ ...	19
Figure 2-13.	Representative trajectories of the ejected droplets as a function of the elapsed time for fluids with values of Z ranging from 2 to 17 at a constant driving voltage of 25 V: (a) $Z = 2.17$, (b) $Z = 3.57$, (c) $Z = 4.08$, (d) $Z = 6.57$, (e) $Z = 7.32$, (f) $Z = 13.68$, and (g) $Z = 17.32$. ⁹⁴	20
Figure 2-14.	Confocal laser scattering microscopic 3D images for inkjet printed single dots obtained from conductive inks with varying solvent compositions: (a) 0, (b) 16, and (c) 32 wt% ethylene glycol. ⁹⁵	21
Figure 2-15.	(a) Three typical coalescing cases of the neighboring ink droplets induced by different dynamic wettabilities of ink droplets on the substrates; ⁹⁶ (b) the effect of drop spacing and time delay on the behavior of a printed line at an intermediate temperature, and the principal printed line pattern with the decrease of drop spacing. ⁹⁷	22
Figure 2-16.	(a) Schematic process of screen printing using the silicone stencil and a pristine graphene ink. (b) Cross-sectional illustration of the screen printing method. ⁵⁹	24

Figure 2-17.	(a) Electrostatic spraying, ⁷¹ (b) air pressure spraying, ⁷¹ and (c) hybrid spraying. ⁷²	25
Figure 2-18.	Wearable antennas by different fabrication methods. (a) Antenna embroidered conductive fibers and yarns. ¹¹⁵ (b)Screen printed textile antenna. ⁹⁹ (c) Inkjet printed textile antenna. ¹¹⁶ (d) Inkjet printed paper antenna. ¹¹⁴ (e) Antenna by copper sheet. ¹¹⁷ (f) Antenna by conductive fabric. ¹¹⁸	26
Figure 2-19.	Schematic sketches for (a) electrostatic, (b) electrolytic and (c) electrochemical capacitors. ⁷	29
Figure 2-20.	Schematic of multilayer capacitor ceramic. ¹⁵⁵	32
Figure 2-21.	Simplified MLCC Manufacturing Process. ¹⁵⁶	32
Figure 3-1.	Geometrical parameters of the dual-port full-duplex textile-based patch antenna. (a) Top view. (b) Side view. Design dimensions: H = 2 mm, L = 80 mm, Lpatch = 45.8 mm, Lstr1 = 19.1 mm, Lstr2 = 25.5 mm, Lstr = 53.6 mm, Lf = 6 mm, Wf = 7 mm, L1 = 4.5 mm, W1 = 1 mm, W2 = 0.8 mm, and dgap = 7 mm ⁹⁹	41
Figure 3-2.	Fabrication of the textile-based antenna. (a) Screen printing of the Ag paste from Dupont onto nonwoven fabrics to fabricate the patch and ground. (b) Direct-write spray coating of barium titanate (BT) UV curable dielectric ink onto the knit fabric substrate assembly (six layers of knit fabric laminated with a thermoplastic polyurethane (TPU) web) to modify the dielectric constant. (c) Final assembly of the printed textile-based antenna (two layers of nonwoven fabric and six layers of knit fabric spray coated with BT	

dielectric ink). Exploded views indicate the different layer compositions. (d)

Final product image of the printed textile-based antenna.....43

Figure 3-3. Fundamental characteristics of UV-curable ink with BT nanoparticles. (a) chemical reaction mechanism of acrylate and urethane UV-curing process ¹⁸⁶. (b) Scanning electron microscopy (SEM) of BT nanoparticles (50,000×; 1 μm of scale bar). (c) Size distribution of the BT nanoparticles. (d) BT nanoparticle size distribution according to intensity of UV-curable ink tested by DLS. (e) X-ray diffraction (XRD) result of the BT dielectric ink after UV curing.....47

Figure 3-4. (a) Flexibility of the knit fabric assembly with BT dielectric ink and (b) an SEM image of the BT with acrylate and urethane UV-curable dielectric ink coated on a single fiber within the fabric after UV curing for 5 min (10,000×, 350 nm of scale bar). (c) Cross-sectional microscope image of Ag screen-printed patch section of the antenna (20×, 100 μm of scale bar). (d) Cross-sectional SEM image of Ag screen-printed patch section of the antenna (150×, 120 μm of scale bar).49

Figure 3-5. Buckling test of the nonwoven substrate (eight layers of nonwoven fabric), knit substrate (eight layers of knit fabric), and combination substrate (two layers of nonwoven fabric and six layers of knit fabric spray coated with BT dielectric ink). (a) Photography of experimental setup. (b) Buckling force displacement curve with fixed–fixed ends.....50

Figure 3-6. Simulated and measured S-parameters of the proposed full-duplex textile antenna with the combination structure (two layers of nonwoven fabric and six layers of knit fabric spray coated with BT dielectric ink). Experimental

	data are represented by solid curves, while simulation data are represented by dotted curves.	51
Figure 3-7.	(a) Experimental setup for the textile antenna with the combination substrate (two layers of nonwoven fabric and six layers of knit fabric spray coated with BT dielectric ink) for 3D radiation pattern measurements in an anechoic chamber. (b) Maximum gain plot at $\varphi = 0^\circ$. (c) Two-dimensional radiation pattern of the textile antenna at 2.3 GHz and $\varphi = 0^\circ$. (d) Three-dimensional radiation pattern of the textile antenna plotted in dB at 2.3 GHz.	52
Figure 4-1.	(a) Schematic of inkjet printing layer-by-layer lamination process. (b) Compared mechanisms of the BT UV curable ink for inkjet printing on three different textile structures: woven, knit and nonwoven fabric with zoomed cross-sectional images.	64
Figure 4-2.	Microscopic images of BT UV curable ink inkjet printed by layer-by-layer process of (1L)6 textile structures; (a) woven fabric, (b) knit fabric, (c) nonwoven fabric.....	68
Figure 4-3.	(a) mIRage TM optical images of woven fabric with dielectric ink, (b) IR spectra of the woven fabric with dielectric ink. (blue line means the higher region of the fabric; red line means the lower regions of the fabric).....	69
Figure 4-4.	(a) mIRage TM image at 1202 cm^{-1} of woven fabric with dielectric ink ($845^*974\text{ }\mu\text{m}$) (b) A zoomed in mIRage TM single frequency ratio ($1202/1412\text{ cm}^{-1}$) image of woven fabric with dielectric ink ($97^*121\text{ }\mu\text{m}$), Simultaneously collected (c) IR spectra and (d) Raman spectra.	71

Figure 4-5. Simultaneous IR/Raman analysis of inkjet-printed nonwoven e-textiles with laser confocal microscopy of pristine side of PET/PA nonwoven fabric, and inkjet-printed Ag nonwoven fabric with Raman and IR spectra respectively.75

Figure 4-6. a) Dielectric constant and b) dielectric loss of the layer-by-layer inkjet-printed nonwoven fabric.....76

Figure 4-7. Mechanism BT ink inkjet printing on fabric process.....77

Figure 4-8. Optical microscope images of Ag coated nonwoven fabric (a) surface image with a bar of 100 μm , (b) cross sectional image with a bar of 100 μm , (c) surface image of the conductive line gap with a bar of 500 μm , (d) surface image of the conductive line gap with a bar of 200 μm . SEM image of (e) the BT UV cured polymer coated fiber by a layer-by-layer process. (5000x, 10 μm bar), (f) the Ag coated fiber. (5000x, 10 μm bar).78

Figure 4-9. (a) An all-inkjet-printed textile array. (b) Bended textile array sample. (c) Schematic illustration of textile array structure. (C1 mean connector 1.) Real-time detection of different mechanical forces using the textile capacitor (d) Sensitivity of textile-based sensor under different pressure. (e) Finger tapping on textile capacitor. (f) Standard weights applied on the textile capacitor (g) Sensor performance taping 1000 times for the textile capacitor.....80

Figure 5-1. Antenna fabrication process (a) Printing of conductive ink on nonwoven fabric and dielectric UV curable ink on knit fabric assemble. (b) All-inkjet-printed antenna structure.....94

Figure 5-2. Optical microscope images of (a) Ag printed nonwoven fabric and BT dielectric UV curable ink printed knit fabric. (b) Ag printed nonwoven fabric.

	(c) BT dielectric UV curable ink printed knit fabric. SEM images of (d) cross sectional Ag printed nonwoven fabric. (e) surface of Ag printed nonwoven fabric. (f) BT dielectric UV curable ink printed knit fabric.....	96
Figure 5-3.	Resistance changes of Ag inkjet-printed nonwoven ground of antenna during bending 1000 cycles and picture of the setup for bending test in the right.	99
Figure 5-4.	(a) All-inkjet-printed textile antenna design. (b) All-inkjet-printed textile antenna simulation and experiment result.....	101
Figure 5-5.	(a) All-inkjet-printed textile antenna bending at vertical direction with R1=21.13 mm cylinder, R2=17.52mm cylinder; R3=13.85mm cylinder; (b) antenna bending at horizontal direction with R1=21.13 mm cylinder, R2=17.52mm cylinder; R3=13.85mm cylinder.....	102
Figure 5-6.	(a) All-inkjet-printed textile antenna mounted on arm, chest, abdomen and back. (b) Measured S-parameters of the textile antenna on arm, chest, abdomen and back.....	104
Figure 6-1.	Proposed mechanism for adsorption of PVP and polymer dispersant onto the surface of BT NPs by hydrogen bonds.	111
Figure 6-2.	(a) Thermal properties of the Ag ink TG (black)/DTA (red) curves. (b) FTIR spectra of the Ag ink dried at 150 °C (red, dash) and annealed under 350 °C (black, line). (c) Thermal properties of the BT ink TGA (black)/DTA (red) curves. (b) FTIR spectra of the BT (blue, dash/dot), BT/PVP (black, line) and annealing under 350 °C (red, dash).....	113
Figure 6-3.	XRD of the cured BT layer under 350 °C for 30 mins.	115

Figure 6-4.	Printing passes influences on single droplet size and roughness. (a) 3D images of single droplet during printing passes of 1, 2, 3, 4 and dry at room temperature (RT) and 150 °C. (b) Roughness of single droplet.	116
Figure 6-5.	Inkjet printing roughness of the cured printed-Ag layer with different printing passes and drop space by laser confocal scanning.	119
Figure 6-6.	80 nm Ag NP ink printing with different voltages and a constant drop space of 25 μm . (18V, 21V, 24V, 27V, 30V.).....	121
Figure 6-7.	The schematic of the inkjet-printing process of Ag/BT-PVP/Ag capacitor.	122
Figure 6-8.	Cross-sectional SEM images of the Ag/BT-PVP/ Ag capacitor with a bar of 50 μm and 5 μm	123
Figure 6-9.	(a) Capacitance and dielectric loss of all-inkjet-printed Ag_BT/PVP_Ag capacitor. (b) BT/PVP nanocomposite dielectric constant.	124
Figure 7-1.	Inkjet printing MLCC process from ink formulation to one-step sintering.....	133
Figure 7-2.	Sintering profile for the Ni/BTO capacitor in a reducing atmosphere.....	134
Figure 7-3.	Morphology and Size Distribution of Ink Nanoparticles (NPs). Nickel NPs a) SEM images and b) size distribution. BTO NPs c) SEM image and d) size distribution.	136
Figure 7-4.	Sintering Influence on the Crystal Structure of Ink Nanoparticles (NPs). (a) Schematic illustration of neck growth between nanoparticles. (b) SEM image of Ni NPs after sintering at 1300 °C with a magnification of 50 000X and a bar of 1 μm , (c) SEM image of BTO NPs after sintering at 1300 °C with a magnification of 50 000X and a bar of 1 μm	137
Figure 7-5.	AFM image of sintered BTO film.	140

Figure 7-6.	XRD result of inkjet printed capacitor before and after sintering at 1300 °C.	140
Figure 7-7.	Cross section image of inkjet-printed Ni capacitor after sintering.	141
Figure 7-8.	Capacitance and dielectric loss of the sintered Ni capacitor.....	142
Figure 8-1.	Mechanism of the BT ink fabrication.	150
Figure 8-2.	(a) TGA curves of untreated BT, BT@PD/PVP, PVP, PD, BT in ethanol, BT in ethylene glycol and BT@PD/PVP in ethylene glycol and ethanol mixture. (b) DTA curves of untreated BT, pure PD, pure PVP, and BT@PD/PVP in ethylene glycol and ethanol mixture. (c) Comparative FTIR of the BT, PD, PVP, and BT@PD/PVP. (d) Comparative Raman of BT, PD, PVP, and BT@PD/PVP.	152
Figure 8-3.	Viscosities of the BT@PD/PVP in ethylene glycol and ethanol mixture solvents at the ratio of 1:2; 1:1; 2:1, 3:1, 4:1. 0.025 Pa·s is the maximum viscosity requirements for the printer used in this paper.	155
Figure 8-4.	Surface tension of the BT ink with different ethylene glycol/ ethanol ratio. (a) EG:E=1:2, (b) EG: E=1:1, (c) EG:E=2:1.....	156
Figure 8-5.	BT NPs ink evaporation based on the Coffee Ring Effect and Marangoni Effect.....	157
Figure 8-6.	3D microscopic images of inkjet printed single dots obtained from BT ink with different solvent ratio of ethylene glycol and ethanol 1:2; 1:1; 2:1, and the height profile of the single droplets at different ratio in vertical direction.	158
Figure 8-7.	Morphologies of the inkjet printed 5 mm* 5 mm BT film using inks with different solvent ratio.	160

1 Introduction

The term ‘smart textile’ is derived from intelligent or smart materials, which can sense stimuli from the environment, react to them and adapt to them by integrating of functionalities in textile structure.² Smart textiles can be fabricated by using textile materials with additional functions (e.g., conductive fibers), embedding with electronics (such as integrating light-emitting diodes to textile cloth), or hybrid approaches combined with commercial electronics and functional textile materials.^{3,4} Key functions of smart textiles include sensors, data processing, actuator, storage, and communication.⁵ The antenna is a vital wireless communication device for receiving and transmitting relevant signals at specific frequencies.⁶ For wearable applications, it is desired that antennas be flexible enough to be suitable for the human body curvature shape and arbitrary directions of body movement. Another key device is a capacitor that can store electrical energy in an electric field.⁷ Wearable capacitors should be flexible or small enough to be integrated into the cloth without impacting comfort. Capacitor and antenna have at least one thing in common: they both require high dielectric constant materials to guarantee good performance.^{8,9} Barium titanate (BT) has a high dielectric constant of 5000 and a low dielectric loss, and this material is very stable with temperature fluctuations.¹⁰ BT can be one of the best choices for antenna and capacitor fabrication.

Printing, such as screen printing, spray coating, inkjet printing, and gravure, is one of the most widely used fabrication methods to produce electronic circuits and devices, for the reason of robustness, cost-effectiveness, and high resolution.^{11,12} The enormous growth in wearable electronics and the need for lighter, smaller, and lower-cost electronics have resulted in great

demand on printing methods. As a result, the printing of BT NPs has great potential to fabricate capacitors and antennas with desired properties (small size, high performance, flexibility, etc.).

While at present, printed electronics have been dominated by organic or conjugated polymers ink to meet the printability requirements.¹³ However, such inks' conductivity and dielectric properties are worse than inks based on metallic nanoparticles or BT NPs. The first challenge is to fabricate metallic nanoparticles conductive inks and BT NPs dielectric inks. Apart from inks design, other challenges including printing parameters, interface between ink and substrate, interfacial properties between different printed layers, selection of curing conditions, etc., will be researched in order to make high-performance antenna and capacitor by printing BT NPs.

The goal for this work was to explore the opportunities of using high dielectric constant BT nanoparticles to fabricate wearable electronics devices (antennas and capacitors) by various printing methods. (Figure 1-1) To reach this goal, the following objectives need to be achieved:

1.1 Research Objectives

The first objective of the research is to prepare flexible and breathable textile antennas and capacitor sensors by printing UV curable BT NPs. Specific tasks include:

- a. Designing barium titanate nanoparticles ink for spraying and inkjet printing, which can alter the dielectric constant of highly porous textile fabrics.
- b. Using screen printing, spray coating, and inkjet printing to design flexible all-textile antennas for wearable application.

- c. Investigating the influence of inkjet printing settings on the different substrates with different porosity and chemical components.
- d. Preparing novel breathable antenna and matching the simulation result.

The second research objective research is to fabricate small-size capacitors by inkjet printing of high-concentration BT NPs inks. Specific tasks include:

- a. Designing high concentration BT NPs dielectric ink for the fabrication of high energy density capacitor using inkjet printing.
- b. Fabricating high-concentration large-size (200 nm) nickel NPs conductive ink for inkjet printing to reduce the roughness of the printed layer.
- c. Printing silver capacitor and nickel capacitor.
- d. Optimization of the co-firing condition of Ni/BT capacitor.

The research presented in this thesis covers the whole process of printing both an antenna and capacitor, including fabricating inks, substrate selection, optimization of printing parameters, and device fabrication. In Chapter 3, a flexible antenna by spray coating and screen printing was fabricated for wearable application. In Chapter 4, a capacitor array was designed via inkjet printing BT UV curable ink for the highly sensitive pressure sensor. In Chapter 5, a breathable and flexible inkjet-printed antenna was used by Ag MOD ink and BT UV curable ink for wearable application. In Chapter 6, an all-inkjet-printed Ag capacitor was achieved with high dielectric permittivity. In Chapter 7, an all inkjet-printed co-fired Ni capacitor was gained. In Chapter 8, the high concentration BT NPs ink was optimized to be suitable for inkjet printing. This study will provide better understanding of the pros and cons of different printing methods for smart textile

applications. This research will provide insight into the novel fabrication of all-textile flexible antennas, and high-resolution and high-energy-density capacitor using printing methods, and it will be a great reference for industry and academia.

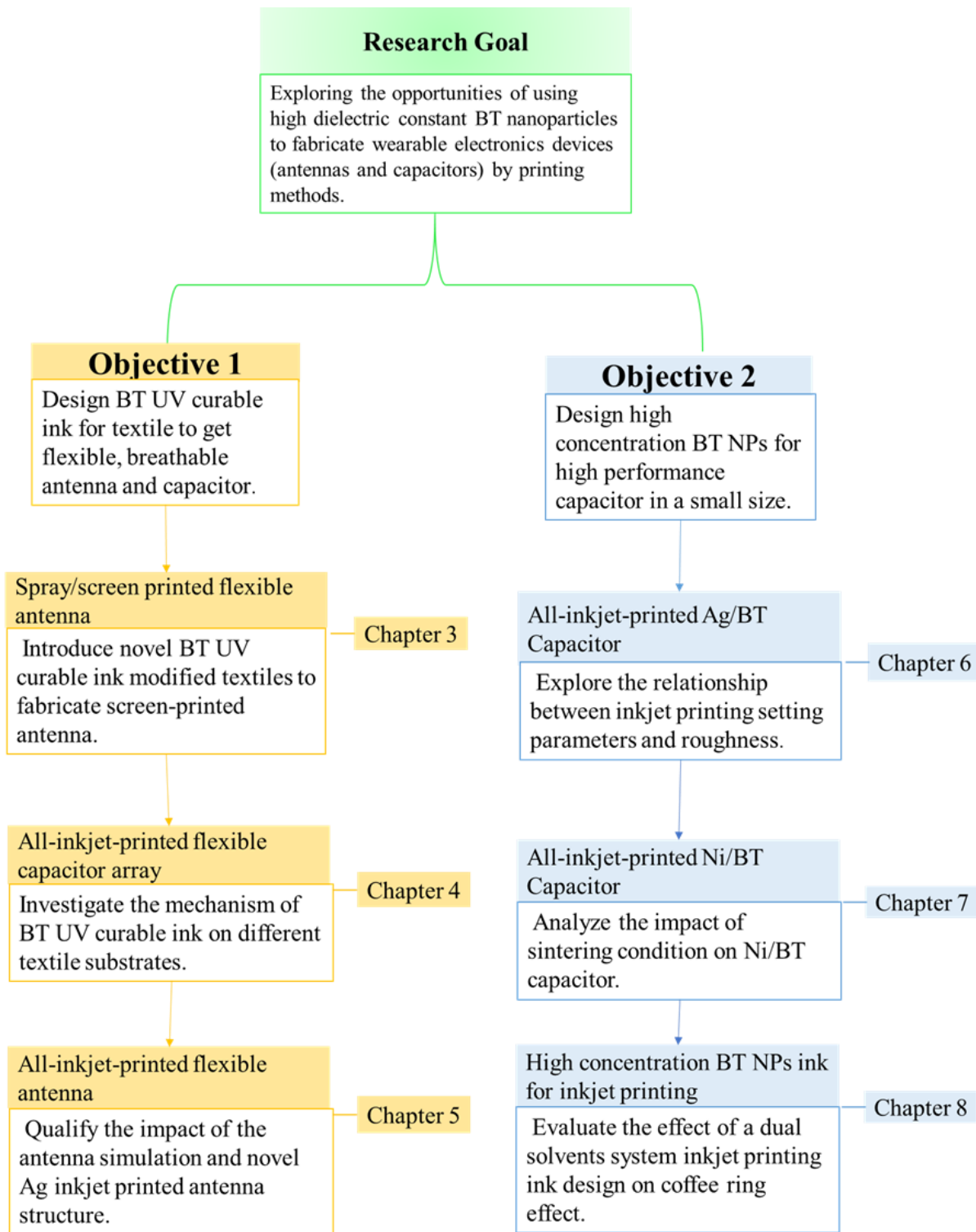


Figure 1-1. Research approach

2 Literature Review

2.1 Barium Titanate (BT)

Dielectric materials are insulators that can get polarized and store electric energy in an applied electric field.¹⁴ They are essential for electronic devices, such as antenna and capacitor. Dielectric materials are categorized into four parts: polymer, ion-gel, solid-state, and inorganic oxide. Inorganic material, also called ceramics, is the most widely used dielectric material. The ceramics are composed of oxides and minerals, including silicon oxide, alumina, and titanate oxide, etc.¹⁴ Among the inorganic oxides, perovskites that have the structure of the ABX_3 group (A=transition metal or alkaline earth, such as Na^{1+} , K^{1+} , Ca^{2+} , Sr^{2+} , Ba^{2+} , Y^{3+} ; B=small cations, such as Ga^{3+} , In^{3+} , Ti^{4+} , Mn^{4+} , Sn^{4+} , Zr^{4+} , Nb^{5+} ; X= non-metallic anions, such as O^{-2} , F^{-1} , Cl^{-1}) are the most known and widely used in electronics. The phase of the perovskites can be cubic, orthorhombic, tetragonal, or trigonal structure.¹⁵ Oxygen is the most common atom in the position X. Examples of perovskites include barium titanate ($BaTiO_3$) (BTO)¹⁵, sodium bismuth titanate ($Bi_{0.5}Na_{0.5}TiO_3$, BNT)¹⁶, $BaSn_{0.15}Ti_{0.85}O_3$ (BTS)¹⁷, $Ba_{0.6}Sr_{0.4}TiO_3$ (BST)¹⁷, and barium titanate hafnate ($BaTi_{(1-x)}Hf_xO_3$, $0 \leq x \leq 0.25$).¹⁸

$BaTiO_3$ (BT) was discovered in the 1940s, and has been an important electronic ceramic material, being incorporated into billions of capacitors every year.¹⁹ During World War II, mica was used in most capacitors. BT was designed to replace mica by doping titanium dioxide (TiO_2) with barium oxide (BaO) at a proper combination. The resultant material showed an extreme high dielectric permittivity over 1000.²⁰

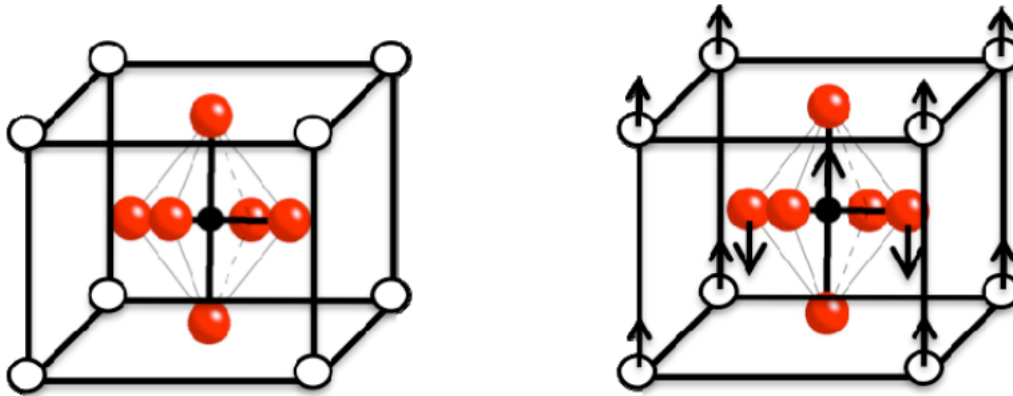


Figure 2-1. The crystal structure of BaTiO₃ at cubic phase (left) and tetragonal phase (right). Displacements of the Ba²⁺ (white), Ti⁴⁺ (black), ions relative to the O²⁻ (red) ions are indicated by the arrows.²¹

BT adopts a crystal structure with a cubic and tetragonal phase at room temperature. The unit cell is shown in Figure 2-1. In its bulk form, BT is cubic above its Curie temperature ($T_c=120^\circ\text{C}$). Below 120°C , it changes to tetragonal phase. After cooling to 0°C and -90°C , orthorhombic and rhombohedral phase is reached, respectively.¹ The structures of different crystal phase along with the spontaneous polarization vectors can be seen in Figure 2-2. Except the cubic phase, all the phases are ferroelectric.

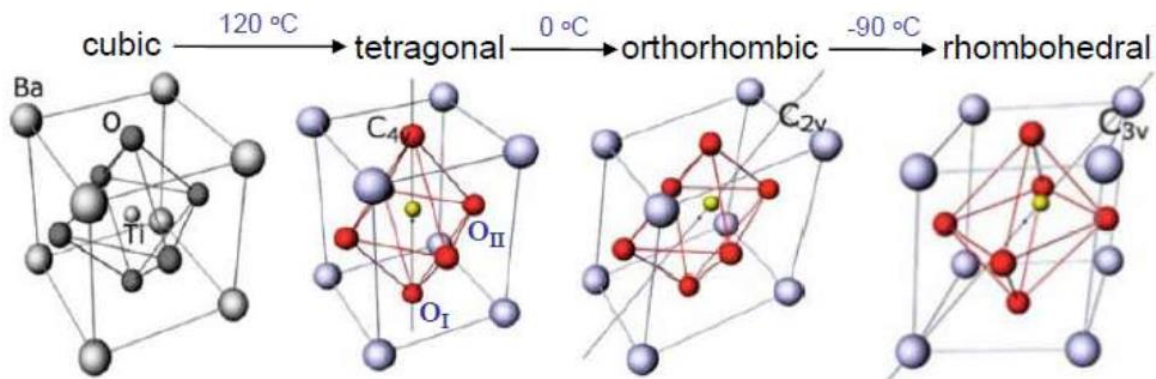


Figure 2-2. Conventional unit cell of BT in polymorphs.²²

Table 2.1. Dielectric permittivity of commonly used ceramics and polymer for capacitors.²³

Composition	Dielectric Permittivity
BaTiO ₃	1700
PMN-PT (65/35)	3640
SiO ₂	3.9
Al ₂ O ₃	9
TiO ₂	80
SrTiO ₃	2000
Fluorinated polyimide	2.6-2.8
Poly(phenyl quinoxaline)	2.8
Polystyrene	2.6
Poly(vinylidene fluoride-co-hexafluoropropylene)	~12

The dielectric constant of ceramics and polymers commonly used in the capacitor are shown in Table 2.1. The perovskite structure materials (BaTiO₃, PMN-PT (65/35), SrTiO₃) have much higher dielectric constant than polymer materials. This is due to the polarization ability in ceramic crystal structure.

In comparison with polymer, ion-gel and solid-state electrolytes dielectric materials, perovskites materials have a high dielectric constant and are very stable at high frequency. However, the need for high-temperature sintering limits the applications into textile materials. In addition, if used in printing methods, ceramic materials can be hard to print out and tend to have cracks in printed layer. Therefore, in order to use the BT material in the smart textile area by printing, ceramic and polymer material combination can be used, which is also called the polymer-matrix composites

(PMC). The PMC systems can have high dielectric constant permittivity of ceramics and good mechanic strength of polymer materials.²⁴

2.2 Printing Method

Printing is one of the most promising methods in the field of flexible and wearable electronics due to the advantages in pattern-versatility, cost-reduction, automation, and scalability^{25, 26} Electronic components have previously been demonstrated to be readily patterned on textiles via printing processes that dispensing conductive, semiconducting and insulating materials.²⁷ Example of electronic textiles (e-textiles) components that have been studies include wearable solar cells²⁸, supercapacitors^{29, 30}, biomonitoring sensors³¹, energy storage materials³², and wearable antennas^{6, 33-35}.

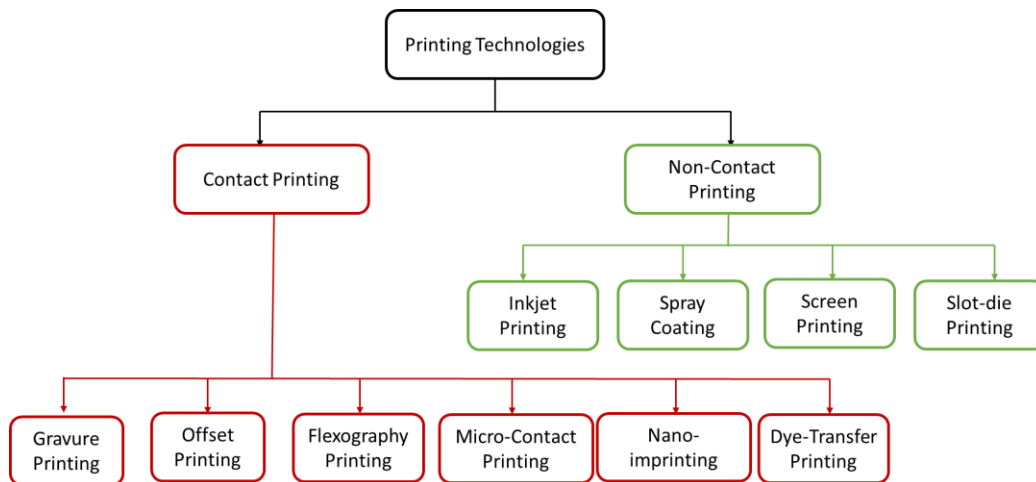


Figure 2-3. The classification of common printing technologies.

Common printing methods can be divided into two categories: contact printing and non-contact printing, as shown in Figure 2-3. Gravure (Figure 2-4a), offset (Figure 2-4b), microcontact printing (Figure 2-4c), and flexography printing (Figure 2-4d) are examples of contact printing, which allows for the direct formation of a pattern. Noncontact printing processes includes spray coating

(Figure 2-4e), screen printing (Figure 2-4f), inkjet printing (Figure 2-4g), and slot-die printing (Figure 2-4h), etc. The characteristics of various printing techniques can be found in Table 2.2 , including ink requirement, printing resolution, thickness, etc.

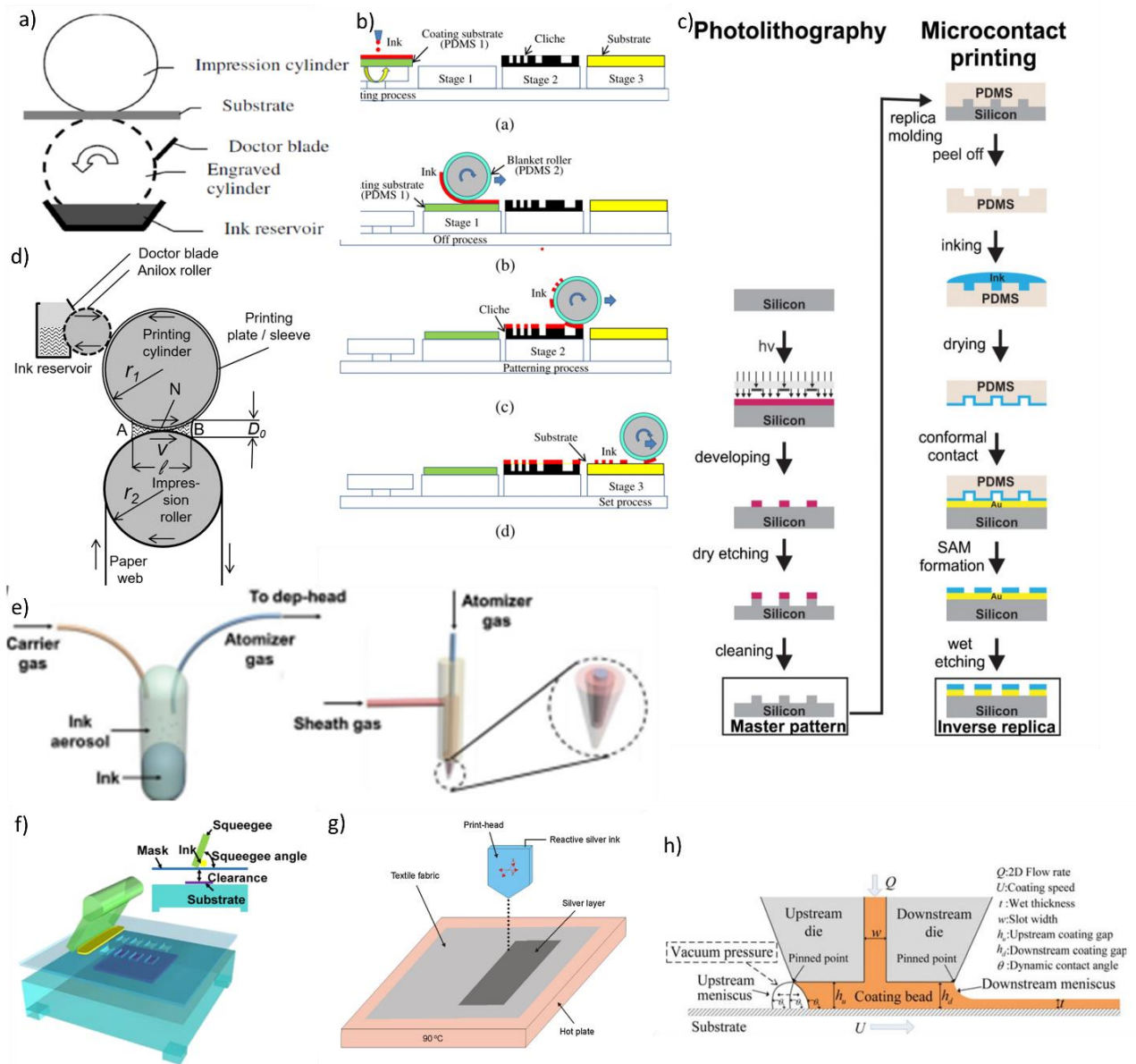


Figure 2-4. Schematic of (a) gravure processes,³⁶ (b) roll offset printing process,³⁷ (c) microcontact printing process,³⁸ (d) flexographic ink splitting process,³⁹ (e) spray coating process,⁴⁰ (f) screen printing,⁴¹ (g) inkjet printing process⁴², and (h) slot-die process.⁴³

Table 2.2. Comparison of various common printing techniques

Printing Techniques	Ink Viscosity (Pa.s)	Ink Surface Tension (mN/m)	Material Wastage	Controlled Environment	Print Resolution (μm)	Print Thickness (μm)	Print Speed (m/s)
Gravure ^{26, 36, 40, 44-48}	0.05-2	30-200	Yes	Yes	50-200	0.02-80	1-15
Offset ^{37, 49-52}	20-100	22-42	Yes	Yes	0.6-300	0.3-17	0.01
Flexographic ^{40, 52-56}	0.05-0.5	13,9-39	Yes	Yes	50-100	5-200	0.2-14
Micro-contact ^{38, 57, 58}	1.5-75	26.5-47.5	Yes	No	0.1-20	0.05-0.4	/
Screen ^{40, 52, 53, 56, 59, 60}	0.5-20	38-47	Yes	No	40-150	0.5-500	≥ 0.2
Inkjet ^{38, 61-68 40, 56, 69, 70}	0.001-0.025	25-50	No	Yes	15-100	0.01-2	0.05-6
Spray coat ^{27, 40, 71 27, 72}	0.0007-1000	/	Yes	No	150-2000	0.3-500	1.5-20
Slot-die ^{40, 43, 73}	0.001-1000	25-500	Yes	No	10-100	5-250	0.02-10

It can be found from Table 2.2 that inkjet printing has relatively good resolution and thin printing thickness, and less material waste. This technique appeals to the industry and academia due to its high total automation, high resolution, mask free and environmental friendliness. Thus, it was selected as the main printing method in this research and will be investigated extensively. For comparison, screen printing and spray coating will also be addressed briefly.

2.2.1 Inkjet Printing

Inkjet printing, developed in 1970s, is regarded as a potential candidate to reduce cost and environmental impact of electronics manufacturing.^{74, 75} Inkjet printing is a non-contact technique that enables material deposition based on a layout designed in computer. As compared to vacuum deposition, which requires post processing for pattern construction, inkjet printing provides a

single step process for patterning. In comparison to screen printing, a widely used industrial patterning process, inkjet provides an avenue for improved sustainability by lowering waste and use of harmful solvents. Due to the viability of automated process, pattern versatility, and ultrathin coatings, the application of inkjet process on electronic materials in flexible electronics,^{76, 77 61, 78-80} high-resolution and flexible conductor⁶², textile capacitors⁸¹ and flexible transistors⁸² have been reported.

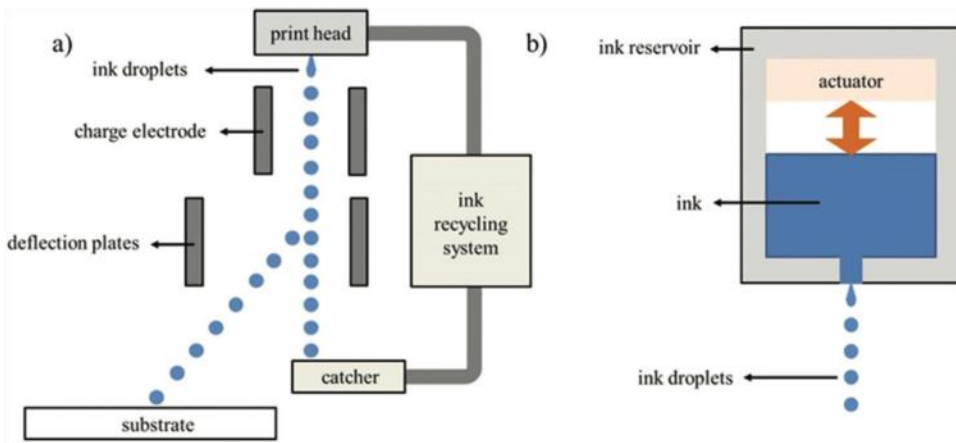


Figure 2-5. The two operation modes of inkjet-printing: (a) continuous inkjet-printing (CIJ) and (b) drop-on-demand (DOD) system.⁸³

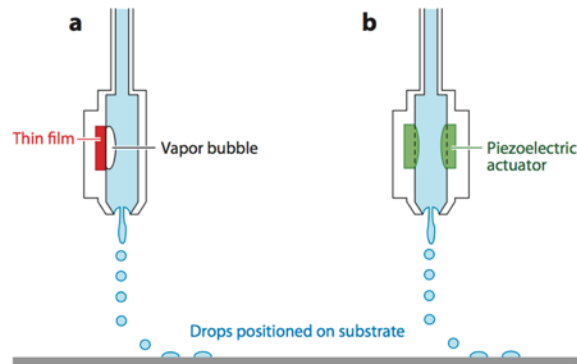


Figure 2-6. Schematic diagram showing the principles of DOD inkjet printing system. (a) a vapor pocket or bubble generated by a thin-film heater (thermal inkjet), (b) a mechanical actuation by a piezoelectric transducer (piezoelectric inkjet).⁸⁴

There are two main inkjet printing modes: continuous and drop-on-demand. (Figure 2-5Figure 2-6) Thin film electrical heater (Figure 2-6a) is used to form vapor bubble to push ink out. This method has a super-fast printing speed. However, there is significant limitation in ink composition and printing size. In high temperature, the nanoparticles inside inks aggregate heavily, which may impact ink properties and clog nozzles. Thus, nanomaterials are not suitable in this type printer. The DOD system uses piezoelectric actuator (Figure 2-6b) to push ink out by applying voltage. Piezo actuator has better control over the droplet. More materials and higher resolution can be printed through DOD printing.⁸⁴

In inkjet printing process, inks are dispensed via openings or nozzles (10-50 μm) on the patterned surface of printhead.⁸³ Inkjet process with fully automated DOD system uses low viscosity inks (≤ 25 cps), which would lead to the formation of ultrathin coatings on substrates and patterns with high resolution. A fundamental challenge is the need for functional materials inks within the printable range for inkjet printing. Furthermore, the spreading of low viscosity inks on a substrate challenges the ability to form devices with high resolution and low surface roughness. It is necessary to understand the printing process and mechanism in order to obtain desired film thickness and roughness. Printing of function materials with ultrathin coating thickness is integral to maintaining flexibility in substrates.

2.2.1.1 Voltage and waveform

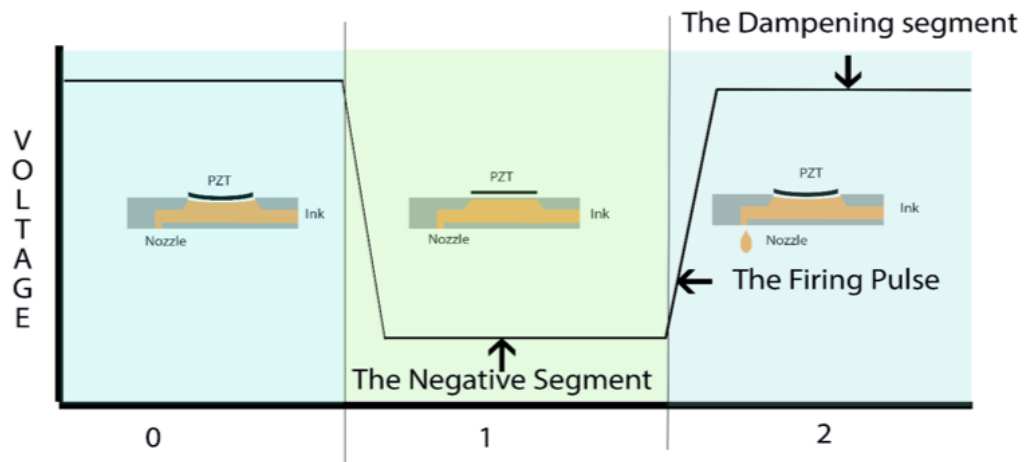


Figure 2-7. Waveform of the piezoelectric printing.

When printer is powered, the print head maintains a specific voltage, causing PZT deformation. Some ink is inside chamber, but it is still in a non-jetting position. In segment 1 (Fill), voltage is decreased and the PZT returns to a resting state, causing the expansion of chamber volume. In segment 2 (Fire), voltage is applied to PZT and cause deformation. At this stage, ink comes out from the nozzle. (Figure 2-7) When the chamber volume shrinks, the excessive ink is ejected. The waveform can control ink printing time, and it needs to take ink's physical property into account in order to push ink out.⁸⁵⁻⁸⁷ Higher voltage can induce heavier PZT deformation, and more ink can be pushed from the chamber. Increase in droplet volume can be achieved by increasing voltage.

From what have been discussed above, waveform and voltage together control the formation of inkjet droplet. The waveform synchronizes the viscosity and surface tension of ink to print each droplet repeatedly, and voltage controls single droplet volume. Extend the firing stage could also increase droplet volume, but the synchronism of the ink drops out and fill in can be complicated. Normally, droplet volume is manipulated by adjusting voltage instead of waveform.⁸⁷

2.2.1.2 Printing speed and frequency

Frequency can directly affect printing speed, which can decide outcome efficiency. Different types of printers have different frequency ranges. The continuous inkjet-printing (CIJ) systems have drop generation rates in the range of 20-60kHz and drop velocity at the nozzle over 10 m/s, while the DOD printing is usually at acoustic frequency of 1-20 kHz. Printing time is not only controlled by nozzle printing speed, but also influenced by printed area. The time t_p to coat an area A is⁸⁸:

$$t_p = A/[d^2fN_jN_H]$$

where d is the drop spacing for the chosen printing grid size, f is the ejector firing frequency, N_j is the number of ejectors in a print head, and N_H is the number of heads.⁸⁸

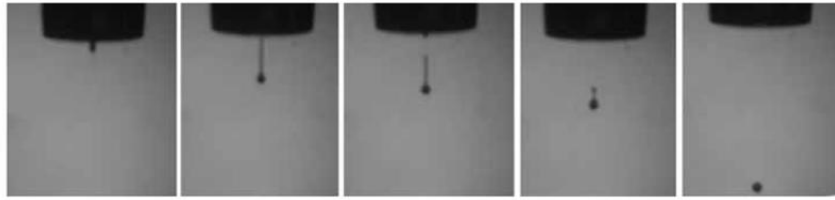


Figure 2-8. Time sequence photographs for the ejection of a 60 μm diameter drop from a nozzle, showing the tail that eventually releases and merges with the main drop.⁸⁸

In Figure 2-8, single droplet ejects from nozzle with a long tail that eventually releases and merges with main drop.⁸⁸ If frequency is not matched with the final droplet formation, droplets merges before contacting the substrate. For every ink, it is crucial to optimize the frequency and voltage to get stable and repeatable droplets. Limitation of frequency and printer head motion speed decide the maximum printing speed for different types of printers. For Fuji film Dimatix (model DMP-2850), printer head motion speed is 300 mm/s.⁸⁷ For other types of printers, print speed can reach 6 m/s.⁷⁰ High speed would benefit large scale fabrication. However, printing high resolution pattern is the priority for inkjet printing. The post-processing, such as drying and sintering steps of printed layer, would cost more time compare to the whole printing process.⁸⁹

2.2.1.3 Height

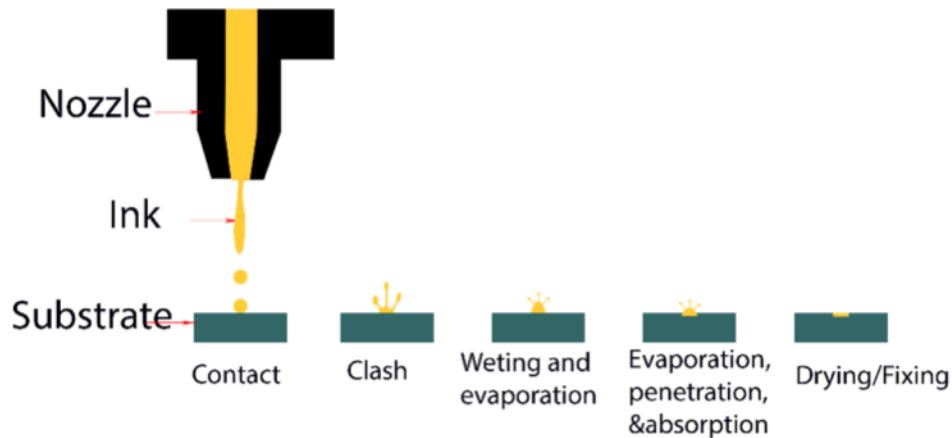


Figure 2-9. Inkjet printing process.

Inkjet process can be divided into the droplet formation process and the contact process between a single droplet and substrate.⁹⁰ Waveform and voltage applied to printing head chamber generate the single droplet. Then each droplet leaves the nozzle and hits the substrate until it is dried. The height between printer head and substrate plays an important role in this process. Because of the relative movement of the printer head and substrate, the height may cause the deviation in droplet drop position.⁸⁸ As shown in Figure 2-9, the inkjet printing can be divided into five processes. Contact process happens when the ink hits the substrate and it can be influenced by the height between the nozzle and substrate; in ~ 0.1 ms after the droplet contacts the substrate, the ink droplet clashes on the substrate.⁷⁷ After a few milliseconds, the ink will be wetting the surface and evaporating.⁷⁷ For glass substrate, the droplet deposition process can be divided into five time-sequential phases: kinematic, spreading, retracting, wetting, and equilibrium. (Figure 2-10)

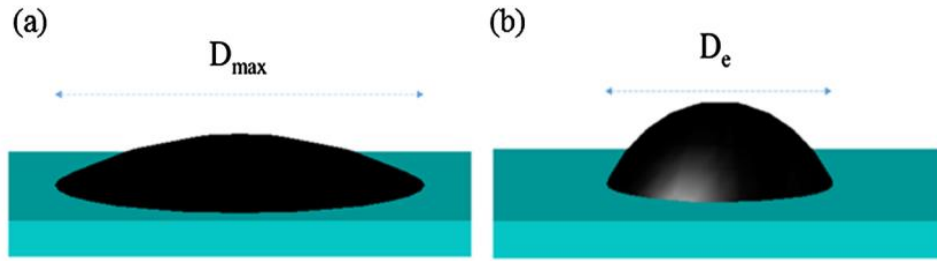


Figure 2-10. Schematic illustration of the single droplet impinges on glass substrate. (a) Spreading process, D_{\max} is the maximum diameter of the droplet; (b) Equilibrium state of a droplet, D_e is the diameter of the droplet.⁶⁶

If substrate is rough or porous, the inks can evaporate, penetrate, and be absorbed on the substrate. During this time, the surface spreading competes with capillary absorption, which is influenced by the coating layer's surface chemistry and geometrical properties of the substrate. Then the ink will dry on the substrate, which may take hours. The interaction between ink and substrate is more affected by surface energy for smooth substrate, and pore size and volume for rough substrate. During drying processes, ink evaporation rate is critical to the inkjet results.^{11, 77} If the ink evaporation rate is too fast, the ink formation process may be impacted negatively. The droplet may dry before it totally leaves the nozzle, which may cause the blocking.

2.2.1.4 Drop space

The frequency decides the drop velocity of droplets, while drop space controls the droplets position in the printing area. The resolution is defined by the Dots per Inch (DPI), which is decided by the drop space of the inkjet printer. Figure 2-11 shows the effects of droplet number and drop space on droplet mergers. For two droplets to merge, drop space needs to be less than $57\ \mu\text{m}$. The droplets merging would be difficult when drop space increases. And for more droplets to merge with each other, the drop space needs to be reduced. Ning et al. fabricated a $2.4\ \mu\text{m}$ channel by altering the

drop space of vertical and horizon space.⁶⁶ Sowade et al. used drop space to control the transistor effects, and investigated the influence of the channel width to channel length ratio (W/L) on the transistor performance.⁸² From these, it can be found that drop space is very important for high-resolution pattern printing.

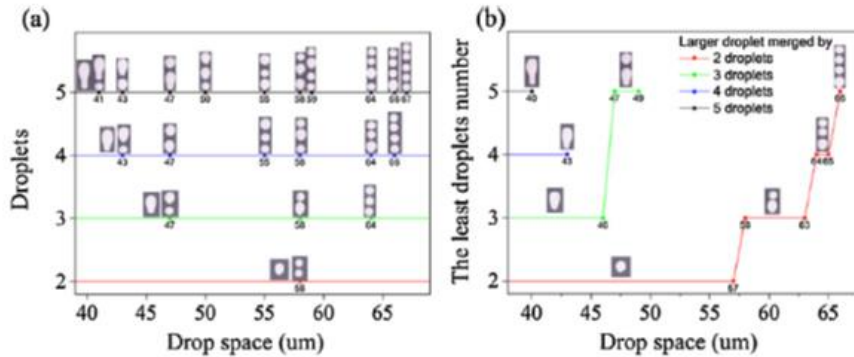


Figure 2-11. (a) Contact phenomenon of two droplets, three droplets, four droplets and five droplets; (b) the least number of droplets for the forming of larger droplet.⁶⁶

2.2.1.5 Ink printability

At a given voltage and waveform, the printing fluids with different viscosity, density, and surface tension may have different drop size and formation process. Navier-Stokes equations can be used to predict the droplet ejection for inks with different physical parameters at certain inkjet setting.⁹¹ The influences of waveform, voltage, height, etc., on inkjet printing are taken into consideration. To ensure that every ink droplet can be printed in the same status, some characteristic numbers can be used to predict the inkjet behavior. Such as Reynolds number (Re), Weber number (We) and Ohnesorge number (Oh)⁹²:

$$Re = v\rho\alpha/\eta$$

$$We = v^2\rho\alpha/\sigma$$

$$Oh = \sqrt{We}/Re = \eta/\sqrt{\rho\alpha\sigma}$$

$$Z = \sqrt{\rho\alpha\sigma}/\eta = Re/\sqrt{We}$$

where, ρ represents density, α represents characteristic length (typically drop diameter), v represents velocity, η represents viscosity, and σ represents surface tension.

Re refers to the ratio of the inertial force to the viscous force. We relates to inertial force and surface tension. Oh relates the viscous force to the inertial force and surface tension.⁹³ Parameter $Z=1/Oh$ is used to indicate printability, which should be in the range from 1 to 10.⁹⁴

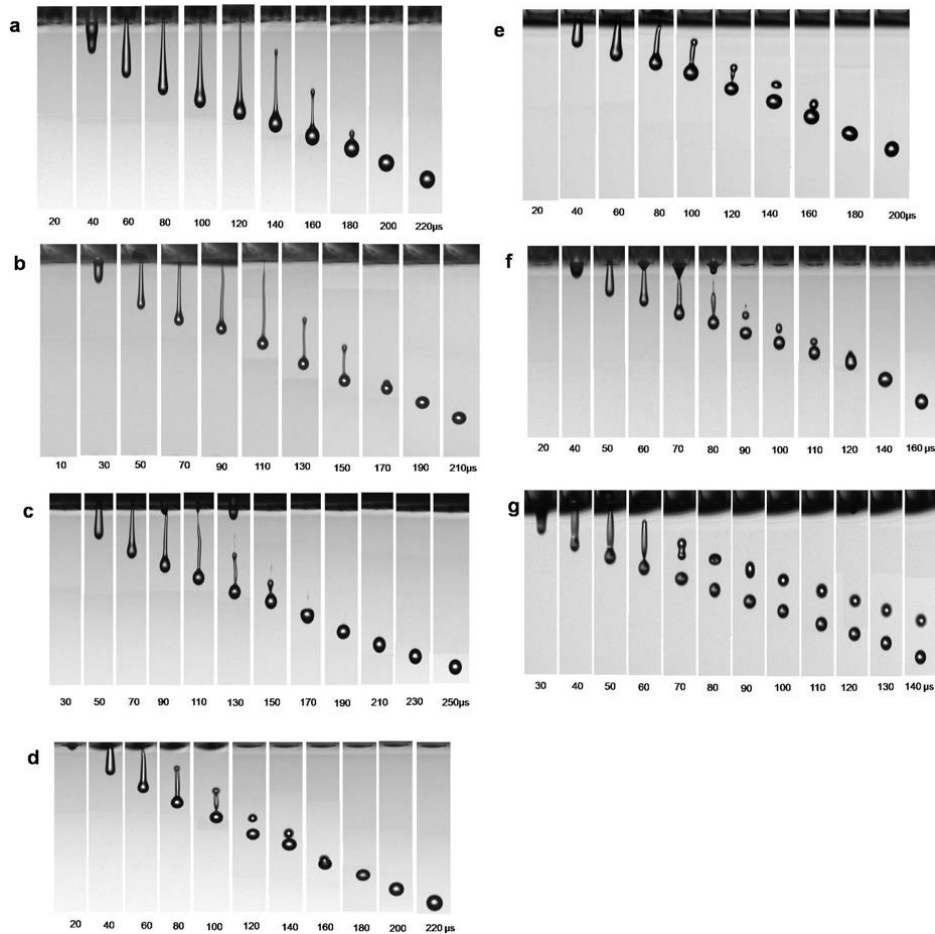


Figure 2-12. Representative photo sequence of drop formation for fluids with values of Z ranging from 2 to 17 at a constant driving voltage of 25 V: (a) $Z = 2.17$, (b) $Z = 3.57$, (c) $Z = 4.08$, (d) $Z = 6.57$, (e) $Z = 7.32$, (f) $Z = 13.68$, and (g) $Z = 17.32$.⁹⁴

The influence of printing parameter Z on the droplet formation is illustrated in Figure 2-12. The formability of single droplet with different Z values can be clearly observed. When Z is from 1 to 4, viscous dissipation prevents drop ejection. When Z is over 14, the droplet is accompanied by satellite droplets.⁹⁴

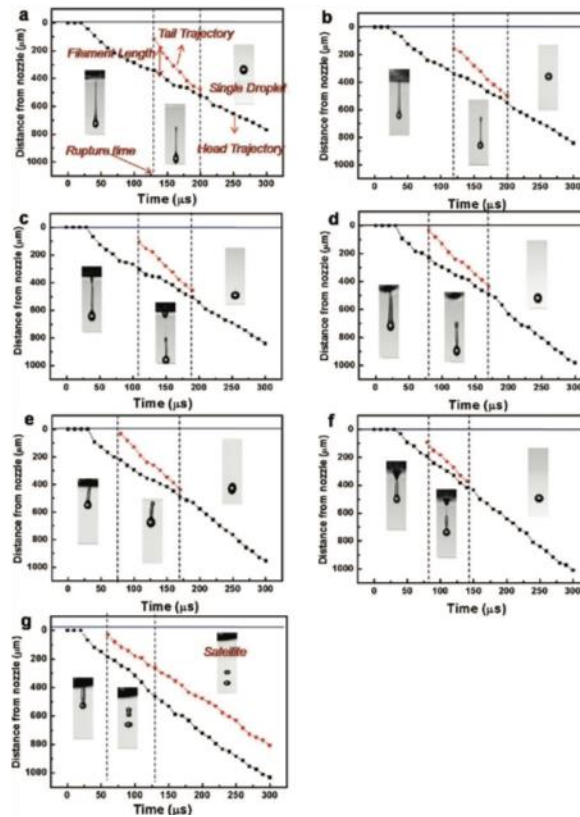


Figure 2-13. Representative trajectories of the ejected droplets as a function of the elapsed time for fluids with values of Z ranging from 2 to 17 at a constant driving voltage of 25 V: (a) $Z=2.17$, (b) $Z=3.57$, (c) $Z=4.08$, (d) $Z=6.57$, (e) $Z=7.32$, (f) $Z=13.68$, and (g) $Z=17.32$.⁹⁴

The droplet formation process can be divided into these stages: the droplets ejected from the nozzle, filament stretch, rupture, liquid recoil, and the formation of a single droplet or satellite.⁹⁴ (Figure 2-13) When Z is in the range of 2-4, the filament elapse time is around 50 μs , the stretched time is approximately 120 μs , and filament rupture time is about 140 μs . With high Z values (>14),

the droplet will be divided into two droplets after 130 μs . This information would be useful to predict the inkjet printing process.

2.2.1.6 Ink drying

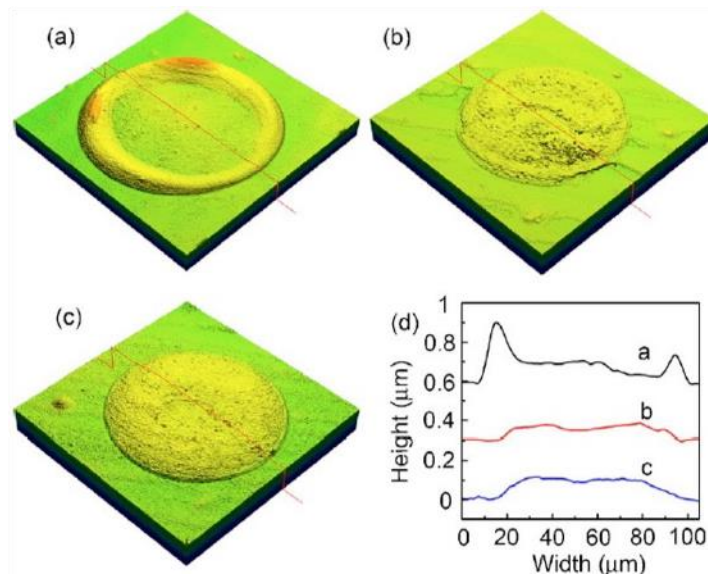


Figure 2-14. Confocal laser scattering microscopic 3D images for inkjet printed single dots obtained from conductive inks with varying solvent compositions: (a) 0, (b) 16, and (c) 32 wt% ethylene glycol.⁹⁵

The droplet drying process is a vital factor for the surface roughness of printed pattern. Yanlin et al. used photonic crystal ink with different water and ethylene glycol ratio to control the ink's dynamic wettability. The range of the surface tension is 0.77-1.5 mN/m. Figure 2-14 shows the surface tension affects the roughness of the printed patterns.⁹⁵

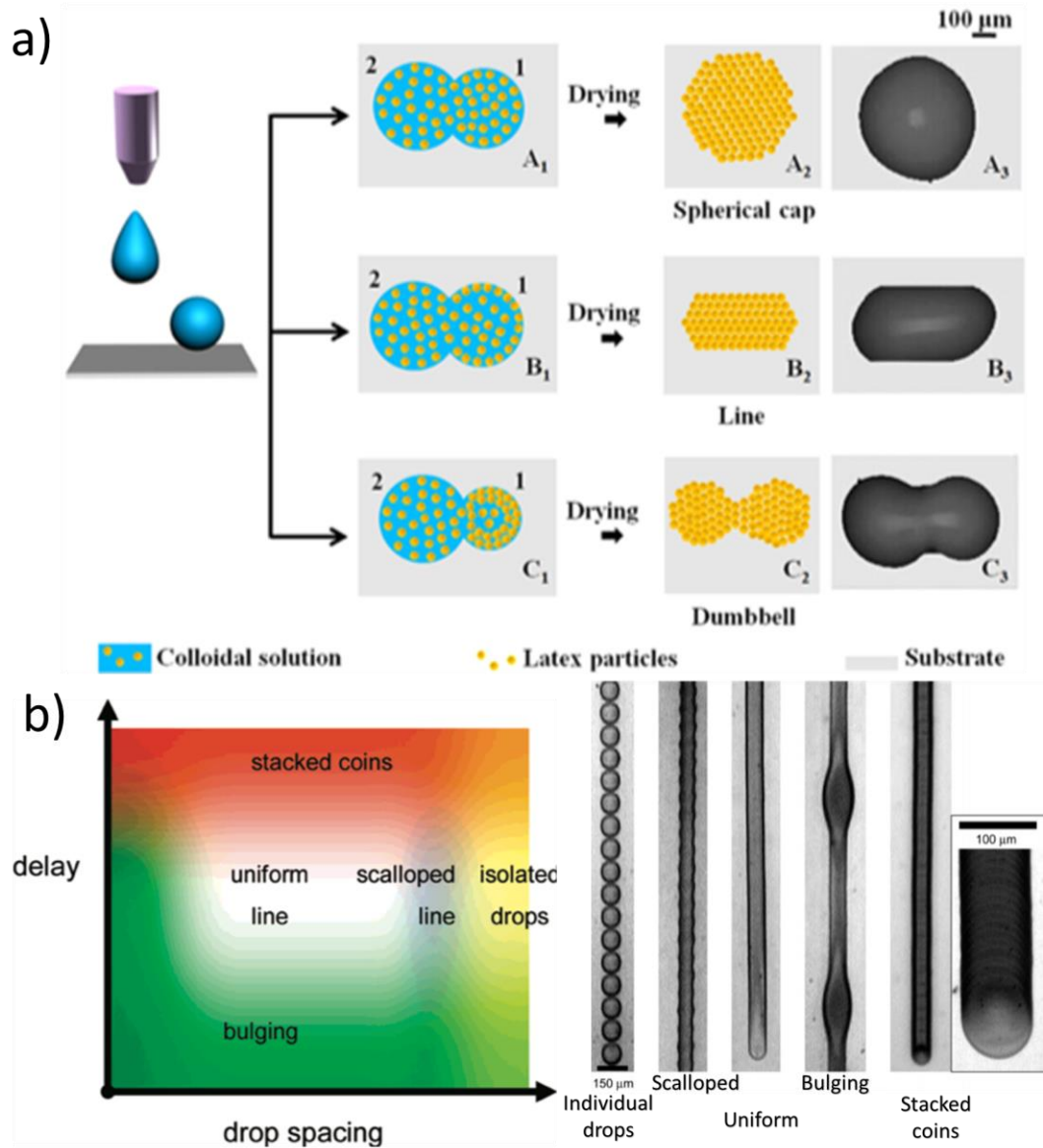


Figure 2-15. (a) Three typical coalescing cases of the neighboring ink droplets induced by different dynamic wettabilities of ink droplets on the substrates;⁹⁶ (b) the effect of drop spacing and time delay on the behavior of a printed line at an intermediate temperature, and the principal printed line pattern with the decrease of drop spacing.⁹⁷

For massive droplets interaction, surface tension and nanoparticle concentration dominate the dynamic wettability of droplets on the substrate, as shown in Figure 2-15. In Figure 2-15a, the surface tension droplet 1 is similar to droplet 2 in case A, while the surface tension of droplet 1 in

case B and C is smaller than droplet 2 due to the fast evaporation of water. In case A and B, the nanoparticle concentration is lower than case C. In case A, two droplets coalesce with each other, and a spherical cap pattern is formed after drying. In case B, some nanoparticles of the droplet 1 assemble and pin on the substrate during the coalescing and drying, and a straight line can be formed. In case C, plenty of nanoparticles assemble and pin on the substrate, which leads to dumbbell formation.

As a complex computer-controlled process, inkjet printing has control over substrate temperature, print delay time, drop space, etc. Soltman et al. used poly (3,4-ethylenedioxythiophene) poly(styrenesulfonate) (PEDOT/PSS) (1.3 %) in water to print out fine lines. The drop spacing and delay time were controlled to observe different primary morphologies, such as a scalloped line, a smooth line, a bulging line, and stacked coins, which are shown in Figure 2-15b.⁹⁷ Increasing the substrate temperature will lead to fast evaporation of ink, which can yield coffee ring. When the ink drops on cold substrate, the formation of coffee ring can be avoided.⁹⁷ In Figure 2-15b, the effect of drop spacing and time delay on the behavior of a printed line at an intermediate temperature is shown. By adjusting the drop spacing and delay time, a uniform line can be obtained.⁹⁷

2.2.2 Screen Printing

Due to the simplicity and scalability, screen printing is widely used in electronics.^{41, 59, 98} Screen printing process is shown in Figure 2-16. Screen masks are used to deposit materials onto large-area substrate by pressing ink through a patterned stencil with a squeegee.^{59, 99} Screen printing inks viscosity ranges from 0.1 to 10 Pa·s and can form films with a thickness from 500 nm to 500 μm.

^{40,95} Screen printing method has low requirement on the substrate and printing materials, so it is widely used in smart textiles.⁴⁰

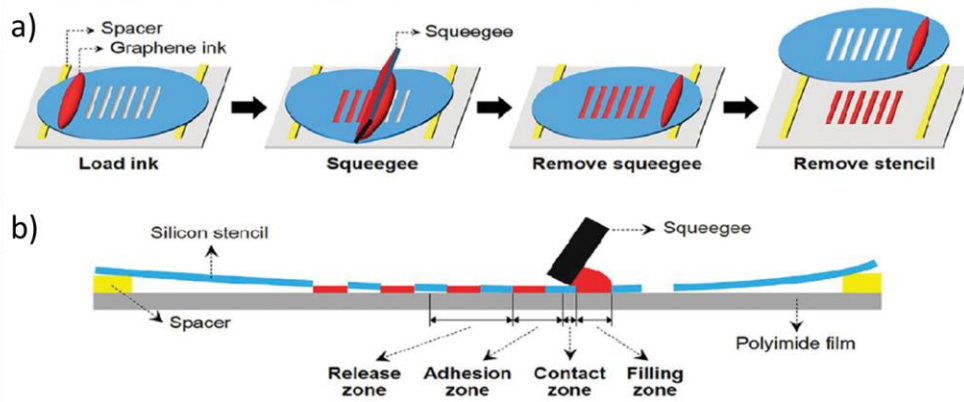


Figure 2-16. (a) Schematic process of screen printing using the silicone stencil and a pristine graphene ink. (b) Cross-sectional illustration of the screen printing method.⁵⁹

2.2.3 Spray Coating

Spray coating is a high throughput non-contact printing method. There are mainly three types of spray techniques: electrostatic spray technique, air pressure spray technique, and hybrid spray technique. The electrostatic spray technique utilizes high voltage that is applied to the nozzle to generate microdroplets.⁷² The droplet size can reach nanometer scale by this method. Air pressure technique use dual-nozzle system with high air pressure which generate the droplets. This method can avoid the nozzle clogging and have a much higher speed than electrostatic spray technique. However, the flow velocity is unstable, due to the collision with air. Hybrid spraying involves both the electrostatic spraying and air pressure spraying techniques.⁷¹ This method is expected to have a low turbulence from air pressure which can improve the stability.⁷¹ The process will make the colloidal suspensions or chemical precursor solutions into numerous 2-5 μm droplets.⁴⁰ The

thickness of the printed layer can be altered by printing speed and voltage. The different spraying techniques can be found in Figure 2-17.

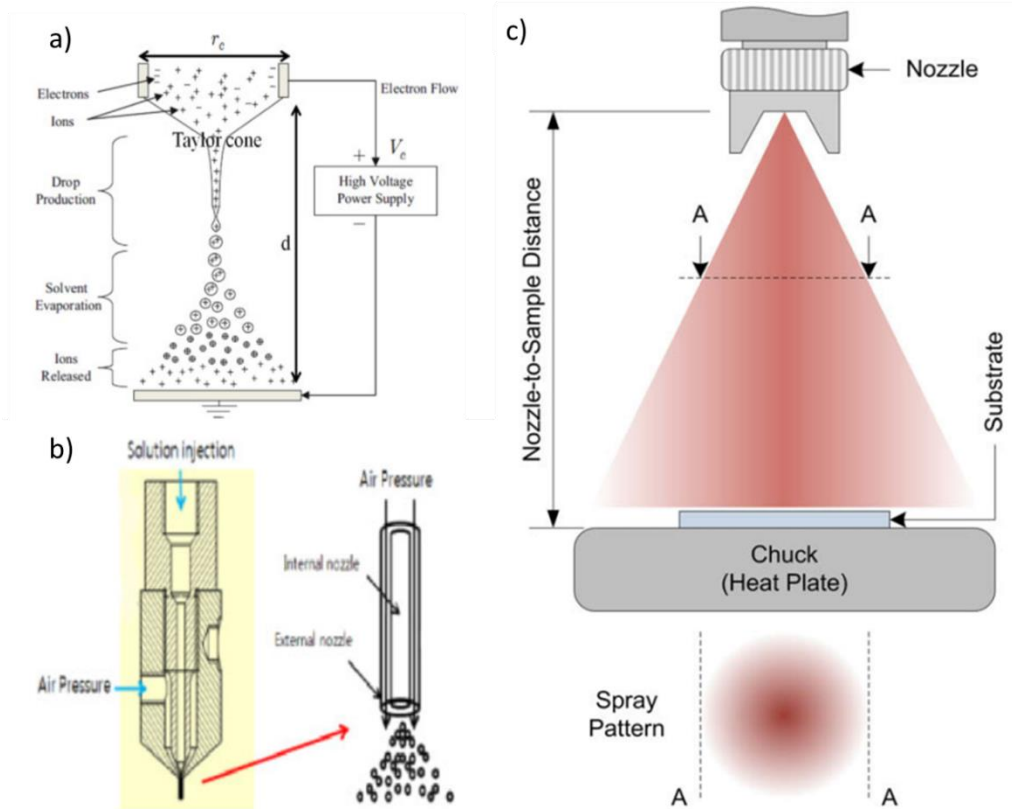


Figure 2-17. (a) Electrostatic spraying,⁷¹ (b) air pressure spraying,⁷¹ and (c) hybrid spraying.⁷²

2.3 Wearable Antenna

In general, antennas are of great importance for wearable electronics in Internet of Things (IoT) applications, serving as a communication platform to convert radio waves as information signals to wirelessly transmit data between sensors, actuators, and processors. For wearable applications specifically, antennas may be distributed across the body for body area networks. It is desired that the antenna be flexible enough to conform to the human body curvature shape and arbitrary directions of bending during the body movement.

Various manufacturing techniques for wearable antennas have been developed, such as screen printing,^{99, 100} metalized adhesive tape¹⁰¹⁻¹⁰⁴, liquid metal¹⁰⁵, embroidered textiles¹⁰⁶⁻¹¹¹, and inkjet printing.¹¹²⁻¹¹⁴ (Figure 2-18) Among these techniques, printing methods, such as screen printing and inkjet printing, are considered as promising methods for the antenna design due to the advantages in pattern-versatility, cost-reduction, automation, and scalability.^{25, 26}

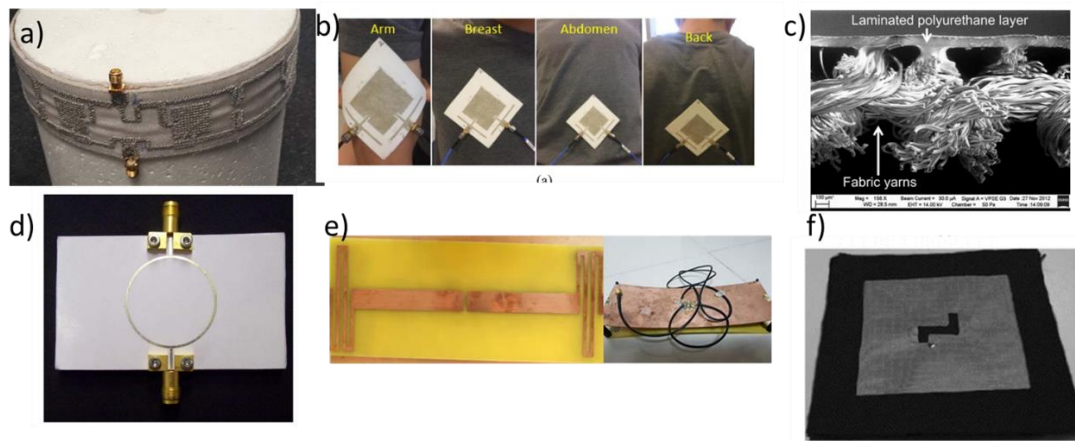


Figure 2-18. Wearable antennas by different fabrication methods. (a) Antenna embroidered conductive fibers and yarns.¹¹⁵ (b) Screen printed textile antenna.⁹⁹ (c) Inkjet printed textile antenna.¹¹⁶ (d) Inkjet printed paper antenna.¹¹⁴ (e) Antenna by copper sheet.¹¹⁷ (f) Antenna by conductive fabric.¹¹⁸

Significant progress in the processing of flexible printed antennas have been previously achieved.^{114, 116, 119-123} Sa'don et al. fabricated a screen-printed graphene antenna for 5G application.¹²⁴ Ryberg et al. presented a patch antenna and a quasi-yagi antenna by inkjet printing of silver nanoparticles on photo-paper. Both antennas demonstrated good matching and acceptable efficiency at frequency of 2.4 GHz.¹¹⁴ The above mentioned antenna are impermeable and not preferred for wearable applications. Due to a textile substrate's inherent flexibility, breathability,

and their ubiquitous use in our daily lives the use of textiles as a building block for electronics is perceived as logical means for wearable antennas.

For wearable antennas, the flexible conductive materials in the patch and ground plane have been widely researched, while flexible dielectric materials for antenna is rarely noticed. The dielectric property of the antenna substrate (dielectric constant and dielectric loss) can decide the bandwidth and the efficiency of the antenna.¹²⁵ For textile material, the dielectric properties are dependent on the constitution of polymer fibers, and packing density.¹²⁶ Considering the high porosity structure of textile materials, the relative permittivity is very low (between 1 and 2). Due to this reason, downsizing antenna materials can be a great challenge. The antenna length needs to match one quarter of the radio-wave wavelength, to ensure efficient transmission and reception of resonance between the radio wave and element.⁶ The wavelength will decrease when transfer from air into high dielectric constant materials.^{127, 128} Therefore, high dielectric constant is very essential to minimize the antenna size.

Even though high dielectric constant materials are essential for small-size patch antennas, the efficiency is poor due to the surface-wave excitation and narrow bandwidth.^{111, 129, 130} The low dielectric constant reduce the surface wave losses which are tied to guided wave propagation within the substrate, gaining acceptable efficiency and high gain. The relations between the size of antenna, width, length, effective length, effective dielectric constant, height and width of the air boundary can be shown as follows¹³¹⁻¹³³:

$$W = \frac{c}{2f_r} \sqrt{\frac{2}{\epsilon_r + 1}}$$

$$L = \frac{c}{2f_r\sqrt{\varepsilon_{eff}}} - 2\Delta L$$

$$\varepsilon_{eff} = \frac{\varepsilon_r + 1}{2} + \frac{\varepsilon_r - 1}{2} \left[1 + 12 \frac{h}{W}\right]^{-1/2}$$

$$\Delta L = 0.412h \frac{\varepsilon_r + 0.3}{\varepsilon_r - 0.258} \times \frac{\frac{W}{h} + 0.264}{\frac{W}{h} + 0.8}$$

$$L_{eff} = \frac{c}{2f_r\sqrt{\varepsilon_{eff}}}$$

$$L = L_{eff} - 2\Delta L$$

$$L_g = 6h + L$$

$$W_g = 6h + W$$

where W is the width, L is the length, ΔL is increment in length and L_{eff} is effective length. L_g and W_g are the length and width of air boundaries. ε_{eff} is the effective dielectric constant, and ε_r is the dielectric constant. f_r is the desired frequency, and c is the light velocity.

Knit fabrics with large loops structure show excellent flexibility and is widely used in the commercial textiles. However, due to the high porosity, the dielectric constant of knit fabric usually is much lower than woven and nonwoven fabric. If we could print high dielectric constant BT NPs onto the knit fabric and increase the dielectric constant, the knit fabric can be used as antenna substrate.

2.4 Capacitor

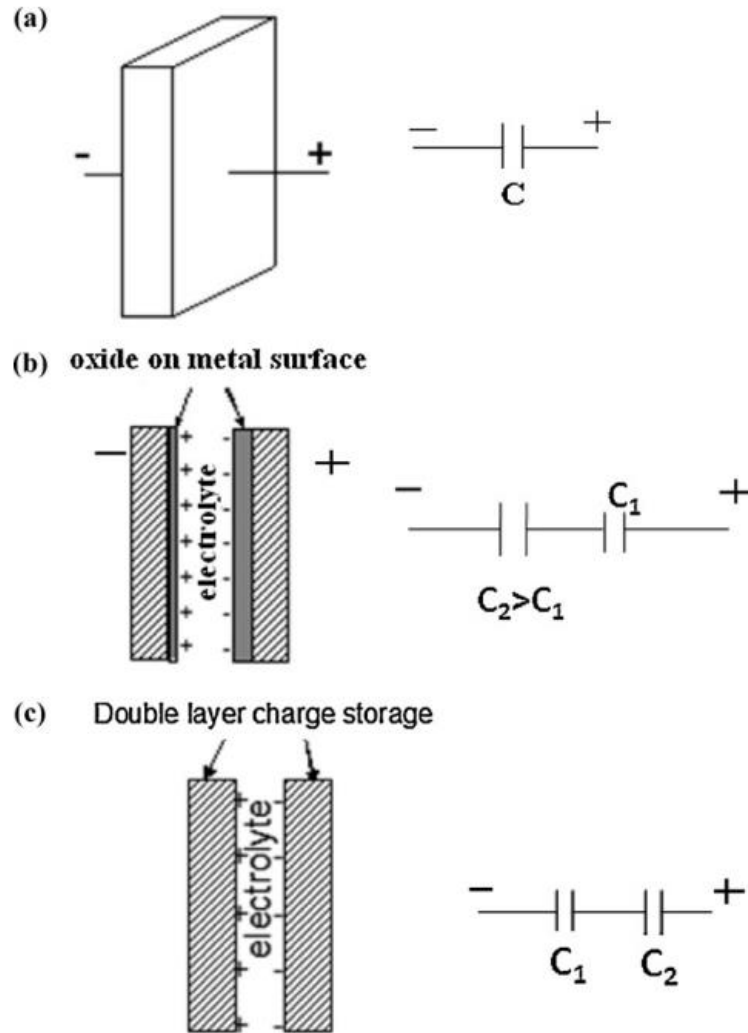


Figure 2-19. Schematic sketches for (a) electrostatic, (b) electrolytic and (c) electrochemical capacitors.⁷

The capacitor is important passive electronic component in a circuit for storing electrical energy in an electric field. There are three types of the capacitors, including electrostatic capacitors, electrolytic capacitors, and electrochemical capacitors, as shown in Figure 2-19. Electrostatic capacitors consist of a pair of conductors separated with dielectric material, such as air, mica, polymer, ceramic material, etc. The capacitance (C) is expressed as⁷:

$$C = \varepsilon_0 \varepsilon_r \frac{A}{d}$$

where proportionality constant $\varepsilon_0=8.9\times 10^{-12}$ F/m. ε_r is the dielectric constant of the dielectric layer. A is the capacitor area. d is the distance between conductors.

Electrolytic capacitor is made of a metal that forms an insulating oxide thin layer through anodization. A solid, liquid, or gel electrolyte covers the dielectric layer, acting as the negative plate of capacitor. There are three families of electrolytic capacitors include aluminum electrolytic capacitor, tantalum electrolytic capacitor and niobium electrolytic capacitor.^{134, 135} The electrolyte capacitor has very high capacitance, but suffer from the poor tolerances, high instability, and gradual loss of capacitance especially when subjected to heat and high voltage.¹³⁶ Electrochemical capacitor is also called supercapacitor, which includes electrochemical double-layer capacitor that relies on the charge storage of ion adsorption, and pseudo-capacitor that are based on the charge storage involving fast surface redox reactions.¹³⁷ The supercapacitor has much higher capacitance value, however, the lower voltages limits.

At present, the wearable capacitors mainly belong to electrochemical capacitors, such as CNTs@SF core-sheath fiber supercapacitor,¹³⁸ and other capacitor fibers^{139, 140}. For wearable application, the capacitors should be robust and stable. Therefore the electrostatic capacitors are more advantageous. The capacitance of the electrostatic capacitors is mainly decided by the dielectric layer. The BaTiO₃ with a perovskite structure has high dielectric constant, and low cost, which can be one of the best options for the capacitors.

To be suitable for low temperature application, BT nanocomposite materials have been widely researched. Konno et. al fabricated BT nanocomposite films by dispersing BT NPs into polyimide (PI) matrix through in situ polymerization.¹⁴¹ Chiang et. al designed BT/polymer composites which can be used from 100 Hz to 10 GHz and -140 to 150°C.¹⁴² To get the BT NPs well dispersed, most of the BT NPs have surface treatment.^{24, 143-146} The size of the BT NPs is also an essential factor for dispersion and dielectric properties.^{147, 148}

The dielectric constant for the two-phase composite (BT/nanocomposite) can be calculated by Lichtenecker equation:^{149, 150}

$$\log \varepsilon_{eff} = v_h \log \varepsilon_h + v_f \log \varepsilon_f$$

where ε_{eff} , ε_h , and ε_f are the dielectric constant of the composite, host (polymer), and filler (BT NPs), respectively. v_h , and v_f are the volume fractions of the host and filler, respectively.

The high concentration of the BT NPs would increase the dielectric constant greatly at low temperature. A considerable need exists for capacitors with small size and large capacity, especially for wearable electronics. Capacitor printed with high-concentration BT NPs ink would have higher energy capability and will be preferred for smart textile applications.

Apart from single layer high-capacity capacitor with small size, multilayer ceramic capacitor (MLCC) is a potential candidate to be used as wearable capacitor. MLCCs are fabricated with a base metal electrode, where successive layers of dielectric and electrodes are stacked¹⁵¹, as shown in Figure 2-20. MLCCs have received increasing attention in energy-storage applications due to the advantages of high-power density, and fast charge/discharge rates.¹⁵² The BaTiO₃-base

MLCCs with high capacitance density are widely used in the electronic devices, and more than two billion pieces are manufactured every year.^{153, 154} Conventional printing method for the MLCCs is shown in Figure 2-21.

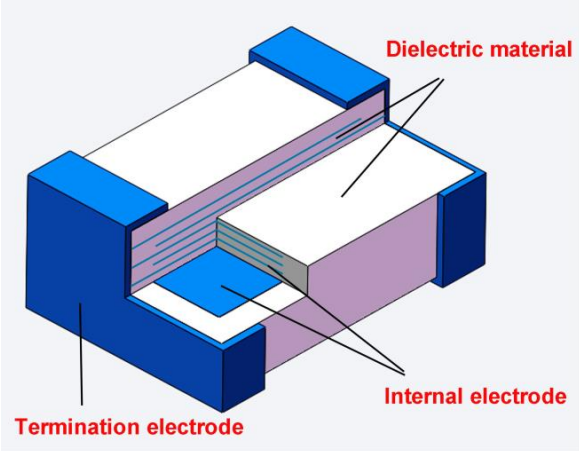


Figure 2-20. Schematic of multilayer capacitor ceramic.¹⁵⁵

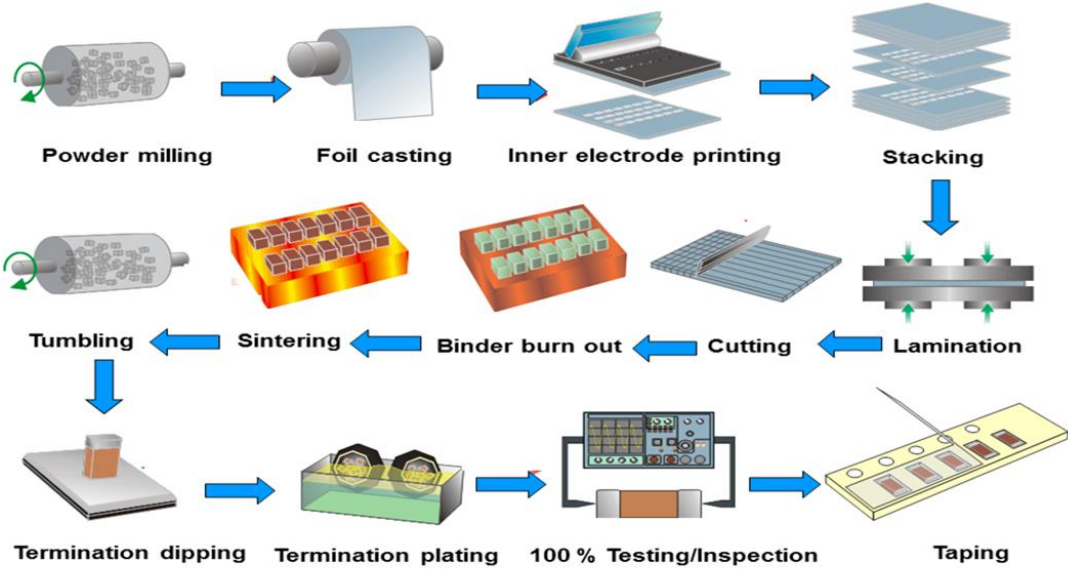


Figure 2-21. Simplified MLCC Manufacturing Process.¹⁵⁶

The capacitance of multilayer capacitor can be expressed as follow¹⁵⁷:

$$C = n\varepsilon_0\varepsilon_r \frac{A}{d}$$

where n is the number of ceramic layers, ε_0 is the dielectric permittivity in air, ε_r is the dielectric constant of ceramic, d is the thickness of the dielectric layer and A is the electrode area. It can be found that thickness is an important factor for capacitance. A major challenge is to obtain the thinnest possible dielectric layers.¹⁵⁸ Inkjet printing is a promising method to replace traditional process as it is capable of printing ultrathin layers.

The energy storage performance of MLCCs is greatly influenced by the morphologies of the internal electrodes.¹⁵⁷ Printing smooth metal electrodes and dielectric layers is very critical.¹⁵⁹ To achieve MLCCs with high capacitance and reliable performance, inks and printing parameters needs to be optimized. Another essential aspect for the capacitor design is to control the sintering condition for BT in order to increase its dielectric constant.^{151, 153, 154, 157, 160}

2.5 Summary of Critical Gaps in Current Knowledge

Previous studies demonstrated that printing methods is widely used in the smart textile area and industry. The use of printing in wearable electronics is quite challenging, as it requires ink formulation, substrate selection, optimization of printing parameters and curing conditions. Failed to meet any requirement would impact the device performance negatively.

BT nanoparticles with high dielectric constant and low dielectric loss have great potential to be used in wearable antennas and capacitors. There are some research gaps need to be filled: 1. use BT to improve the dielectric properties of textile materials by printing and make them suitable for

antenna substrate; 2. prepare high-concentration BT dielectric ink for high-energy density capacitors. 3. study the influence of inkjet printing parameters on the roughness of printed pattern.

3 Direct-Write Spray Coating of a Full-Duplex Antenna for E-Textile Applications

Zhou, Y.; Soltani, S.; Li, B. M.; Wu, Y.; Kim, I.; Soewardiman, H.; Werner, D. H.; Jur, J. S., Direct-Write Spray Coating of a Full-Duplex Antenna for E-Textile Applications. *Micromachines* 2020, 11 (12), 1056. <https://doi.org/10.3390/mi11121056>

Abstract

Recent advancements in printing technologies have greatly improved the fabrication efficiency of flexible and wearable electronics. Electronic textiles (E-textiles) garner particular interest because of their innate and desirable properties (i.e., conformability, breathability, fabric hand), which make them the ideal platform for creating wireless body area networks (WBANs) for wearable healthcare applications. However, current WBANs are limited in use due to a lack of flexible antennas that can provide effective wireless communication and data transfer. In this work, we detail a novel fabrication process for flexible textile-based multifunctional antennas with enhanced dielectric properties. Our fabrication process relies on direct-write printing of a dielectric ink consisting of ultraviolet (UV)-curable acrylates and urethane as well as 4 wt.% 200 nm barium titanate (BT) nanoparticles to enhance the dielectric properties of the naturally porous textile architecture. By controlling the spray-coating process parameters of BT dielectric ink on knit fabrics, the dielectric constant is enhanced from 1.43 to 1.61, while preserving the flexibility and air permeability of the fabric. The novel combination textile substrate shows great flexibility, as only 2 N is required for a 30 mm deformation. The final textile antenna is multifunctional in the sense that it is capable of operating in a full-duplex mode while presenting a relatively high gain of 9.12 dB at 2.3 GHz and a bandwidth of 79 MHz (2.260–2.339 GHz) for each port. Our proposed manufacturing process shows the potential to simplify the assembly of traditionally complex E-textile systems.

3.1 Introduction

In the past decade, wireless body area networks (WBANs) have garnered significant attention as a way to wirelessly communicate between wearable devices placed at various locations across the human body^{35, 161, 162}. These wearable devices can sense physiological signals, such as electrocardiogram (ECG), electroencephalogram (EEG), and electrooculogram (EOG)¹⁶³. Moreover, these devices, when coupled with WBANs, create wearable health monitoring systems that enable a paradigm shift away from traditional, in-person healthcare towards remote telemedicine. A primary challenge to WBANs is that they primarily rely on conventional stiff and heavy antenna designs to wirelessly relay information between devices, which limits practical applications of WBANs in wearables. Having a wearable antenna that is flexible and lightweight, with the same efficiency as a conventional, rigid antenna, is critical for realizing WBANs for telemedicine applications^{80, 164}. It is also important that there is a pathway to fabricating multifunctional wearable antennas, which typically require more complex geometrical features.

The antenna is a necessary wireless communication device for receiving and transmitting relevant signals at specific frequencies⁶. Various wearable antennas with flexible properties exist in the literature, using a range of polymer- and paper-based substrates with permittivity values often ranging from 1.5 to 13^{34, 165}. Textile materials, made of fibrous polymer materials, are ubiquitous in our daily lives, and they offer a light and flexible substrate for wearable systems and devices. The textile antennas¹⁶⁶⁻¹⁶⁸ can be light, flexible, and readily integrated into smart clothing, communicating with other wearable electronics and transmitting the body health data³⁵. Design criteria, such as durability, functionality, and usability, need to be met in order to design convenient and safe textile antennas¹⁶⁹. The safety impact of a textile antenna is defined by its specific

absorption rate (SAR) ¹¹⁷, which measures the rate of absorption of radio-frequency (RF) electromagnetic radiation per unit mass by a human body to evaluate the RF dosimetry ¹⁷⁰. Ideally, all wearable antennas should exhibit low SARs to ensure a low negative impact on human tissues ^{171, 172}.

With these design criteria in mind, researchers have explored multiple textile designs, materials, and manufacturing methods to realize textile-based antennas. For example, researchers have used conductive yarns embroidered into non-conductive woven fabrics to create wearable patch antennas ¹⁷³. These embroidered textile antennas are easy assemble and integrate into wearable systems. However, embroidery can be challenging for large-scale manufacturing processes. In addition, these embroidered antennas show low patch resolution and low wash durability, as the conductive yarns are susceptible to degradation during washing and handling. Nonwoven textiles serve as an alternate material substrate for textile-based antennas ¹⁷⁴. However, these types of antennas employ copper tape as the patch and ground, which make them very fragile, and they are easily broken after a few bending cycles ¹⁰². Printing methods, such as screen printing, are currently the best processes to design textile-based antennas with excellent wash and mechanical durability ^{100, 102, 109}. In our previous work, we reported the use of a nonwoven fabric assembly laminated with a thermoplastic polyurethane (TPU) web to create a porous, flexible, and washable antenna ¹⁷⁴. Employing the breathable TPU web in the screen-printed antenna can work as a protection layer by mechanically entrapping the dielectric materials to enhance their durability ¹⁷⁴. Moreover, the micro-fiber TPU web with an open gap structure enabled breathability. The TPU web encapsulated silver printed on textiles, protecting the conductive area of the antenna from being washed and mechanically deformed ^{100, 174}. A recent textile antenna made of screen-printed

nonwoven fabrics laminated with a TPU web was reported, and a novel dual-port design was used to improve the isolation with enhanced bandwidths ⁹⁹. The antenna showed a low profile and an SAR < 0.37 W/kg ⁹⁹. However, there is still room for improvement regarding the flexibility of these antennas. Current literature focuses on the metallic layers in textile-based antennas rather than the substrate itself. The essential dielectric layers in textile-based antennas play a big role in the antennas' performance. Since the inherent porous structure of textiles limits the ability to achieve a high dielectric constant, it is necessary to reduce the surface wave losses and improve the antenna's bandwidth ¹¹¹. A higher substrate dielectric constant is also needed for the downsizing of antennas ⁶. Although knit fabrics constructed with yarn loops and large air voids are widely used in daily clothing due to their flexibility and comfort, they typically have very low dielectric constants due to the highly porous structure ¹²⁶. This characteristic limits their application as substrates for wearable antennas.

In this work, a multifunctional full-duplex textile-based antenna is introduced with dual ports and a highly flexible nonwoven and knit composite antenna substrate. The antenna is fabricated with a screen-printed patch and ground on a nonwoven fabric and sandwiched onto knit fabrics with a spray-coated dielectric layer. Spray coating is a high-throughput direct-write method that can drive film deposition on a printed substrate to change its dielectric properties. It has been widely used due to its high speed (up to 200 mm/s). Additionally, inks with a wide range of viscosities from 0.7 to 2500 mPa s can be printed ^{175, 176}. To overcome the low dielectric constant of the knit fabric, a dielectric-particle-loaded ink was applied to the fabric by spray coating. The measurement results show that the radiation performance of the fabricated antenna is robust to structural deformation and agrees with the simulated results.

By employing a new fabrication process and material system, a much more flexible antenna substrate can be achieved while, at the same time, its equivalent relative permittivity is increased. As a consequence, for the same design area, the effective wavelength is larger compared to our previously published work⁹⁹. The fabricated antenna exhibits a 79 MHz bandwidth at a center frequency of 2.3 GHz with a remarkable 30 dB isolation between ports, which represents a 15 dB improvement in isolation compared to⁹⁹, and a relatively high gain of 9.12 dB compared with other textile antennas^{107, 109, 112, 118, 177}.

3.2 Materials and Methods

3.2.1 Preparation and Characterization of the Barium Titanate Ultraviolet (UV) Curing Ink

A dielectric ink for direct-write spray coating was prepared by mixing 4 wt.% BaTiO₃ (BT) nanoparticles (200 nm, purchased from Nanostructured Amorphous Materials Inc., Houston, TX, USA) with a urethane and acrylate UV-curable dielectric ink (C3-D1-1032 Dielectric photopolymer, Chem3, LLC, Stony Brook, NY, USA). The mixture was then stirred at 400 rpm for 24 h in order to disperse the nanoparticles, followed by an ultrasonic homogenizing process for 30 min. The solid BT content in the ink was fixed at 4 wt.% in the entire experiment.

The viscosity of the ink under different shear rates was tested using a rheometer (MCR 302, Anton Paar). Surface tension of the ink was tested by a contact angle goniometer (First Ten Angstroms Europe; Cambridge, UK) with an automated syringe to form the pendant drop. The nanoparticle crystal structure phase was tested using a Rigaku SmartLab X-ray Diffractometer (XRD) with a CuK α X-ray radiation source ($\lambda = 0.154$ nm). The XRD pattern was recorded from 2-theta = 10° to 60° at a scanning rate of 3°/min with a step size of 0.05°

A 3D laser-scanning confocal microscope (Keyence, model VK-X1000) and a field emission electron microscope (FESEM) model FEI Quanta 650 were used to characterize the morphology of fabrics printed with conductive ink and BT dielectric ink.

3.2.2 Configuration of Antenna

The flexible antenna design had two separated ports with a high isolation between them to enable transmitting (Tx) and receiving (Rx) functions (i.e., full-duplex operation). shows the configuration of the proposed wearable antenna, which is similar to the design in our previously published work ⁹⁹. The thickness of the textile substrate was 2 mm, which was much thinner than other wearable antennas published in the literature ^{112, 114, 130, 178, 179}. In comparison to a large majority of patch antenna designs, our antenna design used a strip line placed perpendicularly across the two feeds to enhance the bandwidth and isolation between the two ports. The active and ground conductive layers show thicknesses of around 40 μm and conductivity of 1.3×10^6 s/m. The dielectric constant of the antenna is 1.78 and dielectric loss is 0.021. Based on this information, the optimized design parameters listed in Figure 3-1 were determined using an ANSYS High-Frequency Structural Simulator (HFSS). In Figure 3-1, when Port-1 is excited, the electromagnetic energy couples to the strip near Port-2. This feature not only significantly suppresses the mutual coupling between the two feed ports, but also improves impedance matching of the patch antenna and broadens the bandwidth ⁹⁹. The same coupling effect can also be observed on the other strip load when Port-2 is excited, but with the orthogonally aligned surface current distribution. The unidirectional radiation patterns were also similar when either Port-1 or Port-2 was excited. The antenna design has a high isolation of more than 30 dB via the strip load coupling.

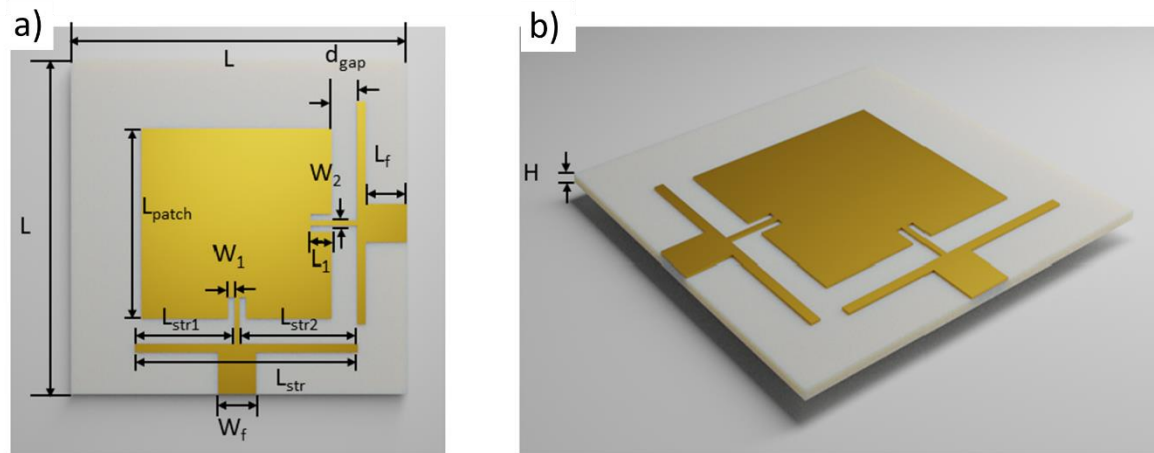


Figure 3-1. Geometrical parameters of the dual-port full-duplex textile-based patch antenna. (a) Top view. (b) Side view. Design dimensions: $H = 2$ mm, $L = 80$ mm, $L_{patch} = 45.8$ mm, $L_{str1} = 19.1$ mm, $L_{str2} = 25.5$ mm, $L_{str} = 53.6$ mm, $L_f = 6$ mm, $W_f = 7$ mm, $L_1 = 4.5$ mm, $W_1 = 1$ mm, $W_2 = 0.8$ mm, and $d_{gap} = 7$ mm⁹⁹.

3.2.3 Dielectric Constant Test

Traditional techniques for permittivity measurements at microwave frequencies can be divided into non-resonant methods and resonant methods¹⁰³. Non-resonant methods mainly use transmission/reflection measurements, but have limited resolution. For our analysis, we used the split post dielectric resonator (SPDR) method to test the permittivity of the samples without damaging them. A 2.45 GHz SPDR was connected to a two-port vector network analyzer (VNA) by high-precision coaxial cables to analyze the samples¹⁸⁰. The device resonates at a specific frequency with a quality factor (Q-factor) over 2000. Because of the high Q factor, it is more sensitive to the dielectric samples than a conventional coil-and-capacitor resonant circuit¹⁸¹. The sample size requirement for the SPDR test is at least $5\text{ cm} \times 5\text{ cm}$, and the sample thickness should be less than 2 mm. The dielectric constant measurements were repeated five times. This method can provide rapid and accurate results at high frequency.

3.2.4 Antenna Fabrication

Nonwoven Evolon[®] fabric (30 wt.% polyamide and 70 wt.% polyester) was obtained from Freudenberg Performance Materials. This nonwoven fabric is an excellent choice for electronics printing due to the numerous condensed fibers exhibiting a high surface area and low surface roughness compared to conventional textiles. Single jersey-knit fabrics composed of 100% polyester (PET) with a basis weight of 145 g/m² were obtained from Hanesbrands Inc. Both the nonwoven and knit fabric thicknesses were ~0.3 mm, as shown in Table 3.1. Prior work has demonstrated that stacking the nonwoven layers can result in a good substrate for antenna fabrication⁹⁹. The commercial knit structure is generally too flexible to keep the antenna stable. Therefore, a combination structure with alternating layers of printed knit fabrics and nonwoven fabrics was chosen for the antenna fabrication. The structured device was assembled with six layers of printed knit fabrics adhered together by a porous TPU web (0.057 mm). The layered knit fabric and TPU structure were heat laminated at 150 °C for 5 min. The TPU web softens above 65 °C and melts under higher temperatures.

Table 3.1. Specification of the fabric for antenna design.

Fabrics	Material	Thickness (mm)	Weight (g/m²)
Nonwoven Fabric	70 wt.% Polyester/30 wt.% Polyamide	0.33	95
Knit Fabric	Polyester	0.31	145

An Asymtek C-341 conformal coating machine fitted with an EFD-781 s series spray valve was used to print the BT dielectric ink on the knit textile to modify the dielectric constant of the substrate. The BT dielectric ink was loaded into a syringe and capped with a plunger. The dispensing pressure was 20 psi, and the air-assist pressure was set to 60 psi. These settings enabled

uniform ejection of ink from the spray valve. The processing included a dispensing velocity of 40 mm/s and a gap of 1 mm between the nozzle and substrate.

Figure 3-2 shows the assembly process of the textile-based antenna. The first step in the fabrication process was to heat press six knit fabrics adhered to TPU webs. Then, the BT dielectric ink was spray coated onto the knit fabric composite to enhance its dielectric constant and was matched to the nonwoven fabrics (Figure 3-2b). Finally, the fabric coated with the BT dielectric ink was cured under a UV radiation machine for 300 s to make sure the photopolymer was completely cured.

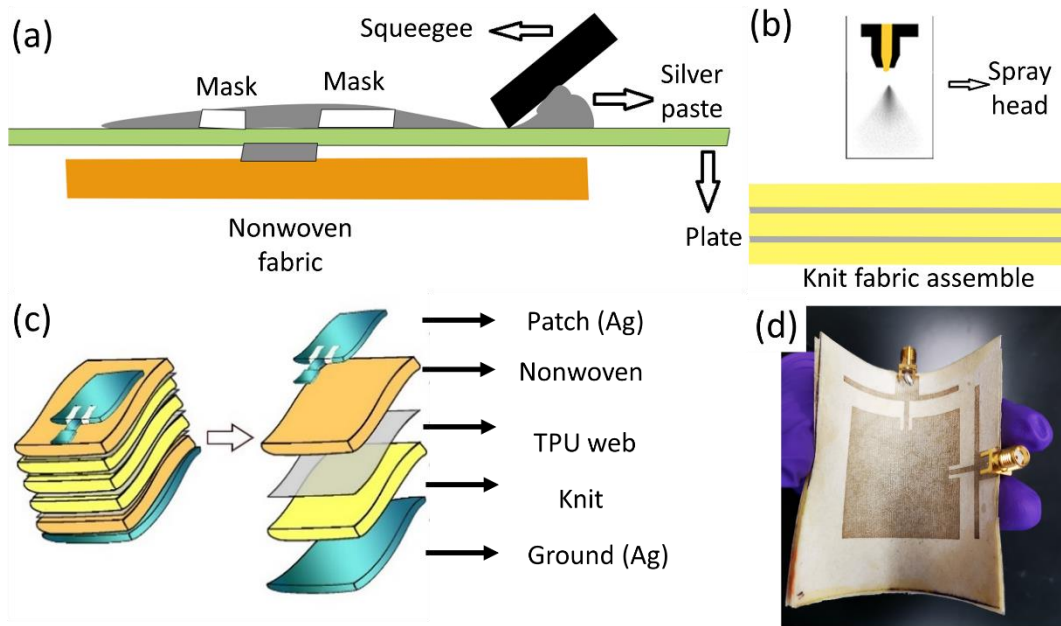


Figure 3-2. Fabrication of the textile-based antenna. (a) Screen printing of the Ag paste from Dupont onto nonwoven fabrics to fabricate the patch and ground. (b) Direct-write spray coating of barium titanate (BT) UV curable dielectric ink onto the knit fabric substrate assembly (six layers of knit fabric laminated with a thermoplastic polyurethane (TPU) web) to modify the dielectric constant. (c) Final assembly of the printed textile-based antenna (two layers of nonwoven fabric and six layers of knit fabric spray coated with BT dielectric ink). Exploded views indicate the different layer compositions. (d) Final product image of the printed textile-based antenna.

The patch and ground patterns were screen printed using a DuPont 5064 H conductive screen-printing silver ink on individual nonwoven fabrics (Figure 3-2a). The nonwoven Evolon[®] fabric

had a low surface roughness ($R_a = 18 \text{ } \mu\text{m}$) and a high surface area ($2.19 \text{ mm}^2 \text{ mm}^{-2}$ of fabric area), allowing the ink to penetrate evenly into the fiber bulk due to the strong capillary wicking force.

The patch design requires very high resolution for the transmission lines ($\sim 1.2 \text{ mm}$) and the gaps ($\sim 1.5 \text{ mm}$), which can be challenging for fabrication on a textile surface. To achieve the high resolution, we used a vinyl mask placed onto the nonwoven fabric and applied uniform pressure and velocity during screen printing to ensure a uniform printed area for the patch design. The printed nonwoven fabric was then cured in an oven at $130 \text{ }^\circ\text{C}$ for 15 min. The same process was repeated for the ground design (i.e., conductive backing). To form the final antenna assembly, the nonwoven patch design, nonwoven ground design, and dielectric printed knit fabrics were heat laminated together with the TPU webs (Figure 3-2c).

A separate TPU web was used as an encapsulation layer to protect the antenna. Two standard SubMiniature version A (SMA) connectors with a $50 \text{ } \Omega$ characteristic impedance were soldered with Chipquik SMDSWLTLFP32 (a low-melting-temperature solder) onto the patch and ground patterns to form a connection. The metal in the solder melted at $170 \text{ }^\circ\text{C}$, which enabled robust connections without damaging the textile component of the antenna. An additional UV-curable encapsulation (Dymax 9001-E-V 3.5) was applied to the edges of the solder areas between the textile antenna and connectors. The encapsulation protected the antenna from breaking and ensured a strong mechanical and electrical connection between the textile antenna and SMA connectors. The final product can be seen in Figure 3-2d.

3.2.5 Characterization of the Antenna

A buckling test was conducted with a commercial tensile tester (Instron, model 5566) to compare the flexibility of different substrates. The sample (8 cm× 8 cm) was gripped between two clamps, where the lower clamp was fixed while the upper clamp moved at 50 mm/min. The tested distance between the two clamps was 70 mm.

The performance of the assembled antenna was tested with Agilent E5071C VNA. The antenna was connected to a VNA using two coaxial cables with SMA connectors to measure the reflection coefficient and mutual coupling. The radiation test was conducted in an anechoic chamber.

3.3 Results and Discussion

3.3.1 Characterization of BT Dielectric Ink

BT nanoparticles were added to a blend of urethane and acrylates (C3-D1-1032 Dielectric photopolymer, Chem3, LLC, USA) to fabricate the polymer/ceramic ink. Processability at room temperature is essential for use in E-textiles, as textile materials cannot sustain high processing temperatures¹⁸². The ink with the photoinitiator using ultraviolet radiation can be polymerized after UV curing, and forms a thin film on the textile substrate (Figure 3-3a). Moreover, the small molecules with low viscosity can help prevent the BT dielectric ink from blocking the spray nozzle (Figure 3-3a). Figure 3-3b displays a scanning electron microscopy (SEM) image of the BT nanoparticles, where it was found that the nanoparticles were a mixture of cubic and polyhedral in shape. The size distribution of the BT nanoparticles shown in Figure 3-3c was obtained by measuring more than 200 particles. The BT nanoparticles used in the dielectric ink exhibited an average size of 211 nm. The size distribution of the BT dielectric ink was tested by a dynamic light

scattering (DLS) method. The main peak of the ink is at less than 1000 nm, indicating that the ink dispersed well only with slight aggregation (Figure 3-3d). This is an indication that the nanoparticle ink will not block the spray nozzle. The viscosity of the BT-UV curing ink may affect the rheological characteristics through printer nozzles, where a high-viscosity ink could lead to nozzle clogging. The BT dielectric ink exhibited Newtonian behavior with a low viscosity of 12 cps, which ensured that the ink could be easily spray coated. The ink surface tension was 37.53 mN/m, and the pendent volume was 3.43 μ L. Ink with low surface tension can prevent nozzle dripping and guarantee decent wettability^{183, 184}. e shows the X-ray diffraction (XRD) pattern of BT dielectric ink after UV curing. The BT dielectric ink shows XRD peaks at 25.85° from the photopolymer. The peaks at 31.50° and 38.85° indicate that the BT nanoparticles exhibit a tetragonal crystal structure, which has a higher dielectric performance compared to cubic BT phase¹⁸⁵.

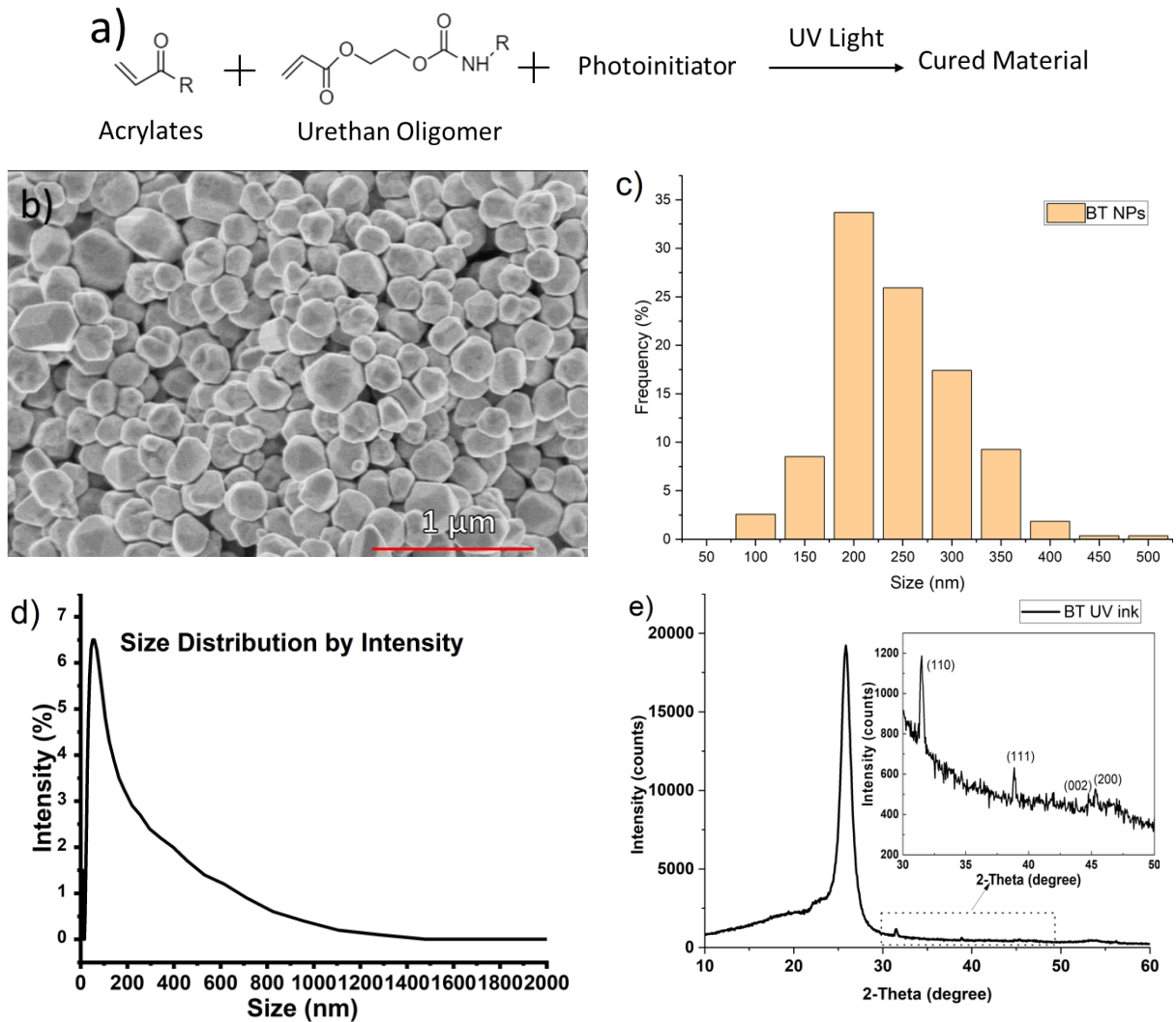


Figure 3-3. Fundamental characteristics of UV-curable ink with BT nanoparticles. (a) Chemical reaction mechanism of acrylate and urethane UV-curing process ¹⁸⁶. (b) Scanning electron microscopy (SEM) of BT nanoparticles (50,000 \times ; 1 μ m of scale bar). (c) Size distribution of the BT nanoparticles. (d) BT nanoparticle size distribution according to intensity of UV-curable ink tested by DLS. (e) X-ray diffraction (XRD) result of the BT dielectric ink after UV curing.

3.3.2 Dielectric Properties of the Printed Textile-Based Antenna

Table 3.2 provides a list of the dielectric properties of various assembly methods with textile layer combinations and the inclusion of spray-coated BT dielectric ink. In the previous study, the textile antennas were made from eight-layer nonwoven fabrics ¹⁸⁷, with a dielectric constant and dielectric loss tested by SPDR of 1.75 and 0.008, respectively. The newly designed textile antenna substrate

made of six knit fabrics spray coated with BT dielectric ink sandwiched between two nonwoven fabrics (Figure 3-2) showed a similar thickness (1.97 mm) and dielectric constant (1.78) to those of the previous study. The direct-write spray-coating process of BT dielectric ink successfully increased the dielectric constant of the six-layered knit fabric structure from 1.43 to 1.61. This demonstrates the potential of using BT dielectric ink to manipulate the dielectric properties of porous materials. As previously mentioned, the dielectric loss can influence the radiation efficiency of the antenna, for which a smaller value is preferred ¹⁸⁸. Although the dielectric loss increased from 0.009 to 0.013 by adding the BT dielectric ink into the knit structure, this is still low compared to the previous studies on textile antennas ¹²⁶.

Table 3.2. Fabric dielectric properties.

Fabric Assembly	Dielectric Constant	Dielectric Loss	Thickness (mm)
Knit Fabric, six Layers	1.43	0.009	1.68
Knit Fabric, six Layers w/BT Dielectric Ink	1.61	0.013	1.60
Knit Fabric, six Layer w/BT Dielectric Ink + two Layers Nonwoven Fabric	1.78	0.021	1.97
Nonwoven Fabric, eight Layers	1.75	0.008	1.94

3.3.3 Characterization of the Printed Textile-Based Antenna

The dielectric-ink-sprayed knit fabric is very flexible, as can be observed in Figure 3-4a. Figure 3-4b shows the BT nanoparticles deposited on the textile fiber after spraying. Nonwoven fabric screen printed with silver conductive ink is shown in Figure 3-4c, d. The silver conductive ink was successfully deposited on the nonwoven fabric and forms a uniform layer around 40 μm thick.

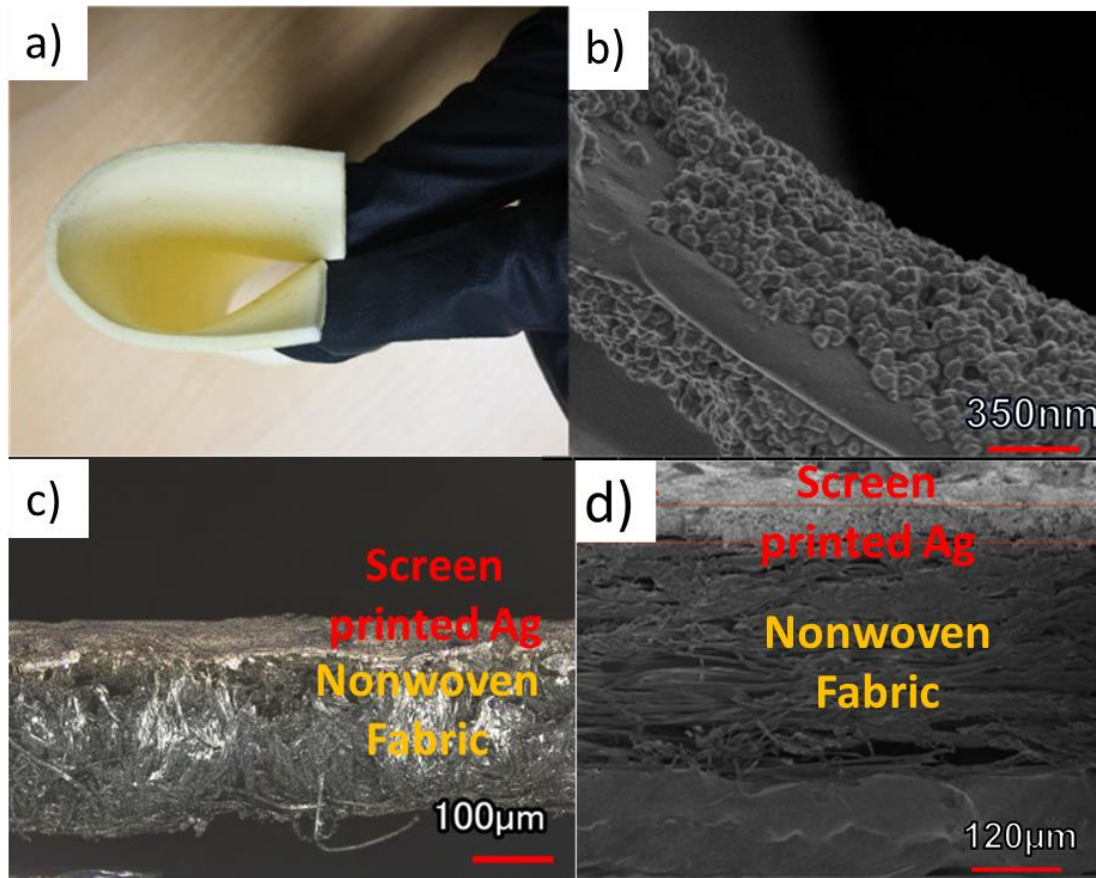


Figure 3-4. (a) Flexibility of the knit fabric assembly with BT dielectric ink and (b) an SEM image of the BT with acrylate and urethane UV-curable dielectric ink coated on a single fiber within the fabric after UV curing for 5 min (10,000 \times , 350 nm of scale bar). (c) Cross-sectional microscope image of Ag screen-printed patch section of the antenna (20 \times , 100 μm of scale bar). (d) Cross-sectional SEM image of Ag screen-printed patch section of the antenna (150 \times , 120 μm of scale bar).

The buckling analysis of the antenna substrate under compression was executed to compare the flexibility of the nonwoven substrate (eight layers of nonwoven fabric), knit substrate (eight layers of knit fabric), and combination substrate (two layers of nonwoven fabric and six layers of knit fabric spray coated with BT dielectric ink). Figure 3-5a displays the shape of the fabric deflection during the test. The buckling of the fabric under the continuously increasing compression loading force was recorded in Figure 3-5b. A total of 4 N is needed to cause 30 mm displacement for the nonwoven fabric assembly, while only 0.7 N is necessary for the knit fabric substrate. The larger

force required to deform the nonwoven fabric by 30 mm indicates that the nonwoven fabric is more rigid than the knit fabric, since it takes more mechanical energy to displace the nonwoven fabric. Regarding the combination substrate (two layers of nonwoven fabric and six layers of knit fabric spray coated with BT dielectric ink), only 2 N was required. The lower force required for the amalgamated substrate indicates that it behaves like a composite structure and demonstrates superior flexibility compared to the nonwoven substrate.

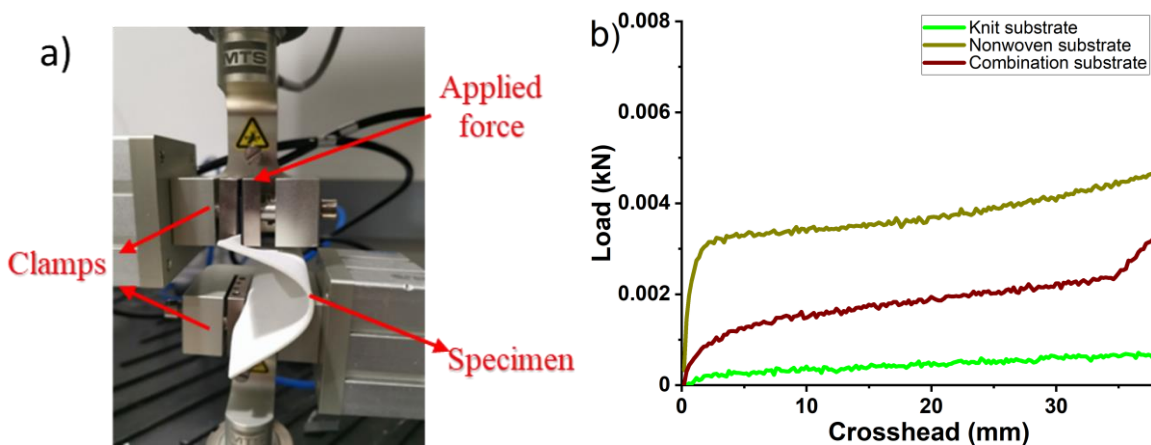


Figure 3-5. Buckling test of the nonwoven substrate (eight layers of nonwoven fabric), knit substrate (eight layers of knit fabric), and combination substrate (two layers of nonwoven fabric and six layers of knit fabric spray coated with BT dielectric ink). (a) Photography of experimental setup. (b) Buckling force displacement curve with fixed–fixed ends.

3.3.4 Simulated and Measured S-Parameter Results for the Printed Textile-Based Antenna

Full-wave simulations of the antenna were performed using an ANSYS HFSS (Figure 3-6). A prototype of the complete antenna design was been constructed and tested to verify its impedance matching and mutual coupling performance. SMA connectors were used to feed both antennas. Two-port reflection coefficient measurements of the prototype antenna were performed using a VNA. The simulated and measured S-parameter results of the proposed two-port antenna with optimized dimensions (Figure 3-1) are provided in Figure 3-6. The antenna exhibits a -10 dB

bandwidth around 79 MHz from 2.26–2.339 GHz, with mutual coupling of less than -30 dB over the entire band. The experimental and simulated results show good agreement for this antenna.

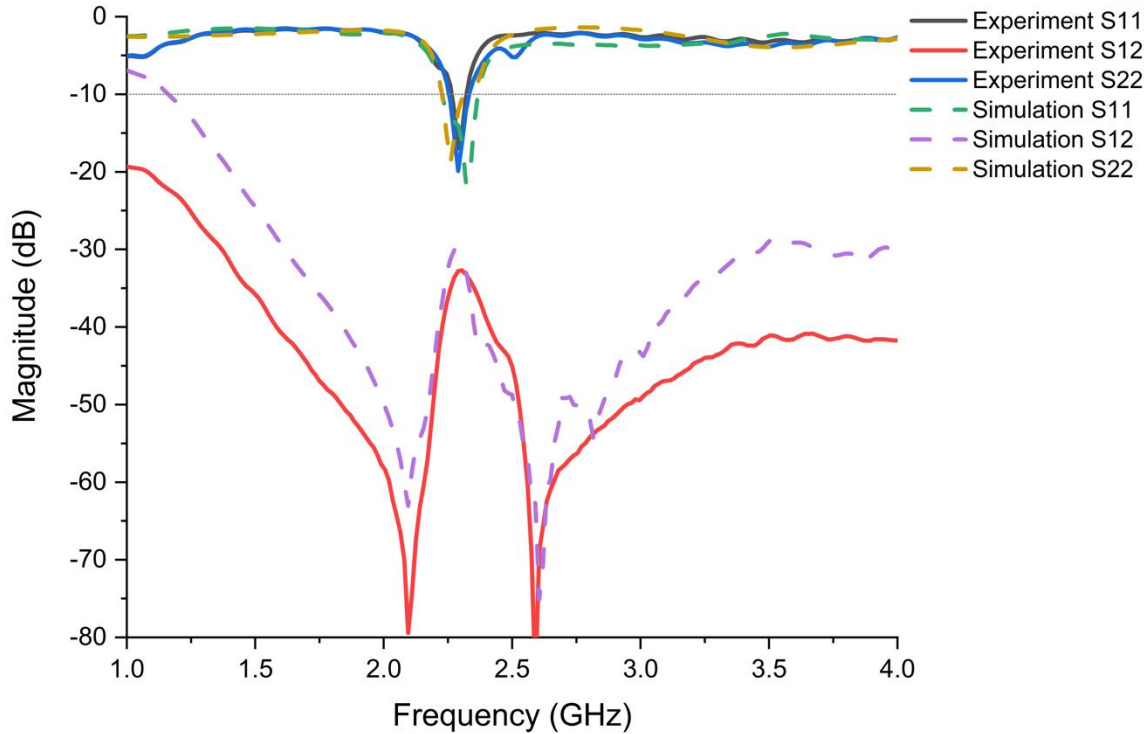


Figure 3-6. Simulated and measured S-parameters of the proposed full-duplex textile antenna with the combination structure (two layers of nonwoven fabric and six layers of knit fabric spray coated with BT dielectric ink). Experimental data are represented by solid curves, while simulation data are represented by dotted curves.

3.3.5 Radiation Pattern and Far-Field Results for the Printed Textile-Based Antenna

The radiation pattern of the antenna was measured in an anechoic chamber (Figure 3-7a). The measurement chamber system was controlled by a computer and equipped with a closed-circuit television camera to visualize the measurements. According to previous work ⁹⁹, a diagonally directed surface current can be predicted as a combination of both the surface current of the conductive patch and the orthogonally polarized current of the load strips. This yields diagonally polarized far-field radiation, which differs from a conventional patch antenna. The broadside gain profile is provided in Figure 3-7b. Clearly, a 9.12 dB maximum gain was measured at the on-

resonance frequency, around 2.3 GHz. This result is a significant improvement over the gain (5.5 dB) of typical textile patch antennas that have been previously reported¹¹⁰. The E-plane radiation pattern at 2.3 GHz for the proposed textile antenna with the amalgamated structure (two layers of nonwoven fabric and six layers of knit fabric spray coated with BT dielectric ink) is provided in Figure 3-7c, while the corresponding 3D radiation pattern is shown in Figure 3-7d. These results indicate that the antenna exhibits a uni-directional radiation performance.

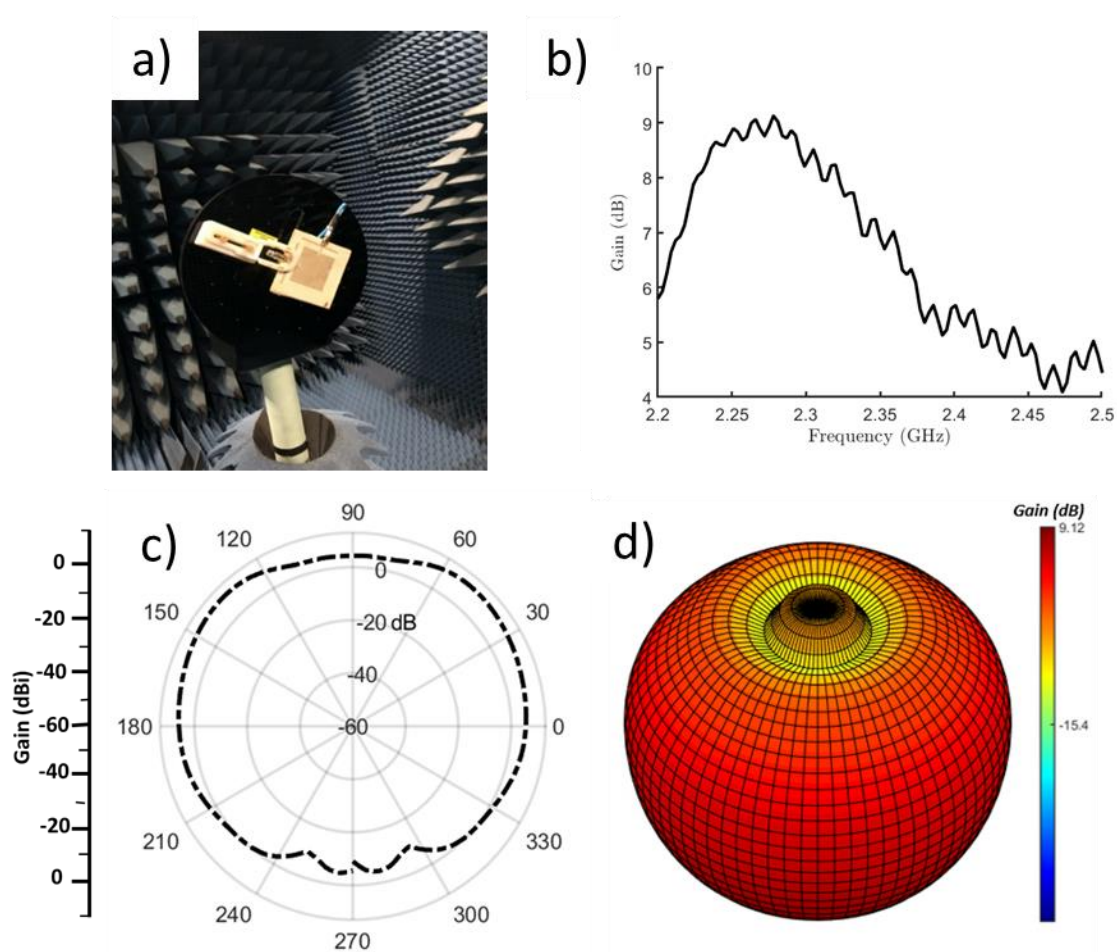


Figure 3-7. (a) Experimental setup for the textile antenna with the combination substrate (two layers of nonwoven fabric and six layers of knit fabric spray coated with BT dielectric ink) for 3D radiation pattern measurements in an anechoic chamber. (b) Maximum gain plot at $\phi = 0^\circ$. (c) Two-dimensional radiation pattern of the textile antenna at 2.3 GHz and $\phi = 0^\circ$. (d) Three-dimensional radiation pattern of the textile antenna plotted in dB at 2.3 GHz.

3.4 Related Work

Table 3.3 shows the comparison between the proposed antenna and recent work reported in the literature, including antenna material, size, bandwidth, and gain. It can be seen from Table 3.3 that our proposed antenna has a relatively high gain. Knit fabric is the most widely used fabric in our daily clothing due to its superior flexibility and breathability, but its poor dielectric properties limit its applications in wearable antennas. In this work, the dielectric constant of knit fabric was enhanced by the printing of BT dielectric ink. Instead of using densely woven fabric, filter paper, and PDMS (Polydimethylsiloxane), as shown in Table 3.3, we employed a combination textile substrate (six layers of knit fabric and two layers of nonwoven fabric) that shows great flexibility and is more suitable for wearable applications. The success of using BT dielectric ink to modify the dielectric properties of porous materials could expand the options of textile materials as antenna substrates.

Table 3.3. Comparison of the antennas proposed in previous works.

Reference	Material	Substrate Dielectric Constant and Loss	Volume (mm ³)	Bandwidth (MHz)	Gain (dBi)
189	Screen-printed Ag ink and PDMS	-	60 × 60 × 2	105	6.987
190	Inkjet-printed Ag layer and 65/35 polyester cotton woven fabric	1.229 and 0.001	37.4 × 28.1 × 1.6	24.5	5.09
191	GO film and cellulose filter paper	3.06, -	119.4 × 70 × 0.46	100	12
167	Copper sheet and jean fabric	1.7 and 0.025	40 × 20 × 0.3	300	4.48
192	Copper sheet and jean fabric	1.7 and 0.085	100 × 100 × 6	240	2.42
193	Nickel-/copper-plated textile and thick felt textile material	1.2 and 0.044	150 × 150 × 4	120	3.5
Proposed	Screen-printed Ag layer and nonwoven/knit fabric spray coated with BT dielectric ink	1.78 and 0.012	80 × 80 × 2	79	9.12

3.5 Conclusions

In this work, a flexible textile-based full-duplex antenna that employs both knit and nonwoven fabrics was demonstrated. The dielectric constant of the flexible knit fabric assembly was enhanced by a direct-write spray coating of BT nanoparticle dielectric ink, making it suitable for integration into a textile-based antenna. This has demonstrated the potential of using BT dielectric ink and spray coating to manipulate the dielectric properties of porous materials. The resultant flexible antenna is dual-mode (i.e., able to simultaneously operate in transmit and receive modes with very high isolation), is robust to bending, and exhibited a gain of 9.12 dB, which is better than typical textile antennas. The textile antenna in this work shows great promise for use as a multifunctional flexible antenna in E-textile systems.

In future studies, we propose exploring additional knit structures that can further reduce the porosity of this layer as well as more dielectric inks, which can aid in increasing the dielectric constant beyond what is reported in this work. In terms of manufacturing, we also propose the use of alternative direct ink writing technologies, such as inkjet printing, in order to enable more customized design. Finally, the incorporation of these devices into textile panels that can be easily implemented in standard cutting and sewing processes would enable their application.

4 All-Inkjet-Printed Barium Titanate Nanoparticles Ultraviolet Ink and Silver Metal-Organic-Decomposition Ink Large-Area Textile Pressure Sensors

Abstract

Printing electronics is a promising method for fabricating electronic textiles (e-textiles) for wearable technology applications. It is essential printed electronics have high electrical conductivity, high dielectric constant, and interfacial compatibility with conductive materials, especially in multi-layered device structures. The inkjet printing process can be used to fabricate ultrathin coatings on flexible and porous textile surfaces by depositing a myriad drops of low viscosity inks (≤ 25 cps), enabling conductive patterning. The thin-film coating process maintains the textiles' flexibility and breathability, which is crucial for enhanced comfort and wearability for e-textiles. In this work, the inkjet process is used with a UV curable urethane-acrylate/barium titanate (BaTiO_3) ink which significantly improved the dielectric constant of the textile and Ag MOD, which fabricated high resolution high conductive ($0.014 \Omega/\text{sq}$) pattern. Nanoparticles are deposited on the fiber through inkjet printing without damaging the flexibility and air permeability of the fabric. We used the fast, low-cost inkjet printing process to fabricate a capacitor array pressure sensor, printing a large area that is highly sensitive (11.4 kPa^{-1}), with a low detection limit (50 Pa), and flexible and mechanically stable. The all-textile fabricated pressure sensor array has great potential in future smart textile applications.

4.1 Introduction

The rapid development of wearable electronics has promoted the need for flexible, durable, washable, comfortable, and lightweight electronic components such as conductors,¹⁹⁴ capacitors,¹⁹⁵ and transistors¹⁹⁶. Electronic textiles (E-textiles) which uphold the fabrics inherent

wearable characteristics, such as flexibility, durability, breathability, lightweight, and washability, make it the ideal platforms for future wearable electronics.^{9, 32, 80, 138, 197-201} E-textiles can sense stimuli from the environment, react to them and adapt to them by integrating electronic functionalities in the textile structure.² Wearable pressure sensors are essential components of e-textiles that can respond to environmental stimuli. These e-textiles satisfy the need for specific functions and mobility and comfort for the user. The sensors should be flexible, comfortable, lightweight, breathable, highly sensitive in the low-pressure range.²⁰² The majority of current pressure sensors are rigid with low sensitivity, typically fabricated as silicon-based strain sensors by micro-electromechanical techniques, which do not meet the desired requirements.²⁰² There have been ongoing developments fabricating highly sensitive and flexible sensors based on Poly(ethylene terephthalate) (PET) film,²⁰³ however, the films' properties make it unsuitable for integrating the sensors for wearable applications. Fabric sensors serve as the ideal platform for integration into wearable products.

E-textiles should provide the need of the specific sensing functions while providing mobility and comfort to the user. Ideally, the electronics would be inconspicuous to the users. The integration of smart fibers within the textile is usually carried out in separate processing procedures, making the construction complex, arduous and time-consuming.^{204, 205} Additionally, the e-textiles should also meet the needs of commercial industry of fast, simple, and low cost manufacturing.²⁰⁶ Inkjet printing is a promising manufacturing technology for producing state-of-the-art thin-films on textile substrates, it is an efficient approach to coat at the fiber level maintaining the flexibility, breathability, robustness while making the fabric functional.⁸⁰ Inkjet printing provides an avenue

to extend the functionality and usefulness of everyday fabrics by thin coating layer of conductive material and dielectric material to have a diverse spectrum of functionalities.^{194, 207}

Inkjet is a revolutionary innovation, providing a number of advantages compared to conventional textile printing. It can achieve high resolution, free pattern, thin-film deposition with less material, and high efficiency. However, inkjet printing can be inhibited from the nozzle clogging, hindering its application in smart textiles.²⁰⁸ Among various conductive ink, metal-organic-decomposition (MOD) is one of the best choices for the conductive textile layer ink to limit nozzle clogging and print the conductive textile layer. Silver MOD ink shows outstanding electrical, and liquid physical properties, as well as durability for inkjet printing. This high metal loading ink has low viscosity, low sintering temperature, and high stability, which attracts huge interest in inkjet printing. The Ag MOD ink is usually cured by heat to evaporate the binding liquid of the ink and sinter the particles to form the Ag film, which can be easily coated on the surface.^{80, 84, 209, 210}

The dielectric ink used in e-textiles by inkjet printing is usually made of polymer material with high printability and low sintering temperature. However, polymer materials usually have low dielectric constants (2-13) and high dielectric losses. The poor dielectric properties limit the applications. Inkjet-processible polymer ink with ceramic nanoparticle filler, called the polymer-matrix composites (PMC), can be a solution.²¹¹ The ceramic filler would enhance the dielectric property of the polymer. This system has a low sintering temperature but better dielectric properties than polymer materials. Moreover, the polymer material can be cured by many technologies, and UV irradiation is one of the most popular methods.²¹² In order to solve the nozzle clogging problem, we use monomer and oligomer mixture with photoinitiator as the solvent, which

can avoid polymer entanglements. With the addition of the BT NP, the BT UV curing ink would enhance the dielectric property of the textile material. The oligomers and monomers are stable with excellent fluidity for inkjet printing.²⁰⁸ Once under UV radiation, the oligomers and monomers are able to polymerize and form a film on the fabric surface, achieving an expected surface coating that modifies the dielectric property. UV-radiation curing has been widely used in industry because of its distinct advantages; the fast-drying of printing inks, quick setting of adhesives, and solvent-free formulation curability at low temperature. The solvent-free formulation can make full use of the material. These make the oligomers and monomers are the ideal substitutes for polymeric binders.

Although more minor of the particles' size, the thinner dielectric film may have a higher dielectric capacitance density. However, small ceramic nanoparticles may have the crystal structure of cubic or pseudo cubic phases instead of the tetragonal phase. Hence, the permittivity decrease with the particle size.²¹³ Nanoparticle dispersion in polymers as dielectric inks could result in inhomogeneous films, creating significant defects on the coatings because of the rapid agglomeration of the nanoparticles.²¹⁴ Layer-by-layer lamination is a promising technique used to produce nanocomposites based on nanoclay.²¹⁵ This method can prevent nanoparticle aggregation, and it requires a one-step process to create a nanocomposite film.

Recent studies have taken a similar approach to fabricate functional nanomaterial with UV curable ink. Rosa's group formulated a UV-curable ink for inkjet printing of yttria-stabilized-zirconia (YSZ)²¹⁶ Hakeim's group designed pigmented UV-curable inks for inkjet printing of textiles.²¹⁷ Ho's group also analyzed the effect of UV-curable inkjet printing parameters on knit fabrics with pigment UV curable ink.²¹⁸ There is could find a lot of research on the pigment UV curable ink on

a textile substrate; however, there are significant research gaps on inkjet printing ceramic UV curable on different textile substrates.

This paper fabricated textile dielectrics via inkjet printing and UV curable urethane-acrylate/BT NP ink. We demonstrated how inkjet-printed UV curable urethane-acrylate/BT NP ink could improve the dielectric constant of textiles through fiber-level interfacial studies within the 3D textile structures. Additionally, the diffusion of the inks was thoroughly analyzed on different textile structures, including woven, knit, and nonwoven fabrics. We developed a porous and highly sensitive capacitance sensor based on nonwoven fabric. A capacitive sensor constructed from three different layered materials, a silver-coated nonwoven fabric for the top and bottom of the structure, a BT/UV curable ink coated Nonwoven fabric for the dielectric layer that is between the two electrodes.

4.2 Experiments

4.2.1 Material

BT dielectric UV curable ink is fabricated by 200 nm BT with UV curable ink. More details on the process can be found in our previous paper.⁸ Liquid X Printed Metal supplied the Ag MOD ink.

4.2.2 Inkjet Printing BT Ink on Woven/ Knit/ Nonwoven Structures

A Fujifilm Dimatix inkjet printer (model DMP-2850, Fujifilm Dimatix) was used to print the BT inks on the textile substrates. The voltage of the piezoelectric actuators at each nozzle was 20 V, the frequency of the drop generation was 23 kHz, and the resolution was 1016 dpi. A laboratory cartridge printer head with 16 nozzles each with a nozzle size of around 21.5 μm was used in the

inkjet printer at a nominal drop volume of 10 pL throughout the entire experiment. The print distance was 1 mm from the print head to the textile substrate. The textile substrates used were woven fabric, knit fabric, and nonwoven fabric.

The woven fabric was made of polyethylene terephthalate (PET) with a plain weave structure manufactured by Hanesbrand Inc.. The knit fabric had jersey structure and made of PET by Hanesbrand Inc.. The nonwoven fabric contained 70% PET and 30 % polyamide (PA) and was manufactured by Evolon.

The two main variables in the process conditions were the number of print passes and the selection of an ex-situ or layer-by-layer annealing process. The three different textile substrates were printed with multiple passes creating different thickness of coated layers. The inkjet-printed textiles were UV cured for 5 minutes at 175 mW/cm^2 intensity with an IntelliRay 400W Lamp UV curing machine (Part #: UV0338) The dielectric property of the inkjet printed square pattern (5 cm *5 cm) on the textile substrates was measured using a LCR meter (Keysight E4980A Precision LCR meter) which was connected with a parallel-plate test fixture with the electrode diameter of 38 mm (Keysight 16451B Dielectric Test Fixture). The dielectric constant and dielectric loss of the fabric in the fabric thickness direction was calculated from the measured capacitance and dissipation factor by following the ASTM standard D150.

4.2.3 Inkjet Printing Ag MOD Ink on Nonwoven Structures

The Fujifilm Dimatix inkjet printer was also used for the conductive textile fabrication. The same print settings were used with a printing frequency of 23 kHz, a printing voltage of 20V, and a drop space of $25 \mu\text{m}$ (1016 dpi). The printing distance between the nozzle and substrate surface was 1

mm. The ink was filtered through a 4 μm polytetrafluoroethylene (PTFE) syringe filter before loading into the cartridge. The fabrics were heated to 60 $^{\circ}\text{C}$ during the printing process. After printing 17 passes, the samples were then heated to 150 $^{\circ}\text{C}$ in an oven for 30 mins to reduce the silver get the conductive fabrics.⁹

4.2.4 Optical Photothermal Infrared (O-PTIR) Spectroscopy

The FTIR and Raman spectra data were collected using a mIRage™ Infrared and Raman (IR+ Raman) instrument (Photothermal Spectroscopy Corp, Santa Barbara, CA). A 532 nm cw probe laser was coaligned with the IR laser beam and focused on the sample, the spot size was around 500 nm. The absorbed IR light caused the sample to heat up, and when the excited molecules return to the ground vibrational state it resulted in a temperature fluctuation at the source modulation frequency.^{32, 33.}

4.2.5 Characterizations

The ink liquid properties were tested by a cone-plate rheometer (MCR 302, Anton Paar) and a goniometer (First Ten Angstroms Europe: Cambridge, UK) to determine the viscosity and surface tension.

Nanostructure and microstructure analysis of the Ag coated fabric and BT cured polymer coated fabric were performed using a Field Emission Scanning Electron Microscope (FEI Verios 460L), a 3D laser scanning confocal microscope (Keyence, model VK-X1000). The conductivity of the Ag coated fabric was measured with a multimeter (Keysight Model 3441A). The durability of the textile capacitor was tested using a commercial tensile tester (MTS Criterion Model 43).

4.3 Results and Discussion

4.3.1 Ink Characterization

In order to solve the nozzle clogging problem, we use the BT NP with the acrylates and urethane monomer UV curing ink to enhance the dielectric property of the textile material. UV-radiation curing has been widely used in industry because of its distinct advantages, the fast-drying of printing inks, quick setting of adhesives, and solvent-free formulation curable at any temperature. The solvent-free formulation can make less waste and full use of the material. The UV curable monomer ink does not need the solvent, so we can directly use it as the solvent for the nanoparticles. Silver MOD ink was selected as the conductive ink because it is stable at room temperature and can be cured at 150 °C to reduce the silver.

To assess the printability of the ink, the viscosity and surface tension were measured. The UV curable BT ink is used to alter the fabric dielectric constant. The viscosity is around 12 cps, and the surface tension is 37.53 mN/m.⁹ The Ag MOD ink has a viscosity of 17.5 cPs, and surface tension is 28.3 mN/m. The inks match the well-studied viscosity and surface tension range which are 1-25 cps and 25-50 mN/m, respectively.⁸⁰ We can then study the ink distribution difference of the UV ink on different textile structures.

4.3.2 Barium Titanate UV Ink Wetting, Absorption and Diffusion on Different Textiles

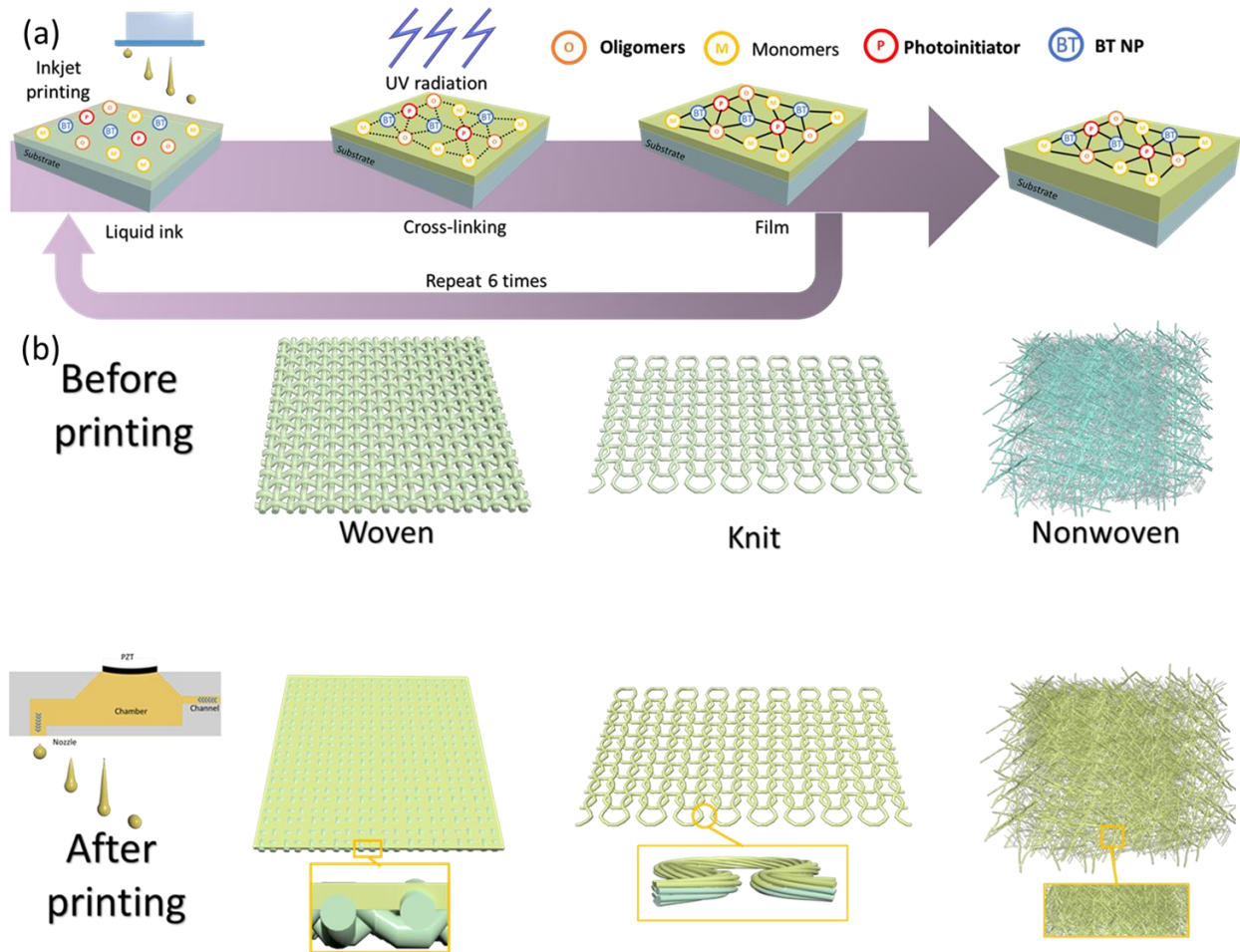


Figure 4-1. (a) Schematic of inkjet printing layer-by-layer lamination process. (b) Compared mechanisms of the BT UV curable ink for inkjet printing on three different textile structures: woven, knit and nonwoven fabric with zoomed cross-sectional images.

The ink and printed substrate interactions during the ink setting and dry process would contribute to different morphology and application after printing. The ex-situ polymerization method would cause the pattern bleeding phenomena which make it difficult to control the printing quality. (Figure S 1.) Therefore, here we chose the layer-by-layer fabrication process of the BT UV curable ink. The ink would cross-link quickly after printing, and form higher viscosity polymer chains on the fiber. In this way, the ink can fix on the textile substrate quickly, instead of spreading along

the fiber directions. The UV curable ink consists of three basic components, which are the photoinitiator, functionalized oligomers (Urethane and acrylate oligomer) and acrylates monomers.²¹⁹ Under the UV light, the photoinitiator generates free radicals. The functionalized oligomers form the backbone of the polymer network, and the monomers act as a reactive diluent to adjust the system viscosity.²²⁰ (Figure 4-1) After the droplets leave the nozzles, they will settle on the substrate surface. For the smooth substrate, the ink would experience the wetting, spreading, and drying process. The wetting process usually happens in 0.1 ms; spreading happens in seconds while drying needs hours.⁷⁷ The UV irradiation would greatly reduce the drying process. However, the ink during the spreading process would also penetrate the porous structure. When ejected drops land the surface of the fibrous substrates, the ink drops show the following behavior in different phases. (Figure 4-1) First, individual drops contact and clash on the surface of the fibers. The inks wet the surface of the fibers and evaporate, which is dependent on multiple factors. The surface energy of the inks and the substrates and vapor pressure of the inks influence this process. The inks penetrate the microstructure to be absorbed into fibers.¹¹ Therefore, the pore size, porosity, and chemical component of the substrate has a tremendous impact. Textiles, as porous substrates, vary significantly from non-porous substrates such as films, silicon wafers, etc. The polymerization of the UV curable urethane and acrylates monomer inks show different penetration morphology into the cross-section of fibrous structures. The three different structures of conventional textiles, woven, knit, and nonwoven fabrics, are compared in this study (Table 4.1).

Table 4.1. Specification of fabrics for inkjet printing e-textiles.

Fabric	Polymer	Weight [g/ m²]	Thickness (um)
Woven	PET	63	110
Knit	PET	145	310
Nonwoven	70 wt% polyester 30 wt% polyamide	95	390

$$\text{Porosity: } P = \frac{V_{Void}}{V_{Total}} \quad (1)$$

$$P = \left(1 - \frac{w}{\rho * h}\right) * 100\% \quad (2)$$

Where: h is fabric thickness (μm); ρ is density of the material (g/cm³); W is fabric weight (g/m²).

The main difference between these structures is the fibers organization method and chemical composition. Woven fabric usually has a highly compact structure due to larger number of filaments per yarns and the tightly interlocked yarn structure. Usually, woven fabric has very low porosity and small pore size. The woven fabric is usually made of thigh-packed yarn, and the porosity usually contains 50-80 % of air by volume, and knitted structures usually have a higher porosity.²²¹ Knit fabrics are composed of loops, which have slight tension between the yarns, and the loops typically provide large void spaces. The large loop structure is what contributes to the large pore size in knit fabrics. Nonwoven fabrics are not made from yarn but directly from randomly organizing fibers. Knit fabrics and nonwoven fabrics usually have high porosity. The ink spreading behavior can be different on these substrates. Equation (1) provides the definition of porosity. Based on Table 4.1 and equation (2), the three fabrics' porosities can be calculated. The porosity of the fabrics used to analyze the ink distribution were 58.5%, 72.46%, and 81.42% for

the woven, knit and nonwoven respectively. Here, we choose three widely used textile fabrics to discuss the ink modification on the textile substrates.

The dense PET woven fabric with low porosity and pore size accumulates more ink on the surface and dent area. The ink penetrates the fabric more in the loose PET knit fabric because of its high porosity and large pore size. The high porosity PET/PA nonwoven fabric with small pore size, the ink shows more penetration and spread on the surface due to high porosity and hydrophilic component. (Figure 4-1) In comparison, the hydrophobic polyester material has an adverse effect on ink penetration.

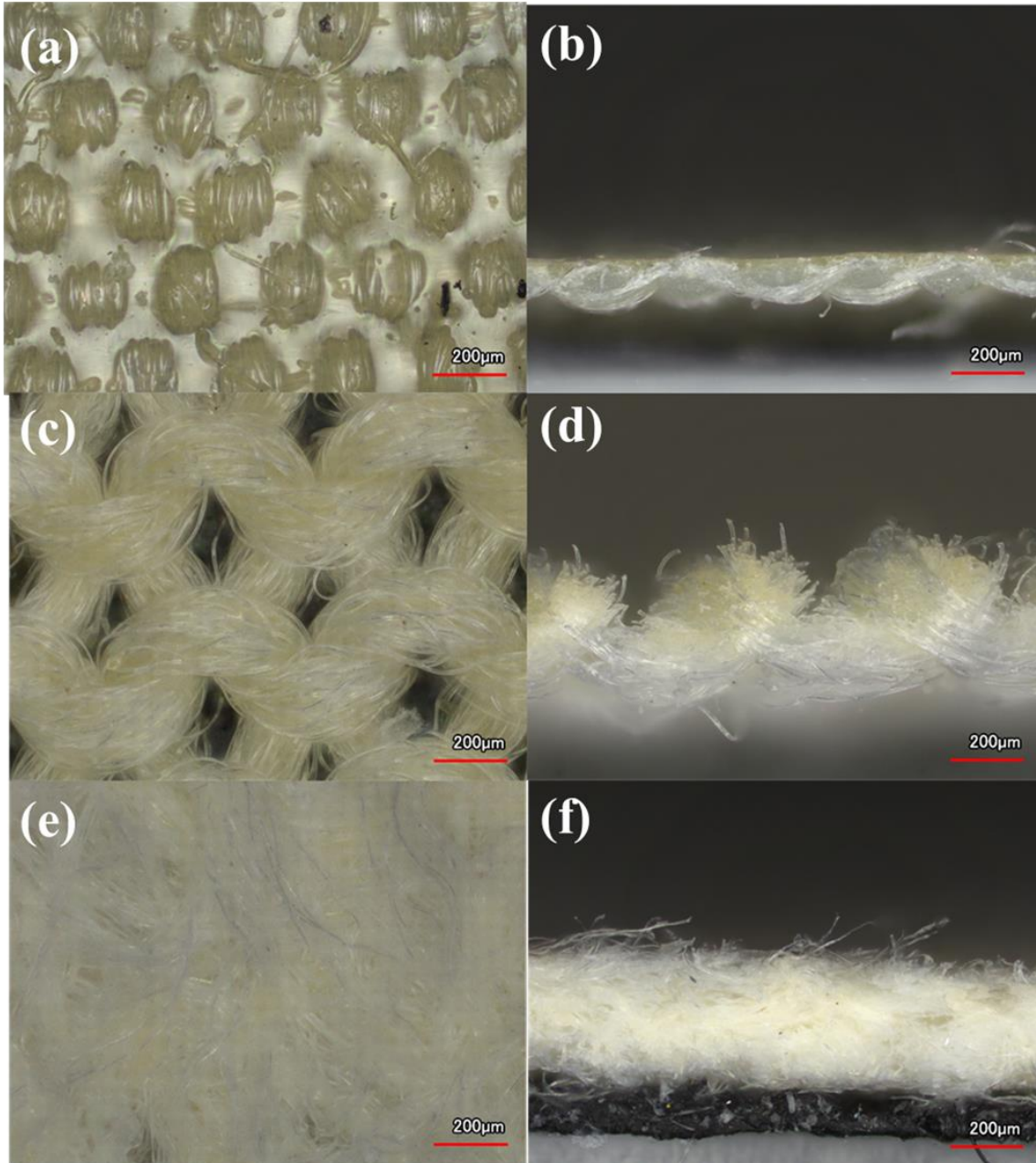


Figure 4-2. Microscopic images of BT UV curable ink inkjet printed by layer-by-layer process of (1L)6 textile structures; (a) woven fabric, (b) knit fabric, (c) nonwoven fabric.

Figure 4-2 shows the BT UV curable inkjet-printed layer-by-layer lamination of 6 layers of ink on different substrate surface morphology and cross-sectional penetration. The ink shows yellow color, which can be very clear on the optical microscopy. According to the cross-sectional optical microscopic images, the ink penetrates into the knit fabric and nonwoven fabric. While the ink

accumulated on the woven fabric, where the top woven fibers also were coated. Further characterization will be proved by O-PTIR. We observed that the ink forms layer to block the fabric voids, which can damage the mechanical property and flexibility of the fabric. We also observed more ink fixed by ex-situ polymerization on the woven fabric surface. (Figure S 2) For the nonwoven structure, the voids distribute randomly and are mostly in the micrometer size. Moreover, the hydrophilic of PA fibers contributes more to the ink penetration and distribution on the fabric. In both methods, we observed the ink penetration on the top and back of the material. (Figure S 3). The voids in the knitted structure can reach 100 μm , which is much larger than the droplet size. So even on the hydrophobic fibers, the ink still can penetrate on the knit fabric. We found that the chemical composition of the fabric, pore size, and porosity play an important role in the ink penetration and spreading.

4.3.3 Characteristics of Barium Titanate UV Inks

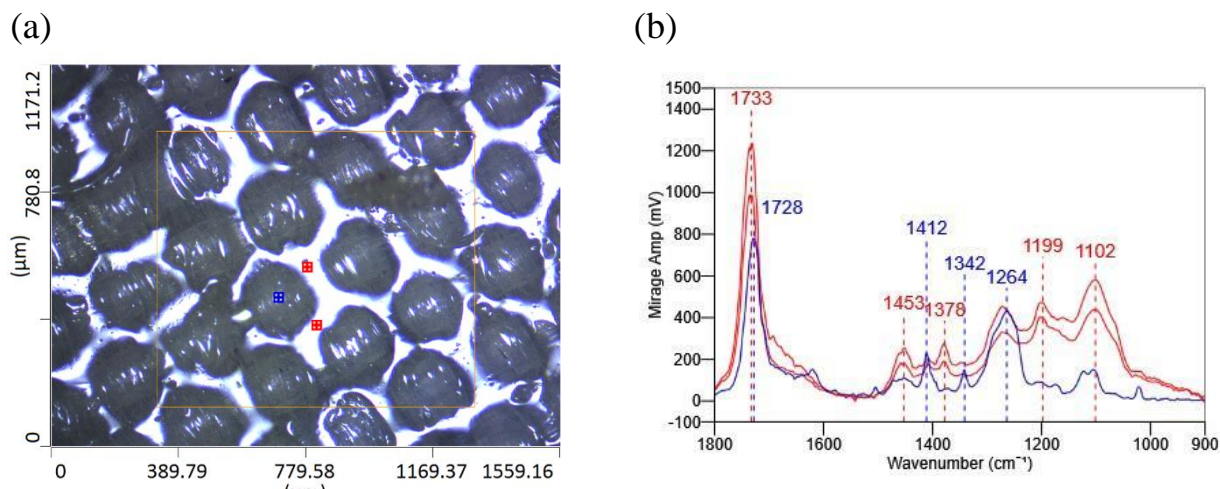


Figure 4-3. (a) mIRage™ optical images of woven fabric with dielectric ink, (b) IR spectra of the woven fabric with dielectric ink. (blue line means the higher region of the fabric; red line means the lower regions of the fabric)

Figure 4-3 shows the FTIR spectrum gathered from the mIRage™ optical image where the blue and red lines represent the higher and lower regions of the PET woven fabric, respectively. Ideally, the higher regions of the woven fabric will show less accumulation of the dielectric ink compared to the lower regions of the fabric due to ink mobility through the porous woven structure (Figure 4-3a). Observation of the FTIR results in Figure 4-3 confirms the accumulation of the dielectric ink to occur in the lower regions of the woven fabric. The FTIR peaks at 1728 cm⁻¹, 1412 cm⁻¹, 1342 cm⁻¹, 1264 cm⁻¹, and 1023 cm⁻¹ all correspond to the different chemical functional groups of the PET woven fabric (Figure 4-3b-blue line, Figure S 4). For example, the peak at 1728 cm⁻¹ represents the stretching of the carbonyl group (C=O) along the PET polymer backbone²²². The peaks at 1412 cm⁻¹ represents the ring semi-circle stretch and the peak at 1342 cm⁻¹ relates the CH₂ wag. The peaks at 1267 cm⁻¹ represents the C-O stretch and the peak at 1023 cm⁻¹ represents aromatic ring in-plane CH bend. Unlike the peaks for the PET woven fabric, the dielectric ink shows different peaks in its FTIR spectrum (Figure 4-3b-red line). The peaks at 1733 cm⁻¹, 1453 cm⁻¹, 1376 cm⁻¹, 1264 cm⁻¹, 1199 cm⁻¹, 1102 cm⁻¹ correspond to the functional groups of the polymers used in the dielectric ink. Although the peak at 1733 cm⁻¹ for the dielectric ink is close to the PET woven fabric peak at 1728 cm⁻¹, the dielectric layer is thick enough to essentially mask any contribution of the PET signal during the mIRage™ analysis. So the peak at 1733 cm⁻¹ corresponds to the deformation vibrations of inner CH groups, terminal CH groups and skeletal stretching vibrations of the dielectric ink.²²³ The other absorption bands between 1445-1480 cm⁻¹ correspond to the CH scissoring mode vibrations and the CH deformation vibrations of end groups.²²⁴ The peak at 1199 cm⁻¹ corresponds to the ν (C-C) acrylic chain vibration.²²⁵ The peak at 1102 cm⁻¹ coincide with the peaks reported for ν_{as}(C-O-C)²²⁶. Overall, the FTIR signals

confirm the accumulation of the dielectric ink in the lower regions of the woven fabric which correspond to the joints of the individual fibers of the textile.

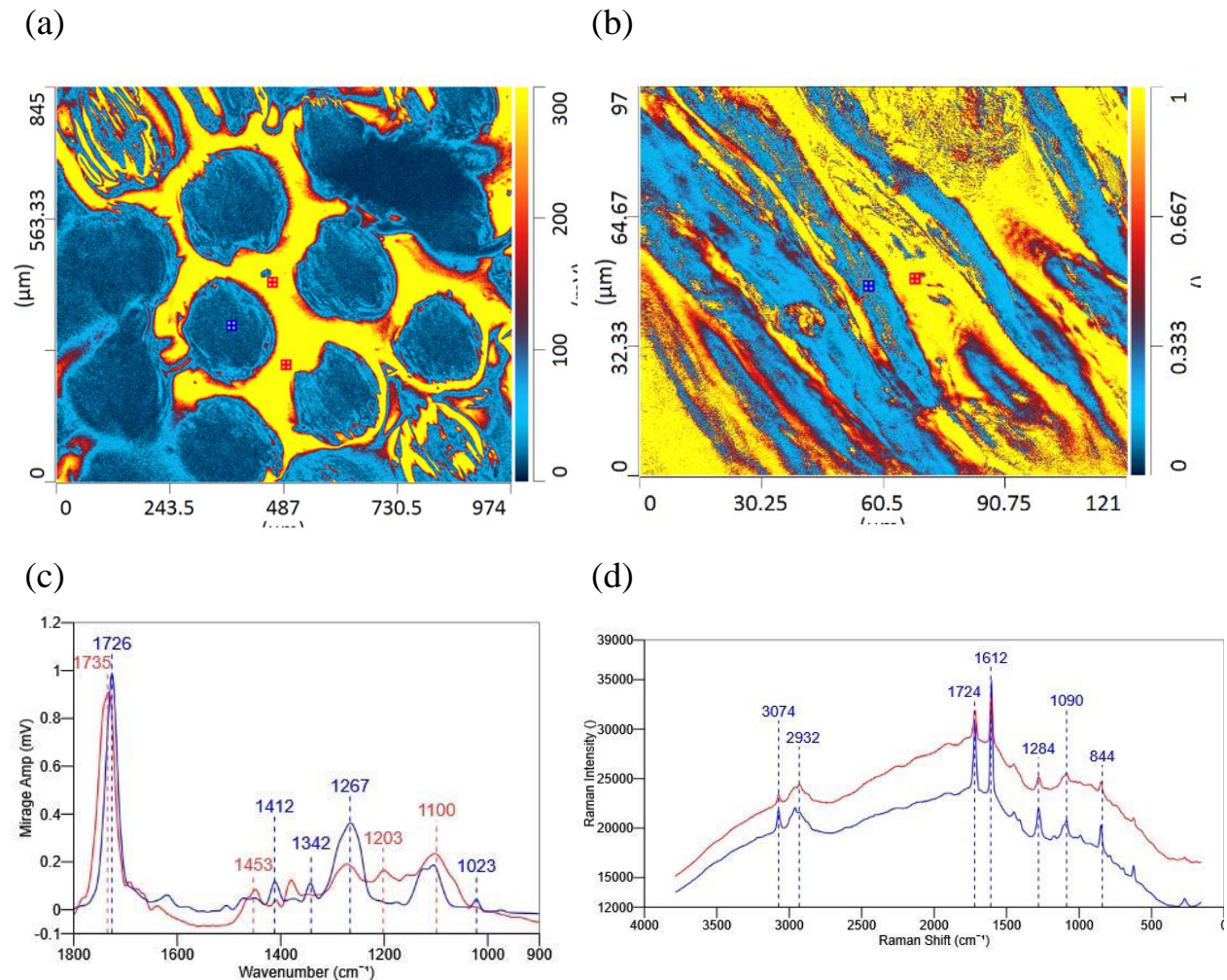


Figure 4-4. (a) mIRage™ image at 1202 cm^{-1} of woven fabric with dielectric ink ($845 \times 974\ \mu\text{m}$) (b) A zoomed in mIRage™ single frequency ratio ($1202/1412\text{ cm}^{-1}$) image of woven fabric with dielectric ink ($97 \times 121\ \mu\text{m}$), Simultaneously collected (c) IR spectra and (d) Raman spectra.

To further confirm the accumulation of dielectric ink in the PET woven fabric, simultaneous acquisition of FTIR and Raman were acquired using the mIRage™ instrument (Figure 4-4). Figure 4-4a and b show O-PTIR images of the dielectric ink distribution on the woven fabric. The images show the intensity differences between the PET woven fabric and dielectric ink. The O-PTIR

image in Figure 4-4a confirms the accumulation of dielectric ink (yellow regions) in the lower jointed regions of the woven fabric and PET fabric regions (blue regions). However, the Z planes of the test may greatly influence the data. Single frequency imaging is hard to tell the difference between PET and BT UV cured polymer. From previous data, we can find PET has a strong peak at 1412 cm^{-1} , while BT UV cured polymer has a strong peak at 1202 cm^{-1} . Single frequency ratio ($1202/1412\text{ cm}^{-1}$) image can better tell the differences between PET and BT cured polymer. Interestingly, the single frequency ratio O-PTIR image in Figure 4-4b shows that the dielectric ink (yellow regions) is also located in the higher regions of the woven fabric. The blue regions in Figure 4-4b represent the uncoated PET fibers of the woven fabric. We confirmed that the inherent porous structure of the woven fabric allows the dielectric ink to penetrate into the lower regions of the fabric, but the results in Figure 4-4b indicate the dielectric ink does not fully penetrate through the woven fabric and can accumulate on some of the higher regions of the fabric. Figure 4-4c and 4d show the simultaneous FTIR and Raman spectrums that correspond to the O-PTIR images. The Raman spectrum in Figure 4-4d and Figure S 5 shows peaks at 625 cm^{-1} , 856 cm^{-1} , 994 cm^{-1} , 1096 cm^{-1} , 1286 cm^{-1} , 1611 cm^{-1} , 1724 cm^{-1} , 2965 cm^{-1} , 3079 cm^{-1} . In the lower areas of the woven fabric, the peaks show more peaks associated with the dielectric ink, and in the higher areas of the fabric the peaks shift from 3079 cm^{-1} to 3074 cm^{-1} , and 2965 cm^{-1} shift to 2932 cm^{-1} indicating the presence of the PET woven fabric. The 2932 cm^{-1} is due to asymmetric CH-stretching from methylene in short segments.²²⁷ The band of the C-O stretching (1100 cm^{-1}) confirms the presence of dielectric ink on the fibers in higher regions of the fabric. According to the high resolution of the O-PTIR, we could easily tell the dielectric ink distribution on the fiber, unlike with conventional IR methods which are difficult to achieve spatial phase resolution at the micron level.

Overall, with the O-PTIR, we could prove the dielectric ink was successfully coated on the fiber surface instead of only the joints of the fibers.

4.3.4 Characteristics of Ag MOD ink

The nonwoven fabric is made of PET and PA, and biocomponent polymers are randomly oriented in the nonwoven microstructure. We choose the different positions of the pristine nonwoven fabric and Ag inkjet-printed nonwoven fabric, which is shown in Figure 4-5a, magnified pristine nonwoven fabric in Figure 4-5b, and magnified Ag modified nonwoven in Figure 4-5c. The different positions 1, 2, 3, 4 show the result of its Raman and IR spectra. The peaks at 1639-^1 and 1546 cm^{-1} are the typical peaks of the explaining amide I of C=O stretching and amide II of N-H, which can represent the PA content. While the peak at 1739 cm^{-1} in the IR spectra represents the ester group (C=O) of PET. While we can also observe the 1712 cm^{-1} peak, which means the ketone (C=O), suggesting the PA polymer is mixing with the PET in this position. In positions 3 and 4, from the IR spectra, we can still observe the PET peaks and PA peaks which means the Ag may be mixed with the fiber. In Figure S 6, we can observe the no peaks in the IR spectra, which prove the total elements. While in the Raman spectra, we can also further prove the Ag coated on the PET and PA fiber. (Figure 4-5e) The Raman singles have obvious enhancement due to the Ag NPs.^{228, 229} From O-PTIR, we see the thin Ag coated on the PET and PA fibers, and also the thick Ag layer without any PET and PA signals in IR spectra. (Figure S 6) This method is a very effective way to trace the ink modification of the porous and rough substrate.

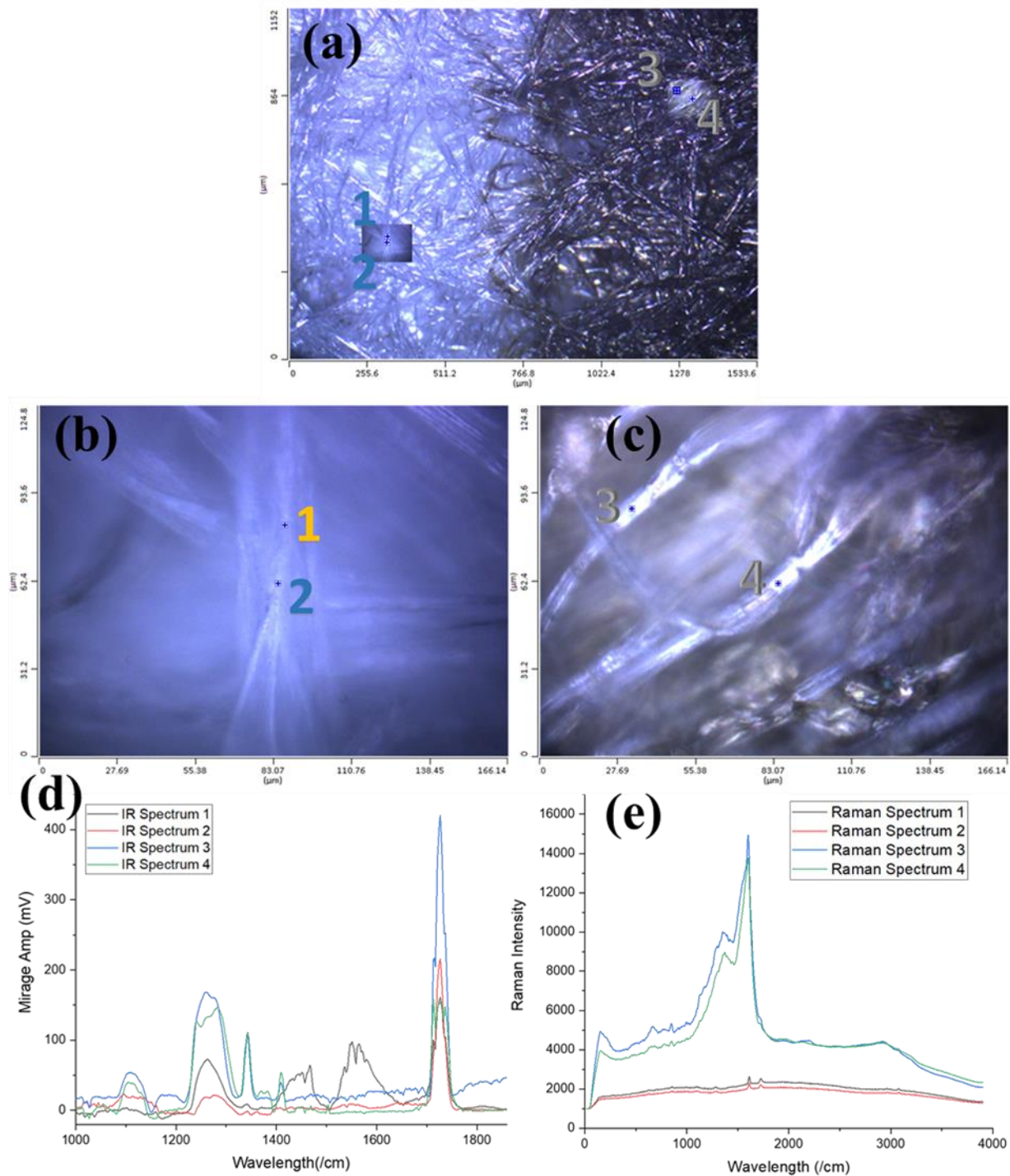


Figure 4-5. Simultaneous IR/Raman analysis of inkjet-printed nonwoven e-textiles with laser confocal microscopy of pristine side of PET/PA nonwoven fabric, and inkjet-printed Ag nonwoven fabric with Raman and IR spectra respectively.

4.3.5 Layer-by-Layer BT UV Cured Nonwoven Fabric Dielectric Properties.

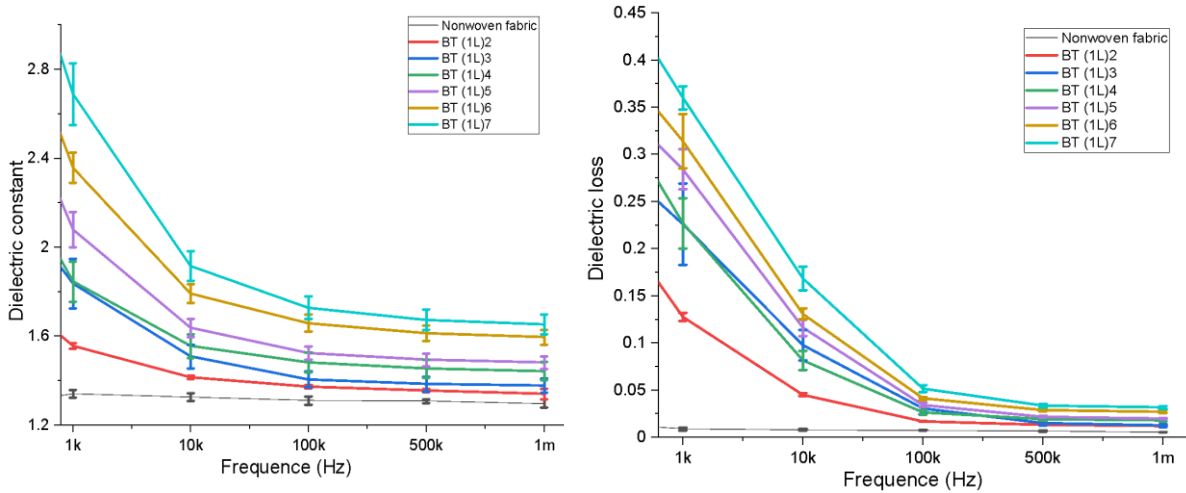


Figure 4-6. a) Dielectric constant and b) dielectric loss of the layer-by-layer inkjet-printed nonwoven fabric.

A LCR meter was used to measure the dielectric constant by calculating the capacitance in the range 1kHz -1M kHz. Because the fabric contains a lot of air gaps and is very soft, we choose the air gap method to measure the dielectric constant. The dielectric fabric thickness can have a large influence on the result. 10 measurements of the thickness were tested, the mean and error are shown in Figure S 7. When the printing and curing is repeated more than 10 times, the film thickness can enhance. When done less than 10 times, the film thickness can be regarded as unchanged.

With inkjet printing, the dielectric constant increases when more ink is deposited on the fiber, and the dielectric constant decreases with the frequency increase. (Figure 4-6) Even printing the same printing pass on the fiber, the curing method can play a big role in the results. Following the BT UV curable ink layer-by-layer lamination polymerization, this enhances the dielectric constant

more than the ex-situ polymerization. (Figure S 8) This further proves the layer-by-layer lamination helps the ink fixate on the printed area and reduces the ink mobility on the fibers.

4.3.6 Textile Capacitor Array

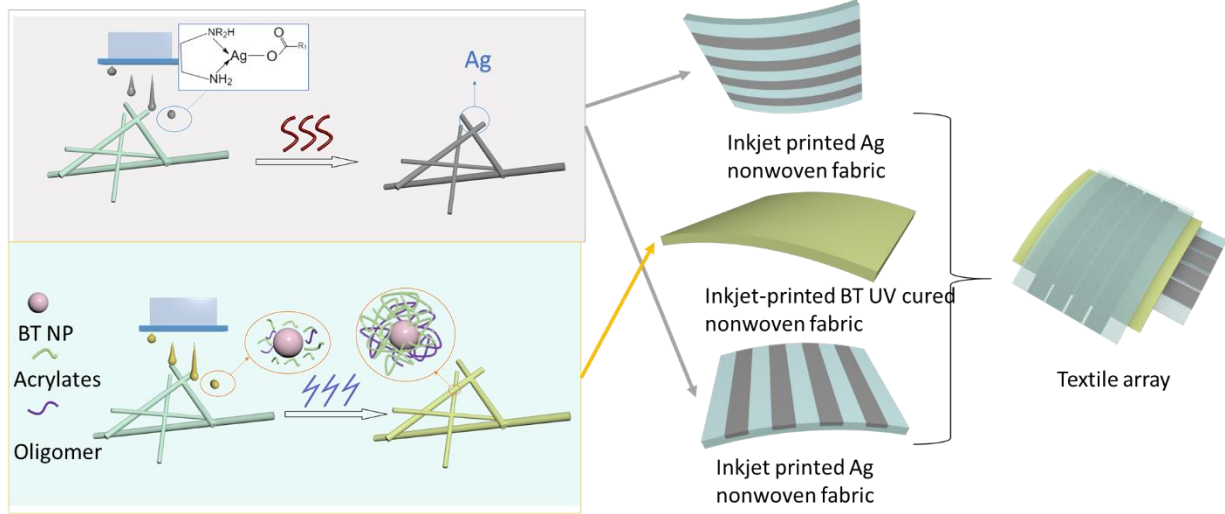


Figure 4-7. Mechanism BT ink inkjet printing on fabric process.

The all-textile capacitor array is based on a structure proposed in Figure 4-7, which consists of a sandwich made of two inkjet printing Ag nonwoven fabric at top and bottom with an inkjet-printed BT UV curable nonwoven fabric by the layer-by-layer process between the conductive layers. Due to the high resolution and mask-free inkjet printing, the conductive layer was printed with 4 lines with a size of 1 cm* 5 cm, with gaps of 1 mm. The inkjet-printed Ag nonwoven fabric shows good conductivity, with a surface resistance lower than 0.014 Ω /sq and a maximum thickness of 0.39 mm. The two conductive sheets are placed with a layer-by-layer BT UV cured nonwoven fabric with a maximum thickness of 0.39 mm and a dielectric constant of 2.7 at 1 kHz, which is much higher than the pristine nonwoven fabric ($k=1.3$).

4.3.7 Microscopic Analysis of the Inkjet Printed E-Textiles

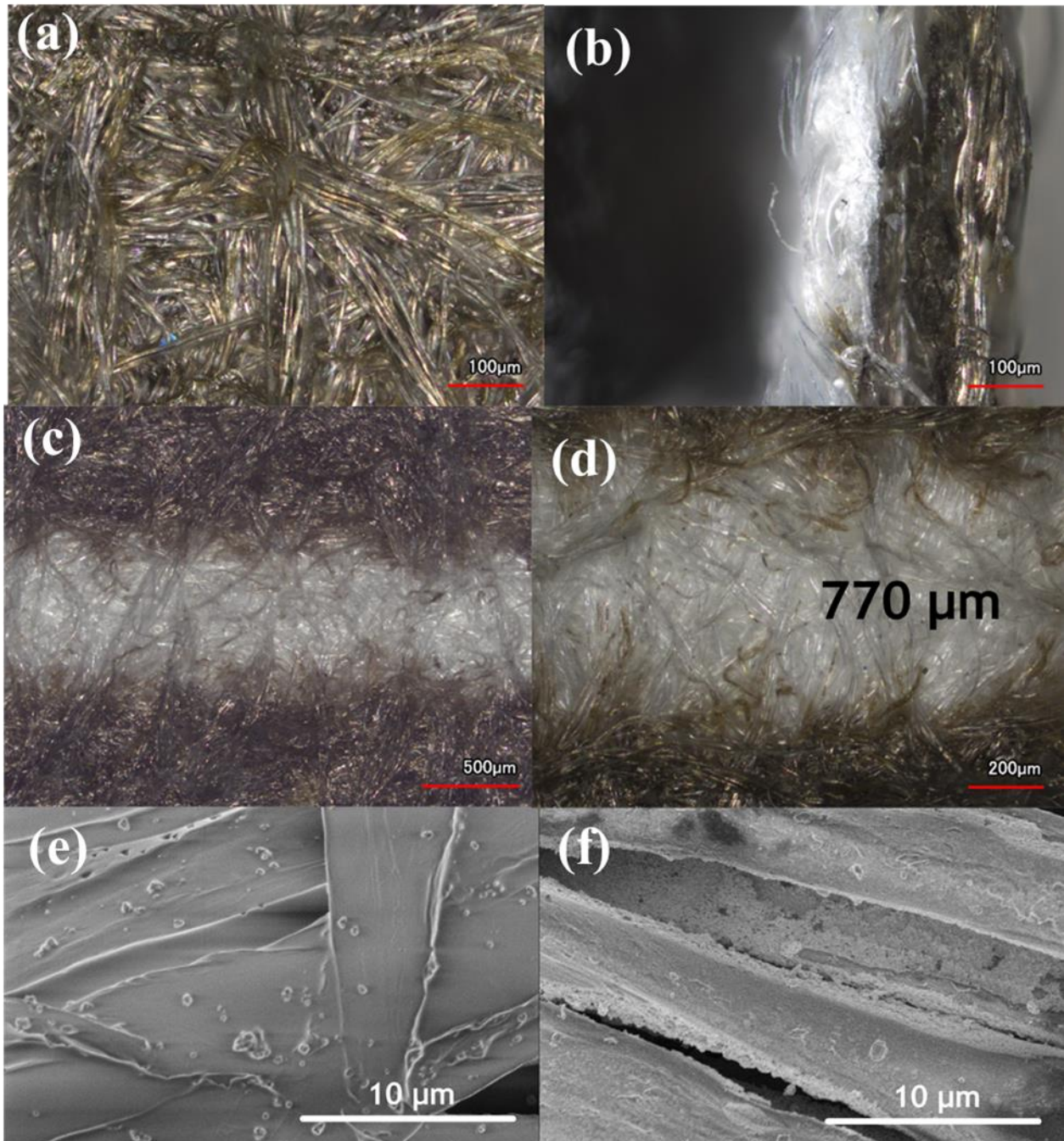


Figure 4-8. Optical microscope images of Ag coated nonwoven fabric (a) surface image with a bar of 100 μm , (b) cross sectional image with a bar of 100 μm , (c) surface image of the conductive line gap with a bar of 500 μm , (d) surface image of the conductive line gap with a bar of 200 μm . SEM image of (e) the BT UV cured polymer coated fiber by a layer-by-layer process. (5000x, 10 μm bar), (f) the Ag coated fiber. (5000x, 10 μm bar).

In order to characterize the functional material diffusion on single fibers, microscopical and SEM images are shown in Figure 4-8. The Ag ink penetrated the nonwoven PET and PA fibers without blocking the gaps between the fibers. (Figure 4-8a, 8b, 8f) This means the functional fabric shows good conductivity while preserving the textile structure. The narrow gap between the conductive lines shows a gap around 800 μm , (770-860 μm) which shows the high concentration and control of inkjet printing. (Figure 4-8c and 8d) The SEM image of the BT UV cured polymer-coated fiber also proves the thin film coating at the fiber level and preserves the textile structure. We could see the BT NPs are coated on the fiber and embedded with the photopolymer. (Figure 4-8e)

4.3.8 Smart Sensor of the Textile Capacitor Array

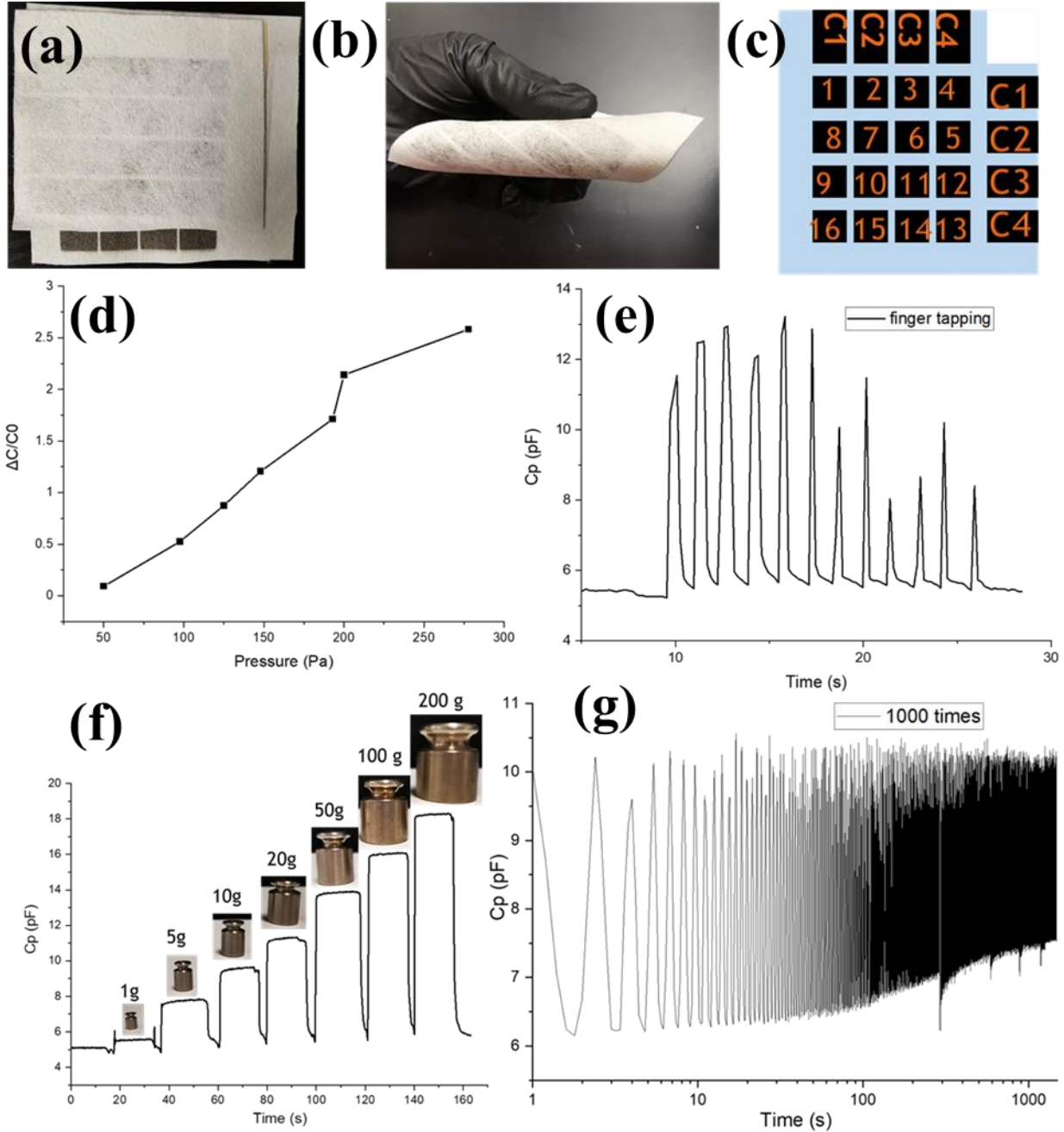


Figure 4-9. (a) An all-inkjet-printed textile array. (b) Bended textile array sample. (c) Schematic illustration of textile array structure. (C1 mean connector 1.) Real-time detection of different mechanical forces using the textile capacitor (d) Sensitivity of textile-based sensor under different pressure. (e) Finger tapping on textile capacitor. (f) Standard weights applied on the textile capacitor (g) Sensor performance tapping 1000 times for the textile capacitor.

The final pressure sensor maintains the mechanical flexibility of the pristine textiles with the BT UV cured polymer and Ag film coating. As a demonstration of the textile capacitor array, the textile-based capacitor shows good flexibility. (Figure 4-9a-9c). To explore the pressure responses of the capacitor array, we measured the capacitance responses to different pressures applied to the sensor. The sensitivity of the pressure sensor is defined as $S = \delta (\Delta C / C_0) / \delta P$, where ΔC is the change in capacitance, C_0 is the capacitance without allied pressure, and P is the applied pressure. $S = 11.4 \text{ kPa}^{-1}$ for the pressure below 0.3 kPa. The capacitor array shows high sensitivity at low pressure. Once the force is applied to the capacitor, the distance between the fabric is greatly reduced, leading to the corresponding rise in the capacitance. (Figure 4-9d) The pressure sensor can be used to detect the finger tapping and weights that are applied on the top. (Figure 4-9f) After 1000 repeated cycles compressing the textile capacitor, the capacitor still maintains capacitance profile changes of more than 20%. (Figure 4-9g) The capacitance change profile was tested for each capacitor sensor in the textile array (Figure S 9) during a 200 repeated pressure loading-and-uploading process.

4.4 Conclusion

In this study, a novel ink for inkjet printing smart textile was used to analyze the ink diffusion on the different textile substrates, considering porosity, pore size, and chemical components. A versatile and facile approach was used to fabricate a highly sensitive and flexible textile pressure sensor array on a textile substrate. A pressure sensor with a multipixel array structure was constructed using inkjet printing of UV Curable ink in a layer-by-layer lamination process and Ag MOD ink through an in-situ curing process on nonwoven fabric, allowing it to maintain the porosity and flexibility of the textiles. The resulting sensor achieves high sensitivity (11.4 kPa^{-1}) at a low-pressure range, stable cycling performance (1000 cycles). Moreover, the low-cost and

high resolution of the inkjet printing method makes it possible for large-area and instant fabrication on textile substrates. These features provide device capabilities for easy integration with textiles, enabling future e-textiles or wearable electronic applications.

5 All-Inkjet-Printed Wearable and Breathable Textile Antenna

Abstract

Next-generation wearable devices demand lightweight, flexible, and breathable antenna designs that are provide facile integration for compatibility with the consumer and manufacturing requirements. This paper presents the design of an all inkjet-printed antenna operating at 2.45 GHz and optimized for human body performance for next-generation wearable antennas. This processing study and demonstration represents a milestone compared to prior printed textile antenna designs that required dense screen-printed interface due to the fabric roughness, impairing breathability and flexibility. The antenna design in this work is realized through inkjet printing of a reactive MOD silver ink on the surface of nonwoven fabric to form the patch and ground. These nonwoven materials were then laminated upon a porous knit fabric in which a barium titanate nanoparticle-based ink was also inkjet-printed to increase the dielectric constant 14.3%. The fabricated patch antenna shows a low return loss of 24.98 dB in free space and preserves its performance even when bent to $>300^\circ$. When applied on in close proximity to the human body, a -10 dB bandwidth was observed from 2.38-2.55 GHz. The breathability of the antenna is retained after inkjet printing. More importantly, after consecutive 1000 bending cycles, the conductivity and return loss of the antenna remained unchanged with excellent stability in signal acquisition and mechanical durability. Moreover, the use of knit fabric makes it easy to integrate into the cloth. The knit fabric allows for a simple integration into a cut and sew process. This work provides an innovative strategy for flexible and breathable textile antennas through inkjet printing for the applications in the field of integrated wearable electronics.

5.1 Introduction

Printing is one of the most promising methods in the field of flexible and wearable electronics due to the advantages in pattern-versatility, cost-reduction, automation, and scalability^{25, 26}. Due to a textile substrate's inherent flexibility, breathability, and their ubiquitous use in our daily lives, the use of textiles as a building block for electronics is perceived as logical means for wearable electronics. Electronic components have been demonstrated previously to be readily patterned on textiles via printing processes that dispensing conductive, semiconducting and insulating materials.²⁷ For example, electronic textiles (e-textiles) can be developed into wearable solar cells²⁸, supercapacitors^{29, 30}, energy harvesters,^{200, 201} biomonitoring sensors³¹, energy storage materials³², and wearable antennas^{6, 33-35, 161}. Often, the e-textile devices underperform their hard component-based devices, and planar flexible film device counterparts due to the non-planar surface of the textile that results in poor mechanical performance of printed electronics. Therefore, a poor dielectric behavior of the porous textile substrate can lead to low dielectric constant devices. These challenges can be overcome by the lamination of flexible silicone or urethane-based film on the textile to create a smooth, high density surface.^{190, 230} These processing solutions, while effective for device performance, limit the surface porosity of the textile which is a major expected benefit of breathability for user comfort.

The latest standardization of WBANs from IEEE 802.15.6 is developing a communication standard for low power devices and operation short range (within the human body) to provide timely data including medical, consumer electronics, personal entertainment and others.^{231, 232} Such networks are essential for collecting healthy data to diagnose the disease before experiencing the symptoms. Moreover, the wearable monitoring systems such as heart rate signals, blood

pressure rates, can respond chronic or fatal diseases timely to save lives. Instead of in-hospital monitoring, WBAN can greatly reduce health costs and improve the quality of life.²³² Antennas are of great importance for wearable electronics and non-wearable Internet of Things (IoT) applications, transducing radio waves to electronic signals to allow wireless data transmission between sensors, actuators, and processors. For wearable applications specifically, antennas may be distributed for body area networks.^{233, 234} For all wearable applications, and some IoT applications, it is desired that the antenna be flexible enough to conform to the human body curvature shape and arbitrary directions of bending during the body movement.^{126, 234}

Various manufacturing techniques for e-textiles, specifically for antennas, have been developed, such as screen printing,^{99, 100} metalized adhesive tape¹⁰¹⁻¹⁰⁴, liquid metal¹⁰⁵, embroidered textiles¹⁰⁶⁻¹¹¹, and inkjet printing¹¹²⁻¹¹⁴. Among these techniques, inkjet printing is considered as a promising method for the antenna design considering the automation of processing, the computer aided design (CAD) capability, and environmental friendliness.²³⁵ These key attributes of inkjet printing therefore promotes simplicity of the process, time and cost efficiency, and the formation of high resolution of patterns.²⁷ Inkjet printing with drop-on-demand (DOD) system requires no masking process while the flexibility to change the device pattern design benefits automated and customized device manufacturing.¹¹⁶

In the inkjet printing process, ink solutions are dispensed via openings or nozzles (10-30 μm) from the printhead in a pixelated pattern on a surface.⁸³ The inkjet process with fully automated DOD system uses low viscosity inks (≤ 25 cps), which would lead to the formation of ultrathin coatings (0.01-1 μm)⁴⁰ on substrates and patterns with high resolution. The control of the ultrathin coating

thickness is integral to maintaining flexibility in substrates after the deposition of functional materials. This is highly important in flexible printed electronics since the functional materials are mostly metals and ceramics that are a high modulus in their bulk form. Due to the viability of the automated process, pattern versatility, and ultrathin coatings, the application of the inkjet process to electronic materials has drawn tremendous attention in flexible electronics.⁷⁶ As such, numerous researchers have demonstrated the uses of inkjet process for flexible electronics, such as high-resolution and flexible conductor⁶², textile capacitors⁸¹ and flexible transistors⁸². DOD system benefits pattern versatility and low-materials waste processing, implying a great potential for e-textile fabrication.⁷⁷ In previous studies, our research has developed the inkjet process for conductive patterns on textiles using particle-free organometallic inks on knit, woven and nonwoven fabrics.^{80, 183, 236} It is important to note that due to the low viscosity of the inks used in inkjet printing, the ink may penetrate the surface of the textile and provide a fiber level coating in the interior of the textile cross-section. This internal coating within the fiber interstices is depended on the similarity of the surface energy of the polymer to the surface tension of the ink. This is relevant when comparing this technique to the broadly used screen-printing of conductive inks (or pastes) that have a higher viscosity and have low penetration into textile and fill the porosity voids to form a composite-like structure.

In previous studies, diverse processing strategies of flexible inkjet-printed antennas have been demonstrated.^{114, 116, 119-123} Budimir et al. reported an inkjet-printed antenna for 5G application (28 GHz) using silver nanoparticle ink on Kapton film with a copper sheet as the ground plane. The device exhibited a return loss of more than 16 dB at 27.75 GHz.¹²³ Ryberg et al. presented a patch antenna and a quasi-yagi antenna by inkjet printing of silver nanoparticles on photo-paper (photo

paper is a paper coated with a light-sensitive chemical formula, which used for inkjet printing²³⁷). Both antennas demonstrated good matching and acceptable efficiency at frequency of 2.4 GHz.¹¹⁴ The aforementioned antenna substrates has poor breathability and wearability. A textile antenna was proposed by Tudor et al.¹¹⁶, through printing silver ink onto polyester cotton fabric, and efficiency of over 60% was achieved. However, an interfacial layer via screen-printing was required to create a smooth surface, resulting in low breathability and flexibility.

This work seeks to resolve the challenge of making a functional wearable antenna while maintaining its flexibility and breathability. In this study, a flexible, wearable fabric patch antenna was fabricated to operate between 2.38-2.55 GHz when applied to a human body. In printing process, the reactive silver ink was in-situ cured on the surface of nonwoven fabric to form a patch and a ground. This layer was then applied upon either side of a knit fabric. The nonwoven layer in this case provides a relatively smooth surface for maximizing the conductive print while retaining porosity. The knit fabric, characterized by a porous and yarn loop, provides high structural integrity and ease of integration in many common garments through panel sewing. However, knit fabrics possess low dielectric constant and geometrical inaccuracy, limiting its applications in wearable antenna.¹²⁶ To resolve this, the dielectric constant of the knit fabric was increased by inkjet printing of a barium titanate (BT) nanomaterial ultraviolet (UV) curable ink. The resulting antenna showed excellent flexibility and stable performance even under extreme bending at 331°, maintaining the performance and shape of the antenna. There are not any cracks on the conductive and dielectric layers. Moreover, this antenna shows a high level of durability with up to 1000 cycles of bending from 60 mm to 30 mm.

Table 5.1. Comparison of Flexible Antenna Reported in the Literature

Ref.	Substrate Material	Volume (mm ³)	ϵ_r	δ	Conductive Material	Bandwidth
¹⁰²	Textile fabric	120×120×3	1.48	0.02	Copper tape	105 MHz
⁹⁹	Nonwoven fabric	80×80×2	1.7	0.01	Ag paste by screen printing	150 MHz
¹⁰⁰	Cotton/PET with screen printed interface layer	42.5×48.5×2.81	1.64	0.02	Ag particle conductive ink by screen printing	~ 124 MHz
²³⁸	PET fabric	80×80×2.4	1.9	-	PEDOT: PSS by screen printing	200 MHz
²³⁹	PET/Cotton with screen printed interface layer	37.4×28.1×1.6			Ag ink by inkjet printing	24.5 MHz
²⁴⁰	PET fabric	101×96×2	1.6	0.01	copper- and nickel-plated	~ 125 MHz
This work	PET knit fabrics plus two nonwoven fabrics	60×70×2	1.7	0.001	reactive Ag ink by inkjet printing	160 MHz

Table 5.1 shows the comparison between the proposed antenna and the work reported in the literature, including antenna volume, dielectric property (relative permittivity and dielectric loss),

bandwidth, and gain. It can be observed that the proposed antenna has a comparable or higher bandwidth. It is an impressive performance as extreme porous knit fabric was used as the antenna substrate with a small size (60×70×2 mm).

5.2 Experimental Section/Methods

5.2.1 Conductive and Dielectric Inks

Reactive silver ink was obtained from Liquid X Printed Metal (Pittsburgh, PA).⁸⁰ The solution was particle-free, containing a mixture of silver carboxylates with an aqueous proprietary ammonia ligand and silver salt that was stable at room temperature. At higher temperature (<200 °C), the solvent begins to volatilize, and silver can be formed by the reaction of the reducing agent with the silver salt. A dielectric ink was prepared by mixing 4 wt.% barium titanate nanoparticles (200 nm, Nanostructured Amorphous Materials Inc., USA) with acrylates and urethane oligomer UV curable dielectric ink (C3-D1-1032 Dielectric photopolymer, Chem3, LLC, USA). More details can be found in.⁹

5.2.2 Fabric Selection

Evolon® nonwoven fabric (Freudenberg Performance Materials, USA) is made of 70/30 polyester polyamide fibers, with a thickness of 0.33 mm, and a weight of 95 g/ m². This nonwoven fabric features a high surface area (~2.05 mm² mm⁻² of fabric area) and low surface roughness (Ra=~18 μm). The suitability of using this nonwoven for antenna fabrication was demonstrated in our previous studies.^{99, 174} 100% polyester (PET) single jersey knit fabric (Hanesbrands Inc, USA), with a thickness of 0.3 mm and weight of 145 g/ m², was used as the antenna substrate due to its flexibility and breathability.

5.2.3 Morphology of the Antenna

The microscopy images of the textile antenna were observed through 3D laser scanning confocal microscope (Keyence, model VK-X1000) and field emission scanning electron microscope (FESEM).

5.2.4 Dielectric Constant Test

Split post dielectric resonator (SPDR) was chosen to test the dielectric constant properties of the fabrics due to its high accuracy. The SPDR test can resonate at a specific frequency with a very high quality factor (Q-factor). Once the fabric samples were inserted into the device, the resonant frequency shifts. The shift and Q-factor can be measured by a 2-port Agilent programmable vector network analyzer (HP 8720D) at aimed frequency (2.45 GHz). The S-parameters (S11, S22, and S21) were adjusted to $S_{11}=S_{22}=-40$ dB by locating the coupling loops within the resonant cavity.

(3)

5.2.5 Inkjet Printing Antenna Process

This section outlines the process of inkjet printing the conductive and dielectric ink on fabrics. A Dimatix DMP-2850 inkjet printer was used for inkjet printing. The Dimatix printer head employs piezoelectric actuators and a cartridge with an ink capacity of 1.5 mL. The printer has 16 nozzles, and each nozzle has a size of 21.5 μm . The resultant droplet volume was 10 pL. The voltage of the piezoelectric actuators was 20 V, frequency of the printer was 23 kHz, and resolution was 1016 dpi for the drop space of 25 μm . It is noted that these operating conditions are highly subjective to the ink viscosity and the drop spacing was optimized for complete coverage of the textile between subsequent drops.

The first step was to print reactive silver ink on the nonwoven substrate heated at a constant temperature of 60 °C during the printing process. After that, the printed samples were annealed at 150 °C for 30 mins. At this temperature, the silver salt in the conductive ink could be reduced to Ag and deposited on the fiber surface. Even though the nonwoven fabric has a relatively low surface roughness, the surface without interface-treating still needed 15 printing passes to achieve high conductivity and sufficient coating on the fiber that resulted in washability of up to 15 laundering cycles.⁸⁰ The BT dielectric UV curable ink was printed on the knit fabric assemble at room temperature. After printing each pass, the sample was sent into the UV curing machine for 2 mins for each side. The printing-curing process was repeated for 20 times.

5.2.6 Antenna Fabrication

The Ag printed nonwoven and BT dielectric UV curable ink printed knit fabrics were laminated with porous TPU web under 150 °C for 5 mins. An SMA connector with a 50 Ω characteristic impedance was soldered to the patch and ground conductors using Chipquik SMDSWLTLFP32 low melt solder. A Dymax 9001-E-V3.5 encapsulate was applied to the edges of the antenna and the connector-antenna interface, then UV curing was conducted for 5 mins on each side to harden the glue. The purpose was to protect the antenna from delamination and strengthen the bond between the SMA connector and textile antenna.

5.2.7 Antenna Measurement

The return loss and impedance of the antenna in free space was evaluated by using VNA (Agilent E 5071C). For bending test, the antenna was taped on the different radius cylinder (R1=21.13 mm cylinder, R2=17.52 mm cylinder; R3=13.85 mm cylinder) in horizontal and vertical direction and

the return loss and impedance was measured. During the test, high precision coaxial cable was used to connect the SMA connector with an Agilent E5071C VNA. Radiation test was measured in an anechoic chamber with a computer to control and a closed-circuit television camera to visualize the measurements. The durability of the conductive layer and the whole antenna was evaluated by bending samples 1000 times with a commercial tensile tester (Instron, model 5566). The sample was gripped between two claps, where the lower clamp was fixed while the upper clamp moved 30mm at a speed of 50 mm/min. The tested distance between the two clamps was 60 mm. The resistance of the ground layer was monitored during bending with Keysight 34410A.

5.2.8 Air Permeability

Air permeability was carried out on an air permeability testing apparatus (Frazier Air Permeability Tester) according to ASTM D 737–18, Standard Test Method for Air Permeability of Textile Fabrics. The air permeability was expressed in $\text{cm}^3/\text{s}/\text{cm}^2$. During the test, a constant pressure drop of 125 Pa was applied across the textile sample. The test area was 38.3 cm^2 .

5.3 Results and Discussion

5.3.1 Inkjet Printing Process on Textiles

The inkjet process of conductive ink and dielectric ink on the textile surface is crucial for achieving high electrical conductivity, dielectric property, and human body comfort. One of the challenges in printing a flexible and conductive layer on a textile platform is a difficulty in conformal layer fabrication due to the inherent roughness and topographical microstructures of textiles. At present, when using metal nanoparticle ink to print an antenna patch and ground layer on a textile substrate via inkjet-printing, a smooth interfacial layer is normally needed.^{78, 79, 239 113, 235} Without interfacial layer, the nanoparticle ink would diffuse into the rough textile surface and distribute unevenly,

which may influence the surface conductivity needed for a high-performance antenna design. However, the addition of interfacial layer, normally performed by screen printing, impacts the flexibility and breathability of textile substrate and deteriorates the fundamental advantages of using textile material in wearable applications.

Inkjet printing with silver MOD ink was used to fabricate the patch and ground layer in this research. An in-situ curing was applied through heating of the substrate as the ink was printed to minimize spreading and increase pattern accuracy during the print process of large area patterns. An important feature of the particle-free inks is the ability to minimize clogging in the printhead, especially the in situ curing process affects the temperature of the printhead due to the proximity to the substrate. Heating the substrate during printing allows for improved deposition control of the inkjet printed pattern through the evaporation of the ink solvent. In general, the reactive silver ink can endure a substrate temperature of 60 - 80°C during the printing process.^{80, 183} When printing at 60 °C, the silver reactive ink's solvent volatilizes quickly, reducing the ink penetration into the textile material and producing a uniform silver coating on the fiber surface. As a post-printing process, an annealing at 150 °C in a thermal oven let the ionized silver reduce back to the elemental form, creating a conductive layer, as shown in Figure 5-1. The in-situ heat-curing inkjet printing process can deposit silver ink onto porous textile substrates without an interfacial layer and achieve high conductivity. Our previous studies have demonstrated the use of this conductive ink to fabricate an array of flexible textile electronics.^{80, 183, 198} When the reactive silver ink is printed onto nonwoven fabric with in-situ curing, a conductive layer can be formed on fiber surface and the resulting conductive fiber bundles structure is similar to the high-frequency "Litz-wires"²⁴²,

which can maximize the conductive path's surface area.²³⁸ The resulting structure compensates the skin effect to reduce sheet resistance at high frequency.²³⁸

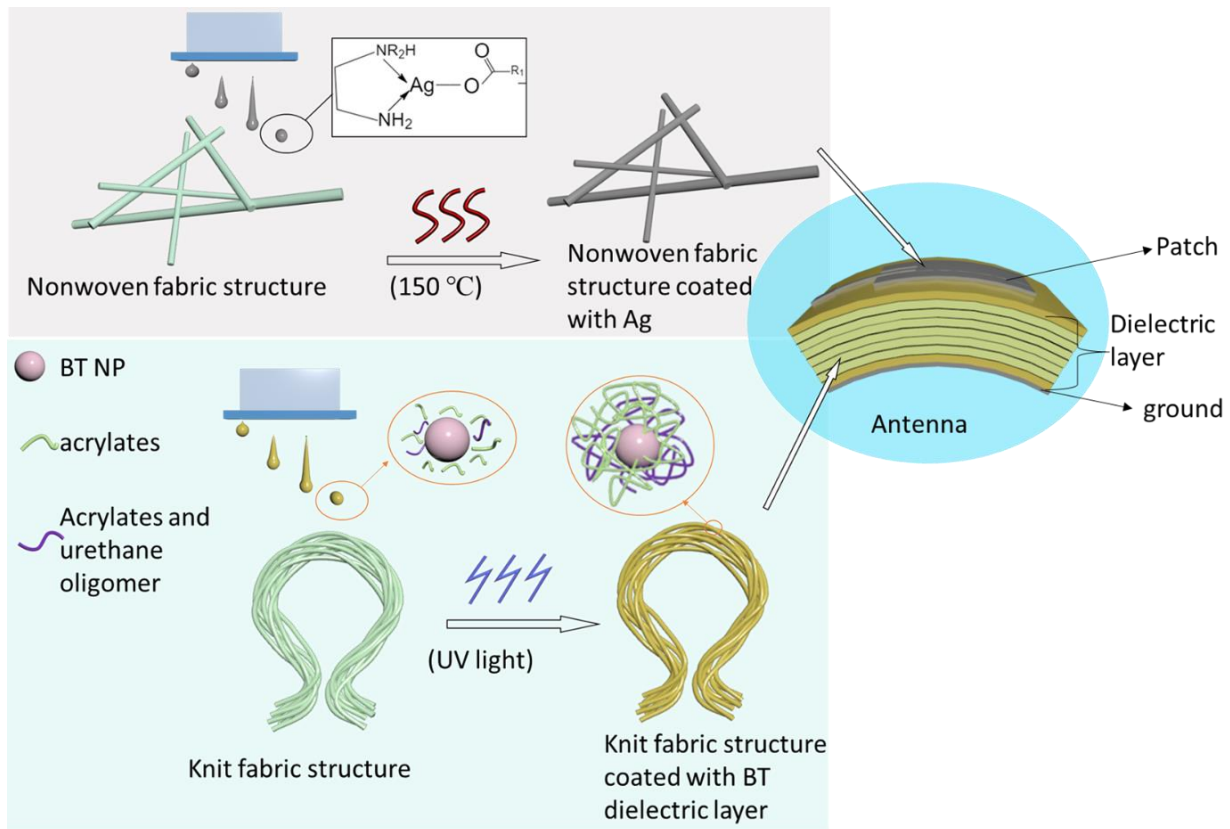


Figure 5-1. Antenna fabrication process (a) Printing of conductive ink on nonwoven fabric and dielectric UV curable ink on knit fabric assemble. (b) All-inkjet-printed antenna structure.

In addition to the need for a highly conductive surface, the dielectric constant and dielectric loss of the substrate impacts the antenna performance. For a textile substrate, the dielectric properties depends on the polymer type, porosity, yarn density, and fabrication methods (woven, nonwoven, knit)²⁴³ To get suitable dielectric properties, the inclusion of high dielectric materials can be employed. But, added high k dielectric materials ultimately limits the flexibility and porosity of textile substrate. In our previous research, the dielectric constant of knit fabric was increased by

spray coating a BT dielectric UV curable ink and the resultant composite knit fabric was used as antenna substrate.⁹ Inkjet printing is a more precise method for even distribution of the dielectric materials on the textiles, particularly for complex antenna designs. In this research, we used inkjet printing to apply a 200 nm BT particle-based ink with a UV curable binder on a polyester knit fabric. The solvent-free UV curable ink includes acrylates, urethane oligomers, and photoinitiator. Under UV light, the initiator produces free radicals, which subsequently initiate cross-linking of acrylates and urethane oligomers by a chain growth. The ink has a low surface tension of 37.53 mN/m and a low viscosity of 12 cps,⁹ permitting high wetting ability on the fabric surface. The spreading of the ink prevents the blocking the porous structure between the yarns. After UV curing, the BT NPs are embedded by the cross-linked polymer network (Figure 5-1). The formation of the polymer film incorporated with BT NPs is demonstrated to control the textile fabric's dielectric property.

5.3.2 Morphology of Inkjet-Printed Textile

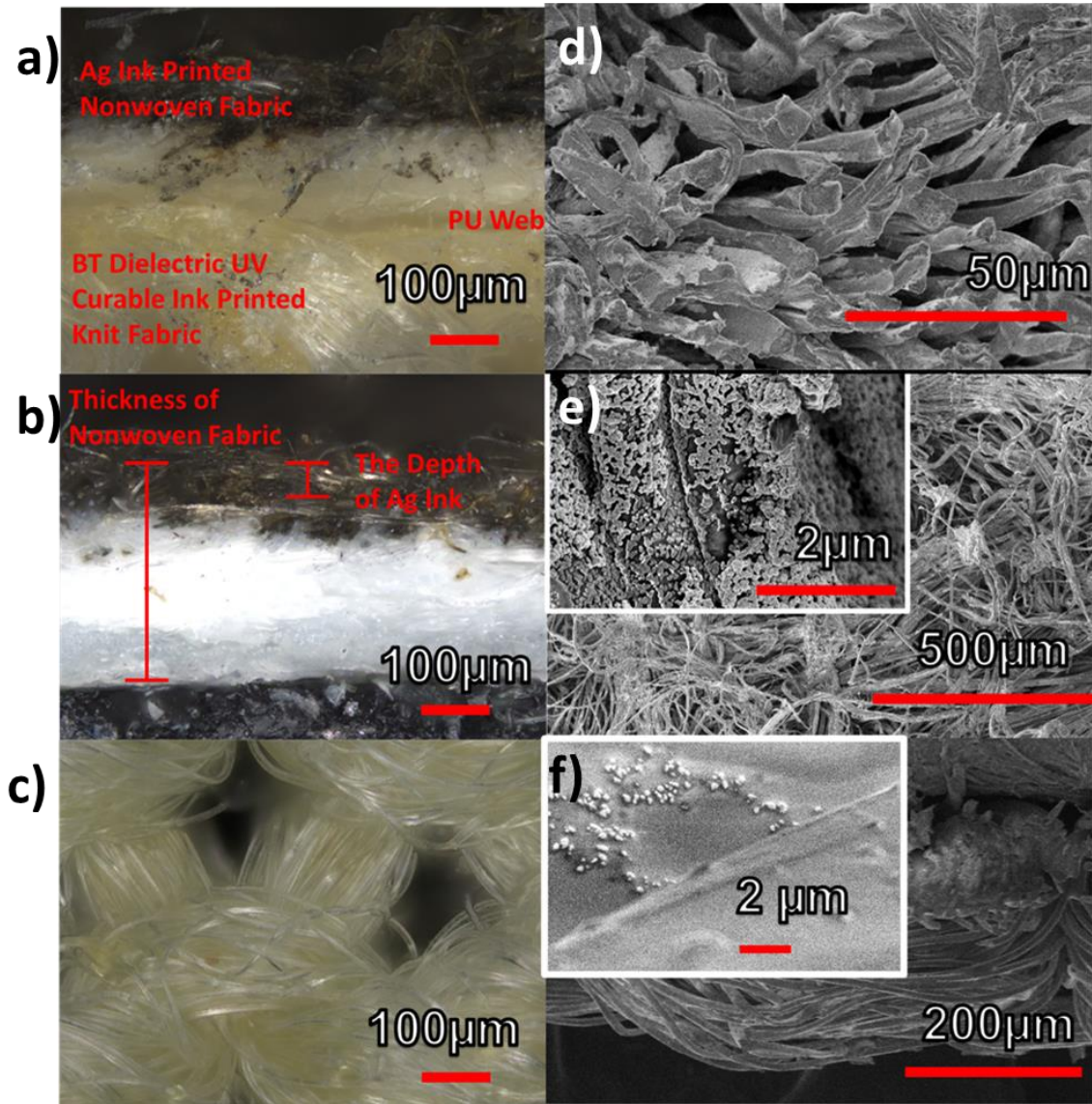


Figure 5-2. Optical microscope images of (a) Ag printed nonwoven fabric and BT dielectric UV curable ink printed knit fabric. (b) Ag printed nonwoven fabric. (c) BT dielectric UV curable ink printed knit fabric. SEM images of (d) cross sectional Ag printed nonwoven fabric. (e) surface of Ag printed nonwoven fabric. (f) BT dielectric UV curable ink printed knit fabric.

Both nanoscale and microscale characterization of the conductive layer on nonwoven fabric and BT dielectric UV curable ink on knit fabric were conducted by 3D laser scanning confocal microscope and scanning electron microscope (SEM), as provided in Figure 5-2,

Figure S 10 and Figure S 11. Figure 5-2a shows the cross section of Ag printed nonwoven fabric and BT dielectric UV curable ink printed knit fabric, bonded with thermoplastic polyurethane (TPU) web. The geometrical information of fabrics after inkjet printing shows that the silver ink was printed evenly on top of the nonwoven fabric, with a depth of 44 μm (Figure 5-2b). A thin film of Ag was deposited on fiber surface, as revealed by Figure 5-2d, 2e and S10. A conductive fiber bundle structure can be observed from Figure 5-2d and Figure S 10a. The gaps between the fibers are still apparent (Figure 5-2e). The morphology of the BT dielectric UV curable ink inkjet-printed knit fabric is shown in Figure 5-2c, 2f and S11. We can find that the fibers in knit fabric are coated with the dielectric UV curable ink, and the BT nanoparticles are incorporated in the photopolymer layer. (Figure 5-2f and Figure S 11).

The jersey knit fabric printed with BT dielectric UV curable ink still shows large voids and gaps between the yarns (Figure 5-2c), indicating that the fabric's air permeability would be retained. Keeping the textile breathability promotes water evaporation in the cloth's microclimate. Water evaporation from the skin helps regulate body temperature in response to environmental changes. Microclimate of the clothing includes the environmental parameters such as the temperature, humidity, and micro-air flow between human skin and textiles. For the comfort of textiles, water vapor and air permeability play an important role in controlling heat loss in terms of the microclimate.^{244, 245} Table S 1 listed the air permeability of the antenna substrate with or without the printing of dielectric ink. The air permeability of knit fabric assemble is 9.43 ± 0.21 , and after printing the dielectric ink the fabric assemble is 9.18 ± 0.21 . After inkjet printing of dielectric ink on the knit fabric assembly, no obvious change in air permeability was observed. The inkjet-printed dense nonwoven fabric is less air-permeable. However, final antenna with two conductive

nonwoven fabric and BT curable ink coated knit fabric assemble dielectric layer still has 4.17 ± 0.01 . The final antenna is still air permeable. This demonstrates the advantages of using inkjet printing in wearable applications.

5.3.3 Electrical Properties of the Inkjet-Printed Textile

The sheet resistance of inkjet-printed Ag conductive layer is $0.014 \Omega/\text{sq}$ measured with four-probe test. It shows good conductivity compared with other antennas.^{246, 247} When used in garments, textile antenna would be subjected to numerous bending cycles, and it is essential to investigate its durability. The resistance of the ground layer in antenna was monitored during repetitive bending by a tensile tester. During cyclical bending test in Figure 5-3, the antenna sample was fixed with two clamps and the distance was moved from 6 cm to 3 cm during bending, with a speed of 4 mm/sec. The force during bending was recorded by the tensile tester and the results are shown in Figure S 12 and Figure S 13. Approximately 7 N is required to bend the antenna from a height of 6 cm to 3 cm, indicating a superior flexibility. The resistance changes were recorded every 0.044s with a multimeter (Keysight 34410A). Because the fibers of the nonwoven fabric top layer were coated with Ag, the changed in fibers' interactions during bending can affect resistance, as reflected by Figure 5-3. After bending 1000 cycles, the printed layer's resistance is in the range of $3.5\text{-}5 \Omega$. The average resistance of the first and the final 20 bending cycles is 4.25Ω and 4.33Ω , respectively, corresponding to a percent change of 1.88%. The average resistances of the first 200, 400, 500, 700, 900, and 1000 bending cycles are 4.20Ω , 4.39Ω , 4.62Ω , 4.66Ω , 4.56Ω , respectively. The resistance changes mostly not influence by the bending behaviors. In contrast, it was reported that the screen printed Ag layer on a textile fabric was fractured after 200 bending cycles.²⁴⁸

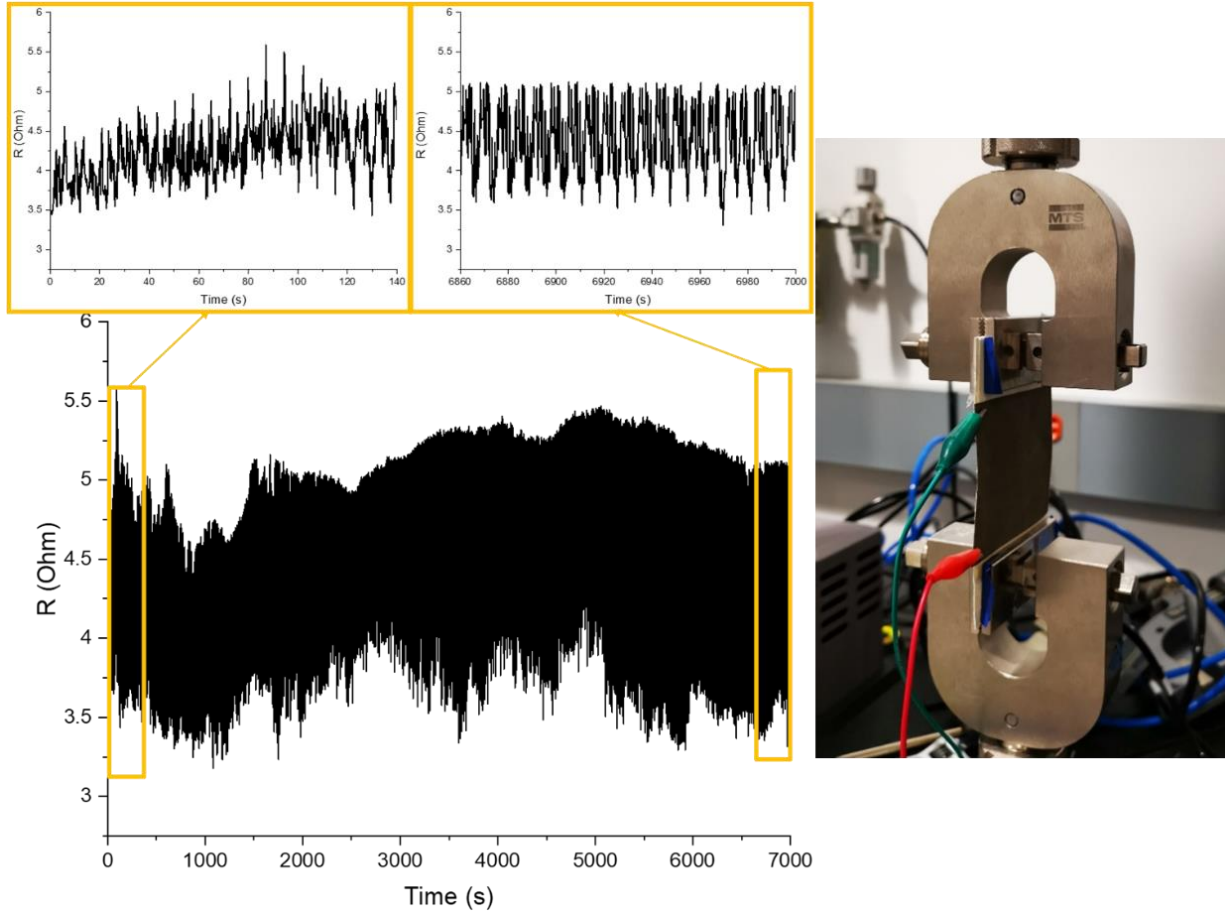


Figure 5-3. Resistance changes of Ag inkjet-printed nonwoven ground of antenna during bending 1000 cycles and picture of the setup for bending test in the right.

5.3.4 Dielectric Properties of the Inkjet-Printed Textile

The values of the resonant frequency (f_0) and quality factor of the resonator were recorded. When the sample was inserted, the resonant frequency f_s was measured. Based on the shift in resonant frequency ($f_0 - f_s$), Q-factor and sample thickness (h), the dielectric constant (ϵ_r) was calculated by equation (3)²⁴⁹. (K_s is a function of the specimen's dielectric constant and thickness which can be computed and tabulated for each SPDR after fabrication.)

$$\epsilon_r = \frac{1 + f_0 - f_s}{hf_0 K_s(\epsilon_r, h)}$$

Table 5.2. Dielectric Property Data Archived for Different Fabric Assembly with SPDR Test

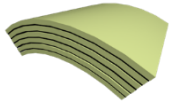
	Samples	Dielectric Constant	Dielectric Loss
	Knit Fabric Assembly	1.40±0.03	0.009±0.001
	Knit Fabric Assembly with BT Dielectric UV Curable Ink	1.61±0.06	0.013±0.001
	Antenna Substrate (Nonwoven Fabric/Knit Fabric Inkjet- Printed BT Dielectric UV Curable Ink)	1.70±0.01	0.016±0.002

Table 2 lists the dielectric constant and dielectric loss of textile antenna substrate as the material layers are constructed on the based knit fabric. It can be found that the polyester knit textile has a very low dielectric constant due to the high porosity and large voids (Figure 5-2c). BT dielectric UV curable ink was successfully used to alter the dielectric constant of the knit fabric. After printing, the dielectric constant of knit fabric assembly increased from 1.40 to 1.61. For the resultant antenna substrate composed of the knit fabric assembly with BT dielectric UV curable ink and two nonwoven fabrics heat laminated with TPU (Figure 5-1), a dielectric constant of 1.70 and dielectric loss of 0.016 is observed. The substrate dielectric constant is essential to the microstrip antenna bandwidth and efficiency.¹¹¹ The dielectric properties obtained here are good enough for a practical textile antenna.

5.3.5 Antenna Simulation and Return Loss

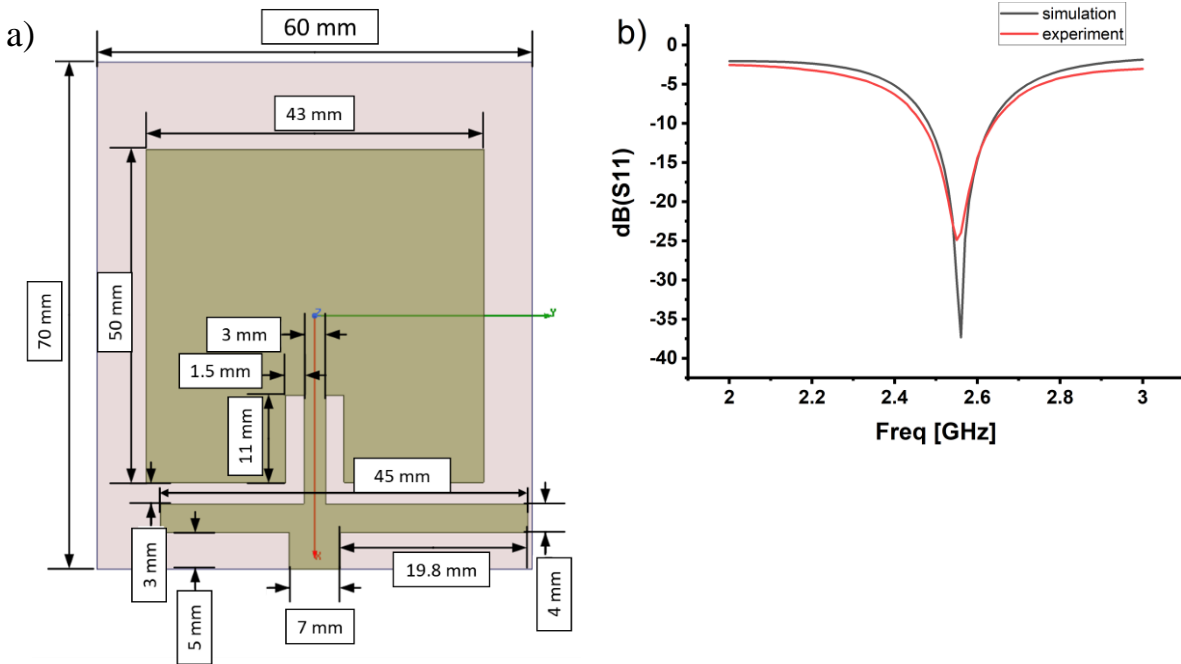


Figure 5-4. (a) All-inkjet-printed textile antenna design. (b) All-inkjet-printed textile antenna simulation and experiment result.

The antenna was first modeled with ANSYS HFSS simulation software using the pattern listed in Figure 5-4a. The simulated and experimental results of the reflection coefficient S_{11} of the fabricated antenna is shown in Figure 5-4b. It can be found that the measured resonant frequency (2.55 GHz) is close to the simulation result (2.56 GHz) by HFSS. A return loss of 25 dB and a bandwidth of 160 MHz from 2.47-2.63 GHz is obtained, which agrees with the simulated result. In the durability test, the antenna was bent 1000-cycles with a tensile tester, and the performance of the antenna is displayed in Figure 5-4c. The inkjet-printed textile antenna retains its sensitivity after the 1000-cycles bending test, indicating high durability. The antenna gain is only 2.5 dBi, which is comparable with other wearable antennas, such as a compact metamaterial-inspired

antenna (1.86 dBi)²⁵⁰ and wearable antenna (1.47 dBi)²⁵¹ and adhesive-bandage-like antenna (2.01 and 1.1 dBi)²⁵².

5.3.6 Antenna Bending Test

Due typical human motion, textile antennas employed within wearables are subjected to bending and deformation under human movements. The bending tests were conducted by bending antennas around three paper cylinders with radii of curvature of 21.16 mm, 17.52 mm, and 13.85 mm, as depicted in Figure 5-5. The flexible antenna length equals to 60 mm in the vertical direction and 80 mm in the horizontal direction. According to equations (1)(2), the antenna bending angle can be calculated, and the results are listed in Table 2. The performance of the antenna was characterized under bending up to 248° in the vertical direction and 331° in the horizontal direction.

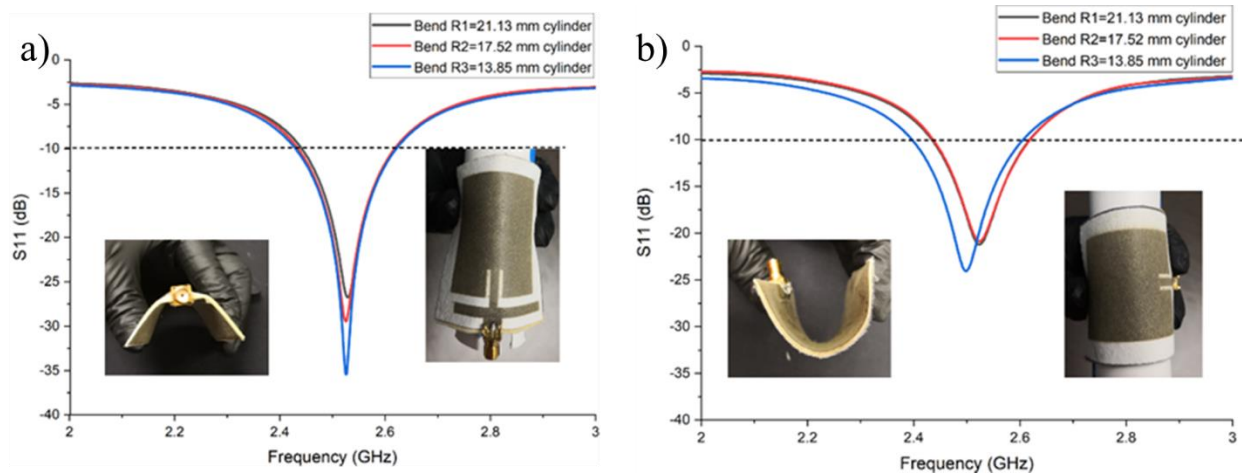


Figure 5-5. (a) All-inkjet-printed textile antenna bending at vertical direction with R1=21.13 mm cylinder, R2=17.52mm cylinder; R3=13.85mm cylinder; (b) antenna bending at horizontal direction with R1=21.13 mm cylinder, R2=17.52mm cylinder; R3=13.85mm cylinder.

The textile antenna bending results in vertical direction are provided in Figure 5-5a. A consistent -10 dB bandwidth (2.43-2.62 GHz) is shown under bending of 163° (R1= 21.13 mm), 196°

(R2=17.52 mm), and 248° (R3=13.85 mm), resulting in a matching bandwidth of 190 MHz. The reflection coefficient slightly increases with the bending angle as the input impedance changes due to the deformation.²³⁸ When bent in the horizontal direction, under the bending angle of 217° and 261°, a -10 dB bandwidth (S11) is observed between 2.43 to 2.62 GHz, resulting in a matching bandwidth of 190 MHz (Figure 5-5b). When bending at 331°, even though bending shifts the resonance frequency, the bandwidth is wide enough to secure a -10 dB of 208 MHz from 2.40 to 2.61 GHz. The bandwidth and resonant frequency have a slight change at the bending angle of 331°, and such a small variation can be ascribed to the fabric compression under extreme conditions. The thickness of the dielectric layer may be slightly modified which may influence the impedance of the antenna.¹⁰⁵ Compared with other antenna bending tests^{99, 174, 253-255}, a bending angle of 331° is a significant improvement. Even at this condition, the antenna still shows good isolation and bandwidth which proves the robustness of the antenna.

5.3.7 Antenna Body Test

Since the textile antenna is targeted for use in wearable applications, it is essential to evaluate the influence of human body loading on antenna performance. To demonstrate the wearability of antenna, the antenna was attached to a human arm, chest, back and abdomen and tested with tape. (Figure 5-6a) The results of the on-body antenna return loss are shown in Figure 5-6b. As can be observed, when the antenna was mounted on the arm, chest, abdomen, and back, the measured S-parameters are similar to that in free space, indicating a robust performance in the wearable application. (Figure 5-6b) Ferreira et al.²⁴⁰ developed textile antennas using copper and nickel plated polyester fabric and examined the effect of bending on the performance. When used on arm, the antenna only showed a bandwidth of 130 MHz with a return loss of 15 dB. In comparison, our antenna can reach 206 MHz with a return loss of 24 dB.

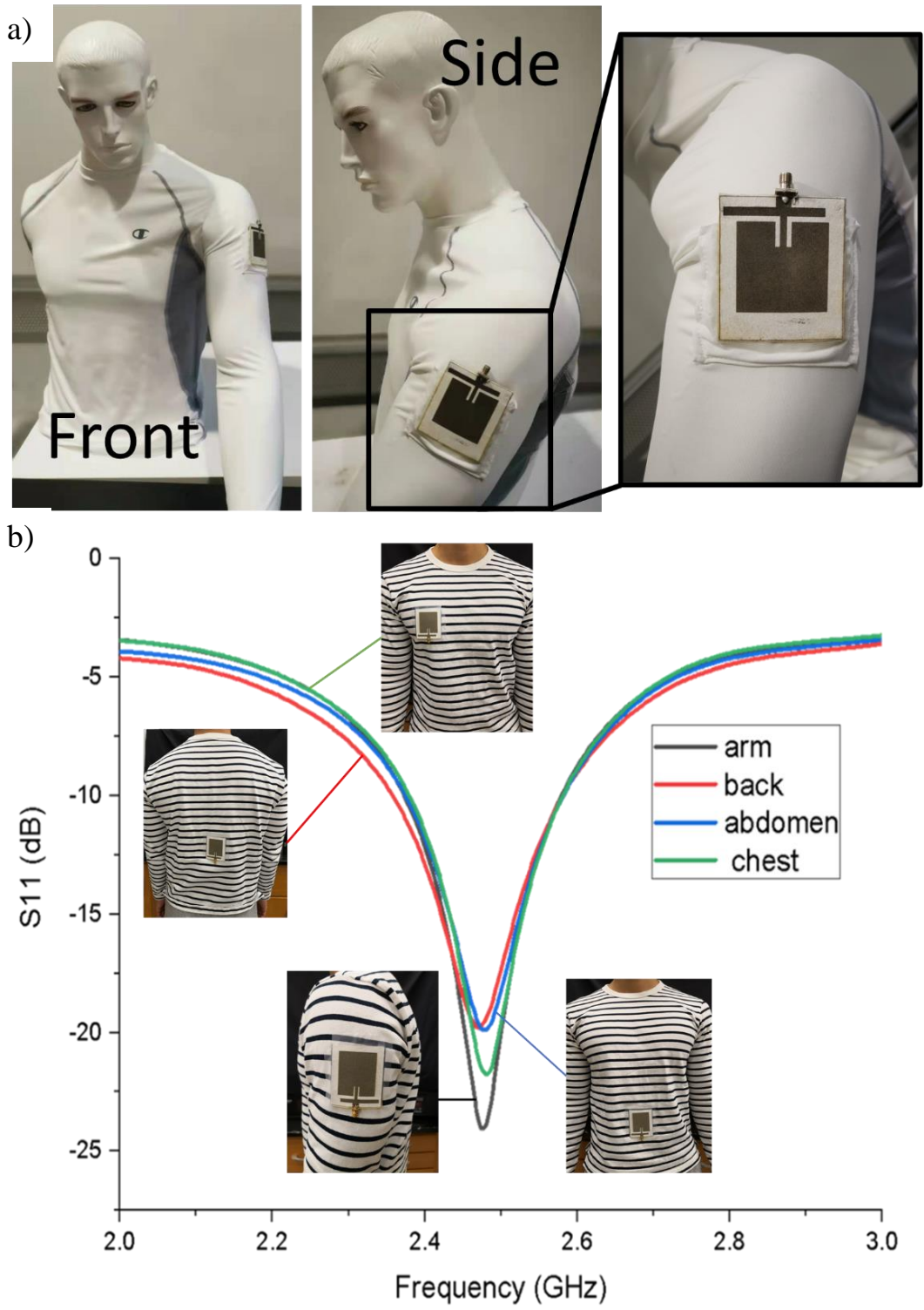


Figure 5-6. (a) All-inkjet-printed textile antenna mounted on arm, chest, abdomen and back. (b) Measured S-parameters of the textile antenna on arm, chest, abdomen and back.

5.4 Conclusion

In this study, for the first time, a flexible and breathable all textile antenna for next-generation wearable devices is prepared by all inkjet printing method without an interface layer by screen printing. The antenna's patch and ground were fabricated with inkjet printing of reactive silver ink on the surface of nonwoven fabric through in-situ curing method. In addition, BT dielectric UV curable ink was printed on the knit fabrics to increase the dielectric constant without blocking the porous structure. The success of using nanoparticle dielectric ink to manipulate the dielectric properties of porous antenna substrate without compromising breathability would have a great impact on textile antenna fabrication. The fabricated antenna successfully radiated at 2.55 GHz with a return loss of 25dB. The flexible textile structure demonstrated a reliable and consistent performance at 2.45 GHz under extreme bending and deformation. This work lays a strong foundation for work in low-cost, wide bandwidth, durable, flexible antenna fabrication with porous textile substrates using inkjet printing process.

6 Fabrication of Barium Titanate Nanocomposite Film with High Permittivity Using Inkjet Printing for Metal-Insulator-Metal Capacitor Application

Abstract

The preparation of fully inkjet-printed capacitor containing ceramic/polymer dielectric layer was presented. A novel high-concentration large-size barium titanate (BT)/polymer ink for inkjet printing was developed, showing a homogenous dispersion and good printability. The influence of drying temperature and printing settings such as drop space, voltage, and printing pass, on the morphology of printed layer was explored. After optimization, uniform printed layer can be achieved. In the end, an all-inkjet-printed capacitor was fabricated using the high-concentration ceramic/polymer ink and commercial silver nanoparticle ink. The printed nanocomposite dielectric layer with a thickness of 5 μm showed a high dielectric constant of 100 at 100 Hz.

6.1 Introduction

Ceramics capacitors with high power density are preferred for high-performance energy-storage devices due to their excellent dielectric properties.²⁵⁶ The capacitance is directly proportional to the dielectric permittivity and inversely proportional to the dielectric layer thickness. Printing is an efficient method to fabricate large-scale and low-cost electronic devices.²⁵⁷ Inkjet printing is a contactless method with high resolution. Drop-on-demand inkjet printer with piezoelectric film is used to get precise droplet control with broad material choices.²⁵⁸ To prevent nozzle from clogging, nanoparticle size inside ceramic inks must be less than 1/100 of the nozzle diameter.²⁵⁹ The nozzle size of the Fuji printer used in this paper is approximately 21.5 μm , so to avoid nozzle clogging during printing, the nanoparticle diameter should be less than 210 nm. When at nanoscale, the dielectric constant increases with size.¹⁰ Therefore, 200 nm BT NPs are chosen to prepare the dielectric ink for inkjet printing. A smooth film with low roughness is essential for a high-energy-

density capacitor. Here, the influence of drying temperature and inkjet printing parameters on roughness, such as voltage, drop space and printing pass, is analyzed in order to achieve homogenous thick films.

Dielectric materials include polymers, inorganic oxides, ion-gels, and solid-state electrolytes.²⁶⁰ Ion-gel and solid-state materials have high dielectric constant; however, they are not very stable at high frequencies. Ceramic materials with high dielectric constants have poor processability for inkjet printing method due to aggregation. Among dielectric ceramic materials, BaTiO₃ (BT) is one of the most extensively studied materials. Its high dielectric constant and low dielectric loss promises various uses in printed electronics.^{10,261} The perovskite structure of the BT nanoparticles (NPs) can exhibit spontaneous polarization due to the displacement of the center atom. Therefore, BT NPs are used as ferroelectric memories²⁶², capacitors²⁶³, and humidity sensors²⁶⁴. However, considering the high-curing temperature (> 1000 °C) and low dielectric strength (~ 2V/ um) of BT NP, the applications are limited.⁶³ . Additionally, the dielectric constant of BT NPs occurs is size-dependent.^{10, 265, 266} where the highest dielectric constant of the BT NPs occurs when the NP diameter is about 1 μm.¹⁰ Polymer dielectric materials are widely adopted in the field of flexible electronics due to their high mechanical flexibility and low-curing temperature. Because of low dielectric constants (2~12) and susceptibility at high electric field frequency, applications of polymer dielectric materials are limited compared to high-k dielectric materials. The polymer-matrix composites (PMC) system would be suitable for inkjet printing, allowing for a low sinter temperature.²¹¹ The PMC system exhibits high dielectric permittivity and processibility. The nanocomposite systems including BT nanoparticles/ epoxy resin ²⁶⁷, BT NPs/Acrylic composites²⁶⁸ etc, were reported.

A high loading of the nanoparticles into a polymer is necessary to achieve high permeability, but this may lead to aggregation of nanoparticles,¹⁴¹ causing muzzle clogging and defects in the printed layer. In this study, 200 nm BT nanoparticles were modified, and polyvinylpyrrolidone (PVP) was chosen as polymer matrix it promotes the dispersibility of BT ink.²⁶⁹ A new nanocomposite combining surface modified barium titanate nanoparticles and PVP polymer was investigated as an inkjet printable dielectric material in the present work. The surface-modified barium titanate nanoparticles are homogeneously dispersed in a solvent, promoting high-quality dielectric films. The ink rheology demonstrated its suitability for inkjet printing and the influence of inkjet printing settings and drying condition on roughness was also studied. All-inkjet-printed metal-insulator-metal (MIM) capacitors were fabricated, and the dielectric property and loss tangent of the dielectric layer was presented.

6.2 Experimental Section

6.2.1 Materials

Barium titanate (200 nm, density 5.85 g/cm³) was purchased from Nanostructured & Amorphous Materials, Inc. The polymer dispersant is a mixture of small molecular chains including nonylphenol, polyoxyalkylene amine derivative, polyethylene glycol, polyethylene glycol, polyvinylpyrrolodone, butyl ethanoate, and ethylene glycol monobutyl ether, which was purchased from US Nano research. Polyvinyl pyrrollidone (PVP, Mw= 40 000 g/mol), ethanol, and ethylene glycol (EG) ($\geq 99\%$) were purchased from Sigma Aldrich. Ag NPs ink was supplied from NovaCentrix.

6.2.2 Fabrication of BT-PVP Composite Ink

Polymer dispersant powder (0.1 g) was added into 1g ethanol and 4g water mixture, followed by sonication for 5 mins. BT NPs powder (2 g) was added into the mixture, followed by six cycles of 30 mins sonication and 5 mins rest. After this process, well dispersed BT NPs solution can be obtained. PVP solution was prepared by adding PVP powder (0.1 g) into 8g ethanol and 2 g water mixture, followed by 5mins sonication. Then, BT-PVP composite ink was obtained by mixing the PVP solution and BT NPs solution, and sonicating for 3 hrs.

6.2.3 Deposition System

A drop-on-demand piezoelectric inkjet technology (Dimatix DMP 2850) was used to deposit Ag NPs ink and BT NPs ink. The cartridge of the print head has 16 nozzles, and each nozzle size is 21.5 μm , linearly spaced at 254 μm . Each time, 1.5 mL ink filtered by a nylon membrane with 5 μm pore size was filled into the cartridge and typical drop size for the printer is 10 pL. The inkjet-printed film's roughness was explored by changing printing voltage, passes, and drop space. 4 specimens were prepared for each condition, and average data was used.

6.2.4 Characterization

A goniometer (First Ten Angstroms, Inc.) and a cone and plate rheometer (model MCR 302, Anton Paar) was used to measure ink surface tension and dynamic viscosity, respectively, performed at room temperature (21°C).

The thermal behavior of the cured films in air was determined with a thermogravimetric analyzer (TGA) (EXSTAR TG/DTA 6200, Seiko Instruments, Inc). TGA and differential thermal analysis

(DTA) of BT/PVP ink were also conducted. The TGA curves for the raw BT powder, polymer surfactant, and PVP were tested to calculate the volume ratio of BT and polymer in the nanocomposite. The tests were performed by heating samples from room temperature to 580°C at a rate of 10 °C/min.

Fourier-transform infrared spectroscopy (FTIR) (Thermo Fisher FTIR models, iS50) analysis was conducted. XRD (Rigaku Smart Lab X-ray diffraction) pattern of all samples was taken with monochromatized Cu-K α radiation with a wavelength of $\lambda=1.5418\text{\AA}$ in 2θ range of 20-60 degree with step size of 0.02°.

Microstructure analysis including surface roughness and 3D topographical images of inkjet-printed layers with drop space of 200 μm , 100 μm , 45 μm , 35 μm , 25 μm , and 15 μm were conducted using Laser confocal microscopy (VK-X1000, Keyence). Cross sectional images of Ag_BT/PVP_Ag capacitor were acquired by the Field Emission Scanning Electron Microscope with EDS (FEI Verios 460L). The dielectric layer property was characterized at different frequencies with a LCR meter.

6.3 Results and Discussion

6.3.1 Inkjet Ink Characterization

Due to the large specific surface area, nanoparticles tend to aggregate during storage. Ultrasonication of the mixture of BT NPs in the ethanol, would break the aggregation and get homogenously dispersed BT NPs solution. For the high-concentration BT NPs ink, the separated BT NPs are likely to reunite due to Brownian motion. Polyvinylpyrrolidone, soluble in water and

ethanol, has good compatibility with BT NPs,²⁷⁰⁻²⁷² and was chosen as host polymer and dispersant. Together with low molecular polymer dispersant containing oligomer, stable and homogenous BT NPs ink was obtained. The low molecular weight polymer dispersant has weaker intermolecular interaction than the high-molecular-weight PVP, so they can penetrate the gaps between BT NPs to modify the nanoparticle surface.¹⁴⁸ Since the small molecule polymer dispersant has short chains and low viscosity, the BT nanoparticles may settle as sediment in the solution due to gravity. Thus, high molecular weight PVP was added to achieve a stable well-dispersed BT NPs ink. The resultant BT NPs shows good dispersity by forming hydrogen bonds with both the dispersant and high-molecular-weight PVP, as shown in Figure 6-1.

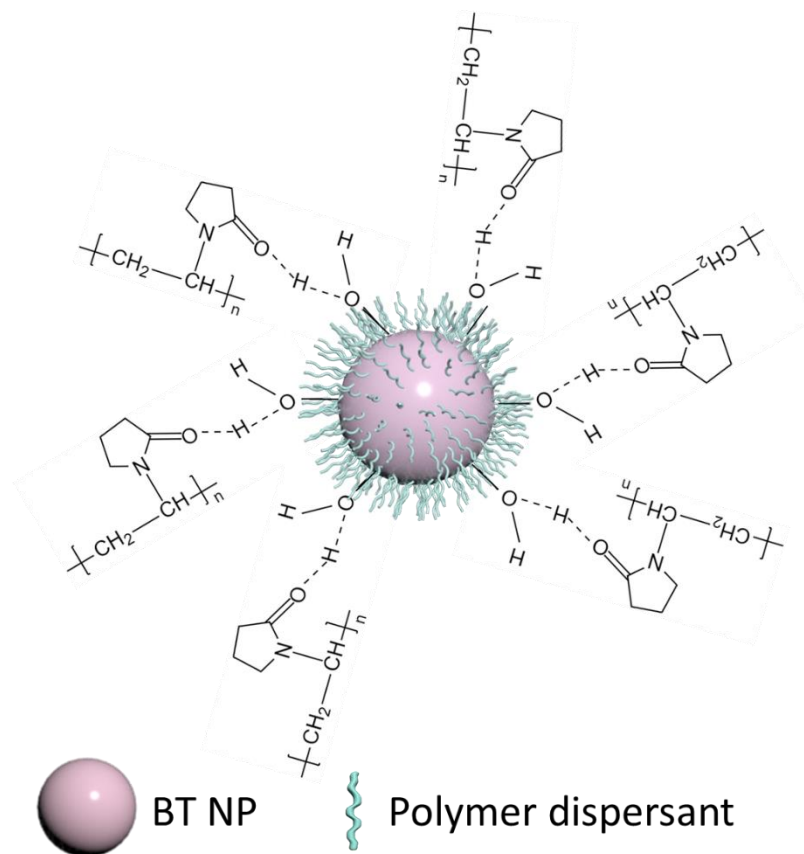


Figure 6-1. Proposed mechanism for adsorption of PVP and polymer dispersant onto the surface of BT NPs by hydrogen bonds.

Table 6.1 shows the properties of conductive and dielectric ink for inkjet printing. The surface tension and viscosity values demonstrate good printability of both inks. Ag nanoparticle size is 80 nm and BT NP is around 200 nm in the respective inks. The ink concentration of the Ag NPs is 25 wt.%, and BT NPs is 16.3 wt.%, corresponding to a volume ratio of 2.9 and 2.6 vol.%. The high-volume ratio of the two inks means fewer printing passes are required to reach the desired thickness, which can save time and energy.

Table 6.1. Ag NPs ink and BT NPs ink properties.

Ink Formulation	Surface Tension (mN/m)	Viscosity (cPs)	Density (kg/m³)	Weight Percentage	Volume Percentage
Commercial Ag NPs ink	31	5	1.18	25 wt.%	2.9 vol.%
BT ink	33	8	0.98	16.3 wt.%	2.6 vol.%

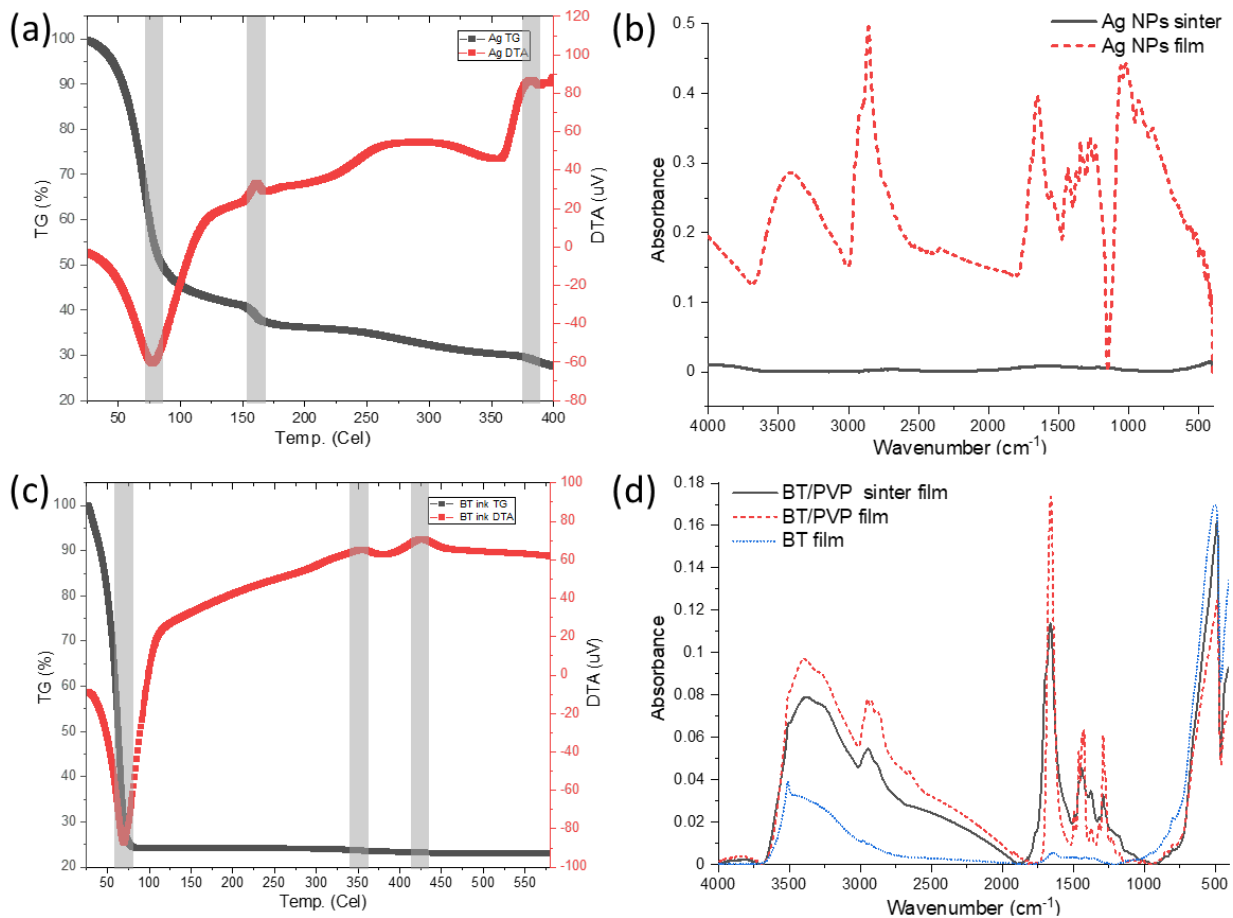


Figure 6-2. (a) Thermal properties of the Ag ink TG (black)/DTA (red) curves. (b) FTIR spectra of the Ag ink dried at 150 °C (red, dash) and annealed under 350 °C (black, line). (c) Thermal properties of the BT ink TGA (black)/DTA (red) curves. (b) FTIR spectra of the BT (blue, dash/dot), BT/PVP (black, line) and annealing under 350 °C (red, dash).

The thermal properties of Ag NPs and BT NPs inks were investigated. Figure 6-2a, and Figure 6-2c show the thermogravimetric (TG) and differential thermal analysis (DTA) of Ag NPs and BT NPs ink, respectively. The DTA curve exhibits peaks at 80°C, 161 °C, 353 °C, and 380 °C. (Figure 6-2a) The peak at 80 °C is due to the solvent's evaporation. At 161 °C, the peak is due to polymer decomposition. At 350 °C, the dark gray Ag layer turns to white. The DTA peaks at 350 °C represent Ag NPs annealing and weight loss associated with polymer burn out. A small peak at 380 °C indicate the complete annealing of the Ag NPs. By comparing the FTIR spectrum of Ag film sintered at 350 °C and the sample dried at 100 °C in Figure 6-2b, it can be found that Ag film

sintered at 350 °C does not have functional groups in the chemical composition, meaning more elemental silver is present. This makes the sintered Ag film more conductive.

The DTA of BT ink (Figure 6-2c) shows a peak at 70 °C, associated with the solvent's evaporation. Polymer decomposition is responsible for the peak at 161 °C. The weak exothermic peaks at 358 °C and 426 °C, relate to the polymer crystallization and combustion, respectively. The FTIR spectrum of raw BT, dried surface-modified BT/PVP film and the film sintered at 350 °C is shown in Figure 6-2d. FTIR spectrum of the polymer surfactant and PVP can be found in Figure S 14. It is worth noticing that the C=O stretch band at 1661 cm⁻¹ for pure PVP and 1654 cm⁻¹ for polymer surfactant shifts to 1648 cm⁻¹ after the formation of BT/PVP nanocomposite, indicating interactions between BT NPs and C=O of PVP host matrix.^{273, 274} In contrast, no significant shift was found between peaks of C-N stretching vibrations in polymer surfactant and PVP (1286 cm⁻¹, and 1284 cm⁻¹), and the BT/PVP nanocomposite (1289 cm⁻¹)²⁷⁵. This suggests a weak interaction with polymer through C-N group. A strong increase of hydroxyl (-OH) groups at 3400 cm⁻¹ in BT/PVP nanocomposite demonstrates the formation of hydrogen bonds between BT nanoparticles and polymer. After sintering, the hydroxyl groups in the PVP layer will cross-link and form a dense film, as indicated by the decrease of the -OH peaks in the sintered BT/PVP nanocomposite film.²⁷⁶ (Figure 6-2d). According to these results, the binder burnout temperature was selected as 150 °C and sinter temperature as 350 °C. TGA curves of raw BT NPs and PVP coated BT NPs, polymer dispersant, and PVP are presented in Figure S 15. According to the TGA data, the polymer host and BT volume percentage is estimated to be 28.4%, and 71.6%, respectively.

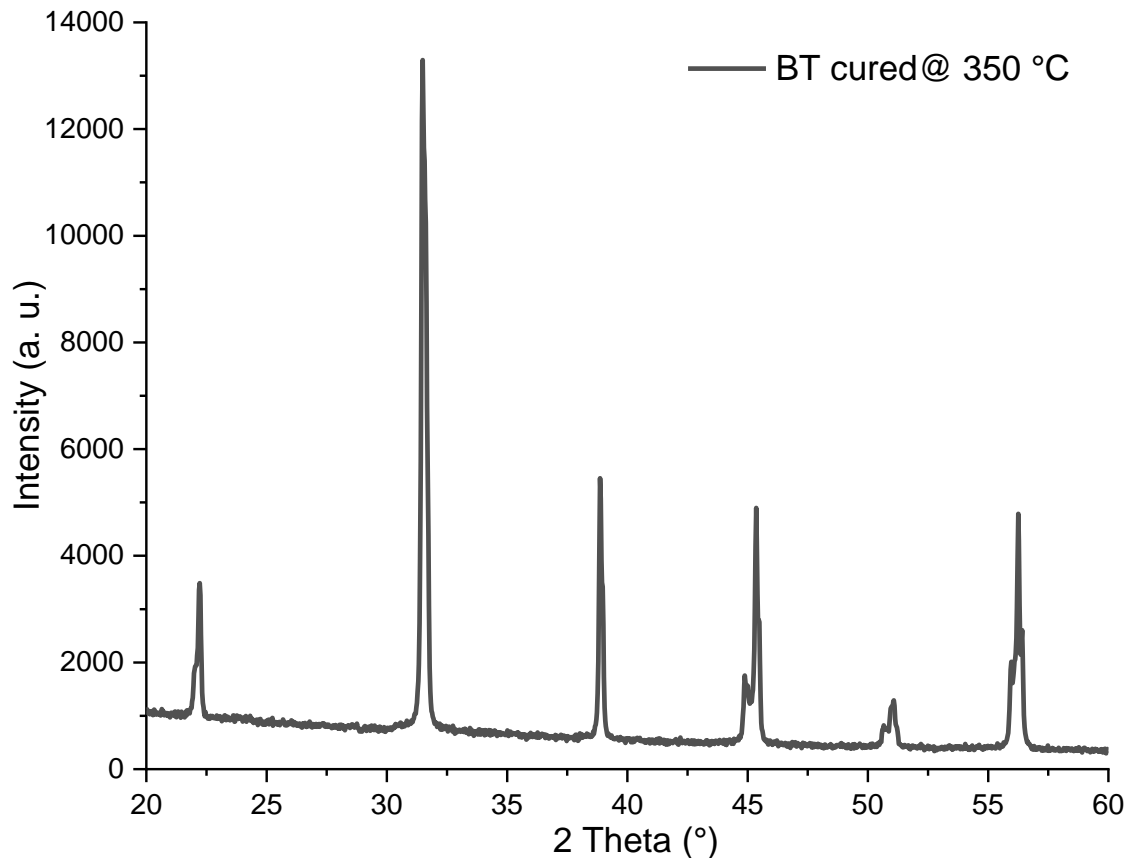


Figure 6-3. XRD of the cured BT layer under 350 °C for 30 mins.

XRD of the sintered BT/PVP nanocomposite film can be found in Figure 6-3. The split peak at $2\theta = 45^\circ$ (200) reveals that the BT NPs are in tetragonal phase. This is particularly important for BT to have a high dielectric constant and low dielectric loss.^{277, 278}

6.3.2 Inkjet Setting Influence on Printed Ag Layer Roughness.

Smooth printed layers are required to avoid capacitor shortcut. Commercial Ag NPs ink was used to study the influence of printing settings on roughness. The inkjet printer head has a plethora of nozzles in the sub-scanning direction (vertical direction). The position of printer head is controlled by a carriage mechanism in the main scanning direction (horizontal direction).²⁷⁹ The drop-on-demand inkjet printer used has a piezoelectric inkjet printhead, where the piezoelectric membrane (PZT) can be deformed when voltage waveform applied. As a result of the pressure, the printer

chamber ejects droplets through nozzle exits.^{280, 281} The printing parameters, such as drop space, voltage, and printing pass, influence the morphology of printed layers. In this work, the drop space is defined as the center-to-center distance between two adjacent droplets.

6.3.2.1 Influence of Inkjet Setting on the Roughness of Printed Single Droplet

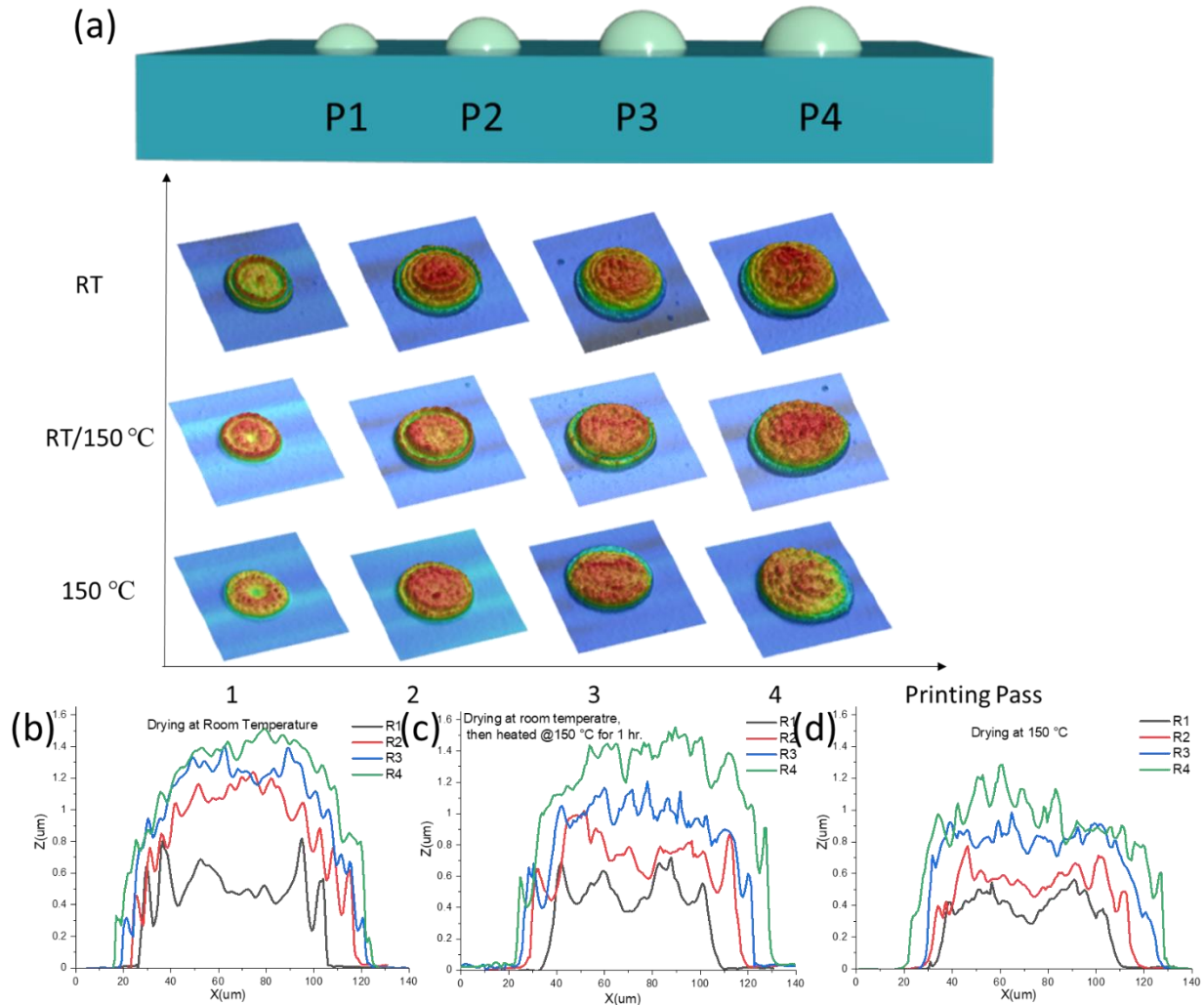


Figure 6-4. Printing passes influences on single droplet size and roughness. (a) 3D images of single droplet during printing passes of 1, 2, 3, 4 and dry at room temperature (RT) and 150 °C. (b) Roughness of single droplet.

The commercial Ag inkjet was printed on a Si substrate with varying printing passes, and dried under ambient conditions. Figure 6-4b reveals that the droplet size and height increase with

printing passes as expected. Spherical deposits of silver nanoparticles with dots size around 80 μm can be observed for a single printing pass. When printing 2 passes, the droplet size is at the range of 93-98 μm . When printing 3 passes, the dot size increased to 100-107 μm . For 4 printing passes, the dot size is about 112 μm . Due to the slow evaporation of the ink and low surface tension, the consecutive printing pass droplets merged with the printed dots on the substrate and formed a new dot with a wider size and increased height.

In addition to defined print parameters, the optimization of the ink drying process is essential to reduce surface roughness. Ag ink contains organic residues and polymer surfactant. Therefore, before sintering, the printed ink needs to be heated at high temperature to burn out the organic residues. Three drying conditions were selected: dry at room temperature, dry at room temperature then burn at 150 $^{\circ}\text{C}$, and directly burn at 150 $^{\circ}\text{C}$. 3D images of the inkjet-printed dots on Si wafer with different drying conditions were taken with a confocal laser scanning microscope, and the results can be seen in Figure 6-4. When directly drying at a high temperature, uneven droplet morphology can be observed. For 1 printing pass, the droplet shows a concave structure. When printing 4 passes, random distribution of ink happens, and this is because the ink dried on the substrate before reaching equilibrium. Therefore, the ink should dry at room temperature first to get a smooth layer, then burn out the polymer surfactant and organic residue at 150 $^{\circ}\text{C}$. After that, the Ag NPs will be sintered at 350 $^{\circ}\text{C}$. It could also be observed that the roughness of printed dots dried at different conditions is similar when printing 1 pass or 2 passes. The reason is the drying time of small droplets is in the range of a few seconds.²⁸²

The single droplet roughness would influence roughness of the dot; however, inkjet printing is a process of the popularity of droplet interactions, and the interaction between each dot is also important. The overall roughness, especially for a large area, is critical.

6.3.2.2 Influence of Inkjet Setting on Roughness of Printed Layer.

The surface roughness can either be calculated on a profile or over a surface area which corresponds to the 2D and 3D roughness profiles, respectively.²⁸³ The profile roughness represents two-dimensional roughness of the surface, while the area surface correlates with the three-dimensional roughness. 3D surface analysis is more widely used in engineering application.²⁸⁴ 3D arithmetical mean height (S_a) was selected to analyze the roughness of printed layer under different print parameters, to determine the best setting for a smooth printed film. S_a can be calculated according to:²⁸⁵

$$S_a = \frac{1}{A} \iint_A |Z(x, y)| dx dy \quad (1)$$

where x and y are the points in the plane area, Z is cross-sectional height and A is area. S_a is the extended concept of arithmetic mean height of a line to a surface. Drop space, printing pass, and printing voltage were manipulated to investigate the influence of printer settings on film roughness.

6.3.2.2.1 Drop Space and Printing Pass

The drop space would greatly influence the printing pattern, as shown in Figure S 16. If the drop space (200 μm) is much larger than the drop's radius (80 μm), the droplets will pin on the substrate and dry. Individual droplets will form the dots pattern on the printed substrate. As the drop space reduces to 100 μm , the isolated drops overlap and merge. However, the pattern still cannot be totally filled by the ink. Further decreasing the drop space (45 μm or 35 μm) will show more

droplet merging. Still, the patterns have some voids not filled by ink, even after 4 printing passes. As a result, drop spaces larger than or equal to 35 μm were not selected. When the drop space is 25 μm , the pattern shows good roughness and a smooth layer. As the drop space continues to reduce to 15 μm and became much smaller than the droplet radius, the roughness significantly increases when printing 4 passes.

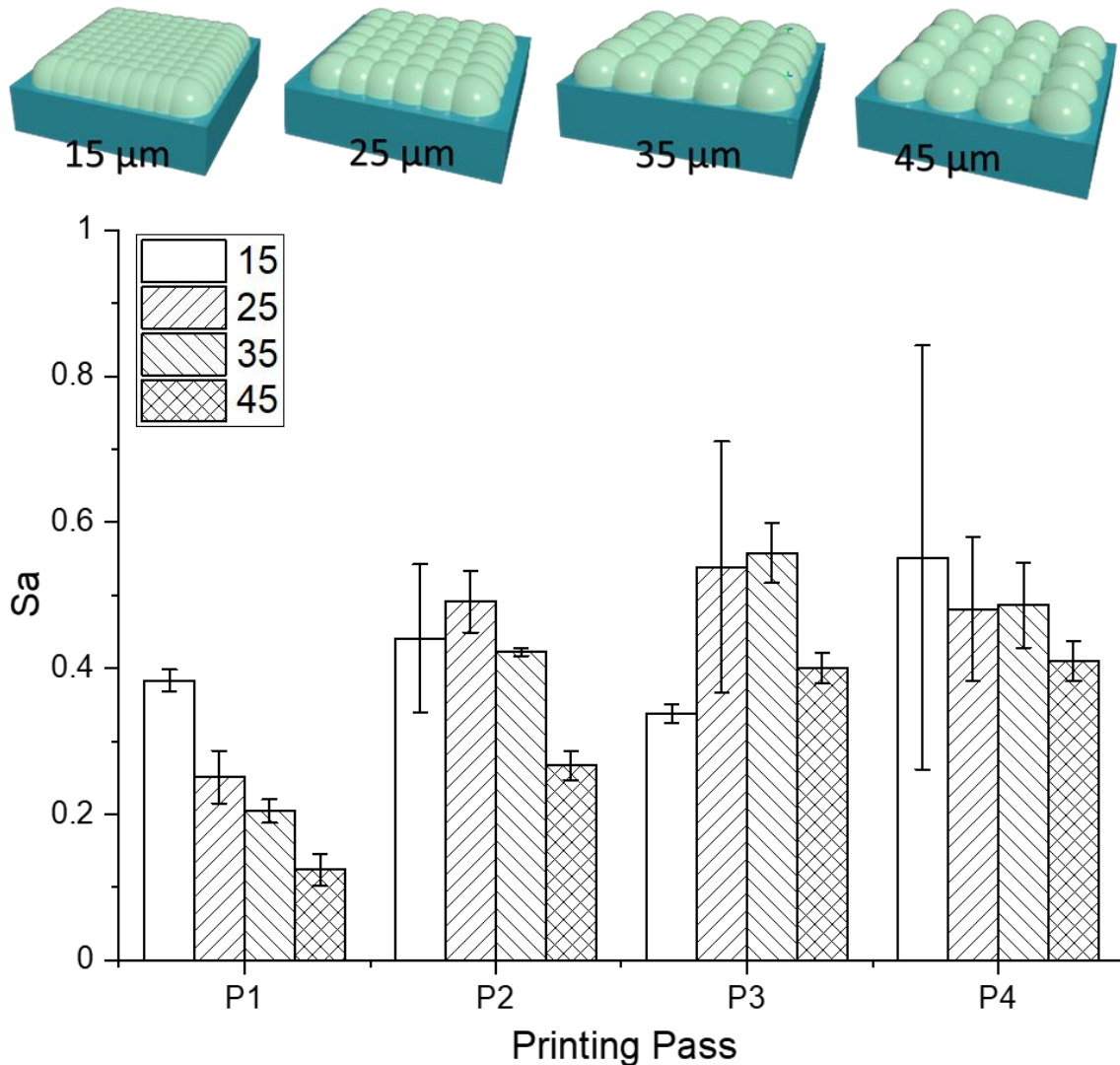


Figure 6-5. Inkjet printing roughness of the cured printed-Ag layer with different printing passes and drop space by laser confocal scanning.

Figure 6-5 shows the calculated roughness of 3D topography obtained from laser confocal scanning in the printed silver film. It can be observed that printed layers with drop space of 35 and

45 μm show relatively lower roughness, and this is because smaller ink volume were deposited on the substrate when using larger drop space. Therefore, the film is very thin, as listed in Table S 2, making the deviation of film height less obvious. When drop space is at 35 and 45 μm , the printed pattern was not fully covered (Figure S 16), even with 4 printing passes, so these two drop spaces settings will not be considered. With a drop space of 25 μm , the roughness is much improved over other conditions. When printing 1 to 4 passes, the area roughness is 0.25, 0.49, 0.54, and 0.48 μm , respectively. For drop space of 15 μm , the area roughness is 0.38, 0.41, 0.34, and 0.55 μm when printing 1, 2, 3, and 4 passes, respectively. At this condition, the high-concentration nanoparticles ink droplets pin on the substrate, form stack coins on the substrate, and overlap with each other.⁹⁷ As a result, the printed area showed bad roughness after 4 print passes due to the accumulation of the droplets on the substrate. Therefore, drop space of 25 μm was selected as the optimal setting.

6.3.2.2.2 Voltage and Printing Pass

Droplet volume of inkjet printing can be precisely controlled by the voltages applied to the piezoelectric membrane. A higher voltage causes larger deformation of the piezoelectric film and pushes more inks out.²⁸⁰ If the voltage is too low, the ink is hard to push out. If the voltage is too high, satellite phenomenon will happen. In this work, voltage ranging from 18 to 30V was studied ranging from 18 to 30V were studied to compare the effect on the roughness of the print pattern.

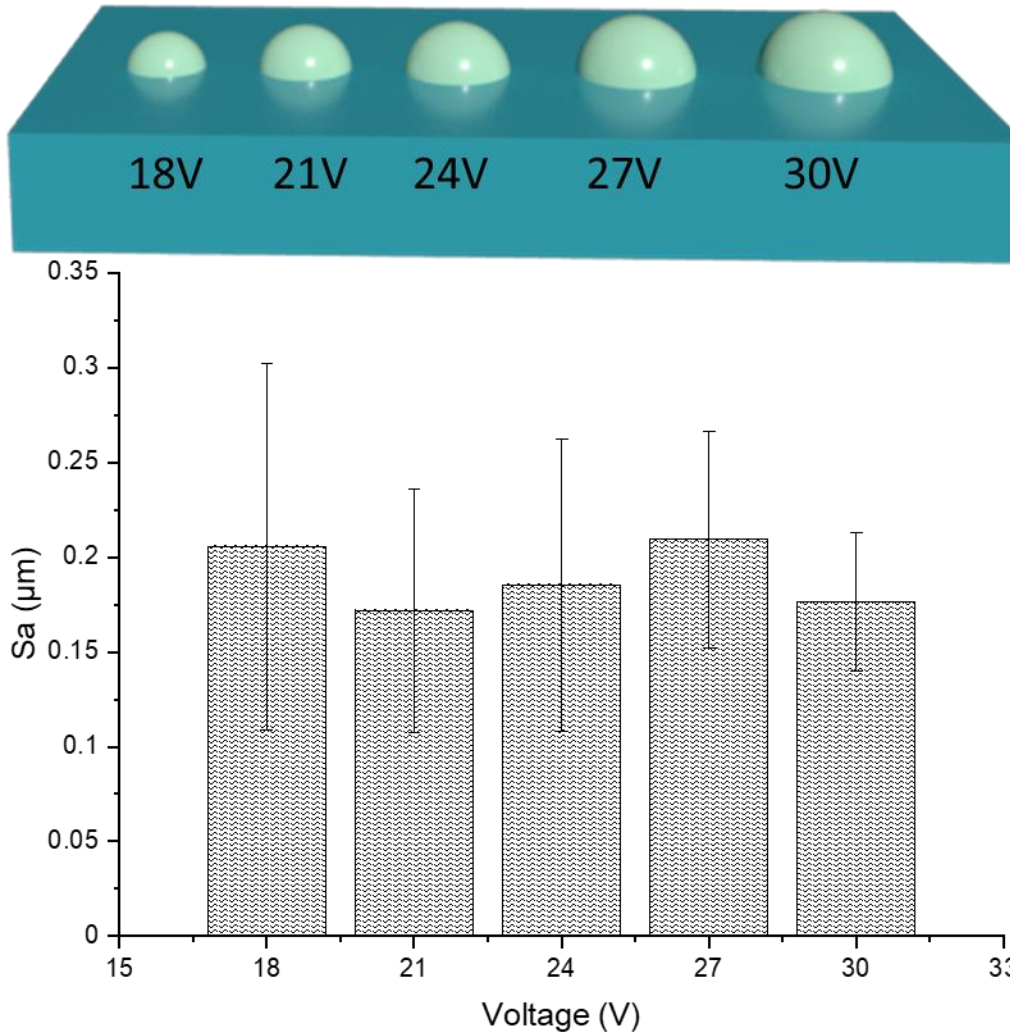


Figure 6-6. 80 nm Ag NP ink printing with different voltages and a constant drop space of 25 μm . (18V, 21V, 24V, 27V, 30V.)

Figure 6-6 shows a minor influence of voltage on roughness. Sa at different voltages (18V, 21V, 24V, 27V, 30V) is 206, 171, 185, 209, and 176 nm. Thus, we still choose the standard 20 V as the printing voltage to printing the Ag ink on Si wafer.

6.3.3 Fabrication of All-inkjet-Printed MIM Capacitor

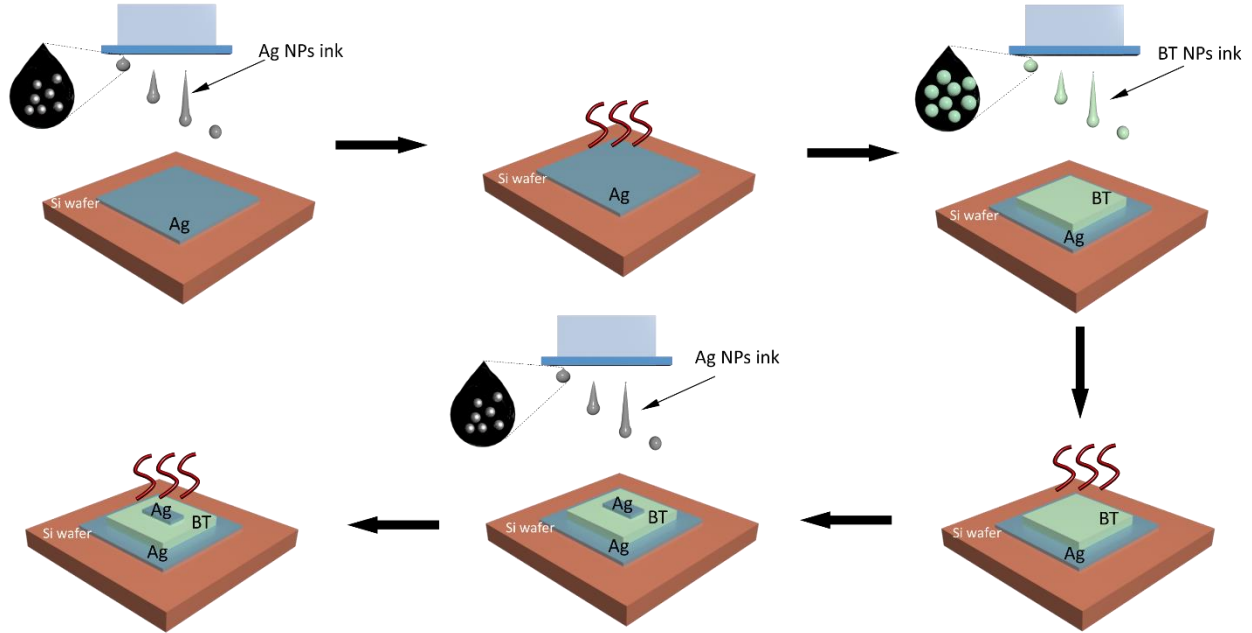


Figure 6-7. The schematic of the inkjet-printing process of Ag/BT-PVP/Ag capacitor.

The fabrication process of the Ag/BT-PVP/Ag capacitor by inkjet printing is illustrated in Figure 6-7. Silver and BT layer were printed on silicon wafer alternatively, serving as the top and bottom electrodes and dielectric layer. The optimized printing settings were used, which are 25 μm drop space and 20 V. After printing the first silver layer on silicon wafer (size: 10 * 10 mm), the sample was dried at room temperature for 2 hours, cured under 150 $^{\circ}\text{C}$ for 1hour, and then 350 $^{\circ}\text{C}$ for 30 mins. Then BT layer was printed (size: 6 * 6 mm), dried and sintered at the same condition. Finally, the top silver electrode was printed (size: 1.5 * 2.5 mm), followed by drying and sintering.

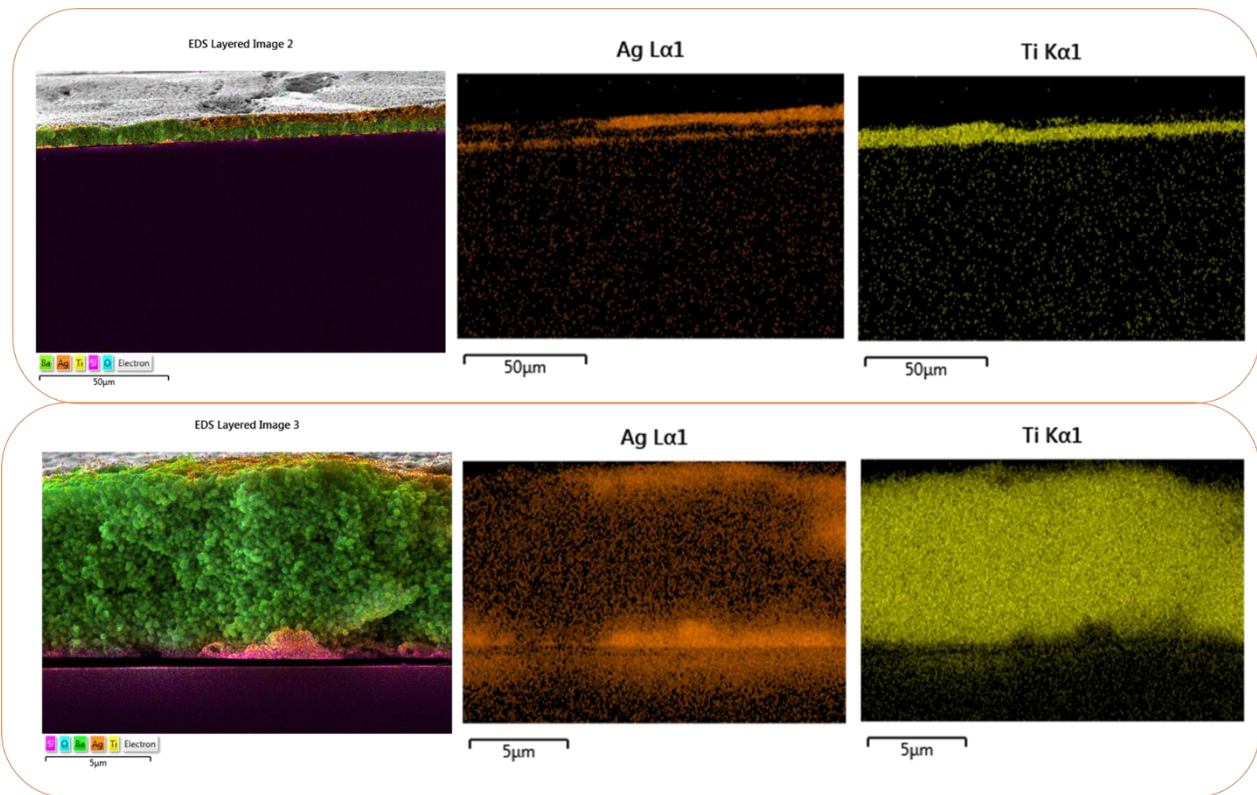


Figure 6-8. Cross-sectional SEM images of the Ag/BT-PVP/Ag capacitor with a bar of 50 μm and 5 μm .

In order to characterize the thickness of the dielectric layer in the capacitor and see if any particle migration between layers occurred. SEM with EDS mapping was conducted, and the results are shown in Figure 6-8. The estimated thickness of BT layer is 5 μm . In the interface between Ag and BT layer, some mixing of the Ag and BT can be observed. This may be due to the penetration of Ag ink with low viscosity and high mobility into the pores between BT NPs. To limit the mixing, PVP/BT volume fraction can be increased to fill the gaps between BT nanoparticles, but this will likely decrease the dielectric constant.

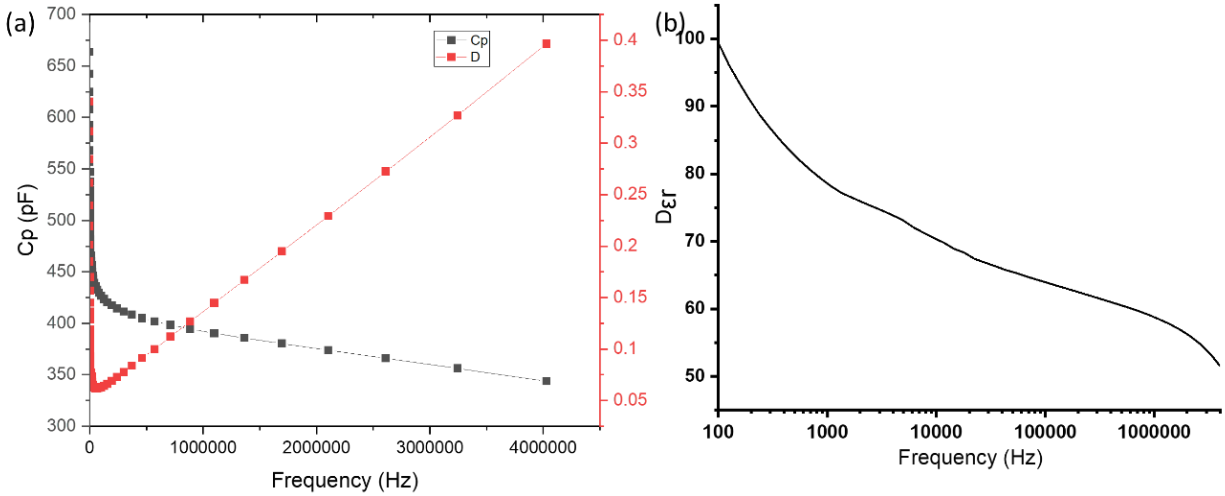


Figure 6-9. (a) Capacitance and dielectric loss of all-inkjet-printed Ag_BT/PVP_Ag capacitor. (b) BT/PVP nanocomposite dielectric constant.

Figure 6-9 shows that dielectric constant of the BT/PVP layer reaches 100 at a frequency of 100 Hz, much higher than other BT/PVP materials.²⁷⁰ For example, this sample is more than twice that of reported 85 wt% BT/PVP film, whose dielectric constant is 30 at 10 kHz.²⁷⁰ The dielectric constant for two-phase composite can be calculated by Lichtenecker equation:^{149, 150}

$$\log \varepsilon_{eff} = v_h \log \varepsilon_h + v_f \log \varepsilon_f$$

where ε_{eff} , ε_h , and ε_f are the dielectric constant of the composite, host (polymer), and filler (BT NPs), respectively. v_h , and v_f are the volume fractions of the host and filler, respectively.

The equation shows that a high-volume fraction of ceramic filler would result in a higher dielectric constant. This could explain the high dielectric properties observed for the BT/PVP nanocomposite in this study. Compared with literature data in Table 6.2, the dielectric constant of the inkjet printed BT/PVP film in this work is comparable or higher.

Table 6.2. Characteristics of PMC (ceramic filler with polymer), published in the literature.

Reference	Ceramic	Content	Polymer	Dielectric Constant (frequency)	Dielectric Loss (frequency)
268	BT NPs (50 nm)	50 wt.%	Acrylic	72 (1k)	1.85 (1k)
	BT NPs (500 nm)	50 wt.%	Acrylic	76 (1k)	1.95 (1k)
278	BT NPs (100-700 nm)	80 wt.%	unsaturated polyester resin (20 wt.%)	50 (1k)	0.024 (1k)
286	BT NPs		epoxy	70 (1M)	0.04 (1M)
287	BT NPs	30 wt.%	PVDF-g-HEMA	333 (1k)	0.73 (1k)
288	BT NPs	1 wt.%	PVDF (2.5 wt.%)	2.46 (10k)	0.01 (10k)
289	BT NPs	50 vol.%	Epoxy Varnish	58 (1k)	0.023 (1k)
144	BT NPs (100 nm)	50 vol.%	polyimide	36 (1k)	0.012 (1k)
290	BT NPs	30 vol%	CEP	52 (1k)	0.08 (1k)
291	BT NPs	20 vol%	regenerated cellulose	22 (1k)	0.085 (1k)
292	BT NPs	50 vol%	P(VDF-HFP)	42 (1k)	0.065 (1k)
293	BT NPs	20 vol.%	PVP	7.4 (20k)	/
294	BST NPs	66.7%	PMMA	42 (1k)	0.007 (1k)

6.4 Conclusion

The successful fabrication of all inkjet-printed capacitor was demonstrated. A high concentration composite ink was developed containing 200 nm BT nanoparticles. Good dispersibility was achieved by adding polymer dispersant (short chain) and PVP (long chain), and hydrogen bonds between the polymers and BT nanoparticles were formed. The influence of inkjet printing settings on the roughness of printed film was studied thoroughly, and it was found that drop space, print pass, and drying temperature had significant effects. After optimization, smooth printed layers can be obtained. The dielectric constant of the printed BT/PVP composite layer is 100 at a frequency of 100 Hz after sintering, much higher than reported materials thanks to its high concentration of

large BT particles. The resultant printed capacitor consisting of a 5 μm thick BT/PVP composite layer, leading to a high capacitance of 176.8 pF/mm² at 100 Hz. The results demonstrated that inkjet printing of composite inks is a promising and efficient method for capacitor fabrication.

7 All-Inkjet-Printed High-Temperature Nickel Capacitor by One Step Co-firing Process

Abstract

Inkjet printing is a low-cost, non-contact computer automated process that enables processing of flexible designs on a wide variety of substrates with minimal material waste. However, fabricating large area ceramic capacitors with high resolution on micrometer length scales remains a critical challenge. An inkjet-printed capacitor is studied by printing 200 nm Nickel (Ni) nanoparticles (NPs) and 200 nm barium titanate (BTO) NPs for the electrode and capacitance layers, respectively. Under a sintering temperature of 1300 °C, BTO NPs achieved a grain size of ~450 nm and the roughness of the sintered-inkjet-printed BTO layer is reported as 150 nm. In addition, the partial oxygen pressure during sintering was optimized to ensure good conductivity of the Ni electrodes and capacitance of the BTO layer. The resultant capacitor (1.5 mm x 2.5 mm) showed a capacitance of 1.1 nF at 100 Hz with a 7 μm BTO layer. The disclosed research provides the foundation to produce base metal electrode multilayer ceramic capacitors (MLCCs) with inkjet printing.

7.1 Introduction

The ceaseless demand for further miniaturization and increasing capacitance of capacitors force manufacturers to use novel techniques that can fabricate layers as thin and small as possible while maintaining economic feasibility.²⁹⁵ Of the various capacitors, multilayer ceramic capacitors (MLCCs) are essential electronic components due to their large capacitance, low cost, and small size.²⁹⁶⁻²⁹⁸ Commercial MLCCs often consist of hundreds of alternating thin dielectric layers and internal electrode layers. Base-metal-electrode (BME) multilayer ceramic capacitors exhibit a denser and more uniform microstructure due to a fine-grained microstructure which can avoid

shrink during ceramic sintering. As a result, BME MLCCs exhibit high capacitance volumetric efficiency.²⁹⁹ The high dielectric properties of BTO make it the most popular dielectric base material for MLCCs.^{151, 300} Nickel has been extensively used as MLCCs' electrode materials due to thermal stability, chemical stability, high theoretical specific capacity, low price, and environmental friendliness.³⁰¹ The performance of Ni BME MLCCs can reach the standard of air-fired MLCCs with Pd/Ag inner electrodes. However, the robust and reliable designs to miniaturize for small-size MLCCs in form factors suitable for a broad array of microelectronic applications remains an unaddressed challenge, limiting the potential use cases and applications of BME MLCCs.²⁹⁹

One of the key inhibitors contributing to this design challenge is the current manufacturing processes of BME MLCC's. The conventional BME MLCC manufacturing process uses high viscosity particle slurries and pastes consisting of conductive materials with polymer binders to form stable printable suspensions. The overall manufacturing process flow involves laminating multiple layers of BTO tape with screen print Ni patterns. The multilayered structures then undergo a series of cutting and heat treatments to burn out polymer binders and condense the capacitor structures. In general, the process is very efficient mostly because of the screen-printing processes involved. However, defects presented by the screen printing process can result in process inefficiencies due to registration alignment, and possible screen contamination can all lead to decreases in the manufacturing process efficiency and productivity.¹ Moreover, screen printing is limited in print resolution and exerts unnecessary stress to the BTO tape film during manufacturing which can lead to final device defects and further decreases manufacturing efficiency.

To address the challenges and problems involved in screen printing, we propose an inkjet processing approach to print novel all-inkjet-printed Ni capacitor structure and design by one step fabrication. Inkjet printing offers a potentially inexpensive solution to print high resolution patterns on small length scales.^{302, 303} Our process employs a piezoelectric drop-on-demand inkjet printer to deposit particle-filled liquid in the desired position. Without the need of mask, inkjet printing can fabricate patterns with low viscosity inks in relatively small amounts, significantly reducing cost and saving energy in the process. Still, inkjet printing poses its own challenge as it requires inks with specific rheological properties. Therefore, careful considerations must be made in terms of materials selection (i.e. functional materials, polymer binders, etc.) and processing to be able to inkjet print MLCCs.

In terms of materials processing, thermal processes are necessary to burnout the polymer binder used to make stable printable suspensions for MLCC manufacturing. The burnout is followed up by high temperature sintering in a well-controlled atmosphere. For MLCCs, the high temperature co-firing of the BTO and Ni layers is an essential step for capacitor fabrication.¹ Base metals like Ni need a reducing atmosphere to protect the metal layers conductivity and prevent oxidation. The oxygen vacancies in the BTO layer lower the device's dielectric property and reliability.²⁹⁷ The pO₂ should be strictly controlled to avoid the Ni layer oxidation and decrease of oxygen vacancy in the BTO layer. To ensure a good conductivity of the Ni electrodes and high capacitance of BTO layer.

In addition to optimizing the sintering conditions, particle size is important for both forming printable inkjet inks and the properties of the functional particle material. For example, the size

effects of BTO ceramics have been well studied^{10, 265, 266} and reported that the dielectric permittivity is maximum when the BTO nanoparticle size is $\sim 1 \mu\text{m}$.¹⁰ For inkjet printing, the material should be less than 1/100 of the nozzle to prevent clogging.²⁵⁹ Our inkjet printing nozzle size is $21.5 \mu\text{m}$ and therefore the size of the nanoparticles should be less than 215 nm. For this study BTO NPs size on average of 200 nm were selected to ensure high permittivity as well as printability. To avoid the penetration of Ni NPs into BTO layer during inkjet printing, a similar size of Ni NPs should be used. However, designing large-size ($\sim 200\text{nm}$) nanoparticle ink for inkjet printing represents a significant challenge in upon itself. Ni NP inks with large nanoparticles ($>100 \text{ nm}$), are mainly designed for high viscosity screen printing pastes.³⁰⁴ Due to the high density, ferromagnetism, and malleability, sizing Ni nanoparticles ink for inkjet printing is challenging.³⁰⁵ Considering these, we employ ball milling and a dual solvent system containing ethylene glycol and ethanol to fabricate well-dispersed nanoparticle ink for inkjet printing.

For these reasons, the objective of this study was to investigate the potential of using inkjet printing for high-temperature sintered MLCCs. Large-size 200 nm Ni NPs and BTO NPs ink were designed for inkjet printing. The effect of sintering temperature on BTO NPs morphology was studied. An all-inkjet-printed high-temperature sintered Ni capacitor ($1.5 \text{ mm} \times 2.5 \text{ mm}$) was fabricated, containing a $7 \mu\text{m}$ BTO layer with a high dielectric constant of 300 at 100 Hz. This study provides the fundamental strategies for further MLCCs fabrication by inkjet printing.

7.2 Experimental Section

7.2.1 Ink Formulation

The nickel ink was prepared by ball milling 10 wt.% nickel NPs (200 nm, SHOEI Chemical Inc.) with 1 wt. % BT NPs (50 nm, US Nano Research) in an ethylene glycol and ethanol solution (ethylene glycol was 44.5 wt.%, and ethanol was 44.5 wt.%) for 48 hrs with zirconia milling media. BTO NPs were added to suppress shrinkage of the nickel layer during sintering.³⁰⁶ To fabricate the BTO NPs ink, 20 wt.% BTO NPs (200 nm, Nanostructured & Amorphous Materials, Inc.) were ball milled with 2 wt.% polymer dispersant (US Nano Research) and 2 wt.% polyvinyl pyrrolidone (PVP, molecular weight (Mw) = 40000 g/mol, Sigma-Aldrich) in 38 wt.% ethylene glycol and 38 wt.% DI water for 48 hrs with zirconia milling media. The polymer dispersant consists of small molecular chains including nonylphenol, polyoxyalkylene amine derivative, polyethylene glycol, polyethylene glycol, polyvinylpyrrolodone, butyl ethanoate, and ethylene glycol monobutyl ether.

7.2.2 Characterization

The liquid properties of the Ni ink and BTO ink were tested using a cone-plate rheometer (MCR 302, Anton Paar) and a goniometer (First Ten Angstroms Europe: Cambridge, UK). The phase composition of the sintered BTO film was characterized using a Rigaku SmartLab X-ray Diffractometer (XRD) with a Cu-K α radiation source ($\lambda=1.5418\text{\AA}$). The respective diffraction patterns were recorded in the range from 20° to 60° (2 θ) using a step interval of 0.02°.

Nanostructure and microstructure analysis of the Ni and BTO NPs, the inkjet-printed film and the annealed film were performed using a Field Emission Scanning Electron Microscope (FEI Verios 460L), a Focused Ion Beam & Scanning Electron Microscope (Thermo Fisher Quanta 3D FEG)

and an Asylum MFP-3D classic Atomic Force microscope (AFM). The dielectric loss and capacitance of the capacitor was tested by a LCR meter (Keysight E4980AL). The capacitance, C , can be calculated with the following equation:

$$C = \frac{\epsilon_0 \epsilon_r A}{d}$$

where $\epsilon_0 = 8.9 \times 10^{-12}$ F/m is the proportionality constant, ϵ_r is the dielectric constant of the dielectric layer, A is the capacitor area (m^2), and d is the distance between conductors (m).

7.2.3 Inkjet Printing and Annealing Process

In this work, a Fujifilm Dimatix printer was employed for inkjet printing. The nozzle height from the substrate was set as 1 mm during printing to achieve high resolution. The ink printing voltage was set at 29 V and 20 V for the Ni ink and BTO ink, respectively, with the standard Dimatix waveform and 25 μm drop spacing.

A primary advantage of using the inkjet process in MLCC fabrication is the reduction of the steps required to form a multilayered structure as the Ni and BTO layers can be printed directly on the same substrate base. Critical criteria for the success of this process are the print resolution, which includes edge wall roughness and surface roughness, as well as the material laydown per print pass. Determining the ability of inkjet printing to meet these criteria is a focus of this work's investigation.

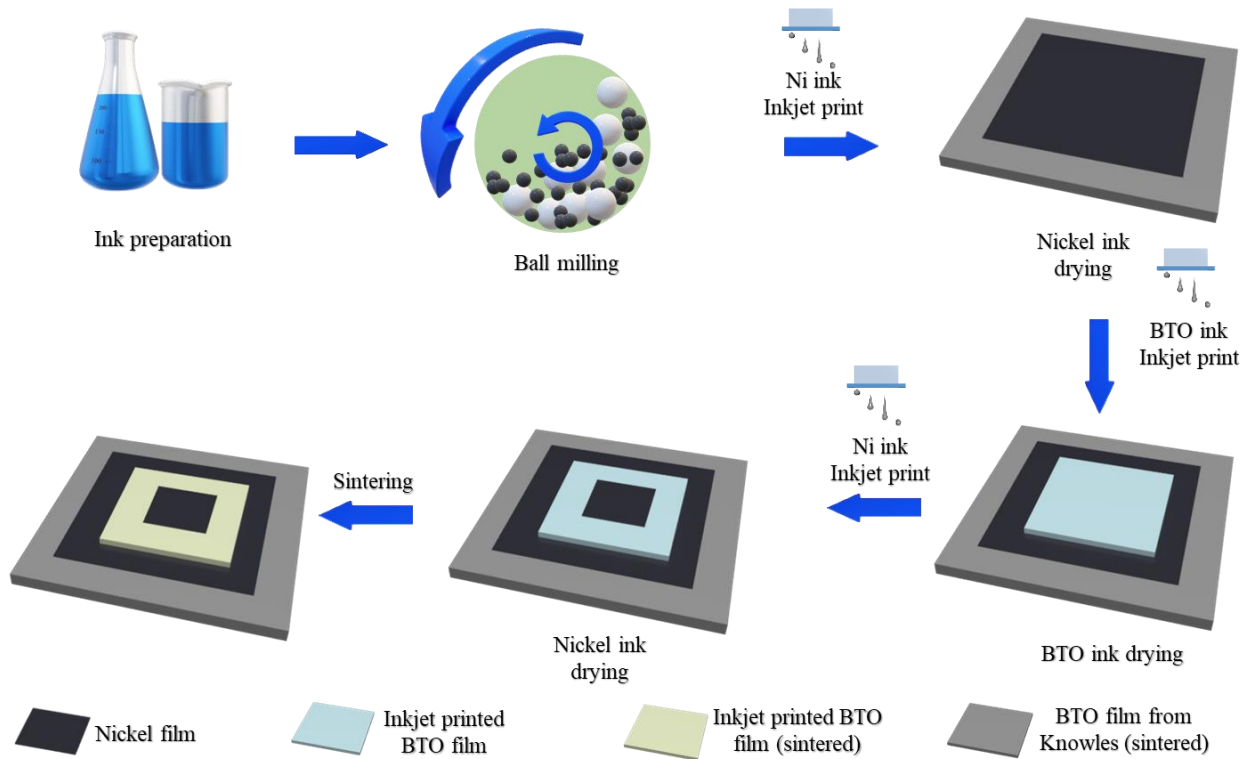


Figure 7-1. Inkjet printing MLCC process from ink formulation to one-step sintering.

Figure 7-1 provides a process layout for the inkjet printed nickel capacitor process, including ink preparation, printing, drying, sintering, and testing. The Ni and BTO inks prepared by ball milling were sonicated 30 mins before inserting into the inkjet printer cartridge. The capacitor was printed by 10 passes of Ni (dried in 60°C for 1 hr), 20 passes of BTO (dried 60°C for 2 hrs), followed by an additional 10 printing passes of Ni on top of the BTO layer. Before sintering the samples, the sample were kept in an oven at 130°C for 20 hrs to binder burnout (BBO).

7.2.4 Drying Process Optimization

Optimization of the ink drying process is critical for the formation of an even printed layer. Heating the substrate can promote the ink drying process. A drying process that is either too slow or too fast could cause an uneven printed layer. Figure S 17 shows the images of printed BTO layer dried

at three conditions: room temperature, 60°C, and 130°C. It clearly reveals that the sample dried at 60°C provides a uniform thickness. Thus, this temperature was chosen as the drying temperature for the remaining investigation in this work.

7.2.5 High Temperature Sintering

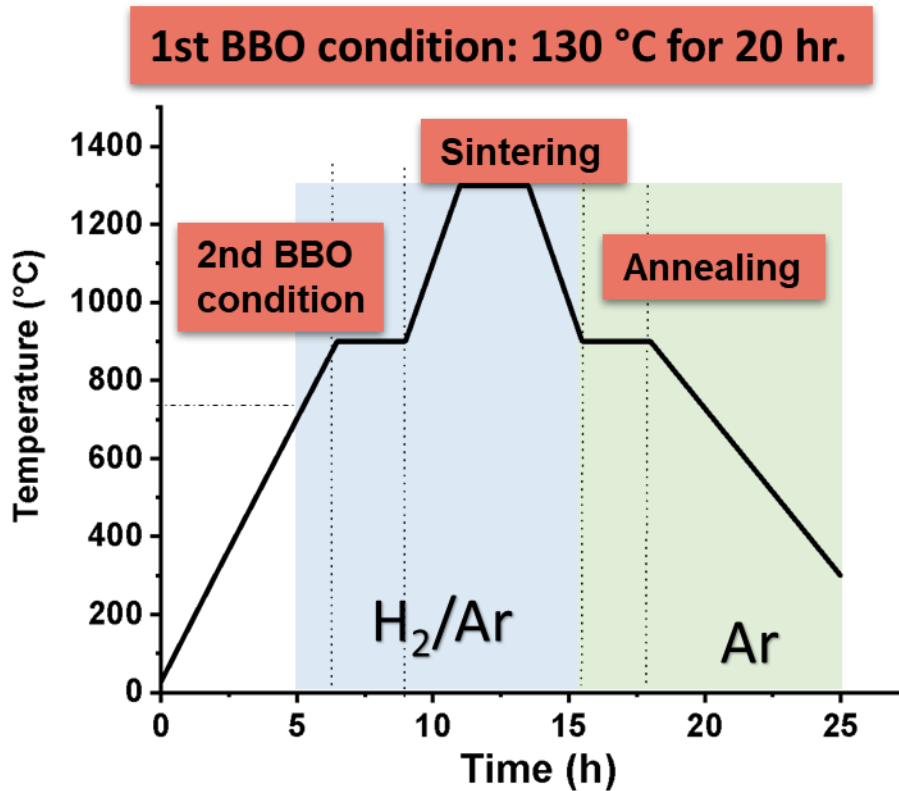


Figure 7-2. Sintering profile for the Ni/BTO capacitor in a reducing atmosphere.

To analyze the effect of sintering temperature on BTO NPs grain size, BTO ink samples printed on Si wafers (1 cm x 1 cm) were sintered at 350 °C, 550 °C, 750 °C, and 1100 °C under ambient air conditions inside furnace for 30 mins.

An inkjet-printed Ni capacitor design with a bottom Ni layer (1 cm x 1cm), middle BTO layer (0.5 cm x 0.5 cm), and top Ni layer (1.5 mm x 2.5 mm) was sintered in a reducing atmosphere according

to the profile shown in Figure 7-2. A tube furnace was used for this sintering process. The sintering was carried out in a reducing atmosphere ($pO_2 < 10^{-11}$) in order to avoid oxidation of the nickel electrodes.¹⁵¹ The H₂ and Ar gas mixture was used to control the pO_2 .³⁰⁷ A high purity gas mixture of 1% H₂ and 99% Ar was used in the furnace at 750 °C. A ramp to 900 °C at 2 °C/min was followed by an isothermal hold for 2.5 hours. This was the second BBO step to completely remove the polymer binder. The temperature was further increased to 1300 °C at a rate of 3.3 °C/min, followed by an isothermal hold for 2.5 hours. The sintered nickel was then cooled to 900 °C at a rate of 3.3 °C/min, and then held isothermally for 2 hours. At this time, the H₂ was stopped to increase the pO_2 and re-oxidize the samples to avoid oxygen vacancies inside BTO layer. Finally, the sintered capacitor was cooled to room temperature at 2.2 °C/min and the Ar flow gas was terminated. The Ni and BTO inks were printed on BTO substrate (Knowles), which can withstand the high temperature (over 1300 °C) process. (Figure S 17)

7.3 Results and Discussion

7.3.1 Ink Characterization

Table 7.1. Ni NPs and BTO NPs inks properties.

Ink Formulation	Surface Tension (mN/m)	Viscosity (cPs)	Density (g/cm³)
10 wt.% Ni NPs (1 wt.% 50 nm BTO)	34.6	9	1.02
20 wt.% BTO NPs ink	64	20	1.3

Table 7.1 shows the rheological properties of the Ni and BTO inks. The surface tension of the Ni and BTO inks are 34.6 mN/m, and 64 mN/m, respectively. The viscosity of Ni ink is 9 cPs, while the BTO ink exhibits a viscosity of 20 cPs. The surface tension and viscosities of the Ni and BTO

inks satisfy the requirements necessary for inkjet printing. The density of the Ni ink (1.02 g/cm^3) is close to water, and BTO ink density is 1.3 g/cm^3 .

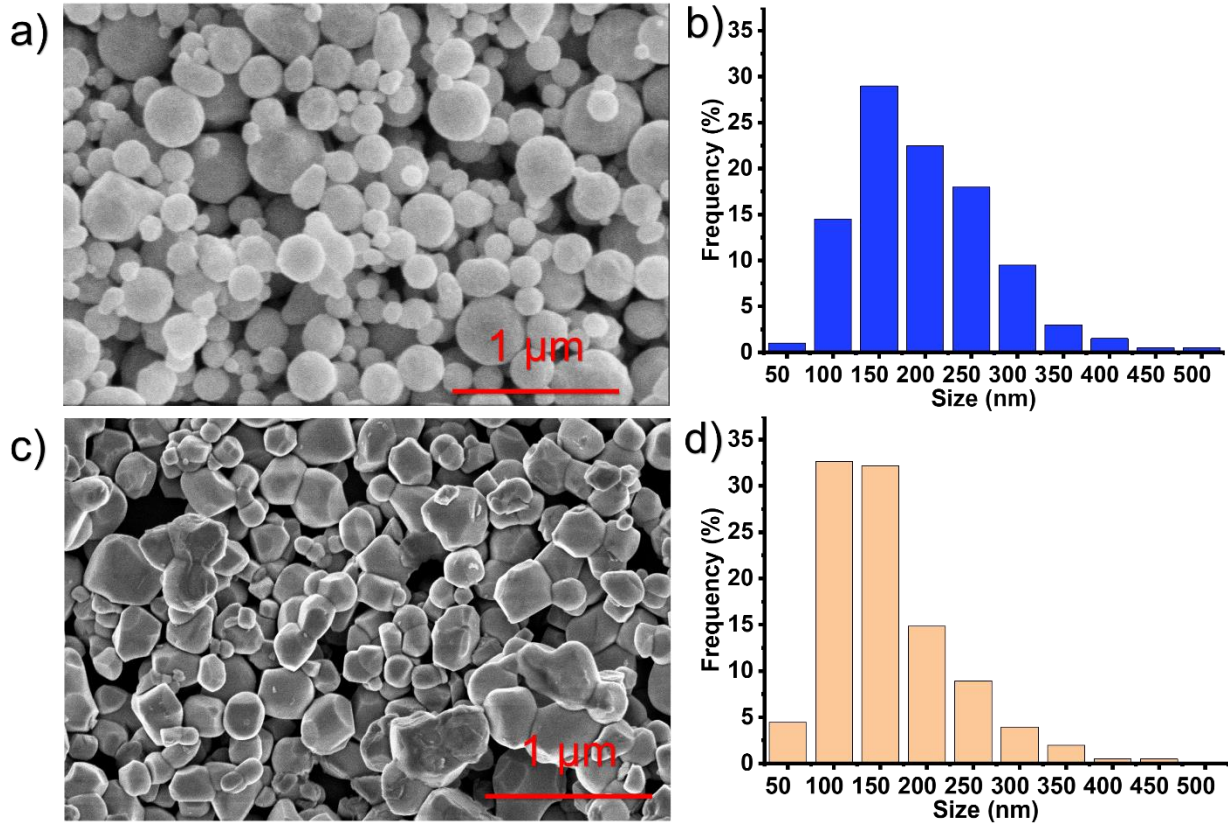


Figure 7-3. Morphology and Size Distribution of Ink Nanoparticles (NPs). Nickel NPs a) SEM images and b) size distribution. BTO NPs c) SEM image and d) size distribution.

Figure 7-3 shows the morphology and size distribution of the Ni and BTO NPs used in the inks. Using the SEM pictures in Figure 7-3a and c, the Ni NPs show an average size of $223.3 \pm 75.3 \text{ nm}$ (Figure 7-3b), while the BTO NPs show an average size of $182.2 \pm 69.7 \text{ nm}$ (Figure 7-3d). BTO and Ni NPs with sizes around 200 nm were chosen for the final capacitor fabrication. These size ranges are commercially available and fit within the size range limits of inkjet printing. In addition, a similar size could also help reduce the penetration of Ni into the BTO layer.

7.3.2 Sintering Effects on Inkjet-Printed Capacitor

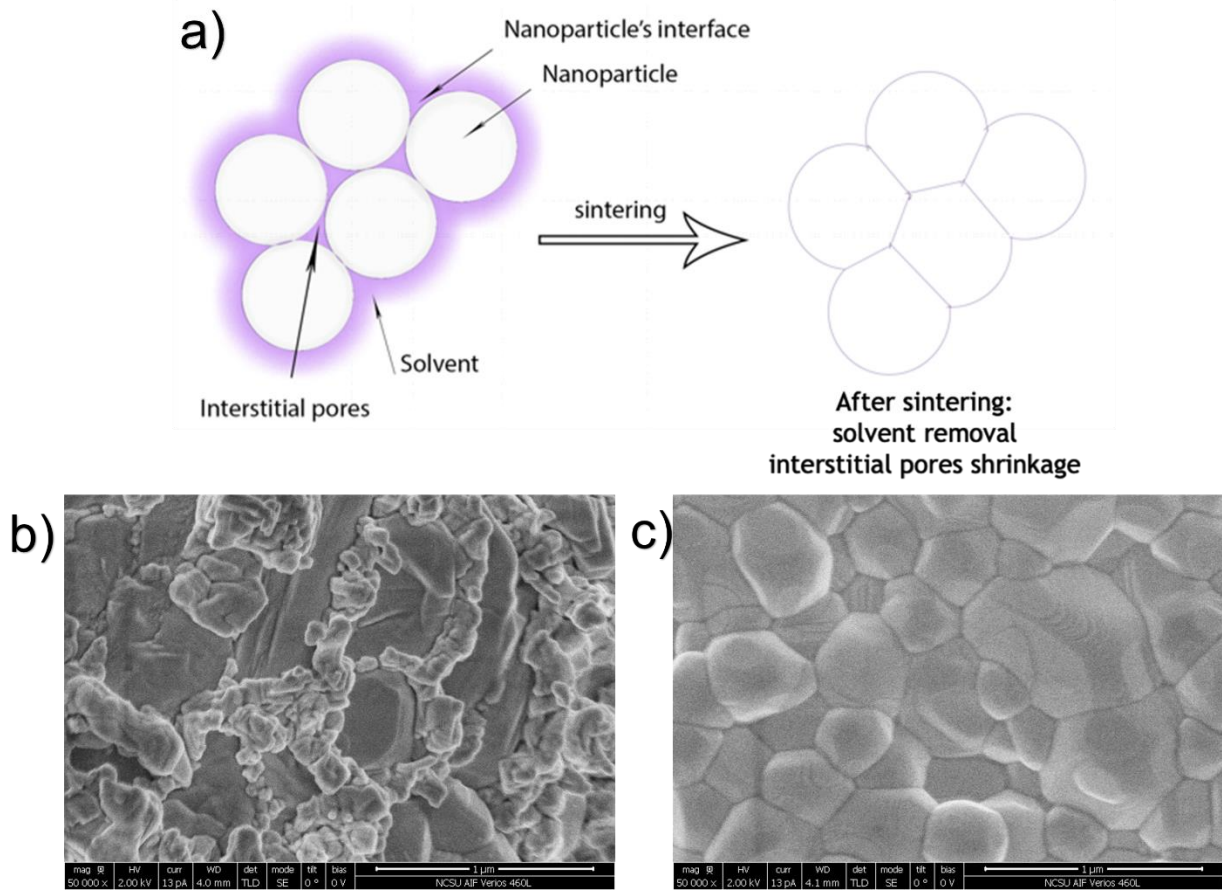


Figure 7-4. Sintering Influence on the Crystal Structure of Ink Nanoparticles (NPs). (a) Schematic illustration of neck growth between nanoparticles. (b) SEM image of Ni NPs after sintering at 1300 °C with a magnification of 50 000X and a bar of 1 μm, (c) SEM image of BTO NPs after sintering at 1300 °C with a magnification of 50 000X and a bar of 1 μm.

To investigate the influence of sintering temperature on the inkjet-printed capacitor, we first investigated the BTO layer. BTO ink was printed on a silicon (Si) wafer (1 cm x 1 cm) and cured in an oven at 150°C for one hour to burn off the organic material in the BTO ink. After the initial curing step, different printed Si wafers were sintered at each of the following different temperatures: 350 °C, 550 °C, 750 °C or 1100 °C for 30 mins. Figure S 18 shows the change in nanoparticle morphology with the different sintering temperatures. As seen in Figure S 18, no

obvious changes in particle morphology were found when sintering at temperatures of 350 and 550 °C and the particle size remained 200 nm. (Figure S 19) However, particle surface smoothing, rounding of pores, and formation of grain boundaries and necking is clearly observed > 750 °C. At 1100 °C, we observe the intersection of grain boundaries, shrinkage of open pores, and slow grain growth. In addition, the nanoparticle size increased to ~300 nm (283 ± 84 nm, Figure S 19). Changes in particle morphology during high-temperature sintering are due to bulk diffusion, grain boundary diffusion, evaporation-condensation, viscous flow, and plastic flow.^{308, 309} Figure S 20 depicts the XRD patterns for BTO NPs sintered at different temperatures. The XRD peaks at 22.2, 31.5, 38.9, 45, 51, 56 degrees represent the reflection planes (100), (110), (111), (200), (210), (211), respectively.³¹⁰ The split peaks at 45° indicate the tetragonal phase of the BTO NPs. It is obvious that sintering temperature did not affect the phase structure of BTO NPs. To investigate the effect of pO₂, an inkjet-printed Ni capacitor with a bottom Ni layer (1 cm x 1cm), BTO layer (0.5 cm x 0.5 cm), and top Ni layer (1.5 mm x 2.5 mm) was sintered in 1100 °C in air condition. When the Ni capacitor directly sintered at air condition, we could observe the black Ni layer turns into green color, indicating oxidation of the Ni (Figure S 21). Further, the SEM images show that while the BTO NPs size increases to 283 ± 84 nm, the open pores and slow grain growth means BTO NPs are not totally sintered.

In order to fully sinter the BTO NPs, a higher temperature is necessary. In the final stage of the sintering, the solvent would be totally removed, and interstitial pores shrink to form closed pores. (Figure 7-4) After sintering in reducing condition following the heating profile shown in Figure 7-2, the Ni electrodes become conductive. The morphology of the capacitor is shown in Figure 7-4b. The 50 nm BTO NPs can be also observed in the Ni layer, which were included to reduce

the layer shrinkage. After annealing at 1300 °C, we can clearly see closed pores, large grain size, and pores shrinkage to a limiting size or disappear in BTO layer. (Figure 7-4c) At this condition, the BTO NPs size grow to 447 ± 147 nm. (Figure S 19)

7.3.3 Substrate Effects on Inkjet-Printed Capacitor.

Shrinkage within the MLCC layers can cause a shortcut in the capacitor. Therefore, it is important to balance the increase in material density while preventing significant shrinkage. To study the impact of shrinkage, a BTO substrate was chosen to fabricate the capacitor. After sintering, again following the profile provided in Figure 7-2, the BTO substrate shrank to 2 cm x 2 cm x 1 mm from 2.54 cm x 2.54 cm x 1.5 mm and caused the capacitor sample to completely delaminate from the substrate. (Figure S 21). The arithmetic average thickness ($H=A(\text{area})/L(\text{length})$) can be calculated from the FIB images (Figure S 22). After sintering, the thicknesses were reduced to 3.68 μm and 1.22 μm . The large shrinkage greatly affected the capacitor's performance and caused a shortcut at high frequency (Figure S 22).

To reduce the shrinkage effect, the BTO substrates were first sintered prior to inkjet printing, following the sintering profile in Figure 7-2. Then, the Ni and BTO inks were inkjet printed on the fired substrate. From Figure S 19, the shrinkage of the Ni capacitor is greatly reduced. The AFM results of sintered BTO NPs on the fired BTO substrate demonstrated that the inkjet printed layer is smooth (Figure 7-5). The AFM image also shows that the grains size of sintered BTO NPs is around 450 nm, which matches the SEM results, and the surface roughness was ~ 150 nm.

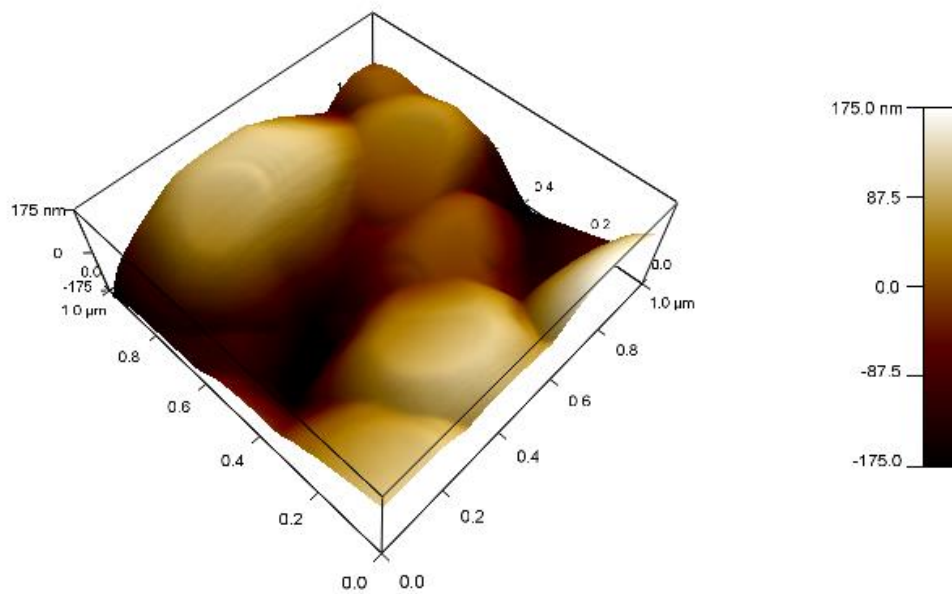


Figure 7-5. AFM image of sintered BTO film.

7.3.4 XRD of the Inkjet-Printed Capacitor Before and After Sintering.

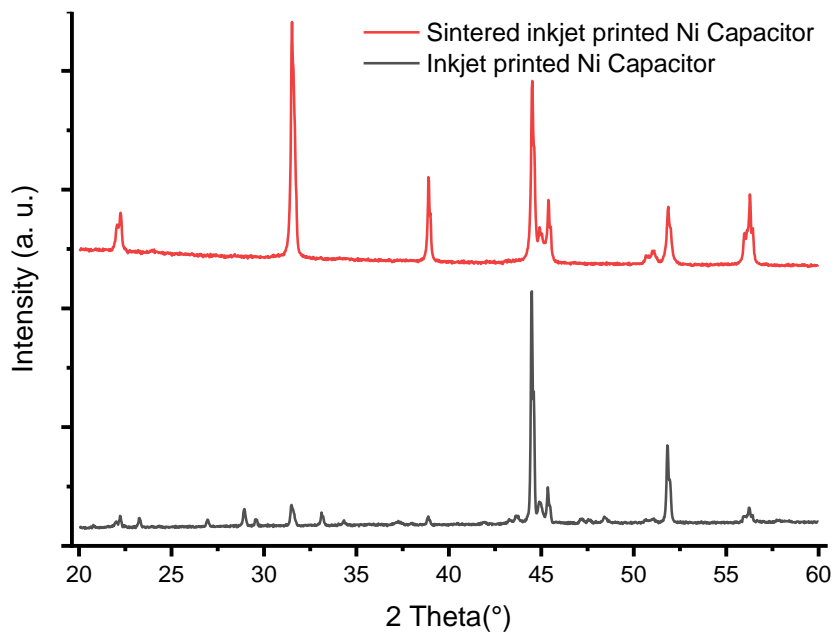


Figure 7-6. XRD result of inkjet printed capacitor before and after sintering at 1300 °C.

Figure 7-6 shows the X-ray diffraction pattern of the all-inkjet-printed Ni/BTO capacitor deposited on fired BTO substrate before and after sintering. And the BTO peaks at 22° , 32° , 39° , 45° , 51° , 56° are (100), (110), (111), (200), (210), and (211) planes^{310, 311}, and this means BTO NPs phase is not changed after sintering. Furthermore, the XRD peaks at 45° , 52° , and 56° split into two peaks, which means the BTO has tetragonal structure that is essential for ferroelectricity. The Ni peaks at 44.5° and 51.8° represent (111) and (200) planes.³¹² It could also be found that Ni NPs are not oxidized after sintering in reducing condition as the NiO peak at 37° is absent.³¹²

7.3.5 Structure of the Inkjet-Printed Capacitor

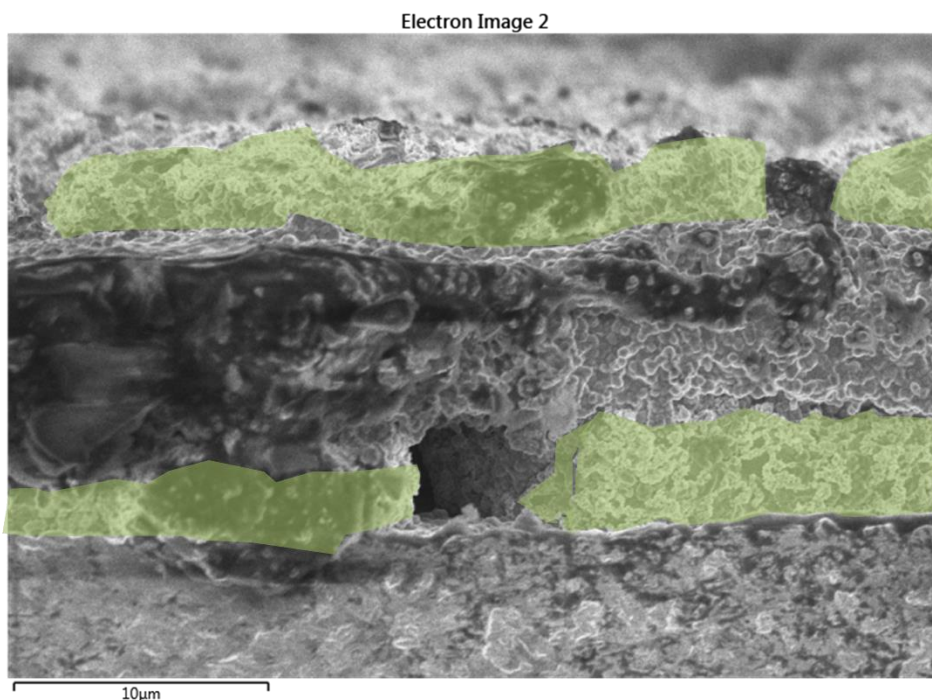


Figure 7-7. Cross section image of inkjet-printed Ni capacitor after sintering.

SEM with EDS was used to investigate the distribution of BTO and Ni layer. (Figure S 23 and Figure S 24) Ba element can be found in the Ni layer from Figure S 23, as 1 wt. % 50 nm nanoparticles were added during nickel ink fabrication with a purpose to limit shrinkage during

sintering. Figure 7-7 shows that the sintered BTO layer thickness is around 7 μm . (Ni layer is shown in green color.) Even though the Ni capacitor structure is not perfect as uneven thickness distribution was observed, it shows the potential of using inkjet printing for MLCCs fabrication. In the future, the Ni ink will be optimized with a suitable polymer binder. The thickness of Ni layer and BTO layer could be further reduced by manipulating inkjet printing settings.

7.3.6 Ni Capacitor

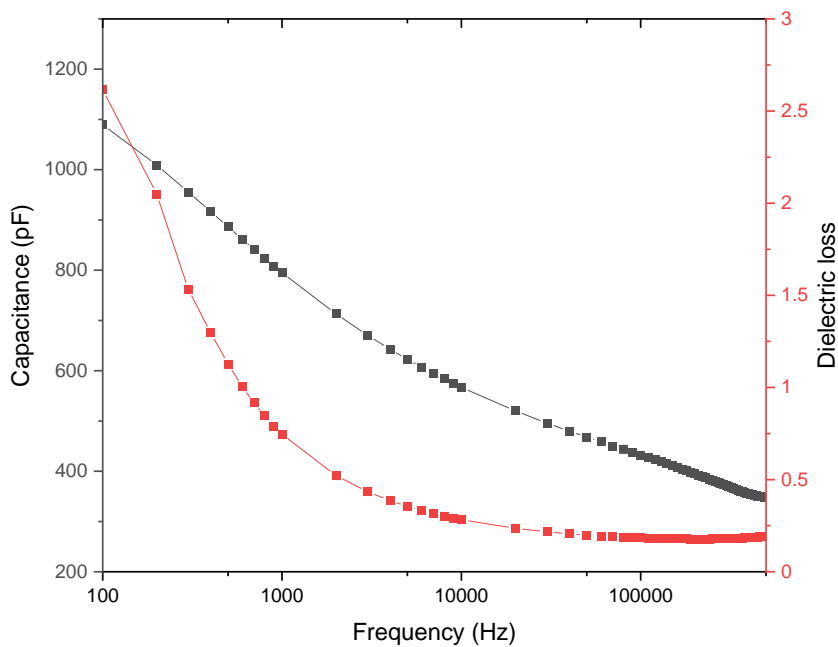


Figure 7-8. Capacitance and dielectric loss of the sintered Ni capacitor.

The capacitance and dielectric loss of the resultant nickel capacitor were measured from 100 to 100k Hz. A maximum capacitance of 1.1 nF was observed when tested at 100Hz. (Figure 7-8) The dielectric constant is around 300 at 100 Hz which is close to the reported BTO precursor ink, but with a much less dielectric loss.³¹³ In future studies, the oxygen pressure should be optimized to further increase dielectric properties of BTO layer. The sintering of BTO in a reducing atmosphere certainly impacted the insulation property, and in order to solve this problem, dopant such as MnO,

CaO, rare earth oxides(Y_2O_3 , Dy_2O_3 , Ho_2O_3 , Er_2O_3), can be added to stabilize BTO NPs and avoid the oxygen vacancies.^{1, 314} In conventional fabrication process of ceramic capacitor, weak adhesion between the layers may cause the delamination during the sintering process¹⁵⁹, and inkjet printing method can be more effective to avoid the cracks and holes.

7.4 Conclusion

We have demonstrated a whole process of the all-inkjet-printed high-temperature sintered Ni capacitor, including Ni NPs and BTO NPs ink design, optimization of sintering temperature and atmosphere, substrate treatment, etc. The resultant Ni capacitor with a size of 1.5 x 2.5 mm showed a capacitance of 1.1 nF, and the BTO layer without doping achieves a dielectric constant of 300 at 100 Hz.

In future research, the thickness of printed Ni and BTO layer will be reduced by manipulating inkjet printing parameters. In addition, the Ni and BTO ink will be optimized to further improve the evenness of printed layer. Finally, multilayer capacitor by printing Ni and BTO alternatively will be researched. This research is very important as it shows the viability and potential of using inkjet printing for minimizing the complexity of Ni MLCC fabrication.

8 High-Concentration Barium Titanate Nano-Inks for Inkjet Printing and Reduced Coffee Ring Effect

Abstract

Coffee ring effect is often one of the most challenging phenomena when it comes to uniform deposition of particle-based functional inks. In this work, an innovative formulation method for ceramic ink containing high concentration barium titanate (BT) nanoparticles (NPs) was developed. Surface modification of BT NPs surface were performed with short-chain polymer dispersant and long-chain polyvinylpyrrolidone to enhance homogenous dispersion in solvents. A dual solvent system with different evaporation rate of solvents was developed to minimize coffee ring effect. The combination of high boiling point solvent (ethylene glycol) and low boiling point solvent (ethanol) induce a gradient surface tension in the droplet and form Marangoni flow. The ratio of the dual solvents was optimized by comparing the surface topographies of printed patterns using inks with different solvent ratio. As 1:1 ratio of ethylene glycol and ethanol was the optimum solvent combination, the printed layer shows good uniformity and fast evaporation. The BT NP ink was inkjet printable even with high nanoparticle concentration (20 wt.%), maintaining a viscosity of 4 cPs and a surface tension of 27 mN/m at room temperature. The ink can be stored for months under ambient condition and the dispersion was stable against aggregation. We demonstrated inkjet printed BT NP ink on Si wafer for dielectric layer formation for printed electronics applications.

8.1 Introduction

The boost of electronics in the global market stimulates high-quality, low-cost, and large-scale electronic components. Compared with conventional approaches such as photolithography,

microcontact printing, screen printing, tape casting, inkjet printing can solve the problem of time-consuming, complicated, and expensive process.³¹⁵⁻³¹⁷ Inkjet printing is a non-contact printing technique have advantages including scalability, low cost, high throughput, less waste, and material conserving.^{316, 318-320} It is the process that jets the droplets from a small orifice and deposits them on the desired position by computer control. This process includes ink flow in the print head, wetting, and drying on the substrate. This method allows for the massive fabrication of less material directly via a digital model in two-dimensional or three-dimensional structures.³²¹

Owing to the ceramic's excellent properties, such as high mechanical strength and hardness, good thermal and chemical stability, electrical and magnetic properties, especially the high relative permittivity, they are widely used in electronic devices.³²² Barium titanate (BT) with unique piezoelectricity and high dielectric constant and low dielectric loss has been widely used in capacitor area.^{211, 323} Capacitors are essential electronic devices, which can be as signal decoupling, filtering, and tuning.²⁵⁷ Screen printed BT nanocomposite ink^{278, 324} and inkjet printed BT polymer precursor ink are widely used in the dielectric layer fabrication. However, both two inks are hard to get thin film deposition. Nanometer-sized particle inkjet printing inks have great potential in thin-film dielectric layer fabrication. The major challenge of inkjet printing is to have inks containing high-concentration functional materials while capable of printing uniform particle deposition and high film homogeneity in an efficient way.⁹⁵

Formulating inkjet printable electronic inks require optimization process of concentration, material stability, surface tension, viscosity, and evaporation rate.^{325, 326} It is challenging to formulate functional inks achieving high functionalities while maintaining stability in inkjet process and

reliability of the functional patterns. Capability of high concentration of electronic materials are often required to achieve advanced functionality with reduced print and process time, especially considering manufacturability. To get the highly dispersed nanoparticles ink, aggressive organic solvents are used, such as N, N-dimethylformamide (DMF)⁶³. As reported in the previous studies, it is highly challenging to increase materials loading in the nanoparticle-based green inks for inkjet processing.

It is important to understand how colloidal stability can be improved in the ink formulation stage. The colloidal stability depends on the nanoparticles' size, density, surface chemistry, and dispersants.³²⁷ Designing the ink need to overcome the hydroxylated filler surface and aggregation of the particles driven by van der wall force. To avoid the aggregation, the solvents and polymer should be carefully chosen. Second, the inkjet ink leaves the micro-size nozzles (20- 100 μm)⁸³ at high velocity (around 10 m/s)⁷⁰. Thus, the surface tension and viscosity must be carefully controlled. The surface tension should be approximately 25-50 mN/m, and viscosity should be around 1-25 cPs.⁸⁰ The ink physical properties should be considered, especially for high viscosity ink, which can directly influence the droplet formation at the nozzle. Third, the low surface tension ink interactions with the substrate would directly influence the printed pattern quality including resolution and roughness.

It is important to understand two aspects of inkjet process to achieve conformal patterns with inkjet printing process. First, stable nanoparticle ink without blocking inkjet printer nozzle is the preliminary requirement for inkjet printing. On the other hand, once the stable jet is created from the nozzle, high-resolution-pattern and its roughness deposited on the substrate are influenced by

the printable ink's fluid dynamic properties, such as the droplet formation, spreading and wetting on the substrate, three-phase contact line (TCL) motion, flow fields inside droplets, and mass transportation within the droplets during drying.³²⁸ The morphologies of the inkjet-printed droplets are decided by the drying process. The existence of the Coffee Ring Effect (CRE) on the hydrophilic surface and Rayleigh instability on the hydrophobic surface would greatly influence the printed uniformity and smoothness.³²⁹ The CRE occurs when an increased evaporation rate at the droplet edge and contact line pinning due to surface irregularities and solute deposition, forming a ring stain that marks the perimeter of the droplet before drying.³³⁰ The capillary-driven flow from the droplet center toward the edge compensated for the evaporation losses and push the material into the rim.³³⁰ To reduce the CRE, the practical way is to take advantage of the Marangoni flow. Another way is a strong increase of viscosity during drying of ink.³³¹

The goal of this study is to design a high-concentration dielectric BT nanoparticle ink capable of printing homogenous layer on Si wafer using inkjet printing. The first challenge is the aggregation issues among nanoparticles, especially for high-concentration system. Small-chain polymer dispersant and long-chain PVP were selected to bond onto BT nanoparticles surface through hydrogen bonding. The surface modified BT NPs dispersed homogeneously in ink without obvious aggregations. The ink uses a dual solvent system containing ethanol and ethylene glycol with different ratios. The roughness of printed layer was analyzed, and the ratio of the dual solvents were optimized. This proposed method can be used to design other functional nanoparticle inks economically and practically.

8.2 Experimental Section

8.2.1 BT Ink Fabrication

First, the polymer dispersant (PD) (US Nano Research), was added to a solvent mixture containing different ratios of ethanol and ethylene glycol. The polymer dispersant is composed of a mixture of small molecular chains including nonylphenol, polyoxyalkylene amine derivative, polyethylene glycol, polyethylene glycol, polyvinylpyrrolodone, butyl ethanoate, and ethylene glycol monobutyl ether. The resulting mixture of polymer dispersant in the ethanol and ethylene glycol solvent mixture was sonicated for 5 minutes. After sonication, BT nanoparticles (200 nm) (US Nano Research) were added into the solution mixture, followed by 3 hours of sonication. Then polyvinylpyrrolidone (PVP) with a molecular weight (Mw) of ~40000 g/mol (Sigma-Aldrich), was introduced into the solution and sonicated for 3 hours. The resultant ink contains 20 wt.% BT nanoparticle, 2 wt.% polymer dispersant and 2 wt.% PVP.

8.2.2 Deposition System

The jet-ability of different solutions was evaluated in a material deposition system based on piezoelectric inkjet technology (Dimatix DMP 2850). The printer head's cartridge uses state-of-the-art silicon micro-electro-mechanical systems (Si-MEMS) with sixteen 21.5- μm -diameter nozzles linearly spaced at 250 μm . The typical drop size for the printer is 10 pL, and each cartridge has an ink capacity of 1.5 mL. The ink was filtered through a nylon membrane with a 5- μm pore size before loading the ink into the printer cartridge. The printer is equipped with a charge-coupled device (CCD) camera system. Droplet formation at the nozzles and trajectory of the drops after ejection was clearly observed and imaged for analysis. The printing voltage is 20V at a frequency

of 23 kHz. The single droplet drop space was 200 μm , and the film printing drop space is 15 μm for 10 passes. The printing height from the substrate to the nozzle was set to 1 mm.

8.2.3 Characterization

The surface tension values were measured at room temperature (21°C) with a goniometer (First Ten Angstroms Europe: Cambridge, UK). Dynamic viscosity was measured at room temperature (21°C) using a cone and plate rheometer (model MCR 302, Anton Paar). Surface modification of BT particles was characterized using Fourier-transform infrared spectroscopy (FTIR) (Thermo Fisher FTIR models, iS50). Thermogravimetric analysis (TGA) and differential thermal analysis (DTA) (EXSTAR TG/DTA 6200, Seiko Instrument, Japan. US) were performed by heating samples from room temperature to 580°C at 10 °C/min. Raman measurements were performed using a Horiba XploRA PLUS Confocal Raman Microscope in a backscattering microconfiguration. Raman spectrums were collected using a 532 nm edge laser set to 10 % power and 2400(400) nm grating focused on the sample surface using 50x magnification. The spectrum was collected from 100 to 4000 cm^{-1} at room temperature with a 2 second acquisition time and accumulation set to 1. The surface images, and topographical profile of the printed pattern were obtained with Laser confocal microscopy (VK-X1000, Keyence).

8.3 Results and Discussion

8.3.1 Ink Stability

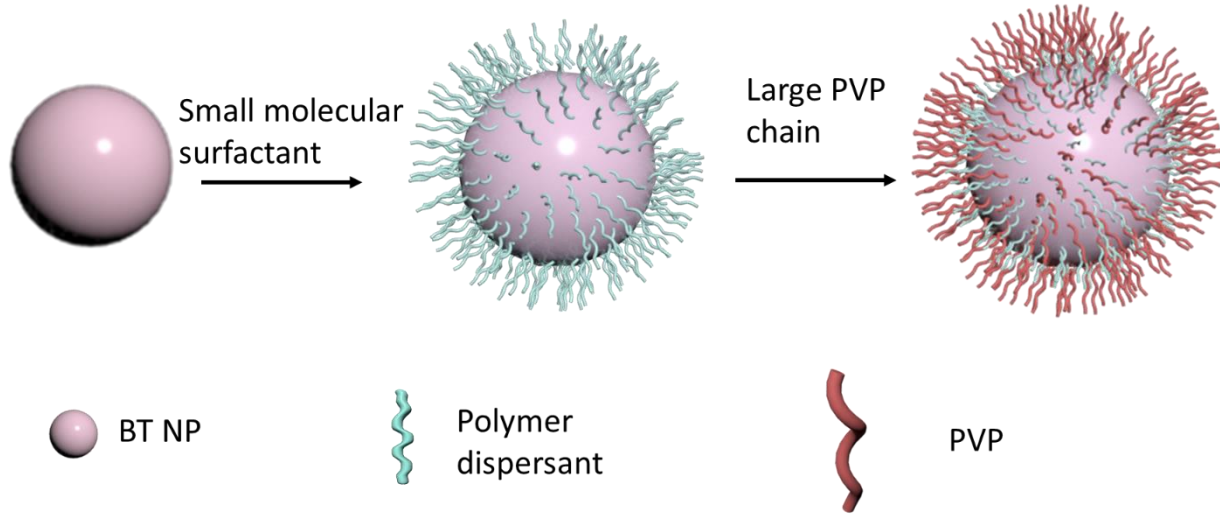


Figure 8-1. Mechanism of the BT ink fabrication.

Good dispersion, and high stability of nanoparticles are the preliminary requirements for inkjet printing³³². The nozzles of the printer are usually less than 100 μm , and would be easily clogged by larger particles or nanoparticle aggregation.³³³ In addition to causing clogging issues, the aggregation of the BT nanoparticles would produce a highly inhomogeneous printed layer, resulting in electric field with local hot spots, which can cause defects and deteriorating the dielectric properties of printed layer. Adding dispersant, surfactant, or coupling agent is an effective method to prepare well-dispersed ink.³³⁴ Adding polymer surfactant and dispersant can cause bubbles in ink. Ethanol can be used as defoamer by reducing the surface tension in the local area and causing local areas to thin rapidly.^{64, 327} Particles in inkjet printing ink should be less than 1/100 of the nozzle to prevent clogging.²⁵⁹ Therefore the size of the nanoparticles should be less than 210 nm. The BT nanoparticles were modified with polyvinylpyrrolidone (PVP) to promote the BT ink's dispersibility.^{269-271, 335} The mechanism of the BT surface-modified process is shown

in Figure 8-1. The low molecular weight polymer dispersant has a short molecular chain and weak intermolecular interaction.¹⁴⁸ The small molecular chains can be easily coated on the nanoparticles' surface instead of interacting with the polymer chains. Moreover, the polymer dispersant can form hydrogen bonding with the hydroxylated filler surface of the BT NPs through its polyethylene oxide parts. The surface-modified high-concentration BT NPs with polymer dispersant can still be easily aggregated after some time. Therefore, long-chain PVP is added to modify the ink viscosity and the surface of the BT NPs to prevent aggregation. After this, the ink can be kept at room temperature for months without evident precipitation. The mechanism is the low molecular chain polymer dispersant, and high molecular chain PVP can work together to disperse BT nanoparticles in ink. The small molecular chains can penetrate the gaps of the nanoparticles after ultrasonication. In contrast, long chains polymer can increase the viscosity of ink and keep the ink stable for a long time.

8.3.2 Characterization of the BT Surface Modification

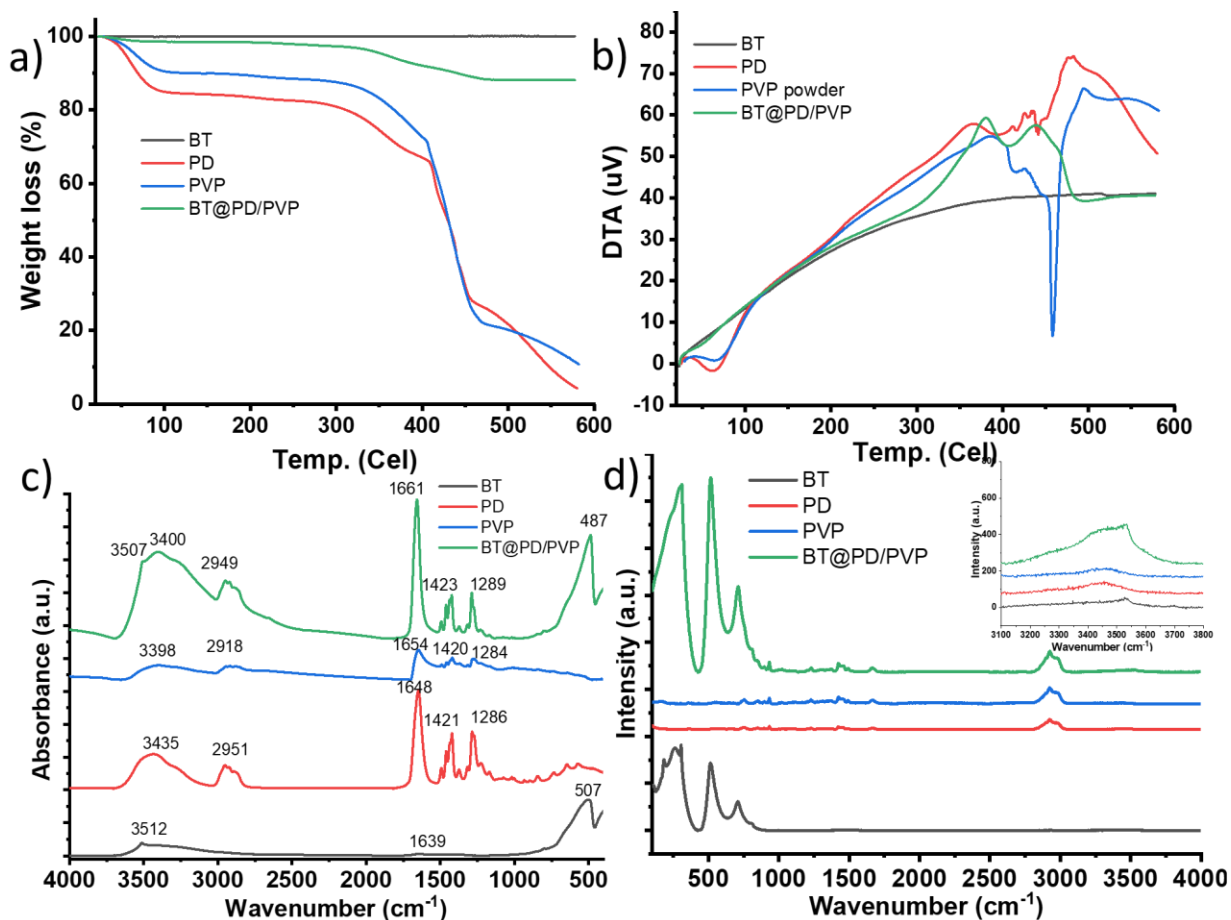


Figure 8-2. (a) TGA curves of untreated BT, BT@PD/PVP, PVP, PD, BT in ethanol, BT in ethylene glycol and BT@PD/PVP in ethylene glycol and ethanol mixture. (b) DTA curves of untreated BT, pure PD, pure PVP, and BT@PD/PVP in ethylene glycol and ethanol mixture. (c) Comparative FTIR of the BT, PD, PVP, and BT@PD/PVP. (d) Comparative Raman of BT, PD, PVP, and BT@PD/PVP.

The TGA, DTA, FTIR, and Raman analysis were used to investigate if the PD and PVP were grafted onto the BT particles' surface. Figure 8-2a shows the TGA curves of BT, PD, PVP, and BT@PD/PVP powder. The surface coated BT (BT@PD/PVP) shows a dramatic weight loss of 11.8% from 324 °C to 483 °C, caused by the decomposition of polymer dispersant and PVP. And the final material shows 18% loss before sintering. The DTA curve of the PVP shows three peaks

at 386, 458, 494 °C, respectively. The exothermic peak at 386 °C, indicates the crystallization of PVP, while the endothermic peak at 458 °C represents the dehydrogenation, carbonization, and decomposition of PVP. The exothermic peak 494°C indicates the combustion of the carbon deposition.³³⁴ The PD has three peaks at 366, 441, and 477 °C. At 366°C, PD begins to crystallize. PD dehydrogenate, carbonize, and decompose at the temperature of 441°C. The combustion of the carbon deposition is at 477°C. BT@PD/PVP shows weak exothermic peaks at 351 °C and 429 °C, corresponding to the crystallization of the polymer and combustion, respectively. Since the polymer content is very low, so the peak is not apparent. The comparison of the FTIR spectra of surface modified BT NPs with those of PVP and PD concluded that the stretching vibration peak of C=O from 1661 to 1654 and 1648 cm⁻¹, and C-N stretching peaking at 1435 cm⁻¹ which shift from 1420 and 1421 cm⁻¹.²⁷² These indicated the N and O atoms from PD and PVP interact with the BT nanoparticles. The strong O-H stretching peak at 3400 cm⁻¹ of the surface modified BT NPs prove the hydrogen bonds between the nanoparticles and polymer. The FTIR shows the peaks of PD and PVP, which prove the polymer were coated on the NPs. And Raman data also shows PD and PVP bonded on the surface modified BT NPs. The hydrogen bonds can be also proved by the Raman at the 3100-3600 cm⁻¹.

8.3.3 Ink Jettability and Liquid Properties

In order to explore the effect of inkjet printing on the formation of BT thin film, the viscosity, evaporation rate, and surface tension of the ink were systematically analyzed. Ethylene glycol (EG) and ethanol (E) are used to fabricate BT ink with good stability due to the hydrogen bonds formed with the hydroxylated BT nanoparticle surface.³³⁶ The ethylene glycol and ethanol ratio determined the ink viscosity, surface tension, and evaporation rate. The high viscosity (16.1 mPa·s)

of EG can facilitate the ink solution membrane to maintain a good resolution, but it is hard to be injected from the printer nozzle. While the low viscosity (0.8 mPa·s) of ethanol can help the ink spread on substrate, but it is difficult to control the diffusive pattern. The high surface tension (47.3 mN/m) of EG may cause the dewetting effect on smooth substrate, while the low surface tension (20.14 mN/m) of ethanol can promote the diffuse on the substrate and reduce the surface tension of ink. Moreover, the low evaporation rate EG (bp=197 °C) facilitate the homogeneous spread of the solute. In contrast, ethanol's fast evaporation rate (bp= 78 °C) would have the advantages of avoiding ink accumulation on the substrate during multiple printing passes. Based on these factors, we investigated the EG and ethanol's combination in order to get a smooth film by manipulating the evaporation rate, surface tension, and viscosity, which are essential factors for inkjet printing.³²⁶

For inkjet printing ink, the ink should be stable in the print head. Faster drying solvents would increase the ink's viscosity at the nozzle and may cause an irreversible nozzle clog. When using ethanol only as the solvent, the nozzle was quickly blogged. Also, the ink should dry soon after being printed on the substrate. Therefore, the pure ethylene glycol solvent is not a good option for inkjet printing. In order to solve the problem, the ethanol and ethylene glycol dual solvents system was researched. The mixture solvent system balances the need to dry fast on the substrate and reliable jetting process in the nozzles. Slow evaporation solvent ethylene glycol and fast evaporate solvent ethanol show good compatibility with BT NPs and are widely used as the BT NPs ink' solvent. Ethylene glycol would minimize the drying at the nozzle and prevent the nozzles from blocking. And fast-evaporation ethanol would reduce the time and energy required to dry the ink on the substrate. Moreover, these solvents are nontoxic and environmentally friendly. They both

served as the carrier to deliver the functional material of ceramic BT NPs to the substrate, while restricting contamination in the workplace and protecting human health and the environment.

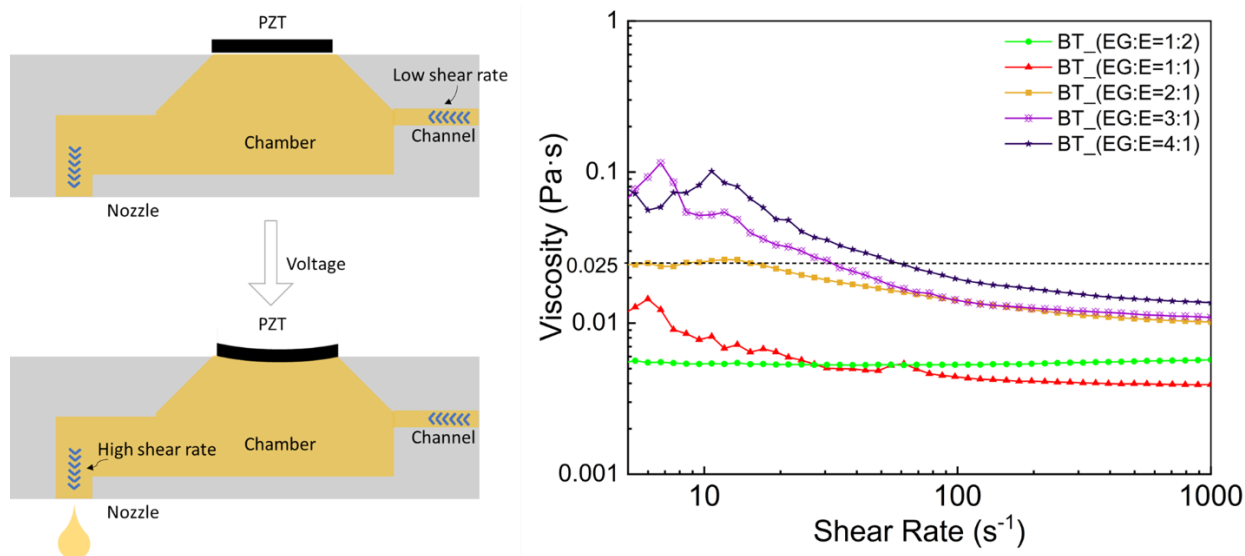


Figure 8-3. Viscosities of the BT@PD/PVP in ethylene glycol and ethanol mixture solvents at the ratio of 1:2; 1:1; 2:1, 3:1, 4:1. 0.025 Pa·s is the maximum viscosity requirements for the printer used in this paper.

Different rheology behaviors are observed for ink formulations with different ethylene glycol and ethanol ratios, as shown in Figure 8-3. At a high ratio of the ethanol (EG: E=1:2), the ink has a low viscosity of 0.0055 Pa·s both at a low shear rate and high shear rate. The viscosity increases with the ration of ethylene glycol. At a high percentage of ethylene glycol, the inks have non-Newtonian rheology with high viscosity at a low shear rate and low viscosity at a high shear rate. (Figure 8-3) When the ratio of EG/E=1:1, 2:1, at low shear rate (5 /s), the viscosity is 0.011 Pa·s and 0.025 Pa·s, respectively; and at high shear rate (1000 /s), the viscosity is around 0.004 Pa·s and 0.011Pa·s, respectively. During inkjet process, inks are subject to low shear rate in the ink supply tube and the print head's narrow channels, and high shear rate in the nozzles part when jetting out. Low shear rate and high shear rate viscosities are equally important and should be less

than the maximum values for inkjet printers. These two inks met the requirements for the printer used in this paper. When the ratio of EG/E=3:1, 4:1, the viscosity at a low shear rate (5 /s) is too high for inkjet printing. Therefore, the inks with solvent ratios of EG: E=1:2, EG: E=1:1, and EG: E=2:1 were selected for further analysis in this paper.



Figure 8-4. Surface tension of the BT ink with different ethylene glycol/ ethanol ratio. (a) EG:E=1:2, (b) EG: E=1:1, (c) EG:E=2:1.

Since the viscosity for inkjet printing is very low, the ink's surface tension is a primary factor deciding the droplet formation and spreading on a specific substrate.³²⁶ The solvents compositions and polymer surfactants can influence the surface tension. Here BT@PD/PVP with different ratios of EG and E are analyzed. Figure 8-4 shows that the surface tension of ink with a ratio of EG:E=1:2, 1:1, 2:1 is 24.38 mN/m, 26.99 mN/m and 28.47 mN/m, respectively. The addition of surfactant reduces the surface tension of solvents; therefore, the differences between the ink systems are not apparent. However, it still plays an important role in the printing quality.

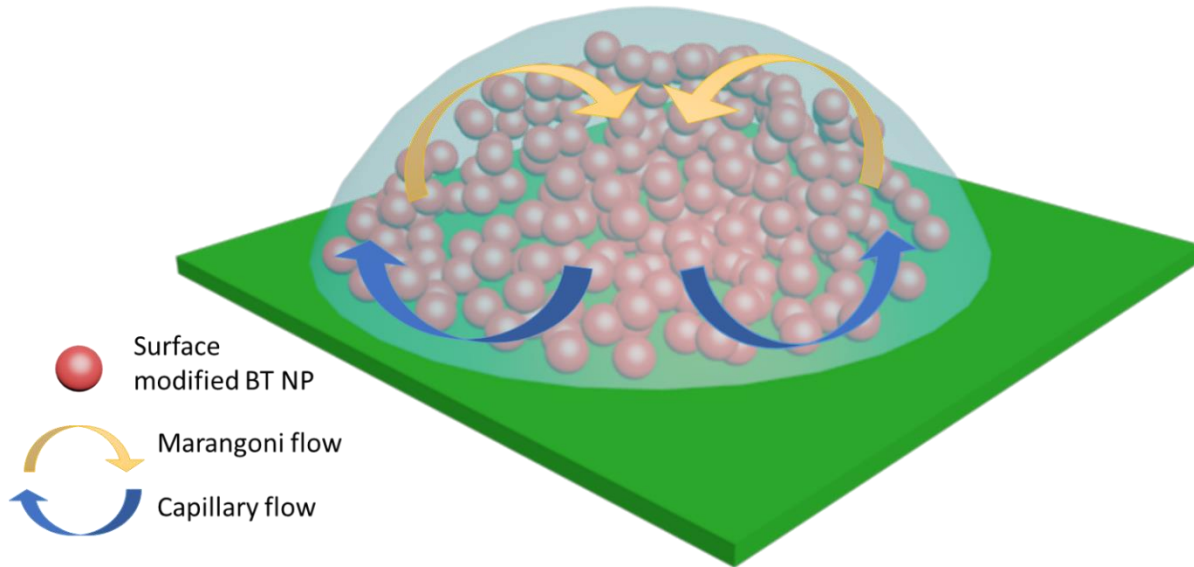


Figure 8-5. BT NPs ink evaporation based on the Coffee Ring Effect and Marangoni Effect.

After the ink deposition on the substrate, the nanoparticles are deposited close to the contact line, pinning the droplet on the substrate.³³⁷ As the ink evaporation continues, a replenishing flow of solvent will carry the nanoparticles from the droplet center to its pinned edge. (Figure 8-5) These conditions are due to the droplet's capillary flow during the evaporation and are usually called coffee ring effect.(CRE)³³⁸ For electronics devices, the CRE is an unwanted phenomenon. To overcome CRE, the Marangoni flow effect which can be archived by controlling the surface tension of the ink. At the Marangoni flow, the particles will flow from low surface tension area to high surface tension area. (Figure 8-5)

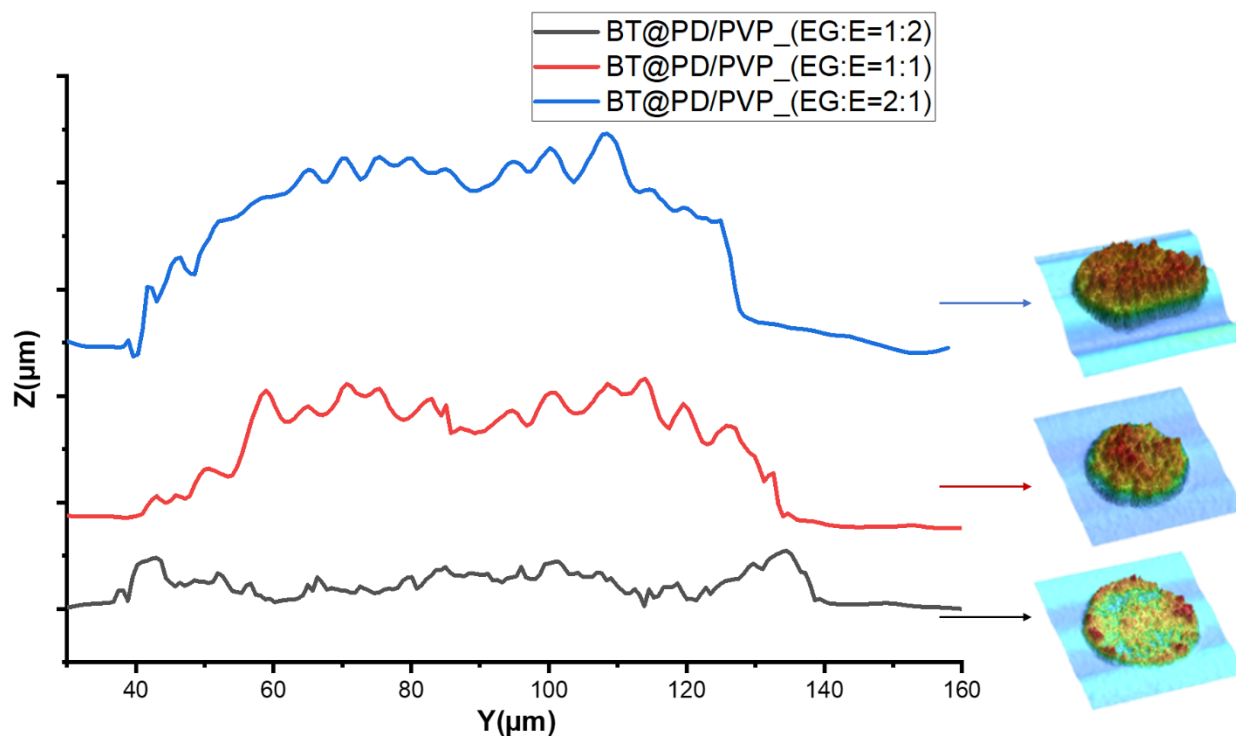


Figure 8-6. 3D microscopic images of inkjet printed single dots obtained from BT ink with different solvent ratio of ethylene glycol and ethanol 1:2; 1:1; 2:1, and the height profile of the single droplets at different ratio in vertical direction.

A single droplet dot was deposited from a drop space of $200\ \mu\text{m}$ by an inkjet printer with a $21.5\ \mu\text{m}$ orifice. 3D images and 2D surface profiles of the inkjet printed single dots obtained from BT ink with different solvent systems are shown in Figure 8-6. Even though the inks have the same weight percentage of BT nanoparticles, the volume percentage is different as solvent densities changed due to different ratios of ethanol and ethylene glycol. When printing a single droplet with the same volume, the BT volume of each ink is different. The droplet size is decided by the surface tension and the thickness is dependent on BT volume ratio. The ink system with small surface tension has a greater volume of fluid in proximity to the contact line. For the same droplet volume, it has a larger size and is more likely to form coffee rings.⁹⁷ When the ethanol is the major part of the ink (EG:E=1:2), the pattern shows a coffee ring shape (Figure 8-6), where BT NPs were

accumulated at the edge of the droplet. The droplet size is around 107 μm , and the height is about 115 nm.(Figure 8-6d) When the ethylene glycol is equal to or more than 50 wt.%, the pattern shows a uniform BT NPs distribution.(Figure 8-6) When the ink with a high boiling point solvent such as ethylene glycol (197 °C) and a low boiling point solvent like ethanol (80 °C), the different evaporation rate of the solvent system would cause a surface tension gradient in the droplet and induce Marangoni flow.⁹⁵ Thus the droplet has a Marangoni flow from the lower surface tension area to the higher surface tension area, reducing coffee ring effect.³³⁸ When the EG/E ratio is 1:1, the CRE is obviously reduced and shows a good roughness from Figure 8-6. The droplet size is around 99 μm , and the height is around 530 nm. When the EG/E ratio is at 2:1, the droplet size is around 90 μm , and the height is around 700 nm. It can be found that the ink solvent containing 50% EG or more is sufficient to overcome the coffee ring effect. But with a high concentration of slow evaporating solvent ethylene glycol, the ink drying time increase enormously. Therefore, this ink is not suitable for inkjet printing. Moreover, in Figure S 25 and Figure 8-6, we could observe the large dot with a small dot at a high concentration of the ethylene glycol in the horizontal direction. This is due to the high viscosity and density of the ink's satellite phenomenon. This further proves the ink solvent ratio should be 1:1 of the ethanol and ethylene glycol.

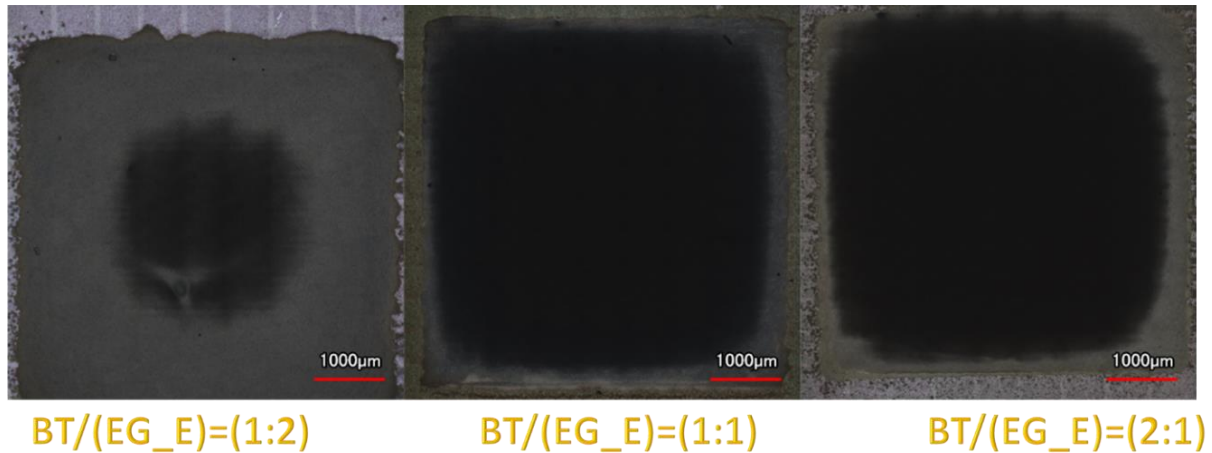


Figure 8-7. Morphologies of the inkjet printed 5 mm* 5 mm BT film using inks with different solvent ratio.

A dried ink film can be considered a huge droplet. Because dielectric printed layer requires a certain thickness, more droplets are necessary. Here, BT inks with different solvent ratios were printed at a drop space of 15 μm and 10 passes to get a thick film. Due to the fast evaporation rate for solvent system EG/E=1:2, poor roughness can be observed in Figure 8-7a. When printing a thick layer, the fast evaporation rate solvent would result in accumulation of nanoparticles in the middle area. While at the ratio of EG/E=1:1, or EG/E= 2:1, the printed films demonstrate good roughness. (Figure 8-7b and 7c) For a very smooth and high surface energy substrate, the droplet deposition process includes phases of kinematic, spreading, retracting, wetting, and equilibrium.⁶⁶ The low surface tension ink at a ratio of EG/E=1:2 shows high spreadability on Si wafer, and the quick evaporation causes the rough edge on the side. The material would pin on the substrate before reaching the equilibrium state of the droplet. Even though, at the ratio of EG/E= 2:1, the film shows good roughness, the slow evaporation of the ink may cause ink accumulation and poor printing quality. Therefore, we would choose the ink at a ratio of EG/E=1:1 to design our ink.

8.4 Conclusion

In summary, we have designed BT ceramic dielectric ink with high weight percentage for inkjet printing which can greatly save printing time and energy. Small-chain polymer dispersant and long-chain PVP were successfully used to modify the surface properties of BT nanoparticles by forming hydrogen bonds and reduce particle aggregation. In addition, the influence of the ratio between high-boiling point solvent ethylene glycol and low-boiling point solvent ethanol on surface tension, viscosity, and morphology of printed dot was explored. It was found that when ink solvent containing 50% ethylene glycol or more, undesired coffee ring effect could be eliminated due to Marangoni Effect. The resultant high-concentration BT dielectric ink is capable of printing uniform layers and would have great potential for the fabrication of inkjet printed capacitor. The proposed ink formulation method may also be suitable for other functional nanoparticle inks for inkjet printing.

9 CONCLUSION AND FUTURE WORK

9.1 Summary and Conclusion

Smart textiles have shown tremendous growth over the past decades. The versatility and potential of the printing method for smart textile fabrications were fully demonstrated in this study. In summary, this research covered the whole process of printing both an antenna and capacitor, including fabricating inks, substrate selection, optimization of printing parameters, and device fabrication.

Preparation of inks with functionalities was the first step, and critical factors including viscosity, surface tension and evaporation rate should be considered. UV curable BT inks for spray coating, and inkjet printing, high-concentration BT inks and Ni conductive inks for inkjet printing were successfully prepared. It was found that the printability, dispersibility, and stability of nanoparticle ink systems depends on the selection of surfactants and dispersants, solvent combination, particle size and processing methods. The use of various commercial inks, including silver MOD and silver nanoparticle inks for inkjet printing, and silver paste for screen printing, were also demonstrated. Apart from inks preparation and printing parameters optimization, curing and sintering conditions are critical to improve the properties of printed layers, such as dielectric properties and conductivity. In the end, flexible and breathable textile antennas and capacitors, as well as rigid miniature capacitors were successfully printed, and these devices exhibit superior performance.

The first objective of the research is to prepare flexible and breathable textile antennas and capacitor sensors by printing UV curable BT NPs. In Chapter 3, a novel dielectric ink consisting of UV curable acrylates, urethane and 4 wt.% 200 nm barium titanate nanoparticles was prepared.

The ink was successfully used to enhance the dielectric properties of the naturally porous textile substrates by direct-write spray coating and inkjet printing in Chapters 3-5, which is key to the performance of the antenna and capacitor.

The textile antenna presented in Chapter 3 using spray coating of UV curable BT inks and screen printing of silver paste is capable of operating in a full-duplex mode, is demonstrated with a relatively high gain of 9.12 dB at 2.3 GHz and a bandwidth of 79 MHz (2.260–2.339 GHz) for each port. However, the use of the screen printing method for patch and ground fabrication decreased the breathability and flexibility of the antenna. The performance of the textile antenna was improved in Chapter 5 by inkjet printing of reactive MOD (metal–organic-decomposition) silver ink and the UV curable BT NPs dielectric ink on textile substrates. The fabricated patch antenna shows a low return loss of 24.98 dB in free space and preserves its performance even when bent to $>300^\circ$. The breathability of the antenna is retained after inkjet printing. More importantly, after consecutive 1000 bending cycles, the conductivity and return loss of the antenna remained unchanged with excellent stability in conductivity and mechanical durability.

Inkjet printing of the UV curable BT ink can also be used to fabricate a textile capacitor, as demonstrated in Chapter 4. The printing of UV curable BT ink significantly improved the dielectric constant of the textile substrate. High resolution and high conductive ($0.014 \Omega/\text{sq}$) patterns were prepared by inkjet printing of Ag MOD ink. The resultant large textile capacitor exhibits high sensitivity (11.4 kPa^{-1}), low detection limit (50 Pa), good mechanical stability is fabricated and can be used as capacitor array pressure sensor.

In addition to using flexible textile substrates, devices that are lightweight and miniature in size are also preferred for wearable applications. The second research objective research was to fabricate small-size capacitors by inkjet printing of high-concentration BT NPs inks.

In Chapter 6, a fully inkjet-printed silver capacitor was prepared by printing a newly developed high-concentration large-size BT/polymer ink and commercial silver MOD ink. After optimization of drying temperature and printing settings, uniformly printed layers were achieved. The printed nanocomposite dielectric layer with a thickness of 5 μm showed a high dielectric constant of 100 at 100 Hz. A high-temperature sintered ink jet-printed nickel capacitor containing consisting of 200 nm Nickel (Ni) nanoparticles (NPs) for electrode layers and 200 nm barium titanate (BTO) NPs for the dielectric layer was prepared in Chapter 7. The sintering temperature, and partial oxygen pressure affected the dielectric constant of BT layer and the conductivity of Ni layers. After optimization of the sintering conditions, the resultant capacitor (1.5 mm x 2.5 mm) showed a capacitance of 1.15 nF at 100 Hz with a 7 μm BTO layer. The disclosed research provides the foundation to produce base metal electrode multilayer ceramic capacitors (MLCCs) with inkjet printing.

High-concentration inks are necessary for the fabrication of high-performance devices. In Chapter 8, an innovative ceramic ink containing high concentration barium titanate nanoparticles (20 wt.%) for inkjet-printing was presented. BT NPs surface were modified with short-chain polymer dispersant and long-chain polyvinylpyrrolidone to ensure good dispersibility in solvent. A dual solvent system containing high boiling point solvent ethylene glycol and low boiling point solvent

ethanol (ration 1:1) could result in a uniform printed layer. The resultant high-concentration ink can be stored for months under ambient conditions with minimal aggregation.

9.2 Future Work

Due to the restriction of time and equipment, future investigations are encouraged to continue in the following aspects:

9.2.1 Ceramic-Metal-Polymer nanocomposites

Current research utilized ceramic (BT)/polymer composite as the capacitance layer of antenna and capacitors. Metal-polymer composites usually exhibit a high dielectric constant (over 1000), but also a high dielectric loss. In comparison, ceramic-metal-polymer composites would improve the dielectric constant while persevering the low dielectric loss. In the future, ceramic-metal-polymer composite ink can be prepared to further improve the performance of the printed antenna and capacitor.

9.2.2 Nickel Inkjet Printing Ink

Ni inkjet printing ink was prepared using ball milling in this study. In the future, nanoparticle surface treatment and dispersants should be investigated to achieve better dispersion and stability.

9.2.3 Barium Titanate Nanoparticles Doping

During high-temperature sintering conditions, the defects of the BT crystal structure reduced the dielectric properties. Moreover, a reducing atmosphere caused oxygen vacancies. To enhance dielectric properties of the barium titanate printed layer, dopant such as MnO, CaO, BaO and rare

earth oxides such as Y_2O_3 , Dy_2O_3 , Ho_2O_3 , Er_2O_3 , can be added to stabilize barium titanate NPs and reduce the oxygen vacancies and crystal defects.

10 Reference

1. Pan, M.-J.; Randall, C. A., A brief introduction to ceramic capacitors. *IEEE Electrical Insulation Magazine* **2010**, 26 (3), 44-50.
2. Van Langenhove, L., *Smart textiles for medicine and healthcare: materials, systems and applications*. Elsevier: 2007.
3. Hu, J.; Meng, H.; Li, G.; Ibekwe, S. I., A review of stimuli-responsive polymers for smart textile applications. *Smart Materials and Structures* **2012**, 21 (5), 053001.
4. Cherenack, K.; van Pieterse, L., Smart textiles: Challenges and opportunities. *Journal of Applied Physics* **2012**, 112 (9), 091301.
5. Çelikel, D. C., Smart e-textile materials. In *Advanced Functional Materials*, IntechOpen: 2020.
6. Inui, T.; Koga, H.; Nogi, M.; Komoda, N.; Suganuma, K., A miniaturized flexible antenna printed on a high dielectric constant nanopaper composite. *Advanced Materials* **2015**, 27 (6), 1112-1116.
7. Shukla, A.; Banerjee, A.; Ravikumar, M.; Jalajakshi, A., Electrochemical capacitors: Technical challenges and prognosis for future markets. *Electrochimica acta* **2012**, 84, 165-173.
8. Sinclair, I., *Passive components for circuit design*. Elsevier: 2000.
9. Zhou, Y.; Soltani, S.; Li, B. M.; Wu, Y.; Kim, I.; Soewardiman, H.; Werner, D. H.; Jur, J. S., Direct-write spray coating of a full-duplex antenna for e-textile applications. *Micromachines* **2020**, 11 (12), 1056.
10. Arlt, G.; Hennings, D.; de With, G., Dielectric properties of fine-grained barium titanate ceramics. *Journal of Applied Physics* **1985**, 58 (4), 1619-1625.

11. Kamyshny, A., Metal-based inkjet inks for printed electronics. *The Open Applied Physics Journal* **2011**, *4* (1), 19-36.
12. Lis, M.; Plaut, M.; Zai, A.; Cipolle, D.; Russo, J.; Fedynyshyn, T., High performance, 3D-printable dielectric nanocomposites for millimeter wave devices. *ACS Applied Materials & Interfaces* **2016**, *8* (49), 34019-34026.
13. Kelly, A. G.; Finn, D.; Harvey, A.; Hallam, T.; Coleman, J. N., All-printed capacitors from graphene-BN-graphene nanosheet heterostructures. *Applied Physics Letters* **2016**, *109* (2), 023107.
14. McPhee, K., An introduction to inorganic dielectrics. *IRE Transactions on Component Parts* **1959**, *6* (1), 3-33.
15. Navrotsky, A., Energetics and crystal chemical systematics among ilmenite, lithium niobate, and perovskite structures. *Chemistry of Materials* **1998**, *10* (10), 2787-2793.
16. Yao, Y.; Li, Y.; Sun, N.; Du, J.; Li, X.; Zhang, L.; Zhang, Q.; Hao, X., High energy-storage performance of BNT-BT-NN ferroelectric thin films prepared by RF magnetron sputtering. *Journal of Alloys and Compounds* **2018**, *750*, 228-234.
17. Wu, M.; Zhang, C.; Yu, S.; Li, L., Effect of sputtering pressure on structural and dielectric tunable properties of BaSn_{0.15}Ti_{0.85}O₃ thin films grown by magnetron sputtering. *Ceramics International* **2018**, *44* (9), 10236-10240.
18. Ihlefeld, J. F.; Borland, W. J.; Maria, J.-P., Dielectric and microstructural properties of barium titanate hafnate thin films. *Thin Solid Films* **2008**, *516* (10), 3162-3166.
19. Scott, J., Applications of modern ferroelectrics. *science* **2007**, *315* (5814), 954-959.

20. Randall, C.; Newnham, R.; Cross, L., History of the first ferroelectric oxide, BaTiO₃. *Materials Research Institute, The Pennsylvania State University, University Park, Pa, USA* **2004**, 1-11.
21. Barber, P.; Balasubramanian, S.; Anguchamy, Y.; Gong, S.; Wibowo, A.; Gao, H.; Ploehn, H. J.; Zur Loye, H.-C., Polymer composite and nanocomposite dielectric materials for pulse power energy storage. *Materials* **2009**, *2* (4), 1697-1733.
22. Blinc, R., Order and disorder in perovskites and relaxor ferroelectrics. In *Ferro-and Antiferroelectricity*, Springer: 2007; pp 51-67.
23. Nalwa, H. S., *Handbook of low and high dielectric constant materials and their applications, two-volume set*. Elsevier: 1999.
24. Dang, Z.-M.; Zhou, T.; Yao, S.-H.; Yuan, J.-K.; Zha, J.-W.; Song, H.-T.; Li, J.-Y.; Chen, Q.; Yang, W.-T.; Bai, J., Advanced calcium copper titanate/polyimide functional hybrid films with high dielectric permittivity. *Advanced Materials* **2009**, *21* (20), 2077-2082.
25. Pan, S.; Zhang, Z.; Weng, W.; Lin, H.; Yang, Z.; Peng, H., Miniature wire-shaped solar cells, electrochemical capacitors and lithium-ion batteries. *Materials Today* **2014**, *17* (6), 276-284.
26. Kang, H.; Kitsomboonloha, R.; Jang, J.; Subramanian, V., High-performance printed transistors realized using femtoliter gravure-printed sub-10 μm metallic nanoparticle patterns and highly uniform polymer dielectric and semiconductor layers. *Advanced Materials* **2012**, *24* (22), 3065-3069.

27. Khan, S.; Lorenzelli, L.; Dahiya, R. S., Technologies for printing sensors and electronics over large flexible substrates: a review. *IEEE Sensors Journal* **2015**, *15* (6), 3164-3185.
28. Lee, Y.-H.; Kim, J.-S.; Noh, J.; Lee, I.; Kim, H. J.; Choi, S.; Seo, J.; Jeon, S.; Kim, T.-S.; Lee, J.-Y.; Choi, J. W., Wearable textile battery rechargeable by solar energy. *Nano Letters* **2013**, *13* (11), 5753-5761.
29. Pu, X.; Liu, M.; Li, L.; Han, S.; Li, X.; Jiang, C.; Du, C.; Luo, J.; Hu, W.; Wang, Z. L., Wearable textile-based in-plane microsupercapacitors. *Advanced Energy Materials* **2016**, *6* (24), 1601254.
30. Yong, S.; Shi, J.; Beeby, S., Wearable textile power module based on flexible ferroelectret and supercapacitor. *Energy Technology* **2019**, *7* (5), 1800938.
31. Jia, Y.; Shen, L.; Liu, J.; Zhou, W.; Du, Y.; Xu, J.; Liu, C.; Zhang, G.; Zhang, Z.; Jiang, F., An efficient PEDOT-coated textile for wearable thermoelectric generators and strain sensors. *Journal of Materials Chemistry C* **2019**, *7* (12), 3496-3502.
32. Tebyetekerwa, M.; Marriam, I.; Xu, Z.; Yang, S.; Zhang, H.; Zabihi, F.; Jose, R.; Peng, S.; Zhu, M.; Ramakrishna, S., Critical insight: challenges and requirements of fibre electrodes for wearable electrochemical energy storage. *Energy & Environmental Science* **2019**.
33. Bussey, H. E., Measurement of RF properties of materials a survey. *Proceedings of the IEEE* **1967**, *55* (6), 1046-1053.
34. Bayram, Y.; Zhou, Y.; Shim, B. S.; Xu, S.; Zhu, J.; Kotov, N. A.; Volakis, J. L., E-textile conductors and polymer composites for conformal lightweight antennas. *IEEE Transactions on Antennas and Propagation* **2010**, *58* (8), 2732-2736.

35. Salonen, P.; Keskilammi, M.; Rantanen, J.; Sydanheimo, L. In *A novel Bluetooth antenna on flexible substrate for smart clothing*, IEEE International Conference on Systems, Man & Cybernetics, 2001; IEEE: 2001; pp 789-794.
36. Zhang, Z.; Ren, X.; Peng, B.; Wang, Z.; Wang, X.; Pei, K.; Shan, B.; Miao, Q.; Chan, P. K. L., Direct patterning of self-assembled monolayers by stamp printing method and applications in high performance organic field-effect transistors and complementary inverters. *Advanced Functional Materials* **2015**, *25* (38), 6112-6121.
37. Lee, T.-M.; Han, H.-S.; Kim, B.; Kwak, S.-W.; Noh, J.-H.; Kim, I., Roll offset printing process based on interface separation for fine and smooth patterning. *Thin Solid Films* **2013**, *548*, 566-571.
38. Perl, A.; Reinhoudt, D. N.; Huskens, J., Microcontact printing: limitations and achievements. *Advanced Materials* **2009**, *21* (22), 2257-2268.
39. Stempien, Z.; Rybicki, E.; Rybicki, T.; Lesnikowski, J., Inkjet-printing deposition of silver electro-conductive layers on textile substrates at low sintering temperature by using an aqueous silver ions-containing ink for textronic applications. *Sensors and Actuators B: Chemical* **2016**, *224*, 714-725.
40. Huang, Q.; Zhu, Y., Printing conductive nanomaterials for flexible and stretchable electronics: A review of materials, processes, and applications. *Advanced Materials Technologies* **2019**, *4* (5), 1800546.
41. Cao, X.; Chen, H.; Gu, X.; Liu, B.; Wang, W.; Cao, Y.; Wu, F.; Zhou, C., Screen Printing as a scalable and low-cost approach for rigid and flexible thin-film transistors using separated carbon nanotubes. *ACS Nano* **2014**, *8* (12), 12769-12776.

42. Stempien, Z.; Rybicki, E.; Patykowska, A.; Rybicki, T.; Szykowska, M., Shape-programmed inkjet-printed silver electro-conductive layers on textile surfaces. *Journal of Industrial Textiles* **2018**, *47* (6), 1321-1341.
43. Ding, X.; Liu, J.; Harris, T. A., A review of the operating limits in slot die coating processes. *AIChE Journal* **2016**, *62* (7), 2508-2524.
44. Secor, E. B.; Lim, S.; Zhang, H.; Frisbie, C. D.; Francis, L. F.; Hersam, M. C., Gravure printing of graphene for large-area flexible electronics. *Advanced materials* **2014**, *26* (26), 4533-4538.
45. Kopola, P.; Aernouts, T.; Guillerez, S.; Jin, H.; Tuomikoski, M.; Maaninen, A.; Hast, J., High efficient plastic solar cells fabricated with a high-throughput gravure printing method. *Solar Energy Materials and Solar Cells* **2010**, *94* (10), 1673-1680.
46. Pudas, M.; Hagberg, J.; Leppävuori, S., Printing parameters and ink components affecting ultra-fine-line gravure-offset printing for electronics applications. *Journal of the European Ceramic Society* **2004**, *24* (10-11), 2943-2950.
47. Kipphan, H., *Handbook of print media: technologies and production methods*. Springer Science & Business Media: 2001.
48. Almusallam, A.; Yang, K.; Zhu, D.; Torah, R. N.; Komolafe, A.; Tudor, J.; Beeby, S. P., Clamping effect on the piezoelectric responses of screen-printed low temperature PZT/Polymer films on flexible substrates. *Smart Materials and Structures* **2015**, *24* (11), 115030.
49. Kanungo, M.; Grigoryev, A.; Wantuck, P. J.; Gervasi, D. J.; Badesha, S. S., Imaging member for offset printing applications. Google Patents: 2016.

50. Fukuda, K.; Yoshimura, Y.; Okamoto, T.; Takeda, Y.; Kumaki, D.; Katayama, Y.; Tokito, S., Reverse-offset printing optimized for scalable organic thin-film transistors with submicrometer channel lengths. *Advanced Electronic Materials* **2015**, *1* (8), 1500145.
51. Darhuber, A. A.; Troian, S. M.; Wagner, S., Physical mechanisms governing pattern fidelity in microscale offset printing. *Journal of Applied Physics* **2001**, *90* (7), 3602-3609.
52. Kusaka, Y.; Mizukami, M.; Yamaguchi, T.; Fukuda, N.; Ushijima, H., Patterning defects in high-speed reverse offset printing: lessons from contact dynamics. *Journal of Micromechanics and Microengineering* **2019**, *29* (4), 045001.
53. Hösel, M.; Søndergaard, R. R.; Angmo, D.; Krebs, F. C., Comparison of fast roll-to-roll flexographic, inkjet, flatbed, and rotary screen printing of metal back electrodes for polymer solar cells. *Advanced engineering materials* **2013**, *15* (10), 995-1001.
54. Brumm, P.; Sauer, H. M.; Dörsam, E., Scaling behavior of pattern formation in the flexographic ink splitting process. *Colloids and Interfaces* **2019**, *3* (1), 37.
55. Lupo, D.; Clemens, W.; Breitung, S.; Hecker, K., OE-A roadmap for organic and printed electronics. In *Applications of Organic and Printed Electronics*, Springer: 2013; pp 1-26.
56. Moonen, P. F.; Yakimets, I.; Huskens, J., Fabrication of transistors on flexible substrates: from mass-printing to high-resolution alternative lithography strategies. *Advanced materials* **2012**, *24* (41), 5526-5541.
57. Ruiz, S. A.; Chen, C. S., Microcontact printing: A tool to pattern. *Soft Matter* **2007**, *3* (2), 168-177.

58. Quist, A. P.; Pavlovic, E.; Oscarsson, S., Recent advances in microcontact printing. *Analytical and bioanalytical chemistry* **2005**, *381* (3), 591-600.
59. Hyun, W. J.; Secor, E. B.; Hersam, M. C.; Frisbie, C. D.; Francis, L. F., High-resolution patterning of graphene by screen printing with a silicon stencil for highly flexible printed electronics. *Advanced Materials* **2015**, *27* (1), 109-115.
60. Riemer, D. E., The theoretical fundamentals of the screen printing process. *Microelectronics International* **1989**.
61. Li, Y.; Torah, R.; Beeby, S.; Tudor, J. In *An all-inkjet printed flexible capacitor on a textile using a new poly(4-vinylphenol) dielectric ink for wearable applications*, 2012 IEEE Sensors, 10/2012; IEEE: 2012; pp 1-4.
62. Ko, S. H.; Pan, H.; Grigoropoulos, C. P.; Luscombe, C. K.; Fréchet, J. M.; Poulidakos, D., All-inkjet-printed flexible electronics fabrication on a polymer substrate by low-temperature high-resolution selective laser sintering of metal nanoparticles. *Nanotechnology* **2007**, *18* (34), 345202.
63. Lim, J.; Kim, J.; Yoon, Y. J.; Kim, H.; Yoon, H. G.; Lee, S.-N.; Kim, J., All-inkjet-printed metal-insulator-metal (MIM) capacitor. *Current Applied Physics* **2012**, *12*, e14-e17.
64. Magdassi, S., *The chemistry of inkjet inks*. World Scientific: 2010.
65. Li, J.; Mishukova, V.; Östling, M., All-solid-state micro-supercapacitors based on inkjet printed graphene electrodes. *Applied Physics Letters* **2016**, *109* (12), 123901.
66. Ning, H.; Tao, R.; Fang, Z.; Cai, W.; Chen, J.; Zhou, Y.; Zhu, Z.; Zheng, Z.; Yao, R.; Xu, M.; Wang, L.; Lan, L.; Peng, J., Direct patterning of silver electrodes with

- 2.4 μm channel length by piezoelectric inkjet printing. *Journal of Colloid and Interface Science* **2017**, *487*, 68-72.
67. Li, R. a.; Zhang, Y.; Cao, Y.; Liu, Z., Ink penetration of uncoated inkjet paper and impact on printing quality. *BioResources* **2015**, *10* (4).
68. Wheeler, J. S. R.; Yeates, S. G., Polymers in inkjet printing. In *Fundamentals of Inkjet Printing*, Hoath, S. D., Ed. Wiley-VCH Verlag GmbH & Co. KGaA: Weinheim, Germany, 2015; pp 117-140.
69. Bevione, M.; Chiolerio, A., Benchmarking of inkjet printing methods for combined throughput and performance. *Advanced Engineering Materials* **2020**, 2000679.
70. McIlroy, C.; Harlen, O.; Morrison, N., Modelling the jetting of dilute polymer solutions in drop-on-demand inkjet printing. *Journal of Non-Newtonian Fluid Mechanics* **2013**, *201*, 17-28.
71. Kim, D. S.; Kim, J. S.; Lee, M. C., Thin film forming technique based on hybrid spray coating using electrostatic force and air pressure. *Japanese Journal of Applied Physics* **2014**, *53* (5S3), 05HC08.
72. Abdellah, A.; Fabel, B.; Lugli, P.; Scarpa, G., Spray deposition of organic semiconducting thin-films: Towards the fabrication of arbitrary shaped organic electronic devices. *Organic Electronics* **2010**, *11* (6), 1031-1038.
73. Blake, T. D., The physics of moving wetting lines. *Journal of colloid and interface science* **2006**, *299* (1), 1-13.
74. Laurila, M.-M.; Khorramdel, B.; Mantysalo, M., Combination of E-jet and inkjet printing for additive fabrication of multilayer high-density RDL of silicon interposer. *IEEE Transactions on Electron Devices* **2017**, *64* (3), 1217-1224.

75. Salim, A.; Lim, S., Review of recent inkjet-printed capacitive tactile sensors. *Sensors* **2017**, *17* (11), 2593.
76. Li, Y.-P.-Q. Y.; Yi, Inkjet conductive inks for printing textile materials and applications. *Journal of Fiber Bioengineering and Informatics* **2019**, *12* (1), 11-24.
77. Kettle, J.; Lamminmäki, T.; Gane, P., A review of modified surfaces for high speed inkjet coating. *Surface and Coatings Technology* **2010**, *204* (12-13), 2103-2109.
78. Yang, L.; Rida, A.; Vyas, R.; Tentzeris, M. M., RFID tag and RF structures on a paper substrate using inkjet-printing technology. *IEEE Transactions on Microwave Theory and Techniques* **2007**, *55* (12), 2894-2901.
79. Yang, L.; Tentzeris, M. M. In *Design and Characterization of Novel Paper-based Inkjet-Printed RFID and Microwave Structures for Telecommunication and Sensing Applications*, 2007 International Microwave Symposium (IMS 2007), 6/2007; IEEE: 2007; pp 1633-1636.
80. Kim, I.; Shahariar, H.; Ingram, W. F.; Zhou, Y.; Jur, J. S., Inkjet process for conductive patterning on textiles: maintaining inherent stretchability and breathability in knit structures. *Advanced Functional Materials* **2019**, *29* (7), 1807573.
81. Yang-Pei-Qi Yi, Y. L., Inkjet conductive inks for printing textile materials and applications. *Journal of Fiber Bioengineering and Informatics* **2019**, *12* (1), 11-24.
82. Sowade, E.; Mitra, K. Y.; Ramon, E.; Martinez-Domingo, C.; Villani, F.; Loffredo, F.; Gomes, H. L.; Baumann, R. R., Up-scaling of the manufacturing of all-inkjet-printed organic thin-film transistors: Device performance and manufacturing yield of transistor arrays. *Organic Electronics* **2016**, *30*, 237-246.

83. Mattana, G.; Loi, A.; Woytasik, M.; Barbaro, M.; Noël, V.; Piro, B., Inkjet-printing: A new fabrication technology for organic transistors. *Advanced Materials Technologies* **2017**, 2 (10), 1700063.
84. Derby, B., Inkjet printing of functional and structural materials: fluid property requirements, feature stability, and resolution. *Annual Review of Materials Research* **2010**, 40 (1), 395-414.
85. El-Molla, S. Inkjet printing & spray deposition techniques for flexible electronic applications. Technische Universität München, 2017.
86. Pucci, K., What Is a Waveform. Imagexpert Web site. <https://imagexpert.com/what-is-a-waveform/>.(accessed 0621,2021)
87. FUJIFILM Dimatix Ink Tutorial
88. Street, R. A.; Wong, W. S.; Ready, S. E.; Chabinyk, M. L.; Arias, A. C.; Limb, S.; Salleo, A.; Lujan, R., Jet printing flexible displays. *Materials Today* **2006**, 9 (4), 32-37.
89. Ning, H.; Tao, R.; Fang, Z.; Cai, W.; Chen, J.; Zhou, Y.; Zhu, Z.; Zheng, Z.; Yao, R.; Xu, M., Direct patterning of silver electrodes with 2.4 μm channel length by piezoelectric inkjet printing. *Journal of colloid and interface science* **2017**, 487, 68-72.
90. Singh, M.; Haverinen, H. M.; Dhagat, P.; Jabbour, G. E., Inkjet printing-process and its applications. *Advanced Materials* **2010**, 22 (6), 673-685.
91. Fromm, J. E., Numerical calculation of the fluid dynamics of drop-on-demand jets. *IBM Journal of Research and Development* **1984**, 28 (3), 322-333.

92. Zhou, L. Y.; Fu, J.; He, Y., A review of 3D printing technologies for soft polymer materials. *Advanced Functional Materials* **2020**, 2000187.
93. Bergeron, V.; Bonn, D.; Martin, J. Y.; Vovelle, L., Controlling droplet deposition with polymer additives. *Nature* **2000**, 405 (6788), 772-775.
94. Jang, D.; Kim, D.; Moon, J., Influence of fluid physical properties on ink-jet printability. *Langmuir* **2009**, 25 (5), 2629-2635.
95. Kim, D.; Jeong, S.; Park, B. K.; Moon, J., Direct writing of silver conductive patterns: Improvement of film morphology and conductance by controlling solvent compositions. *Applied Physics Letters* **2006**, 89 (26), 264101.
96. Liu, M.; Wang, J.; He, M.; Wang, L.; Li, F.; Jiang, L.; Song, Y., Inkjet printing controllable footprint lines by regulating the dynamic wettability of coalescing ink droplets. *ACS Applied Materials & Interfaces* **2014**, 6 (16), 13344-13348.
97. Soltman, D.; Subramanian, V., Inkjet-printed line morphologies and temperature control of the coffee ring effect. *Langmuir* **2008**, 24 (5), 2224-2231.
98. Kumar Singh, V.; Mazhari, B., Impact of scaling of dielectric thickness on mobility in top-contact pentacene organic thin film transistors. *Journal of Applied Physics* **2012**, 111 (3), 034905.
99. Mao, C. X.; Zhou, Y.; Wu, Y.; Soewardiman, H.; Werner, D. H.; Jur, J. S., Low-profile strip-loaded textile antenna with enhanced bandwidth and isolation for full-duplex wearable applications. *IEEE Transactions on Antennas and Propagation* **2020**, 1-1.

100. Scarpello, M. L.; Kazani, I.; Hertleer, C.; Rogier, H.; Vande Ginste, D., Stability and efficiency of screen-printed wearable and washable antennas. *IEEE Antennas and Wireless Propagation Letters* **2012**, *11*, 838-841.
101. Yuehui, O.; Karayianni, E.; Chappell, W. J. In *Effect of Fabric Patterns on Electrotexile Patch Antennas*, 2005 IEEE Antennas and Propagation Society International Symposium, 2005; IEEE: 2005; pp 246-249.
102. Subramaniam, S.; Gupta, B., Design and development of flexible fabric antenna for body-worn applications and its performance study under flat and bent positions. *Microwave and Optical Technology Letters* **2011**, *53* (9), 2004-2011.
103. Sankaralingam, S.; Gupta, B., Determination of dielectric constant of fabric materials and their use as substrates for design and development of antennas for wearable applications. *IEEE Transactions on Instrumentation and Measurement* **2010**, *59* (12), 3122-3130.
104. Salonen, P.; Rahmat-Samii, Y.; Schaffrath, M.; Kivikoski, M. In *Effect of textile materials on wearable antenna performance: A case study of GPS antennas*, IEEE Antennas and Propagation Society Symposium, 2004., IEEE: 2004; pp 459-462.
105. Cosker, M.; Lizzi, L.; Ferrero, F.; Staraj, R.; Ribero, J.-M., Realization of 3-D flexible antennas using liquid metal and additive printing technologies. *IEEE Antennas and Wireless Propagation Letters* **2016**, *16*, 971-974.
106. Wang, Z.; Zhang, L.; Bayram, Y.; Volakis, J. L., Embroidered conductive fibers on polymer composite for conformal antennas. *IEEE Transactions on Antennas and Propagation* **2012**, *60* (9), 4141-4147.

107. Wang, Z.; Lee, L. Z.; Psychoudakis, D.; Volakis, J. L., Embroidered multiband body-worn antenna for GSM/PCS/WLAN communications. *IEEE Transactions on Antennas and Propagation* **2014**, *62* (6), 3321-3329.
108. Volakis, J. L.; Zhang, L.; Wang, Z.; Bayram, Y. In *Embroidered flexible RF electronics*, 2012 IEEE International Workshop on Antenna Technology (iWAT), IEEE: 2012; pp 8-11.
109. Mao, C.-X.; Vital, D.; Werner, D. H.; Wu, Y.; Bhardwaj, S., Dual-polarized embroidered textile armband antenna array with omnidirectional radiation for on-/off-body wearable applications. *IEEE Transactions on Antennas and Propagation* **2019**, *68* (4), 2575-2584.
110. Locher, I.; Klemm, M.; Kirstein, T.; Troster, G., Design and characterization of purely textile patch antennas. *IEEE Transactions on Advanced Packaging* **2006**, *29* (4), 777-788.
111. Gupta, B.; Sankaralingam, S.; Dhar, S. In *Development of wearable and implantable antennas in the last decade: A review*, 2010 10th Mediterranean Microwave Symposium (MMS), 08/2010; IEEE: 2010; pp 251-267.
112. Chauraya, A.; Whittow, W. G.; Vardaxoglou, J. Y. C.; Li, Y.; Torah, R.; Yang, K.; Beeby, S.; Tudor, J., Inkjet printed dipole antennas on textiles for wearable communications. *IET Microwaves, Antennas & Propagation* **2013**, *7* (9), 760-767.
113. Ahmad, W.; Budimir, D. In *Inkjet-printed antennas for 28 GHz 5G applications*, 2016 Asia-Pacific Microwave Conference (APMC), 2016/12//; IEEE: 2016; pp 1-4.

114. Dancila, D.; Moossavi, R.; Siden, J.; Zhang, Z.; Rydberg, A., Antennas on paper using ink-jet printing of nano-silver particles for wireless sensor networks in train environment. *Microwave and Optical Technology Letters* **2016**, *58* (4), 754-759.
115. Mao, C.-X.; Vital, D.; Werner, D. H.; Wu, Y.; Bhardwaj, S., Dual-polarized embroidered textile armband antenna array with omnidirectional radiation for on-/off-body wearable applications. *IEEE Transactions on Antennas and Propagation* **2020**, *68* (4), 2575-2584.
116. Tudor, J.; Vardaxoglou, J. C.; Torah, R.; Li, Y.; Whittow, W. G.; Chauraya, A.; Beeby, S.; Yang, K., Inkjet printed dipole antennas on textiles for wearable communications. *IET Microwaves, Antennas & Propagation* **2013**, *7* (9), 760-767.
117. Saleh, G.; Sibaii, F.; Alashban, N.; Alkhateeb, H.; Hegazi, F.; Hegazi, M., Effects of tissues and geometric shapes of phantoms on the specific energy absorption rate. *International Journal of RF and Microwave Computer-Aided Engineering* **2018**, *28* (3), e21252.
118. Kaivanto, E. K.; Berg, M.; Salonen, E.; de Maagt, P., Wearable circularly polarized antenna for personal satellite communication and navigation. *IEEE Transactions on Antennas and Propagation* **2011**, *59* (12), 4490-4496.
119. Shin, K. Y.; Hong, J. Y.; Jang, J., Micropatterning of graphene sheets by inkjet printing and its wideband dipole-antenna application. *Advanced materials* **2011**, *23* (18), 2113-2118.
120. Cook, B. S.; Shamim, A., Inkjet printing of novel wideband and high gain antennas on low-cost paper substrate. *IEEE Transactions on Antennas and Propagation* **2012**, *60* (9), 4148-4156.

121. Eom, S.-H.; Seo, Y.; Lim, S., Pattern switchable antenna system using inkjet-printed directional bow-tie for bi-direction sensing applications. *Sensors* **2015**, *15* (12), 31171-31179.
122. Mäntysalo, M.; Mansikkamäki, P., An inkjet-deposited antenna for 2.4 GHz applications. *AEU-International Journal of Electronics and Communications* **2009**, *63* (1), 31-35.
123. Ahmad, W.; Budimir, D. In *Inkjet-printed antennas for 28 GHz 5G applications*, 2016/12//; IEEE: 2016; pp 1-4.
124. Sa'don, S. N. H.; Jamaluddin, M. H.; Kamarudin, M. R.; Ahmad, F.; Dahlan, S. H., A 5G graphene antenna produced by screen printing method. *Indones. J. Electr. Eng. Comput. Sci* **2019**, *15*, 950-1055.
125. Brebels, S.; Ryckaert, J.; Come, B.; Donnay, S.; Walter De, R.; Beyne, E.; Mertens, R. P., SOP integration and codesign of antennas. *IEEE Transactions on Advanced Packaging* **2004**, *27* (2), 341-351.
126. Salvado, R.; Loss, C.; Gonçalves, R.; Pinho, P., Textile materials for the design of wearable antennas: A survey. *Sensors* **2012**, *12* (11), 15841-15857.
127. Byungje, L.; Harackiewicz, F. J., Miniature microstrip antenna with a partially filled high-permittivity substrate. *IEEE Transactions on Antennas and Propagation* **2002**, *50* (8), 1160-1162.
128. Lo, T.; Hwang, Y.; Lam, E.; Lee, B., Miniature aperture-coupled microstrip antenna of very high permittivity. *Electronics Letters* **1997**, *33* (1), 9-10.
129. Salonen, P.; Rahmat-Samii, Y.; Schaffrath, M.; Kivikoski, M. In *Effect of textile materials on wearable antenna performance: a case study of GPS antennas*, IEEE

- Antennas and Propagation Society Symposium, 2004., 2004; IEEE: 2004; pp 459-462
Vol.1.
130. Hertleer, C.; Rogier, H.; Vallozzi, L.; Van Langenhove, L., A textile antenna for off-body communication integrated into protective clothing for firefighters. *IEEE Transactions on Antennas and Propagation* **2009**, 57 (4), 919-925.
 131. Balanis, C. A., *Antenna theory: analysis and design*. John wiley & sons: 2016.
 132. Zavosh, F.; Aberle, J. T., Improving the performance of microstrip-patch antennas. *IEEE Antennas and Propagation Magazine* **1996**, 38 (4), 7-12.
 133. Dwivedi, S., Analysis and simulation of sierpinski carpet type fractal multiband antenna for wide band applications. *International Journal of Electronics Communication and Computer Engineering* **2014**, 6 (4), 460-462.
 134. Stevens, J.; Geiculescu, A.; Strange, T. In *Dielectric aluminum oxides: Nanostructural features and composites*, CARTS-CONFERENCE, COMPONENTS TECHNOLOGY INSTITUTE INC.: 2007; p 63.
 135. Kárník, T., Niobium oxide for capacitor manufacturing. URL: http://www.metal2012.com/files/proceedings/metal_08/Lists/Papers/087.pdf (дата обращения 01.10.2012) **2008**.
 136. Palneedi, H.; Peddigari, M.; Hwang, G.-T.; Jeong, D.-Y.; Ryu, J., High-performance dielectric ceramic films for energy storage capacitors: Progress and outlook. *Advanced Functional Materials* **2018**, 28 (42), 1803665.
 137. Wang, Y.; Song, Y.; Xia, Y., Electrochemical capacitors: Mechanism, materials, systems, characterization and applications. *Chemical Society Reviews* **2016**, 45 (21), 5925-5950.

138. Zhang, M.; Zhao, M.; Jian, M.; Wang, C.; Yu, A.; Yin, Z.; Liang, X.; Wang, H.; Xia, K.; Liang, X., Printable smart pattern for multifunctional energy-management e-textile. *Matter* **2019**, *1* (1), 168-179.
139. Pu, X.; Li, L.; Liu, M.; Jiang, C.; Du, C.; Zhao, Z.; Hu, W.; Wang, Z. L., Wearable self-charging power textile based on flexible yarn supercapacitors and fabric nanogenerators. *Advanced Materials* **2016**, *28* (1), 98-105.
140. Jost, K.; Dion, G.; Gogotsi, Y., Textile energy storage in perspective. *Journal of Materials Chemistry A* **2014**, *2* (28), 10776.
141. Abe, K.; Nagao, D.; Konno, M., Fabrication of highly refractive BaTiO₃ nanocomposite films using heat resistant polymer as matrix. *European Polymer Journal* **2013**, *49* (11), 3455-3459.
142. Popielarz, R.; Chiang, C. K.; Nozaki, R.; Obrzut, J., Dielectric properties of polymer/ferroelectric ceramic composites from 100 Hz to 10 GHz. *Macromolecules* **2001**, *34* (17), 5910-5915.
143. McMorrow, B.; Chartoff, R.; Lucas, P.; Richardson, W.; Anderson, P., Particle surface treatment for nanocomposites containing ceramic particles. *Composite Interfaces* **2006**, *13* (8-9), 801-817.
144. Xie, S.-H.; Zhu, B.-K.; Wei, X.-Z.; Xu, Z.-K.; Xu, Y.-Y., Polyimide/BaTiO₃ composites with controllable dielectric properties. *Composites Part A: Applied Science and Manufacturing* **2005**, *36* (8), 1152-1157.
145. Ye, H.-J.; Shao, W.-Z.; Zhen, L., Tetradecylphosphonic acid modified BaTiO₃ nanoparticles and its nanocomposite. *Colloids and Surfaces A: Physicochemical and Engineering Aspects* **2013**, *427*, 19-25.

146. Mukherjee, N.; Wavhal, D.; Timmons, R. B., Composites of plasma surface functionalized barium titanate nanoparticles covalently attached to epoxide matrices: Synthesis and evaluation. *ACS Applied Materials & Interfaces* **2010**, *2* (2), 397-407.
147. Ihlefeld, J. F.; Borland, W. J.; Maria, J.-P., Enhanced dielectric and crystalline properties in ferroelectric barium titanate thin films. *Advanced Functional Materials* **2007**, *17* (7), 1199-1203.
148. Dang, Z. M.; Lin, Y. Q.; Xu, H. P.; Shi, C. Y.; Li, S. T.; Bai, J., Fabrication and dielectric characterization of advanced BaTiO₃/polyimide nanocomposite films with high thermal stability. *Advanced Functional Materials* **2008**, *18* (10), 1509-1517.
149. Lichtenecker, K., Die dielektrizitätskonstante natürlicher und künstlicher mischkörper. *Physikalische Zeitschrift* **1926**, *27*, 115-158.
150. Simpkin, R., Derivation of Lichtenecker's logarithmic mixture formula from Maxwell's equations. *IEEE Transactions on Microwave Theory and Techniques* **2010**, *58* (3), 545-550.
151. Hernández-López, A.; Aguilar-Garib, J.; Guillemet-Fritsch, S.; Nava-Quintero, R.; Dufour, P.; Tenailleau, C.; Durand, B.; Valdez-Nava, Z., Reliability of X7R multilayer ceramic capacitors during high accelerated life testing (HALT). *Materials* **2018**, *11* (10), 1900.
152. Liu, X.; Li, Y.; Sun, N.; Hao, X., High energy-storage performance of PLZS antiferroelectric multilayer ceramic capacitors. *Inorganic Chemistry Frontiers* **2020**, *7* (3), 756-764.
153. Yoon, J.; Shin, D.; Jeong, D.; Lee, H., Control of connectivity of Ni electrode with heating rates during sintering and electrical properties in BaTiO₃ based multilayer

- ceramic capacitors. *Transactions on electrical and electronic materials* **2012**, *13* (4), 181-184.
154. Wang, D.; Zhou, D.; Song, K.; Feteira, A.; Randall, C. A.; Reaney, I. M., Cold-sintered COG multilayer ceramic capacitors. *Advanced Electronic Materials* **2019**, *5* (7), 1900025.
155. Jia, W.; Hou, Y.; Zheng, M.; Xu, Y.; Zhu, M.; Yang, K.; Cheng, H.; Sun, S.; Xing, J., Advances in lead-free high-temperature dielectric materials for ceramic capacitor application. *IET Nanodielectrics* **2018**, *1* (1), 3-16.
156. Brown, D., Multilayer ceramic capacitors: Mitigating rising failure rates. 7.
157. Cai, Z.; Zhu, C.; Wang, H.; Zhao, P.; Chen, L.; Li, L.; Wang, X., High-temperature lead-free multilayer ceramic capacitors with ultrahigh energy density and efficiency fabricated via two-step sintering. *Journal of Materials Chemistry A* **2019**, *7* (24), 14575-14582.
158. Reinheimer, T.; Baumann, V.; Binder, J. R., Fabrication of flexible multilayer composite capacitors using inkjet printing. *Nanomaterials* **2020**, *10* (11), 2302.
159. Jiang, W.; Hu, Y.; Bao, S.; Lijie, S.; Yuwei, Z.; Cui, Y.; Qiang, L. In *Analysis on the causes of decline of MLCC insulation resistance*, 2015 16th International Conference on Electronic Packaging Technology (ICEPT), 8/2015; IEEE: 2015; pp 1255-1257.
160. Lee, W.-H.; Su, C.-Y., Improvement in the temperature stability of a BaTiO₃-based multilayer ceramic capacitor by constrained sintering. *Journal of the American Ceramic Society* **2007**, *90* (10), 3345-3348.

161. Werner, D. H.; Jiang, Z. H., *Electromagnetics of body area networks: antennas, propagation, and RF systems*. John Wiley & Sons: 2016.
162. Jiang, Z. H.; Brocker, D. E.; Sieber, P. E.; Werner, D. H., A compact, low-profile metasurface-enabled antenna for wearable medical body-area network devices. *IEEE Transactions on Antennas and Propagation* **2014**, *62* (8), 4021-4030.
163. Li, B. M.; Yildiz, O.; Mills, A. C.; Flewellin, T. J.; Bradford, P. D.; Jur, J. S., Iron-on carbon nanotube (CNT) thin films for biosensing E-Textile applications. *Carbon* **2020**, S0008622320306266.
164. Martinez, I.; Mao, C.-X.; Vital, D.; Shahariar, H.; Werner, D. H.; Jur, J. S.; Bhardwaj, S., Compact, low-profile and robust textile antennas with improved bandwidth for easy garment integration. *IEEE Access* **2020**, *8*, 77490-77500.
165. Dwivedi, S. In *Effect of thickness of substrate on antenna design for advance communication*, 2017 7th International Conference on Cloud Computing, Data Science & Engineering-Confluence, IEEE: 2017; pp 770-774.
166. Yadav, A.; Kumar Singh, V.; Kumar Bhoi, A.; Marques, G.; Garcia-Zapirain, B.; de la Torre Díez, I., Wireless body area networks: UWB wearable textile antenna for telemedicine and mobile health systems. *Micromachines* **2020**, *11* (6), 558.
167. Singh, S.; Verma, S., Printed compact asymmetric dual L-strip fed split-ring shaped EBG-based textile antenna for WBAN applications. *Microwave and Optical Technology Letters* **2020**, *62* (12), 3897-3904.
168. Sandeep, D. R.; Prabakaran, N.; Madhav, B.; Narayana, K.; Reddy, Y. P., Semicircular shape hybrid reconfigurable antenna on jute textile for ISM, Wi-Fi, Wi-

- MAX, and W-LAN applications. *International Journal of RF and Microwave Computer-Aided Engineering* **2020**, 30 (11), e22401.
169. Ashyap, A. Y. I.; Zainal Abidin, Z.; Dahlan, S. H.; Majid, H. A.; Saleh, G., Metamaterial inspired fabric antenna for wearable applications. *International Journal of RF and Microwave Computer-Aided Engineering* **2019**, 29 (3), e21640.
170. Priyadarshini, S. J.; Hemanth, D. J., Investigation and reduction methods of specific absorption rate for biomedical applications: A survey. *International Journal of RF and Microwave Computer-Aided Engineering* **2018**, 28 (3), e21211.
171. Yadav, A.; Singh, V. K.; Yadav, P.; Beliya, A. K.; Bhoi, A. K.; Barsocchi, P., Design of circularly polarized triple-band wearable textile antenna with safe low SAR for human health. *Electronics* **2020**, 9 (9), 1366.
172. Yalduz, H.; Tabaru, T. E.; Kilic, V. T.; Turkmen, M., Design and analysis of low profile and low SAR full-textile UWB wearable antenna with metamaterial for WBAN applications. *AEU-International Journal of Electronics and Communications* **2020**, 126, 153465.
173. Aguilar-Garib, J. A.; Tijerina-García, O.; Garza-Guajardo, J. In *SINTERING OF MLCC'S BARIUM TITANATE WITH MICROWAVES*, Ampere 2019, 2019-09-09; Universitat Politècnica de València: 2019.
174. Shahariar, H.; Soewardiman, H.; Muchler, C. A.; Adams, J. J.; Jur, J. S., Porous textile antenna designs for improved wearability. *Smart Materials and Structures* **2018**, 27 (4), 045008.
175. Hon, K.; Li, L.; Hutchings, I., Direct writing technology—Advances and developments. *CIRP annals* **2008**, 57 (2), 601-620.

176. Obata, K.; Schonewille, A.; Slobin, S.; Hohnholz, A.; Unger, C.; Koch, J.; Suttman, O.; Overmeyer, L., Hybrid 2D patterning using UV laser direct writing and aerosol jet printing of UV curable polydimethylsiloxane. *Applied Physics Letters* **2017**, *111* (12), 121903.
177. Hong, Y.; Tak, J.; Choi, J., An all-textile SIW cavity-backed circular ring-slot antenna for WBAN applications. *IEEE Antennas and Wireless Propagation Letters* **2016**, *15*, 1995-1999.
178. Mendes, C.; Peixeiro, C., A dual-mode single-band wearable microstrip antenna for body area networks. *IEEE Antennas and Wireless Propagation Letters* **2017**, *16*, 3055-3058.
179. Dierck, A.; Rogier, H.; Declercq, F., A wearable active antenna for global positioning system and satellite phone. *IEEE Transactions on Antennas and Propagation* **2013**, *61* (2), 532-538.
180. Idolor, O.; Guha, R.; Grace, L. In a dielectric resonant cavity method for monitoring of damage progression in moisture-contaminated composites, *American Society for Composites* **2018**, 2018-11-07; DEStech Publications, Inc.: 2018.
181. Works, C.; Dakin, T.; Boggs, F., A resonant-cavity method for measuring dielectric properties at ultrahigh frequencies. *Electrical Engineering* **1944**, *63* (12), 1092-1098.
182. Mcconnell, R. L.; Meyer, M.; Petke, F.; Haile, W., Polyester adhesives in nonwovens and other textile applications. *Journal of Coated Fabrics* **1987**, *16* (3), 199-208.
183. Shahariar, H.; Kim, I.; Soewardiman, H.; Jur, J. S., Inkjet printing of reactive silver ink on textiles. *ACS applied materials & interfaces* **2019**, *11* (6), 6208-6216.

184. Hoth, C. N.; Steim, R.; Schilinsky, P.; Choulis, S. A.; Tedde, S. F.; Hayden, O.; Brabec, C. J., Topographical and morphological aspects of spray coated organic photovoltaics. *Organic Electronics* **2009**, *10* (4), 587-593.
185. Muralidhar, C.; Pillai, P. K. C., XRD studies on barium titanate (BaTiO₃)/polyvinylidene fluoride (PVDF) composites. *Journal of Materials Science* **1988**, *23* (2), 410-414.
186. Masson, F.; Decker, C.; Jaworek, T.; Schwalm, R., UV-radiation curing of waterbased urethane–acrylate coatings. *Progress in Organic Coatings* **2000**, *39* (2-4), 115-126.
187. Can, S.; Yilmaz, A. E., Reduction of specific absorption rate with artificial magnetic conductors: Reduction of SAR with AMCs. *International Journal of RF and Microwave Computer-Aided Engineering* **2016**, *26* (4), 349-354.
188. Mongia, R. K.; Ittipiboon, A.; Cuhaci, M., Measurement of radiation efficiency of dielectric resonator antennas. *IEEE Microwave and Guided Wave Letters* **1994**, *4* (3), 80-82.
189. Ramli, M. R.; Ibrahim, S.; Ahmad, Z.; Abidin, I. S. Z.; Ain, M. F., Stretchable conductive ink based on polysiloxane–silver composite and its application as a frequency reconfigurable patch antenna for wearable electronics. *ACS applied materials & interfaces* **2019**, *11* (31), 28033-28042.
190. Whittow, W. G.; Chauraya, A.; Vardaxoglou, J. C.; Li, Y.; Torah, R.; Yang, K.; Beeby, S.; Tudor, J., Inkjet-printed microstrip patch antennas realized on textile for wearable applications. *IEEE Antennas and Wireless Propagation Letters* **2014**, *13*, 71-74.

191. Tang, D.; Wang, Q.; Wang, Z.; Liu, Q.; Zhang, B.; He, D.; Wu, Z.; Mu, S., Highly sensitive wearable sensor based on a flexible multi-layer graphene film antenna. *Science Bulletin* **2018**, *63* (9), 574-579.
192. Velan, S.; Sundarsingh, E. F.; Kanagasabai, M.; Sarma, A. K.; Raviteja, C.; Sivasamy, R.; Pakkathillam, J. K., Dual-band EBG integrated monopole antenna deploying fractal geometry for wearable applications. *IEEE antennas and wireless propagation letters* **2014**, *14*, 249-252.
193. Yan, S.; Soh, P. J.; Vandenbosch, G. A., Low-profile dual-band textile antenna with artificial magnetic conductor plane. *IEEE Transactions on Antennas and Propagation* **2014**, *62* (12), 6487-6490.
194. Stoppa, M.; Chiolerio, A., Wearable electronics and smart textiles: A critical review. *Sensors* **2014**, *14* (7), 11957-11992.
195. Torres-Canas, F.; Yuan, J.; Ly, I.; Neri, W.; Colin, A.; Poulin, P., Inkjet printing of latex-based high-energy microcapacitors. *Advanced Functional Materials* **2019**, *29* (31), 1901884.
196. Schwartz, G.; Tee, B. C.; Mei, J.; Appleton, A. L.; Kim, D. H.; Wang, H.; Bao, Z., Flexible polymer transistors with high pressure sensitivity for application in electronic skin and health monitoring. *Nat Commun* **2013**, *4*, 1859.
197. Vervust, T.; Buyle, G.; Bossuyt, F.; Vanfleteren, J., Integration of stretchable and washable electronic modules for smart textile applications. *Journal of The Textile Institute* **2012**, *103* (10), 1127-1138.

198. Li, B. M.; Kim, I.; Zhou, Y.; Mills, A. C.; Flewwellin, T. J.; Jur, J. S., Kirigami-inspired textile electronics: K.I.T.E. *Advanced Materials Technologies* **2019**, *4* (11), 1900511.
199. Gao, Z.; Song, N.; Zhang, Y.; Li, X., Cotton-textile-enabled, flexible lithium-ion batteries with enhanced capacity and extended lifespan. *Nano Letters* **2015**, *15* (12), 8194-8203.
200. Gao, H.; Minh, P. T.; Wang, H.; Minko, S.; Locklin, J.; Nguyen, T.; Sharma, S., High-performance flexible yarn for wearable piezoelectric nanogenerators. *Smart Materials and Structures* **2018**, *27* (9), 095018.
201. Gao, H.; Asheghali, D.; Yadavalli, N. S.; Pham, M. T.; Nguyen, T. D.; Minko, S.; Sharma, S., Fabrication of core-sheath nanoyarn via touchspinning and its application in wearable piezoelectric nanogenerator. *The Journal of The Textile Institute* **2020**, *111* (6), 906-915.
202. Liu, M.; Pu, X.; Jiang, C.; Liu, T.; Huang, X.; Chen, L.; Du, C.; Sun, J.; Hu, W.; Wang, Z. L., Large-area all-textile pressure sensors for monitoring human motion and physiological signals. *Adv Mater* **2017**, *29* (41).
203. Wang, X.; Zhang, H.; Yu, R.; Dong, L.; Peng, D.; Zhang, A.; Zhang, Y.; Liu, H.; Pan, C.; Wang, Z. L., Dynamic pressure mapping of personalized handwriting by a flexible sensor matrix based on the mechanoluminescence process. *Adv Mater* **2015**, *27* (14), 2324-31.
204. Lv, J.; Jeerapan, I.; Tehrani, F.; Yin, L.; Silva-Lopez, C. A.; Jang, J.-H.; Joshua, D.; Shah, R.; Liang, Y.; Xie, L.; Soto, F.; Chen, C.; Karshalev, E.; Kong, C.;

- Yang, Z.; Wang, J., Sweat-based wearable energy harvesting-storage hybrid textile devices. *Energy & Environmental Science* **2018**, *11* (12), 3431-3442.
205. Kwon, S.; Kim, H.; Choi, S.; Jeong, E. G.; Kim, D.; Lee, S.; Lee, H. S.; Seo, Y. C.; Choi, K. C., Weavable and highly efficient organic light-emitting fibers for wearable electronics: A scalable, low-temperature Process. *Nano Lett* **2018**, *18* (1), 347-356.
206. Atalay, O.; Atalay, A.; Gafford, J.; Walsh, C., A highly sensitive capacitive-based soft pressure sensor based on a conductive fabric and a microporous dielectric layer. *Advanced Materials Technologies* **2018**, *3* (1), 1700237.
207. Pizarro, F.; Villavicencio, P.; Yunge, D.; Rodriguez, M.; Hermosilla, G.; Leiva, A., Easy-to-build textile pressure sensor. *Sensors (Basel)* **2018**, *18* (4).
208. Huang, Y.; Cao, B.; Xu, C.; Fan, Q.; Shao, J., Synthesis process control and property evaluation of a low-viscosity urethane acrylate oligomer for blue light curable ink of textile digital printing. *Textile Research Journal* **2014**, *85* (7), 759-767.
209. Walker, S. B.; Lewis, J. A., Reactive silver inks for patterning high-conductivity features at mild temperatures. *J Am Chem Soc* **2012**, *134* (3), 1419-21.
210. Smith, P. J.; Shin, D. Y.; Stringer, J. E.; Derby, B.; Reis, N., Direct ink-jet printing and low temperature conversion of conductive silver patterns. *Journal of Materials Science* **2006**, *41* (13), 4153-4158.
211. Mikolajek, M.; Friederich, A.; Kohler, C.; Rosen, M.; Rathjen, A.; Krüger, K.; Binder, J. R., Direct inkjet printing of dielectric ceramic/polymer composite thick films: Inkjet printing of composite thick films. *Advanced Engineering Materials* **2015**, *17* (9), 1294-1301.

212. Saleh, E.; Woolliams, P.; Clarke, B.; Gregory, A.; Greedy, S.; Smartt, C.; Wildman, R.; Ashcroft, I.; Hague, R.; Dickens, P.; Tuck, C., 3D inkjet-printed UV-curable inks for multi-functional electromagnetic applications. *Additive Manufacturing* **2017**, *13*, 143-148.
213. *Nanopackaging: nanotechnologies and electronics packaging*. Springer: New York, NY, 2008; p 543.
214. Blattmann, C. O.; Pratsinis, S. E., Single-step fabrication of polymer nanocomposite films. *Materials* **2018**, *11* (7), 1177.
215. Okada, A.; Usuki, A., Twenty years of polymer-clay nanocomposites. *Macromolecular Materials and Engineering* **2006**, *291* (12), 1449-1476.
216. Rosa, M.; Barou, C.; Esposito, V., Zirconia UV-curable colloids for additive manufacturing via hybrid inkjet printing-stereolithography. *Materials Letters* **2018**, *215*, 214-217.
217. Hakeim, O. A.; Arafa, A. A.; Zahran, M. K.; Abdou, L. A. W., UV-curable encapsulation of surface—Modified organic pigments for inkjet printing of textiles. *Colloids and Surfaces A: Physicochemical and Engineering Aspects* **2014**, *447*, 172-182.
218. Li, N.-w.; Ho, C.-p.; Yick, K.-l.; Zhou, J.-y., Effect of UV-curable inkjet printing parameters on physical, low-stress mechanical, and aesthetic properties of polypropylene knitted fabrics. *Fibers and Polymers* **2020**, *21* (12), 2788-2798.
219. Mendes-Felipe, C.; Oliveira, J.; Etxebarria, I.; Vilas-Vilela, J. L.; Lanceros-Mendez, S., State-of-the-Art and Future Challenges of UV curable polymer-based smart materials for printing technologies. *Advanced Materials Technologies* **2019**, *4* (3).

220. Endruweit, A.; Johnson, M. S.; Long, A. C., Curing of composite components by ultraviolet radiation: A review. *Polymer Composites* **2006**, *27* (2), 119-128.
221. Guidoin, R.; King, M.; Marceau, D.; Cardou, A.; De La Faye, D.; Legendre, J.-M.; Blais, P., Textile arterial prostheses: Is water permeability equivalent to porosity? *Journal of Biomedical Materials Research* **1987**, *21* (1), 65-87.
222. Edge, M.; Wiles, R.; Allen, N.; McDonald, W.; Mortlock, S., Characterisation of the species responsible for yellowing in melt degraded aromatic polyesters—I: Yellowing of poly (ethylene terephthalate). *Polymer degradation and stability* **1996**, *53* (2), 141-151.
223. Gusarova, N.; Chernysheva, N.; Yas'ko, S.; Kazantseva, T.; Ushakov, I.; Trofimov, B., Radical addition of secondary phosphine sulfides and selenides to vinyl selenides. *Synthesis* **2008**, *2008* (17), 2743-2746.
224. Bertie, J. E.; Jones, R. N.; Keefe, C. D., Infrared intensities of liquids XII: accurate optical constants and molar absorption coefficients between 6225 and 500 cm^{-1} of benzene at 25 C, from spectra recorded in several laboratories. *Applied spectroscopy* **1993**, *47* (7), 891-911.
225. Coronado, J. M.; Kataoka, S.; Tejedor-Tejedor, I.; Anderson, M. A., Dynamic phenomena during the photocatalytic oxidation of ethanol and acetone over nanocrystalline TiO_2 : simultaneous FTIR analysis of gas and surface species. *Journal of Catalysis* **2003**, *219* (1), 219-230.
226. Nor, H. M.; Ebdon, J. R., Ozonolysis of natural rubber in chloroform solution Part 1. A study by GPC and FTIR spectroscopy. *Polymer* **2000**, *41* (7), 2359-2365.

227. Verma, S. P.; Wallach, D. F., Multiple thermotropic state transitions in erythrocyte membranes a laser-Raman study of the CH-stretching and acoustical regions. *Biochimica et Biophysica Acta (BBA)-Biomembranes* **1976**, *436* (2), 307-318.
228. Ning, S.; Zhengkun, W.; Mu, J.; Jie, Z., Flexible carbon fiber cloth decorated by Ag nanoparticles for high Raman enhancement. *Optical Materials Express* **2021**, *11* (4).
229. Guo, H.; Xing, B.; White, J. C.; Mukherjee, A.; He, L., Ultra-sensitive determination of silver nanoparticles by surface-enhanced Raman spectroscopy (SERS) after hydrophobization-mediated extraction. *Analyst* **2016**, *141* (18), 5261-5264.
230. Tudor, J.; Vardaxoglou, J. Y. C.; Torah, R.; Li, Y.; Whittow, W. G.; Chauraya, A.; Beeby, S.; Yang, K., Inkjet printed dipole antennas on textiles for wearable communications. *IET Microwaves, Antennas & Propagation* **2013**, *7* (9), 760-767.
231. Chavez-Santiago, R.; Sayrafian-Pour, K.; Khaleghi, A.; Takizawa, K.; Wang, J.; Balasingham, I.; Li, H.-B., Propagation models for IEEE 802.15. 6 standardization of implant communication in body area networks. *IEEE Communications Magazine* **2013**, *51* (8), 80-87.
232. Movassaghi, S.; Abolhasan, M.; Lipman, J.; Smith, D.; Jamalipour, A., Wireless body area networks: A Survey. *IEEE Communications Surveys & Tutorials* **2014**, *16* (3), 1658-1686.
233. Gao, G.-P.; Hu, B.; Wang, S.-F.; Yang, C., Wearable circular ring slot antenna with EBG structure for wireless body area network. *IEEE Antennas and Wireless Propagation Letters* **2018**, *17* (3), 434-437.
234. Al-Sehemi, A. G.; Al-Ghamdi, A. A.; Dishovsky, N. T.; Atanasov, N. T.; Atanasova, G. L., Flexible and small wearable antenna for wireless body area network

- applications. *Journal of Electromagnetic Waves and Applications* **2017**, *31* (11-12), 1063-1082.
235. El Gharbi, M.; Fernández-García, R.; Ahyoud, S.; Gil, I., A review of flexible wearable antenna sensors: Design, fabrication methods, and applications. *Materials* **2020**, *13* (17), 3781.
236. Li, B. M.; Kim, I.; Zhou, Y.; Mills, A. C.; Flewellin, T. J.; Jur, J. S., Kirigami-inspired textile electronics: K.I.T.E. *Advanced Materials Technologies* **2019**, *4* (11), 1900511.
237. Hosseini, S. G.; Pourmortazavi, S. M.; Fathollahi, M., Orthogonal array design for the optimization of silver recovery from waste photographic paper. *Separation Science and Technology* **2005**, *39* (8), 1953-1966.
238. Li, Z.; Sinha, S. K.; Treich, G. M.; Wang, Y.; Yang, Q.; Deshmukh, A. A.; Sotzing, G. A.; Cao, Y., All-organic flexible fabric antenna for wearable electronics. *Journal of Materials Chemistry C* **2020**, *8* (17), 5662-5667.
239. Whittow, W. G.; Chauraya, A.; Vardaxoglou, J.; Li, Y.; Torah, R.; Yang, K.; Beeby, S.; Tudor, J., Inkjet-printed microstrip patch antennas realized on textile for wearable applications. *IEEE Antennas and Wireless Propagation Letters* **2014**, *13*, 71-74.
240. Ferreira, D.; Pires, P.; Rodrigues, R.; Caldeirinha, R. F., Wearable textile antennas: Examining the effect of bending on their performance. *IEEE Antennas and Propagation Magazine* **2017**, *59* (3), 54-59.

241. Idolor, O.; Guha, R.; Grace, L. In *A Dielectric Resonant Cavity Method for Monitoring of Damage Progression in Moisture-Contaminated Composites*, 2018/11//; DEStech Publications, Inc.: 2018.
242. Hayt, A.; William, H., Buck, Engineering Electromagnetics. New York: McGraw-Hill College: 2004.
243. Mustata, F. S. C.; Mustata, A., Dielectric behaviour of some woven fabrics on the basis of natural cellulosic fibers. *Advances in Materials Science and Engineering* **2014**, 2014.
244. Zhong, W.; Xing, M. M.; Pan, N.; Maibach, H. I., Textiles and human skin, microclimate, cutaneous reactions: an overview. *Cutan Ocul Toxicol* **2006**, 25 (1), 23-39.
245. Bedek, G.; Salaun, F.; Martinkovska, Z.; Devaux, E.; Dupont, D., Evaluation of thermal and moisture management properties on knitted fabrics and comparison with a physiological model in warm conditions. *Appl Ergon* **2011**, 42 (6), 792-800.
246. Amaro, N.; Mendes, C.; Pinho, P. In *Bending effects on a textile microstrip antenna*, 2011 IEEE Antennas and Propagation Society International Symposium and USNC/URSI National Radio Science Meeting, 07/2011; IEEE: 2011; pp 282-285.
247. Ferreira, D.; Pires, P.; Rodrigues, R.; Caldeirinha, R. F. S., Wearable Textile Antennas: Examining the effect of bending on their performance. *IEEE Antennas and Propagation Magazine* **2017**, 59 (3), 54-59.
248. Paul, G.; Torah, R.; Yang, K.; Beeby, S.; Tudor, J., An investigation into the durability of screen-printed conductive tracks on textiles. *Measurement Science and Technology* **2014**, 25 (2), 025006.

249. Krupka, J., Precise measurements of the complex permittivity of dielectric materials at microwave frequencies. *Materials Chemistry and Physics* **2003**, 79 (2-3), 195-198.
250. Chaturvedi, D.; Raghavan, S., A compact metamaterial-inspired antenna for WBAN application. *Wireless Personal Communications* **2019**, 105 (4), 1449-1460.
251. Hu, B.; Gao, G.-P.; He, L.-L.; Cong, X.-D.; Zhao, J.-N., Bending and on-arm effects on a wearable antenna for 2.45 GHz body area network. *IEEE Antennas and Wireless Propagation Letters* **2015**, 15, 378-381.
252. Chi, Y.-J.; Chen, F.-C., On-body adhesive-bandage-like antenna for wireless medical telemetry service. *IEEE transactions on antennas and propagation* **2014**, 62 (5), 2472-2480.
253. Song, L.; Rahmat-Samii, Y., A systematic investigation of rectangular patch antenna bending effects for wearable applications. *IEEE Transactions on Antennas and Propagation* **2018**, 66 (5), 2219-2228.
254. Kellomaki, T.; Heikkinen, J.; Kivikoski, M. In *Effects of bending GPS antennas*, 2006 Asia-Pacific Microwave Conference, 12/2006; IEEE: 2006; pp 1597-1600.
255. Amaro, N.; Mendes, C.; Pinho, P. In *Bending effects on a textile microstrip antenna*, 2011 IEEE International Symposium on Antennas and Propagation (APSURSI), IEEE: 2011; pp 282-285.
256. Ueno, S.; Sakamoto, Y.; Nakashima, K.; Wada, S., Low-temperature fabrication of titanium metal/barium titanate composite capacitors via hydrothermal method and their dielectric properties. *Journal of the Ceramic Society of Japan* **2014**, 122 (1426), 447-451.

257. Ramesh, S.; Shutzberg, B. A.; Huang, C.; Gao, J.; Giannelis, E. P., Dielectric nanocomposites for integral thin film capacitors: Materials design, fabrication and integration issues. *IEEE Transactions on Advanced Packaging* **2003**, *26* (1), 17-24.
258. Shafiee, A.; Ghadiri, E.; Mat Salleh, M.; Yahaya, M.; Atala, A., Controlling the surface properties of an inkjet-printed reactive oxygen species scavenger for flexible bioelectronics applications in neural resilience. *IEEE Journal of the Electron Devices Society* **2019**, *7*, 784-791.
259. Kosmala, A.; Zhang, Q.; Wright, R.; Kirby, P., Development of high concentrated aqueous silver nanofluid and inkjet printing on ceramic substrates. *Materials Chemistry and Physics* **2012**, *132* (2-3), 788-795.
260. Wu, X.; Fei, F.; Chen, Z.; Su, W.; Cui, Z., A new nanocomposite dielectric ink and its application in printed thin-film transistors. *Composites Science and Technology* **2014**, *94*, 117-122.
261. Ihlefeld, J.; Laughlin, B.; Hunt-Lowery, A.; Borland, W.; Kingon, A.; Maria, J.-P., Copper compatible barium titanate thin films for embedded passives. *Journal of Electroceramics* **2005**, *14* (2), 95-102.
262. Ashiri, R.; Nemati, A.; Sasani Ghamsari, M.; Sanjabi, S.; Aalipour, M., A modified method for barium titanate nanoparticles synthesis. *Materials Research Bulletin* **2011**, *46* (12), 2291-2295.
263. Brennecka, G. L.; Ihlefeld, J. F.; Maria, J.-P.; Tuttle, B. A.; Clem, P. G., Processing technologies for high-permittivity thin films in capacitor applications: Processing technologies for thin films in capacitor applications. *Journal of the American Ceramic Society* **2010**, *93* (12), 3935-3954.

264. Yuk, J.; Troczynski, T., Sol–gel BaTiO₃ thin film for humidity sensors. *Sensors and Actuators B: Chemical* **2003**, *94* (3), 290-293.
265. Tsurumi, T.; Hoshina, T.; Takeda, H.; Mizuno, Y.; Chazono, H., Size effect of barium titanate and computer-aided design of multilayered ceramic capacitors. *IEEE Transactions on Ultrasonics, Ferroelectrics and Frequency Control* **2009**, *56* (8), 1513-1522.
266. Peet, J.; Senatore, M. L.; Heeger, A. J.; Bazan, G. C., The role of processing in the fabrication and optimization of plastic solar cells. *Advanced Materials* **2009**, *21* (14-15), 1521-1527.
267. Manika, G. C.; Psarras, G. C., Barium titanate/epoxy resin composite nanodielectrics as compact capacitive energy storing systems. *Express Polymer Letters* **2019**, *13* (8), 749-758.
268. Lombardi, M.; Guerriero, A.; Kortaberria, G.; Mondragon, I.; Sangermano, M.; Montanaro, L., Effect of the ceramic filler features on the properties of photopolymerized BaTiO₃-acrylic composites. *Polymer Composites* **2011**, *32* (8), 1304-1312.
269. Li, J.; Inukai, K.; Takahashi, Y.; Tsuruta, A.; Shin, W., Thin film coating with highly dispersible barium titanate-polyvinylpyrrolidone nanoparticles. *Materials* **2018**, *11* (5), 712.
270. Kobayashi, Y.; Kosuge, A.; Konno, M., Fabrication of high concentration barium titanate/polyvinylpyrrolidone nano-composite thin films and their dielectric properties. *Applied Surface Science* **2008**, *255* (5), 2723-2729.

271. Lakshmi, N. V.; Tambe, P.; Sahu, N. K., Giant permittivity of three phase polymer nanocomposites obtained by modifying hybrid nanofillers with polyvinylpyrrolidone. *Composite Interfaces* **2017**, *25* (1), 47-67.
272. Yu, K.; Niu, Y.; Zhou, Y.; Bai, Y.; Wang, H.; Randall, C., Nanocomposites of surface-modified BaTiO₃ nanoparticles filled ferroelectric polymer with enhanced energy density. *Journal of the American Ceramic Society* **2013**, *96* (8), 2519-2524.
273. Vasudevan, P.; Thomas, S.; Biju, P. R.; Sudarsanakumar, C.; Unnikrishnan, N. V., Synthesis and structural characterization of sol-gel derived titania/poly (vinyl pyrrolidone) nanocomposites. *Journal of Sol-Gel Science and Technology* **2012**, *62* (1), 41-46.
274. Ryu, J.; Kim, H.-S.; Hahn, H. T., Reactive sintering of copper nanoparticles using intense pulsed light for printed electronics. *Journal of Electronic Materials* **2010**, *40* (1), 42-50.
275. Hwang, H. J.; Oh, K. H.; Kim, H. S., All-photonic drying and sintering process via flash white light combined with deep-UV and near-infrared irradiation for highly conductive copper nano-ink. *Sci Rep* **2016**, *6*, 19696.
276. Fan, C.-L.; Shang, M.-C.; Hsia, M.-Y.; Wang, S.-J.; Huang, B.-R.; Lee, W.-D., Poly(4-vinylphenol) gate insulator with cross-linking using a rapid low-power microwave induction heating scheme for organic thin-film-transistors. *APL Materials* **2016**, *4* (3).
277. Sangermano, M.; Lombardi, M.; Guerriero, A.; Kortaberria, G.; Mondragon, I.; Pirri, F.; Montanaro, L., Epoxy/BaTiO₃ light-cured composites as organic capacitors. *Macromolecular Materials and Engineering* **2013**, *298* (6), 634-643.

278. Hanemann, T.; Gesswein, H.; Schumacher, B., Development of new polymer–BaTiO₃-composites with improved permittivity for embedded capacitors. *Microsystem Technologies* **2011**, *17* (2), 195-201.
279. Taki, H.; Otsuka, S., Driving waveform generating device and method for ink-jet recording head. Google Patents: 2001.
280. Shah, M. A.; Lee, D.-G.; Lee, B. Y.; Kim, N. W.; An, H.; Hur, S., Actuating voltage waveform optimization of piezoelectric inkjet printhead for suppression of residual vibrations. *Micromachines* **2020**, *11* (10), 900.
281. Gardner, D. A., Individual voltage trimming with waveforms. Google Patents: 2007.
282. Smith, P. J.; Shin, D. H., Inkjet-based micromanufacturing. *John Wiley & Sons* **2012**.
283. Gadelmawla, E.; Koura, M.; Maksoud, T.; Elewa, I.; Soliman, H., Roughness parameters. *Journal of materials processing Technology* **2002**, *123* (1), 133-145.
284. Mah, J.; Samson, C.; McKinnon, S. D.; Thibodeau, D., 3D laser imaging for surface roughness analysis. *International Journal of Rock Mechanics and Mining Sciences* **2013**, *58*, 111-117.
285. Sadowski, Ł.; Czarnecki, S.; Hoła, J., Evaluation of the height 3D roughness parameters of concrete substrate and the adhesion to epoxy resin. *International Journal of Adhesion and Adhesives* **2016**, *67*, 3-13.
286. Das, R. N.; Poliks, M. D.; Lauffer, J. M.; Markovich, V. R. In *High Capacitance, Large Area, Thin Film, Nanocomposite Based Embedded Capacitors*, 56th Electronic Components and Technology Conference 2006, 2006; IEEE: 2006; pp 1510-1515.

287. Lin, M.-F.; Lee, P. S., Formation of PVDF-g-HEMA/BaTiO₃ nanocomposites via in situ nanoparticle synthesis for high performance capacitor applications. *Journal of Materials Chemistry A* **2013**, *1* (46), 14455.
288. Mallick, S.; Ahmad, Z.; Qadir, K. W.; Rehman, A.; Shakoor, R. A.; Touati, F.; Al-Muhtaseb, S. A., Effect of BaTiO₃ on the sensing properties of PVDF composite-based capacitive humidity sensors. *Ceramics International* **2020**, *46* (3), 2949-2953.
289. Xu, J.; Bhattacharya, S.; Pramanik, P.; Wong, C. P., High dielectric constant polymer-ceramic (Epoxy varnish-barium titanate) nanocomposites at moderate filler loadings for embedded capacitors. *Journal of Electronic Materials* **2006**, *35* (11), 2009-2015.
290. Suematsu, K.; Arimura, M.; Uchiyama, N.; Saita, S.; Makino, T., Synthesis of BaTiO₃/polymer composite ink to improve the dielectric properties of thin films. *Composites Part B: Engineering* **2016**, *104*, 80-86.
291. Zhang, C.; Yin, Y.; Yang, Q.; Shi, Z.; Hu, G.-H.; Xiong, C., Flexible Cellulose/BaTiO₃ Nanocomposites with High Energy Density for Film Dielectric Capacitor. *ACS Sustainable Chemistry & Engineering* **2019**, *7* (12), 10641-10648.
292. Kim, P.; Jones, S. C.; Hotchkiss, P. J.; Haddock, J. N.; Kippelen, B.; Marder, S. R.; Perry, J. W., Phosphonic acid-modified barium titanate polymer nanocomposites with high permittivity and dielectric strength. *Advanced Materials* **2007**, *19* (7), 1001-1005.
293. Kang, B. J.; Lee, C. K.; Oh, J. H., All-inkjet-printed electrical components and circuit fabrication on a plastic substrate. *Microelectronic Engineering* **2012**, *97*, 251-254.
294. Mikolajek, M.; Reinheimer, T.; Bohn, N.; Kohler, C.; Hoffmann, M. J.; Binder, J. R., Fabrication and characterization of fully inkjet printed capacitors based on

- ceramic/polymer composite dielectrics on flexible substrates. *Sci Rep* **2019**, *9* (1), 13324.
295. Tseng, W. J.; Lin, S.-Y.; Wang, S.-R., Particulate dispersion and freeform fabrication of BaTiO₃ thick films via direct inkjet printing. *Journal of Electroceramics* **2006**, *16* (4), 537-540.
296. Im, D. H.; Hyun, S. H.; Park, S. Y.; Lee, B. Y.; Kim, Y. H., Preparation of high dispersed nickel pastes for thick film electrodes. *Journal of Materials Science* **2006**, *41* (19), 6425-6430.
297. Paulsen, J. L.; Reed, E. K., Highly accelerated lifetesting of base-metal-electrode ceramic chip capacitors. *Microelectronics Reliability* **2002**, *42* (6), 815-820.
298. Yamamatsu, J.; Kawano, N.; Arashi, T.; Sato, A.; Nakano, Y.; Nomura, T., Reliability of multilayer ceramic capacitors with nickel electrodes. 5.
299. Liu, D.; Sampson, M. J., Reliability evaluation of base-metal-electrode multilayer ceramic capacitors for potential space applications. *CARTS Proceeding* **2011**, 5-63.
300. Tseng, W. J.; Lin, C.-L., Effect of dispersants on rheological behavior of BaTiO₃ powders in ethanol–isopropanol mixtures. *Materials Chemistry and Physics* **2003**, *80* (1), 232-238.
301. Li, B.; Zheng, M.; Xue, H.; Pang, H., High performance electrochemical capacitor materials focusing on nickel based materials. *Inorganic Chemistry Frontiers* **2016**, *3* (2), 175-202.
302. Ishida, Y.; Nakagawa, G.; Asano, T., Inkjet printing of nickel nanosized particles for metal-induced crystallization of amorphous silicon. *Japanese Journal of Applied Physics* **2007**, *46* (9B), 6437-6443.

303. Seifert, T.; Sowade, E.; Roscher, F.; Wiemer, M.; Gessner, T.; Baumann, R. R., Additive manufacturing technologies compared: Morphology of deposits of silver ink using inkjet and aerosol jet printing. *Industrial & Engineering Chemistry Research* **2015**, *54* (2), 769-779.
304. Liu, S.; Tam, S. K.; Ng, K. M., Dual-reductant synthesis of nickel nanoparticles for use in screen-printing conductive paste. *Journal of Nanoparticle Research* **2021**, *23* (3).
305. Sakai, Y.; Futakuchi, T.; Adachi, M., Preparation of inkjet-printed NiO films for Ba(Ti,Zr)O₃-Based ceramics and application to multilayer ceramics with Ni electrodes. *Japanese Journal of Applied Physics* **2008**, *47* (9), 7630-7634.
306. Ueyama, R.; Kuribayashi, K.; Koumoto, K., Fabrication and evaluation of Ni-MLCC used of new BaTiO₃ resinate. *Journal of the Ceramic Society of Japan* **2004**, *112* (1308), 458-461.
307. Naito, K.; Tsuji, T.; Watanabe, S., The control of very low oxygen partial pressures with stabilized zirconia cell. *Solid State Ionics* **1980**, *1* (5-6), 509-518.
308. Ring, T. A., *Fundamentals of ceramic powder processing and synthesis*. Elsevier: 1996.
309. German, R. M., *Sintering theory and practice*. 1996.
310. Sharma, S.; Sharma, A.; Tomar, M.; Puri, N. K.; Gupta, V., NO_x sensing properties of barium titanate thin films. *Procedia Engineering* **2014**, *87*, 1067-1070.
311. Pratap, A.; Joshi, N. J.; Rakshit, P. B.; Grewal, G. S.; Shrinet, V., Dielectric behavior of nano barium titanate filled polymeric composites. *International Journal of Modern Physics: Conference Series* **2013**, *22*, 1-10.

312. Lee, J.-Y.; Lee, J.-H.; Hong, S.-H.; Lee, Y. K.; Choi, J.-Y., Coating BaTiO₃ nanolayers on spherical Ni powders for multilayer ceramic capacitors. *Advanced Materials* **2003**, *15* (19), 1655-1658.
313. Lee, B.; Zhang, J., Preparation, structure evolution and dielectric properties of BaTiO₃ thin films and powders by an aqueous sol–gel process. *Thin Solid Films* **2001**, *388* (1-2), 107-113.
314. Kishi, H.; Mizuno, Y.; Chazono, H., Base-metal electrode-multilayer ceramic capacitors: Past, present and future perspectives. **2003**, *42* (1), 16.
315. Huang, Q.; Zhu, Y., Printing conductive nanomaterials for flexible and stretchable electronics: A review of materials, processes, and applications. *Advanced Materials Technologies* **2019**, *4* (5).
316. Zhou, P.; Yu, H.; Zou, W.; Wang, Z.; Liu, L., High-resolution and controllable nanodeposition pattern of Ag nanoparticles by electrohydrodynamic jet printing combined with coffee ring effect. *Advanced Materials Interfaces* **2019**, *6* (20).
317. Dossou-Yovo, C.; Mougnot, M.; Beaudrouet, E.; Bessaudou, M.; Bernardin, N.; Charifi, F.; Coquet, C.; Borella, M.; Noguera, R.; Modes, C.; Lejeune, M.; Laurier, P.; Detemmerman, D.; Escure, P.; Laville, H.; Delhotes, N.; Verdeymes, S., Inkjet Printing Technology: A novel bottom-up approach for multilayer ceramic components and high definition printed electronic devices. *Journal of Microelectronics and Electronic Packaging* **2012**, *9* (4), 187-198.
318. Li, P.; Liang, C.; Bao, B.; Li, Y.; Hu, X.; Wang, Y.; Zhang, Y.; Li, F.; Shao, G.; Song, Y., Inkjet manipulated homogeneous large size perovskite grains for efficient and large-area perovskite solar cells. *Nano Energy* **2018**, *46*, 203-211.

319. Yoshimura, M.; Gallage, R., Direct patterning of nanostructured ceramics from solution—differences from conventional printing and lithographic methods. *Journal of Solid State Electrochemistry* **2008**, *12* (7-8), 775-782.
320. Chen, S.; Su, M.; Zhang, C.; Gao, M.; Bao, B.; Yang, Q.; Su, B.; Song, Y., Fabrication of nanoscale circuits on inkjet-printing patterned substrates. *Adv Mater* **2015**, *27* (26), 3928-33.
321. Friederich, A.; Binder, J. R.; Bauer, W.; Derby, B., Rheological control of the coffee stain effect for inkjet printing of ceramics. *Journal of the American Ceramic Society* **2013**, *96* (7), 2093-2099.
322. Chen, Z.; Li, Z.; Li, J.; Liu, C.; Lao, C.; Fu, Y.; Liu, C.; Li, Y.; Wang, P.; He, Y., 3D printing of ceramics: A review. *Journal of the European Ceramic Society* **2019**, *39* (4), 661-687.
323. Zhang, X.; He, Q.; Gu, H.; Wei, S.; Guo, Z., Polyaniline stabilized barium titanate nanoparticles reinforced epoxy nanocomposites with high dielectric permittivity and reduced flammability. *Journal of Materials Chemistry C* **2013**, *1* (16).
324. Randall, C. A., Scientific and Engineering Issues of the state-of-the-art and future multilayer capacitors. *Journal of the Ceramic Society of Japan* **2001**, *109* (1265), S2-S6.
325. Talbot, E. L.; Yang, L.; Berson, A.; Bain, C. D., Control of the particle distribution in inkjet printing through an evaporation-driven sol-gel transition. *ACS Appl Mater Interfaces* **2014**, *6* (12), 9572-83.
326. Kang, H. R., Water-based ink-jet ink. I, Formulation. *Journal of imaging science* **1991**, *35* (3), 179-188.

327. Tawiah, B.; Howard, E. K.; Asinyo, B., The chemistry of inkjet inks for digital textile printing—Review. *BEST* **2016**, 4, 61-78.
328. Chen, R.; Zhang, L.; Zang, D.; Shen, W., Wetting and drying of colloidal droplets: Physics and pattern formation. *Advances in Colloid Science* **2016**, 3-25.
329. Deegan, R. D.; Bakajin, O.; Dupont, T. F.; Huber, G.; Nagel, S. R.; Witten, T. A., Capillary flow as the cause of ring stains from dried liquid drops. *Nature* **1997**, 389 (6653), 827-829.
330. de Gans, B.-J.; Schubert, U. S., Inkjet printing of well-defined polymer dots and arrays. *Langmuir* **2004**, 20 (18), 7789-7793.
331. Reinheimer, T.; Azmi, R.; Binder, J. R., Polymerizable ceramic ink system for thin inkjet-printed dielectric layers. *ACS Applied Materials & Interfaces* **2020**, 12 (2), 2974-2982.
332. Anton, N.; Benoit, J. P.; Saulnier, P., Design and production of nanoparticles formulated from nano-emulsion templates—a review. *J Control Release* **2008**, 128 (3), 185-99.
333. Lee, H.-H.; Chou, K.-S.; Huang, K.-C., Inkjet printing of nanosized silver colloids. *Nanotechnology* **2005**, 16 (10), 2436-2441.
334. Fu, J.; Hou, Y.; Zheng, M.; Wei, Q.; Zhu, M.; Yan, H., Improving dielectric properties of PVDF composites by employing surface modified strong polarized BaTiO₃ particles derived by molten salt method. *ACS Appl Mater Interfaces* **2015**, 7 (44), 24480-91.

335. Patra, A.; Pal, A.; Sen, S., Polyvinylpyrrolidone modified barium zirconate titanate /polyvinylidene fluoride nanocomposites as self-powered sensor. *Ceramics International* **2018**, *44* (10), 11196-11203.
336. Kyrpal, R.; Nikulin, A.; Ragulya, A., Optimization of ink composition for advanced inkjet printing of BaTiO₃ dielectric films. **2015**, 4.
337. Deegan, R. D.; Bakajin, O.; Dupont, T. F.; Huber, G.; Nagel, S. R.; Witten, T. A., Contact line deposits in an evaporating drop. *Physical review E* **2000**, *62* (1), 756.
338. Nayak, L.; Mohanty, S.; Nayak, S. K.; Ramadoss, A., A review on inkjet printing of nanoparticle inks for flexible electronics. *Journal of Materials Chemistry C* **2019**, *7* (29), 8771-8795.

APPENDICES

Appendix-1: Supporting Information for Chapter 4

Supporting Information for Chapter 4

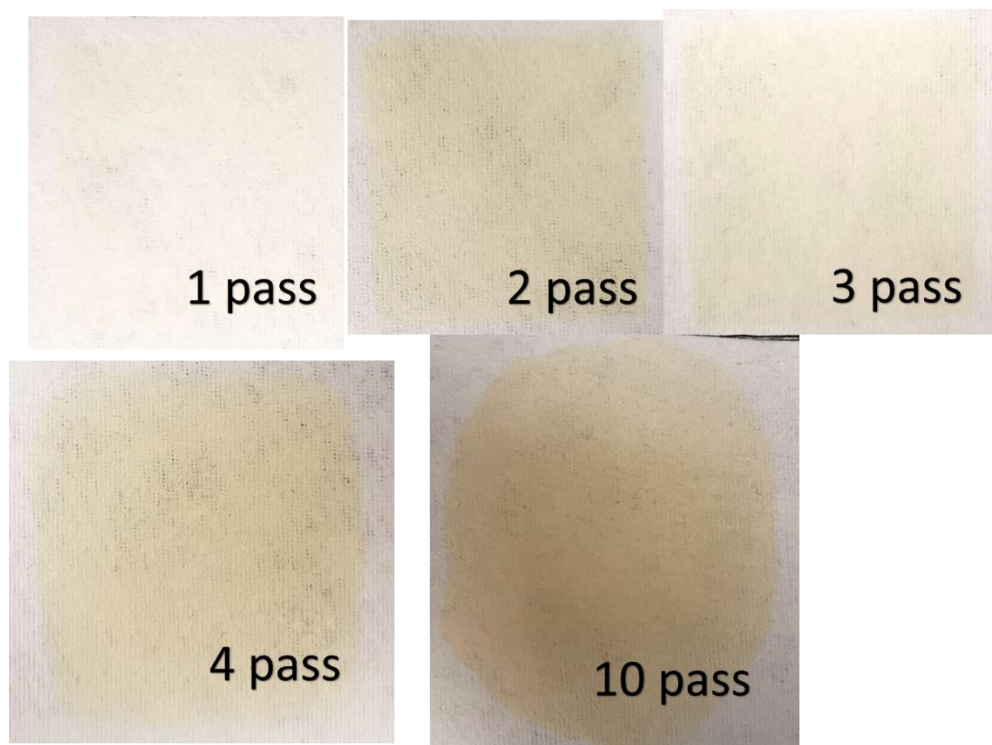


Figure S 1. Inkjet-printed nonwoven fabric by ex-situ polymerization method with different passes.

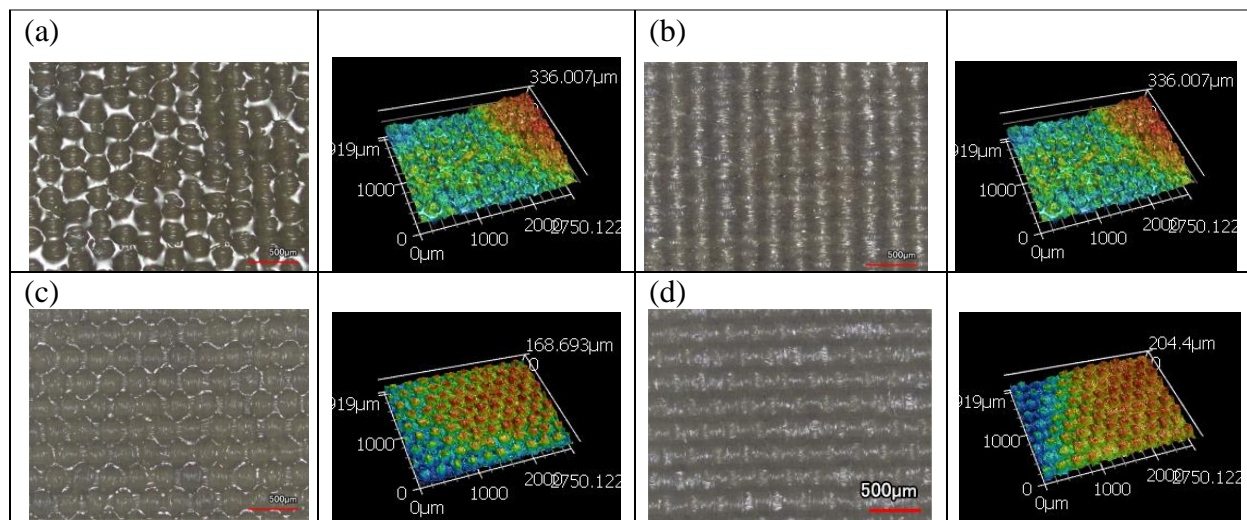


Figure S 2. Optical images of top side (a), (c), back side (b), (d). (a) (b) (1L)6, (c) (d), (6L).

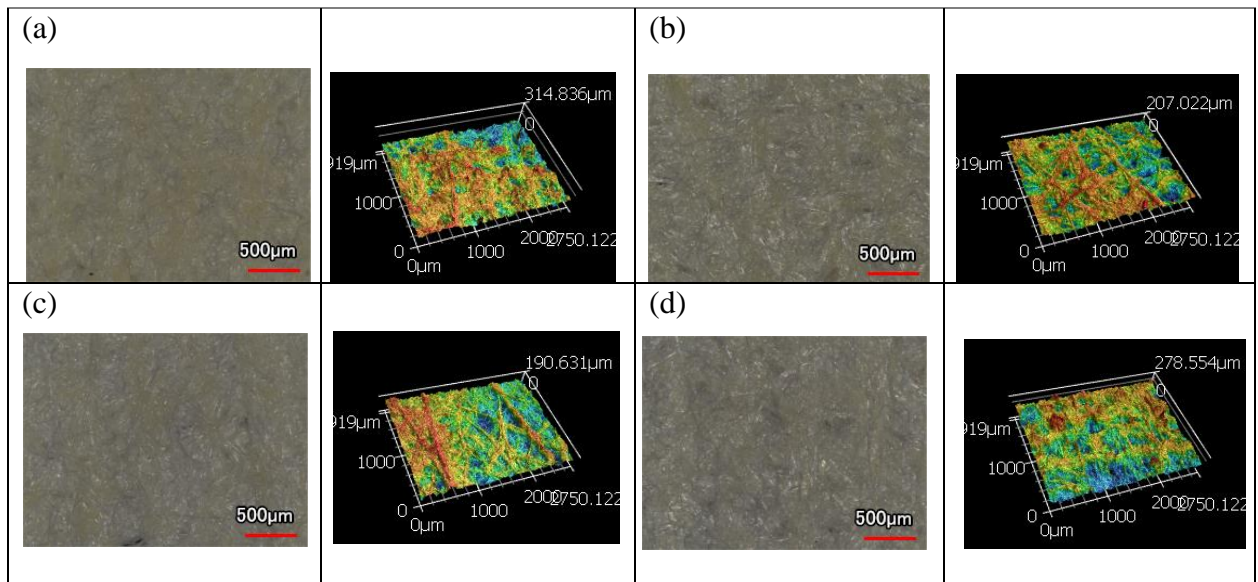


Figure S 3. Optical images of woven fabricate (a), (c) top side (b), (d) back side. (a)(b) Inkjet printed UV curable BTO ink (1L)6, (c), (d) Inkjet printed UV curable BTO ink 6L.

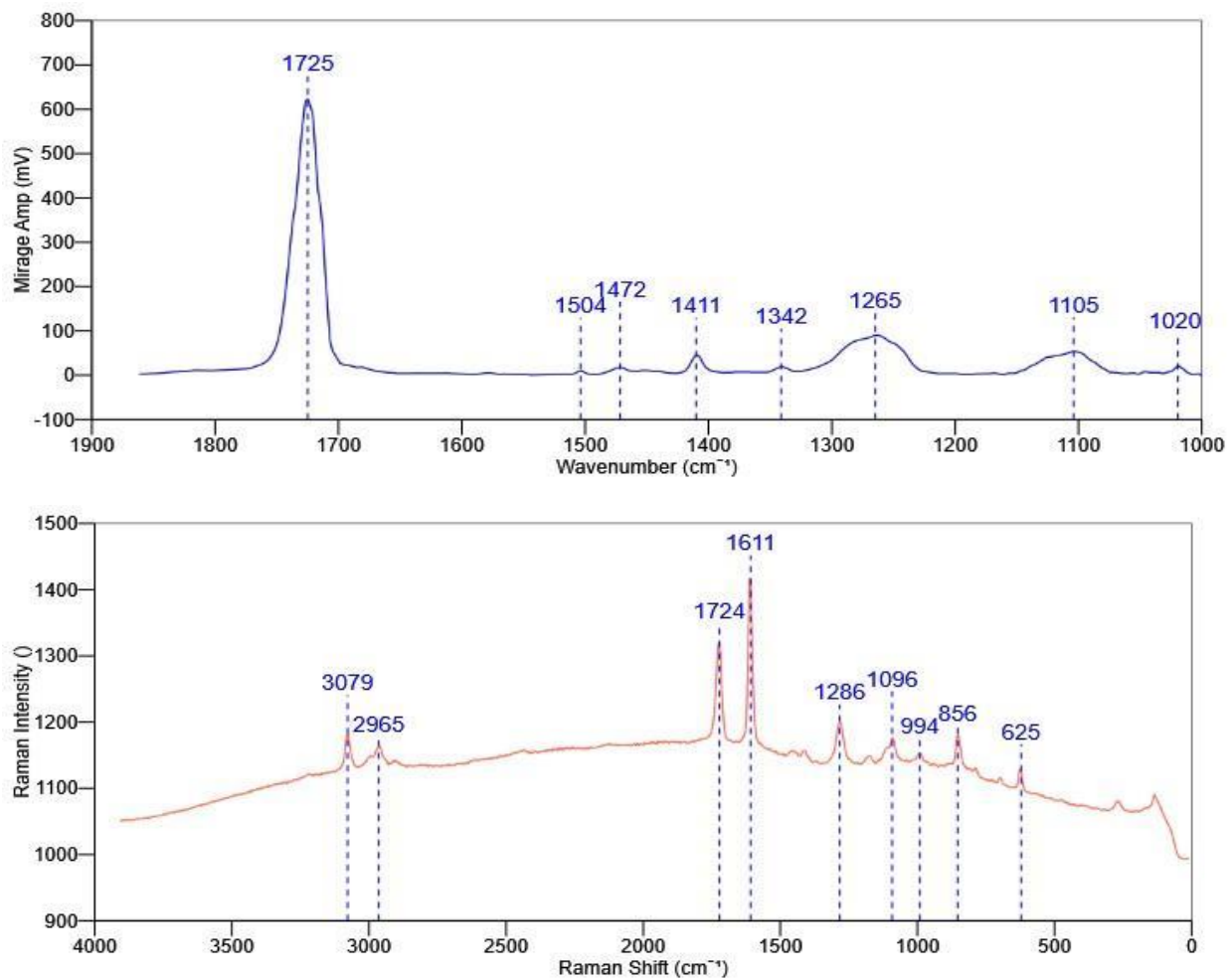


Figure S 4. Pristine PET IR spectra and Raman spectra.

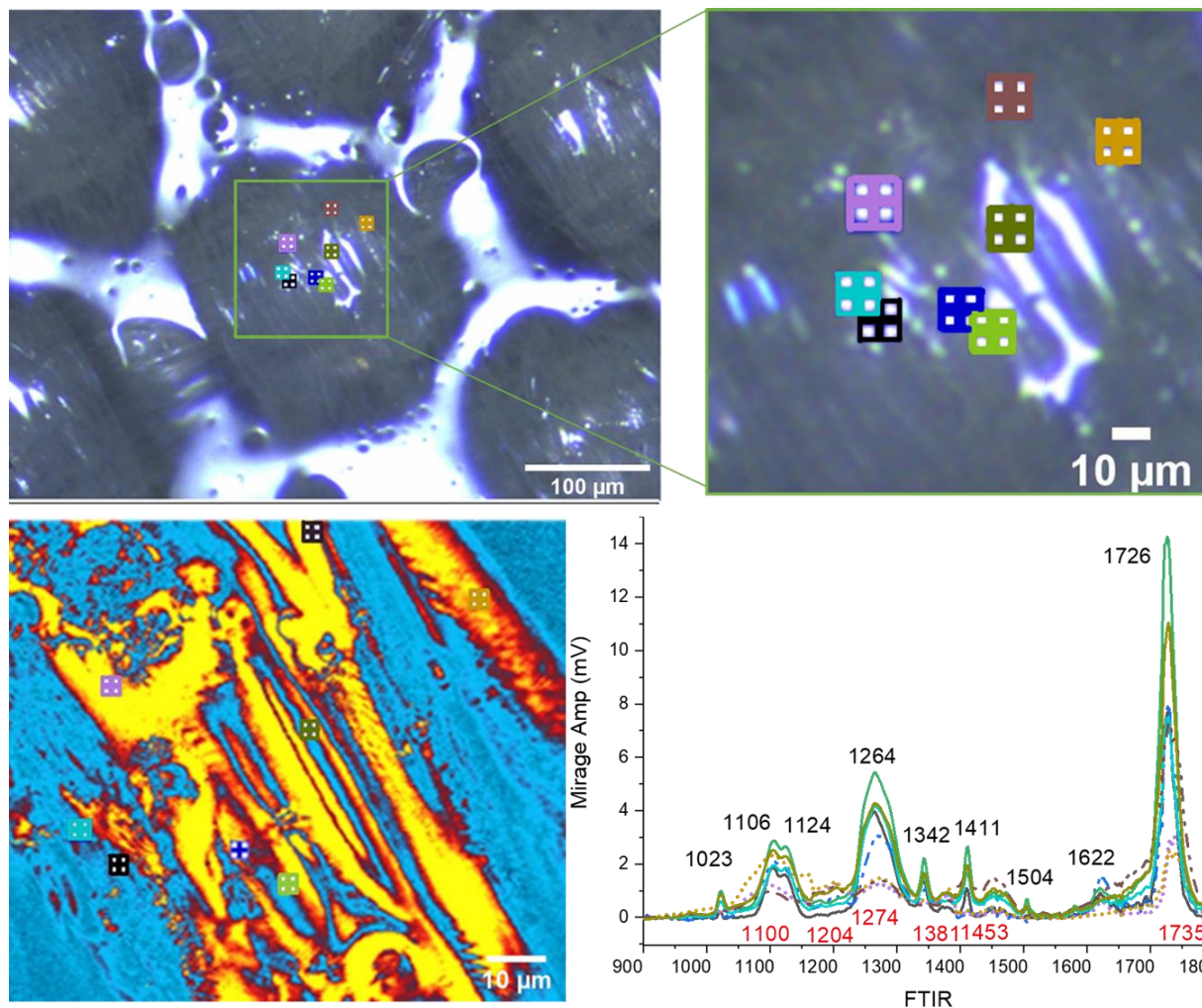


Figure S 5. mIRage™ optical images of woven fabric with dielectric ink, IR spectra of the woven fabric with dielectric ink.

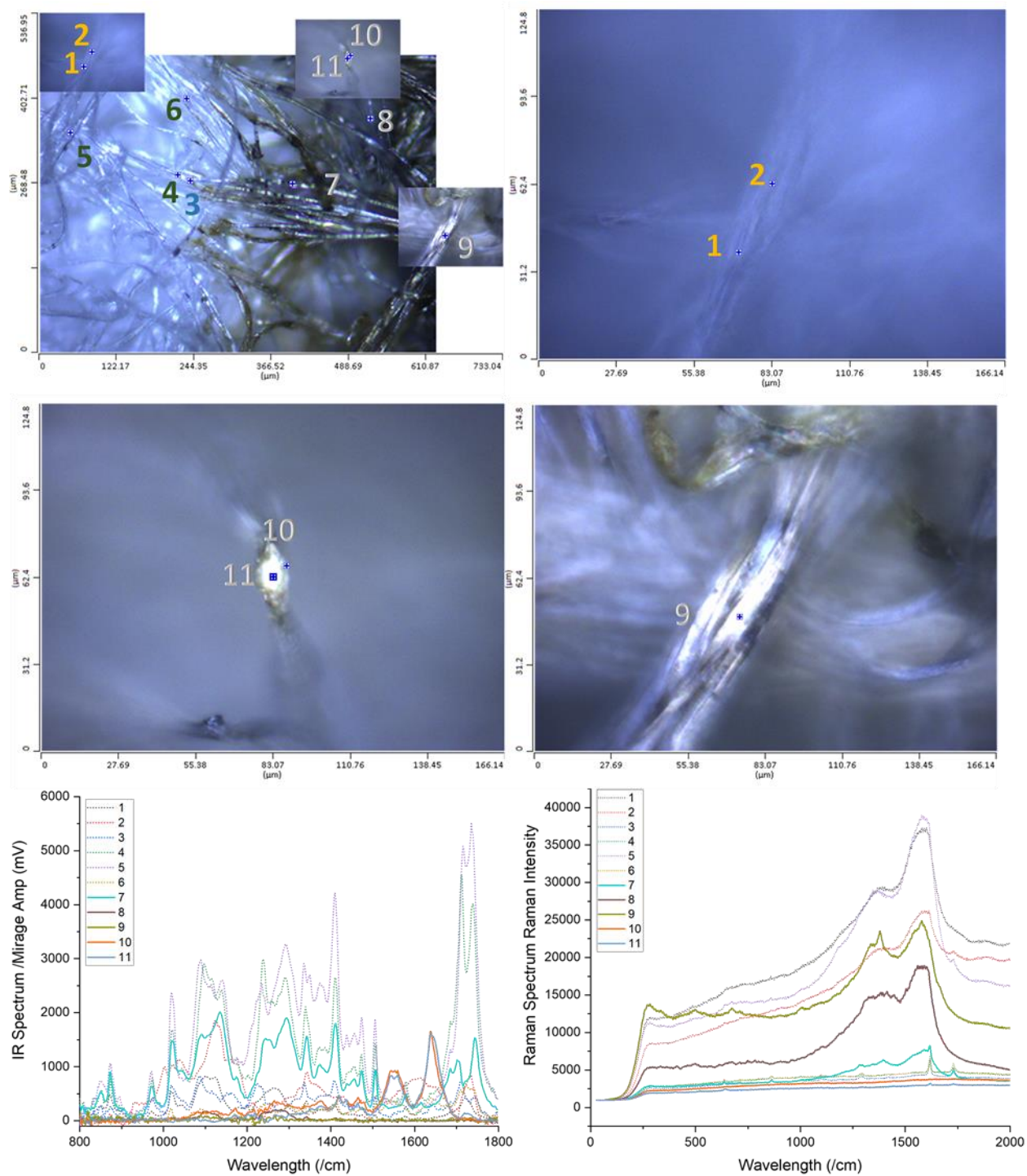


Figure S 6. Simultaneous IR/Raman analysis of inkjet-printed nonwoven e-textiles with laser confocal microscopy of pristine side of PET/PA nonwoven fabric, and inkjet-printed Ag nonwoven fabric with Raman and IR spectra respectively.

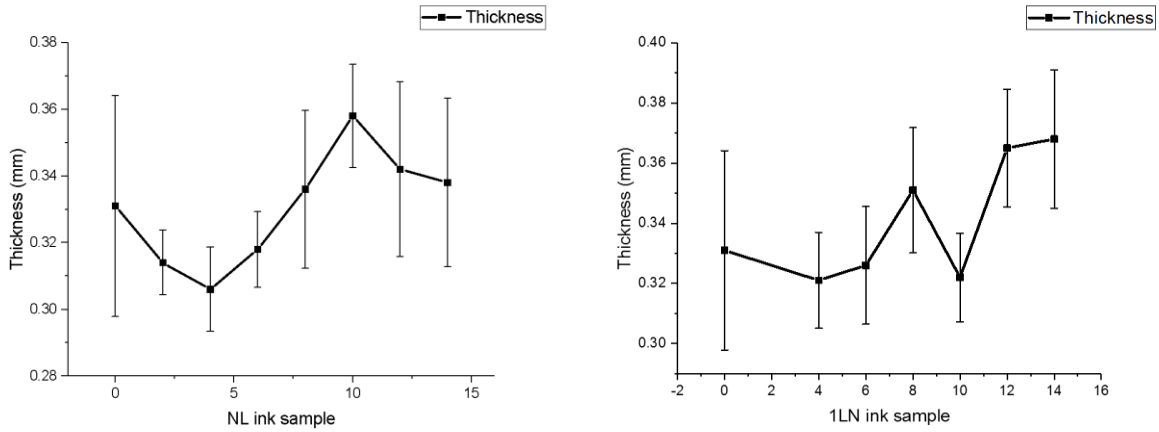


Figure S 7. Dielectric ink influence on film thickness by ex-situ polymerization method and layer-by-layer lamination.

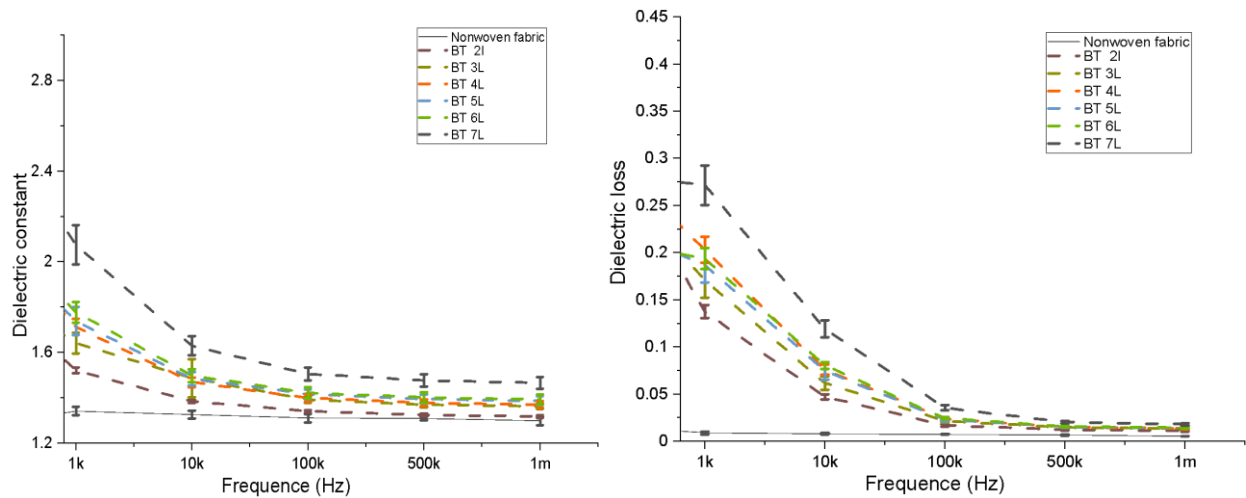
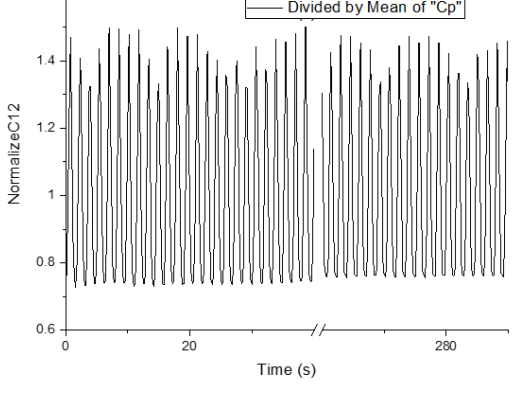
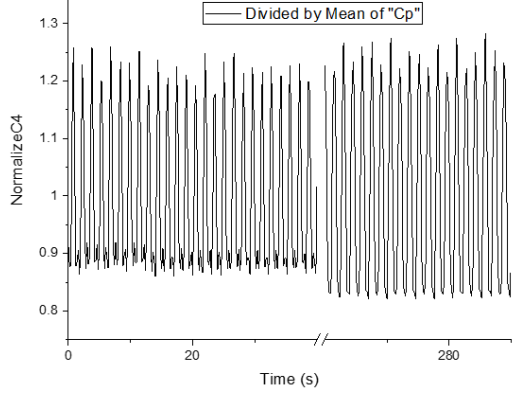
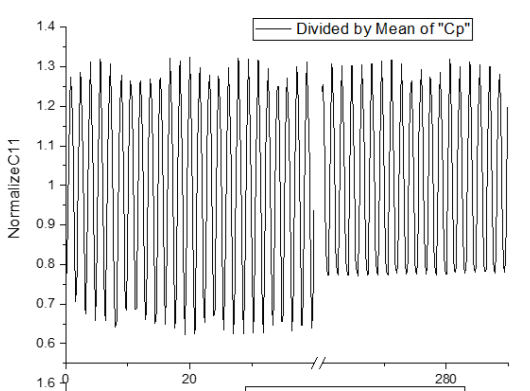
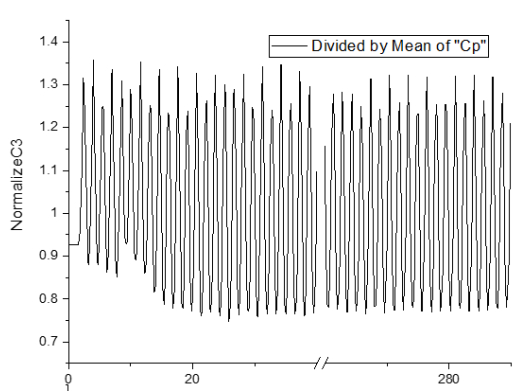
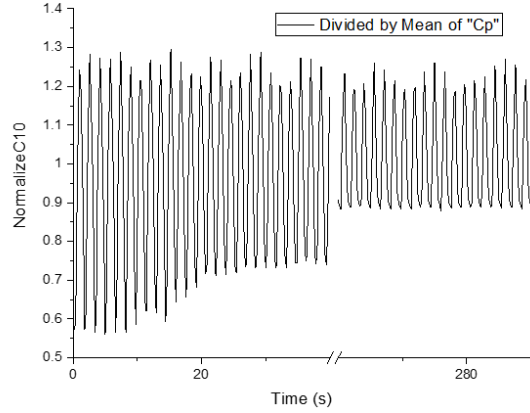
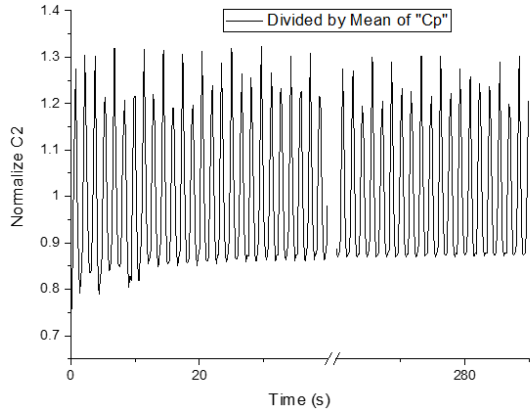
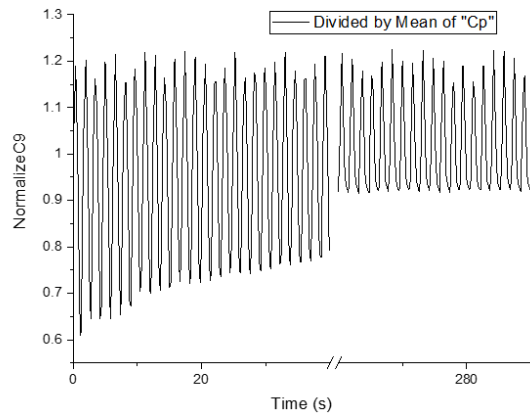
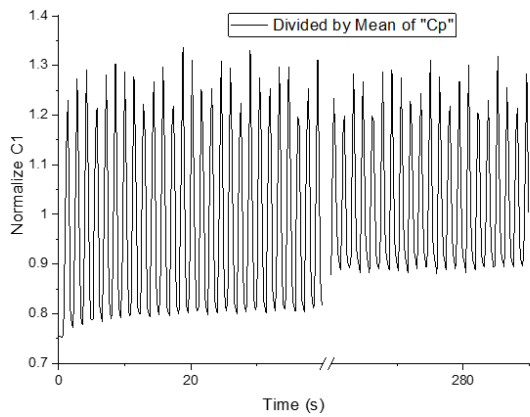


Figure S 8. a) Dielectric constant and b) dielectric loss of the inkjet-printed nonwoven fabric by ex-situ polymerization method.



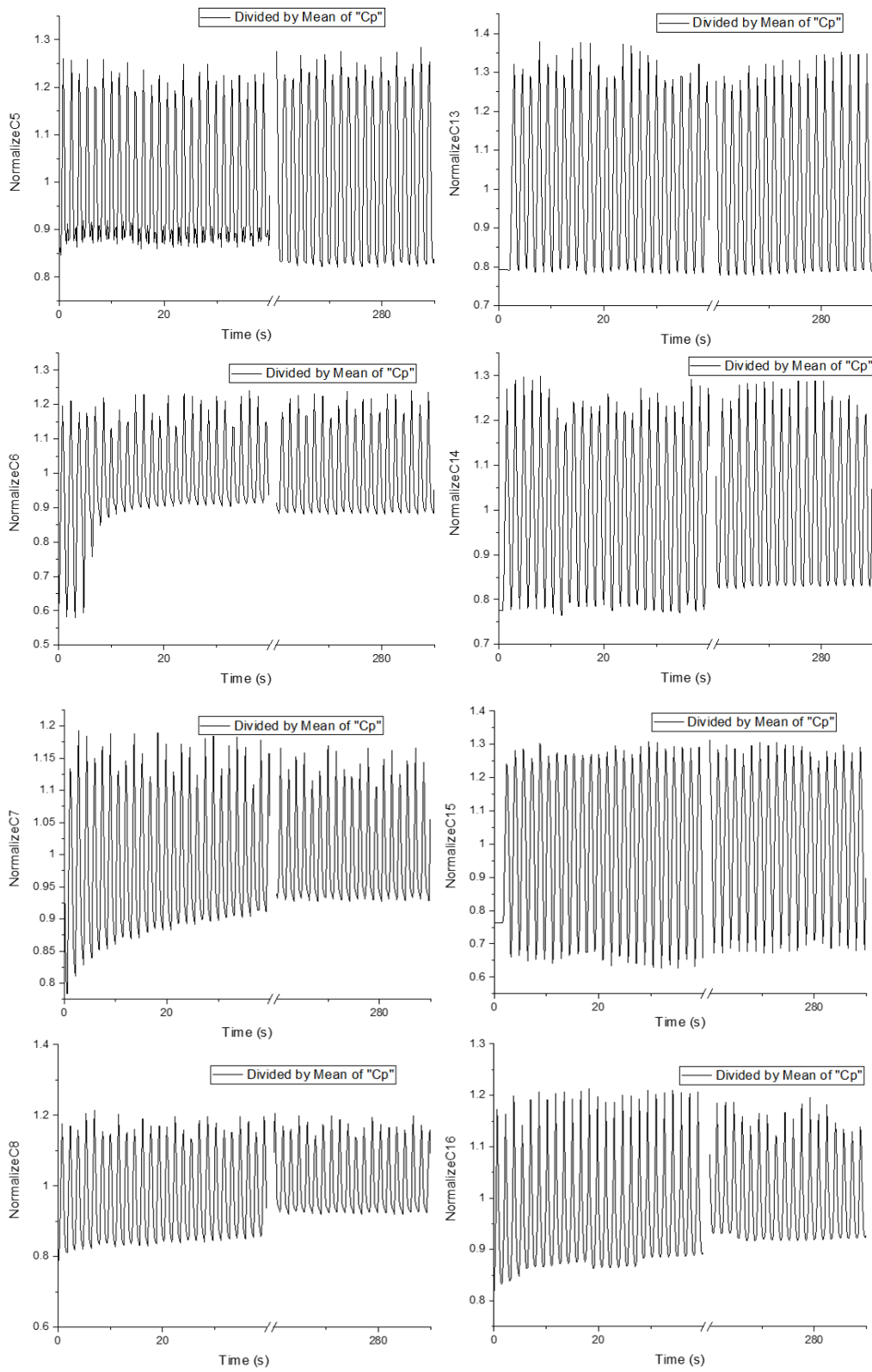


Figure S 9. Sensor performance taping 200 times for the textile capacitor array.

Appendix-2: Supporting Information for Chapter 5

Supporting Information for Chapter 5

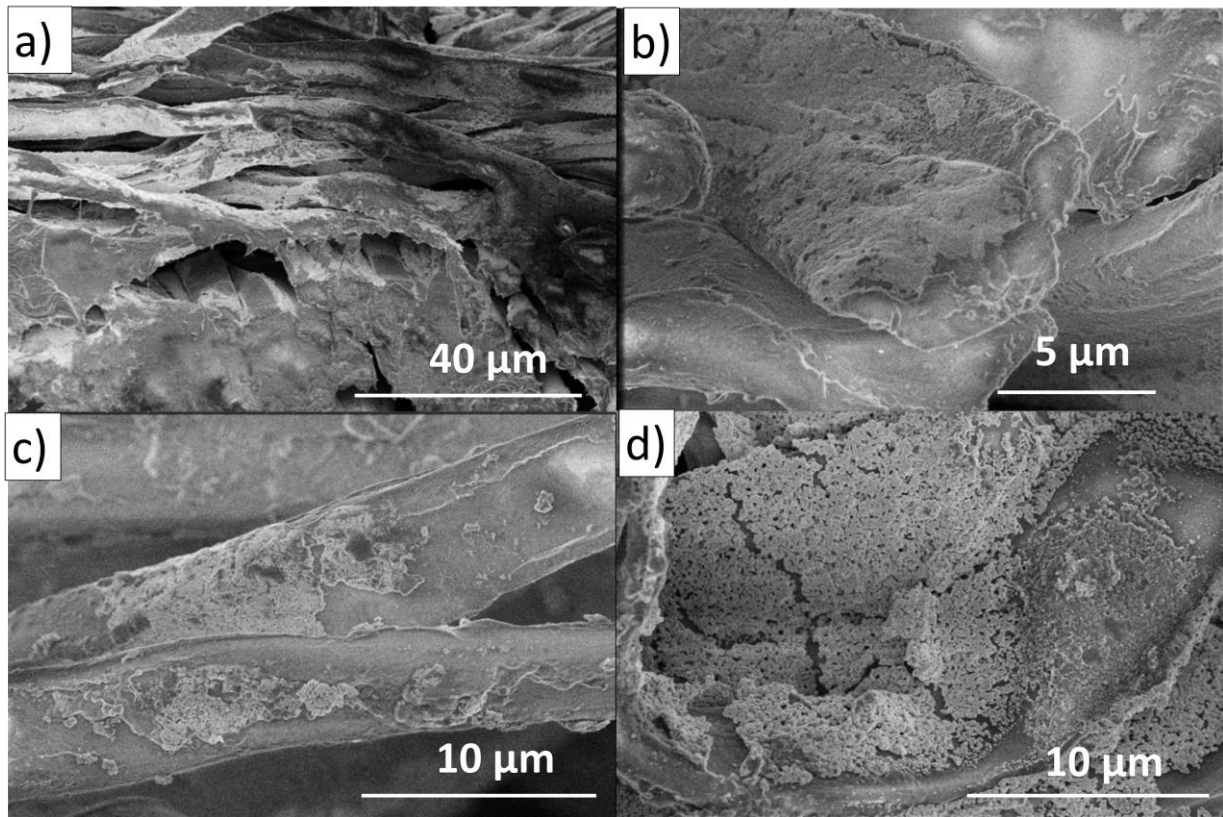


Figure S 10. (a) Cross sectional SEM image of Ag inkjet-printed nonwoven fabric. (b, c, d) SEM image of Ag inkjet-printed fiber.

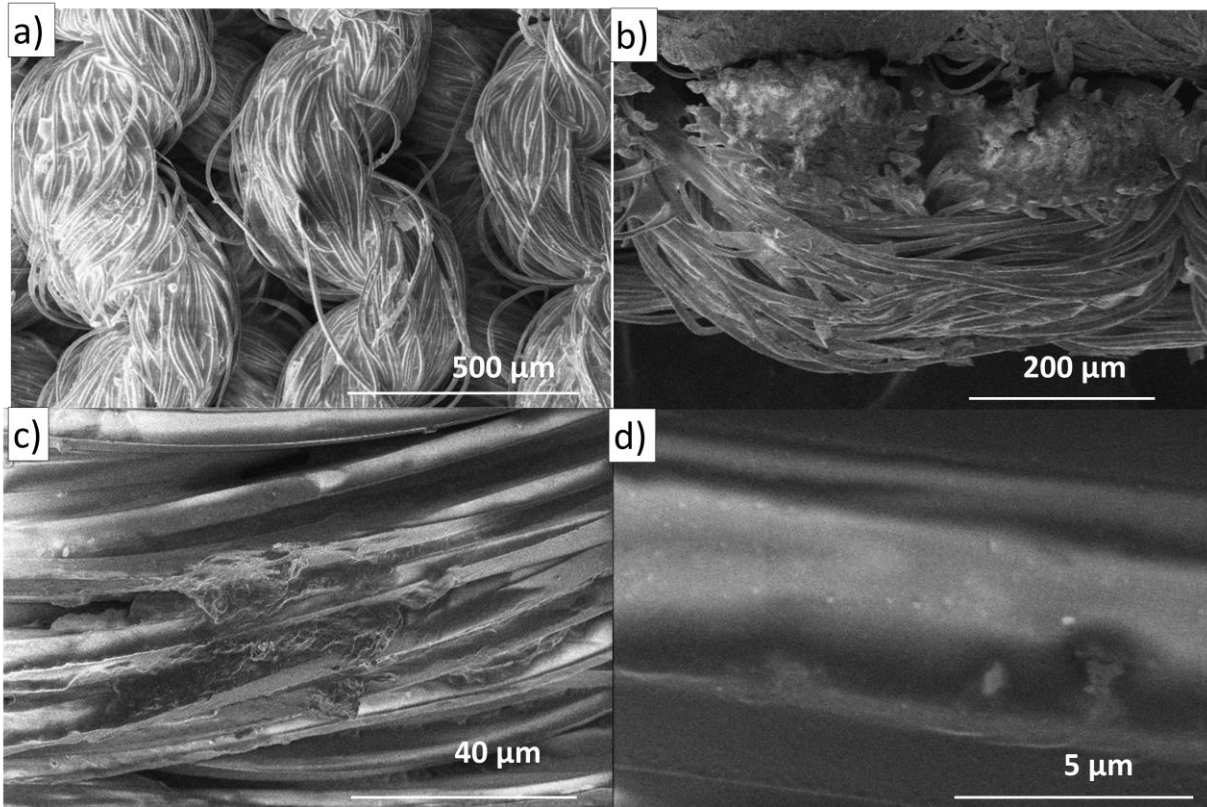


Figure S 11. (a) Surface SEM image of the in-situ BT dielectric UV curable inkjet-printed knit fabric structure. (b) Cross sectional SEM image of the in-situ BT dielectric UV curable inkjet-printed knit fabric. Surface SEM image of the in-situ BT dielectric UV curable inkjet-printed knit fabric (c) loop. (d) fiber.

Table S 1. Air- permeability of the printed E-textile

Air-Permeability of the Antenna Substrate (cm³/s/cm²)	
Knit Fabric Assemble	9.43 ±0.21
Inkjet-Printed Dielectric Ink Knit Fabric Assemble	9.18 ±0.21
Antenna	4.17 ±0.01

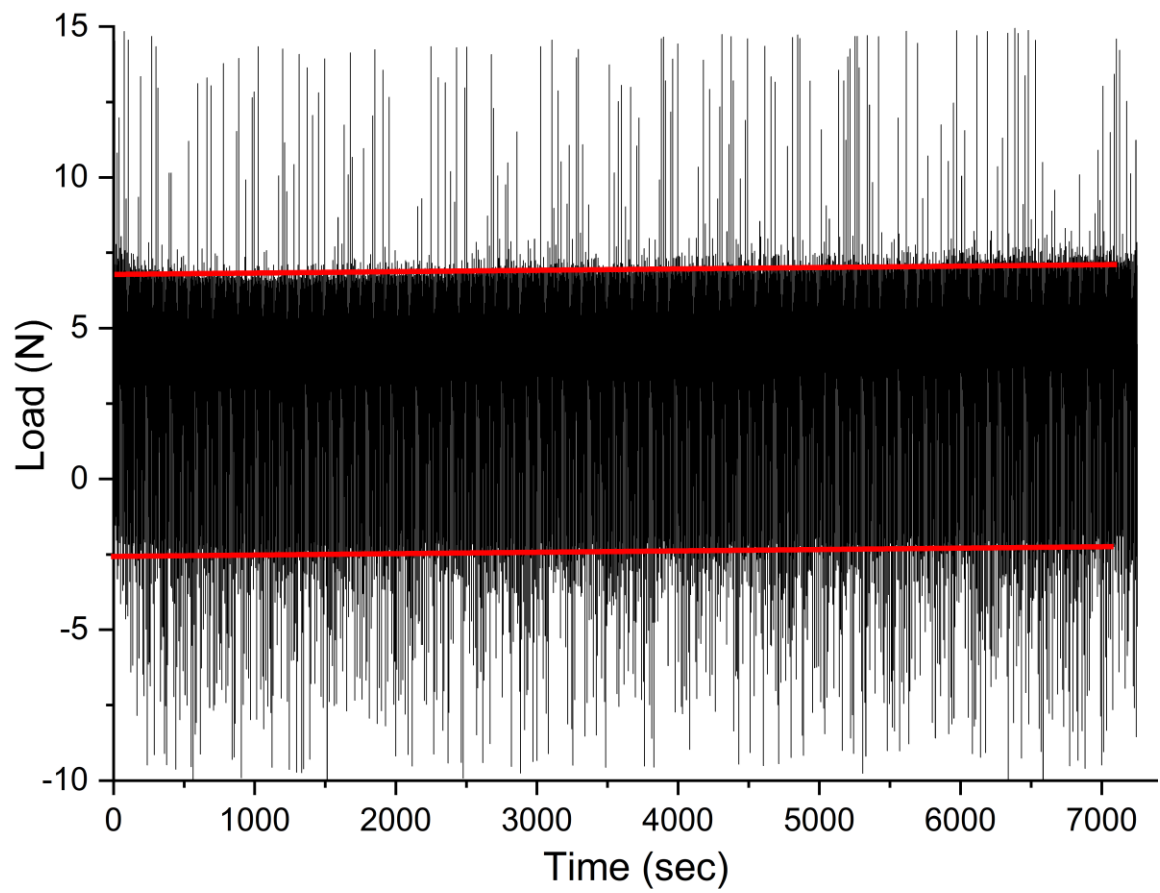


Figure S 12. Buckling force displacement curve with fixed-fixed ends for 1000 cycles

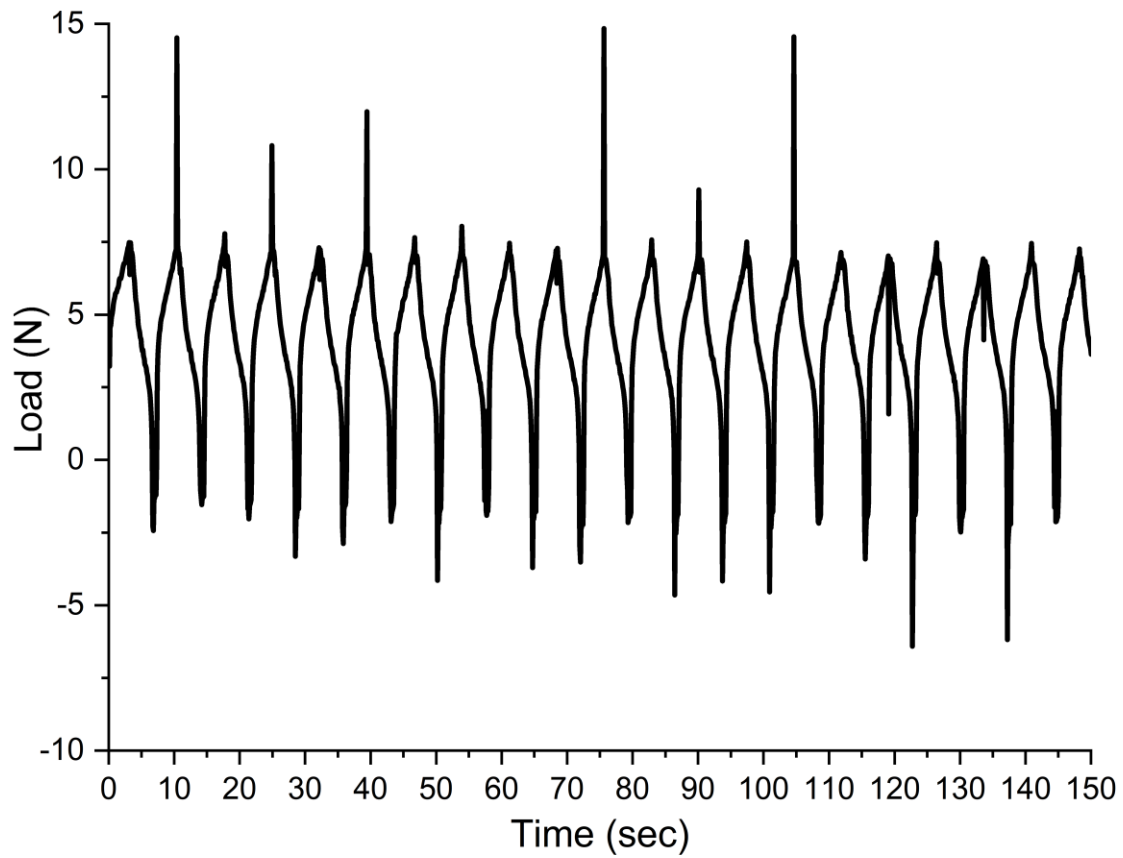


Figure S 13. Buckling force displacement curve with fixed-fixed ends for the first 20 cycles

Appendix-3: Supporting Information for Chapter 6

Supporting Information for Chapter 6

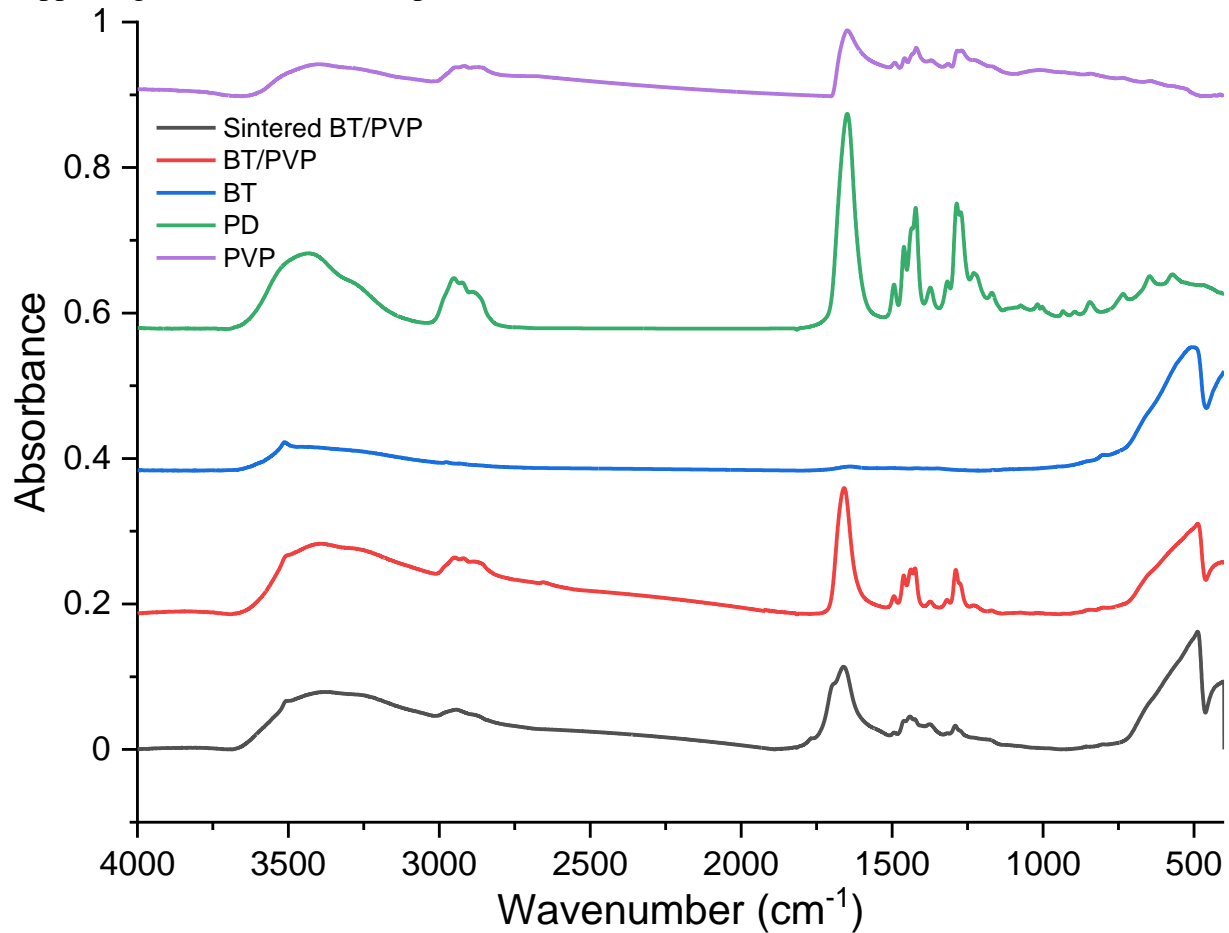


Figure S 14. FTIR of raw BT powder, polymer surfactant, PVP, printed BT/PVP nanocomposite film and sintered BT/PVP film by inkjet printing.

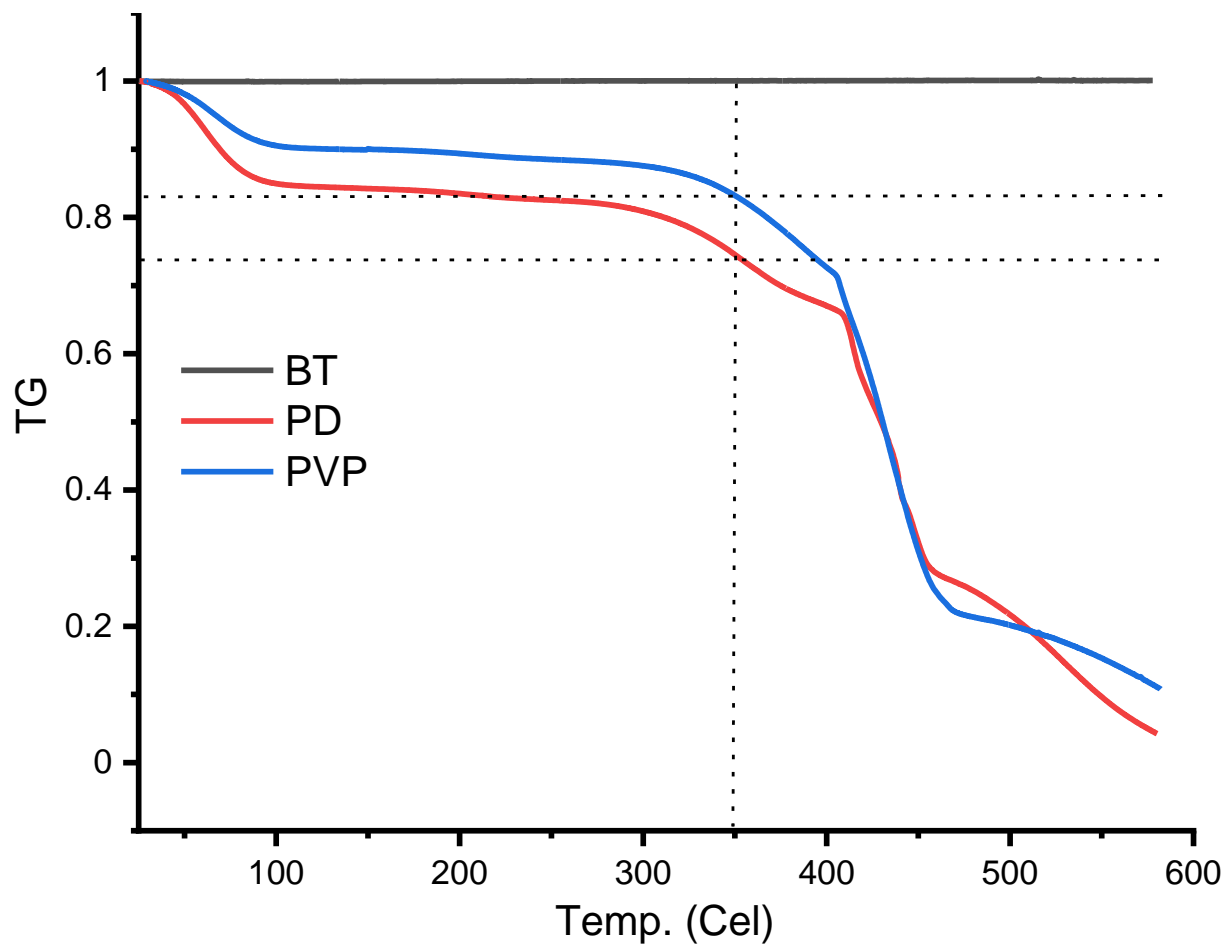


Figure S 15. TGA of raw BT powder, polymer surfactant, and PVP from 25°C to 580 °C.

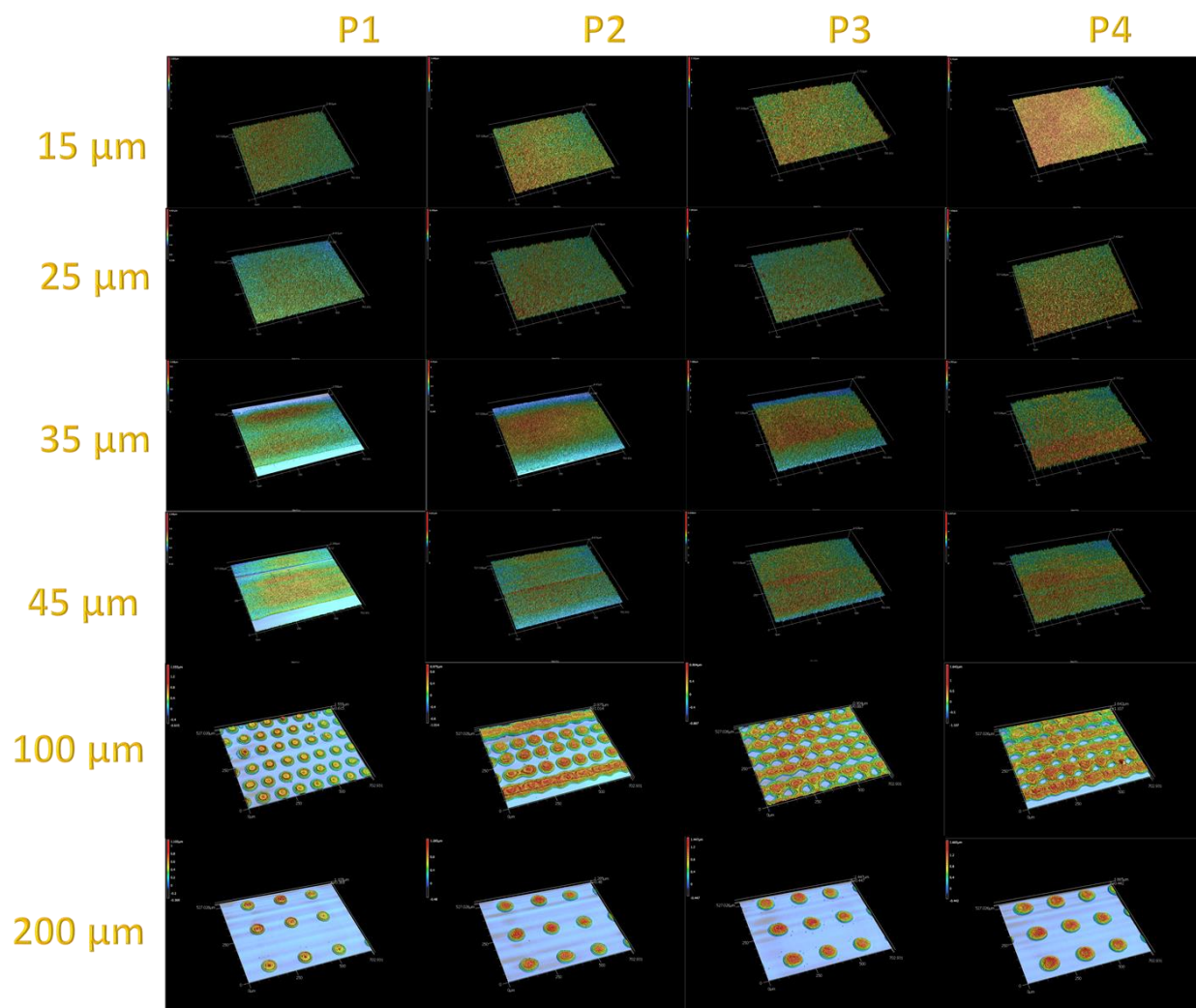


Figure S 16. 3D images of different drop space (15 μm , 25 μm , 35 μm , 45 μm , 100 μm , and 200 μm .) inkjet printing different pass (1, 2, 3, 4).

Table S 2. Inkjet printing setting

Drop space (μm)	Resolution (Dpi)	Printing 1 mm* 1 mm volume (pL)	Printed Ag 1pass thickness (μm)
15	1693	44890	1.302
25	1016	16810	0.487
35	726	8410	0.244
45	564	5290	0.153
100	254	1000	/
200	127	250	/

Appendix-4: Supporting Information for Chapter 7

Supporting Information for Chapter 7

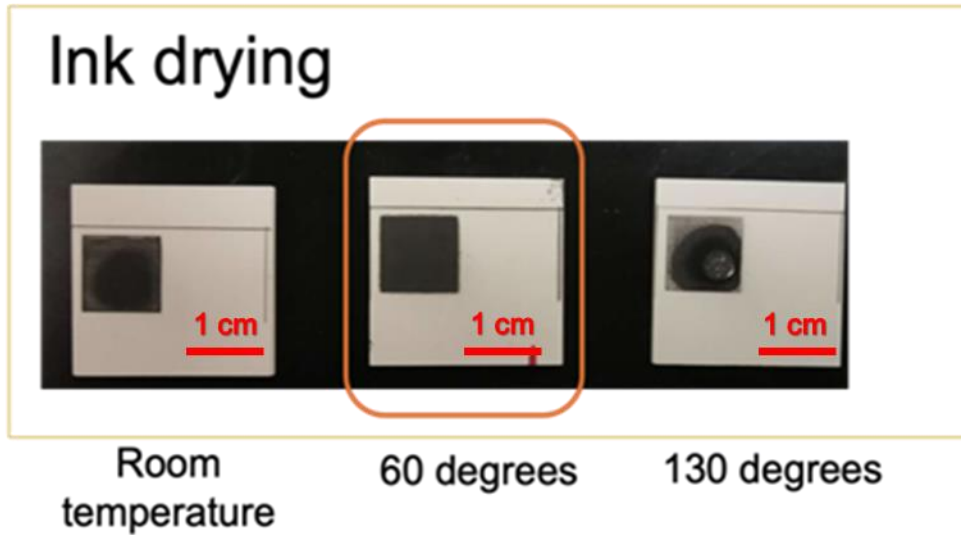


Figure S 17. The Ni ink drying temperature analysis under room temperature, 60 °C, and 130 °C.

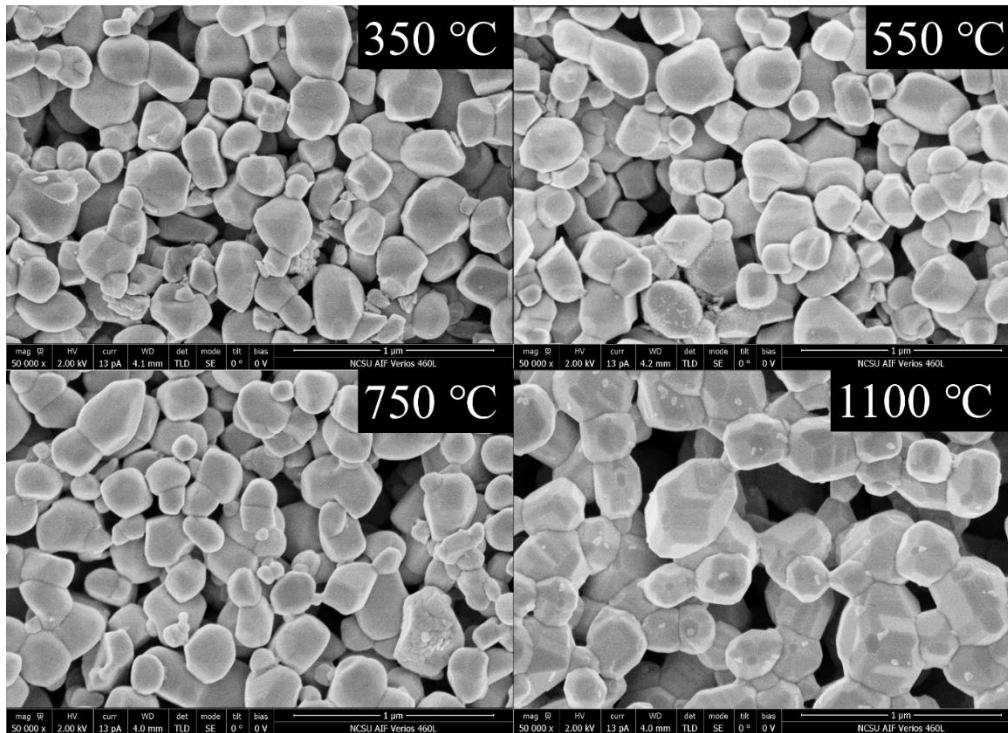


Figure S 18. SEM of 200 nm BTO printed layer cured at 150 degree and sintered at 350 °C, 550 °C, 750 °C, 1100 °C for 30 mins.

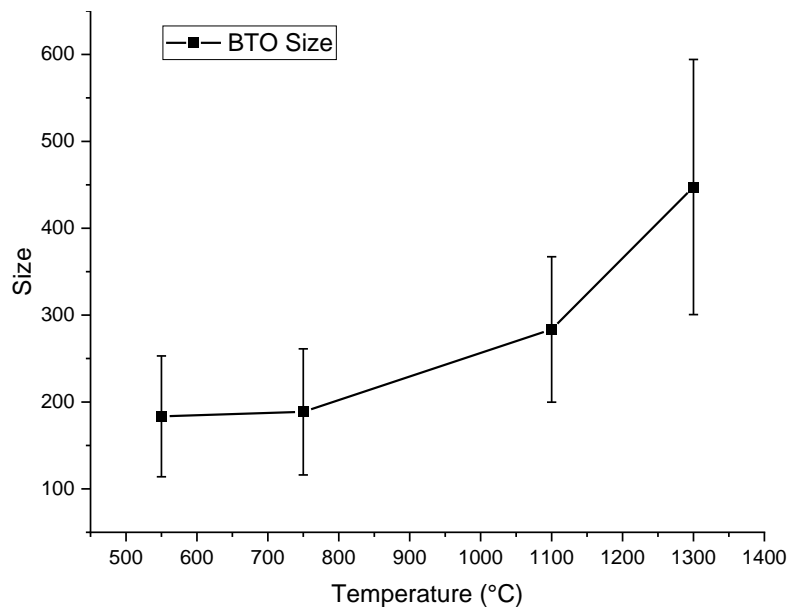


Figure S 19. BTO nanoparticle average size and deviation under sintering at 550 °C, 750 °C, 1100 °C and 1300 °C.

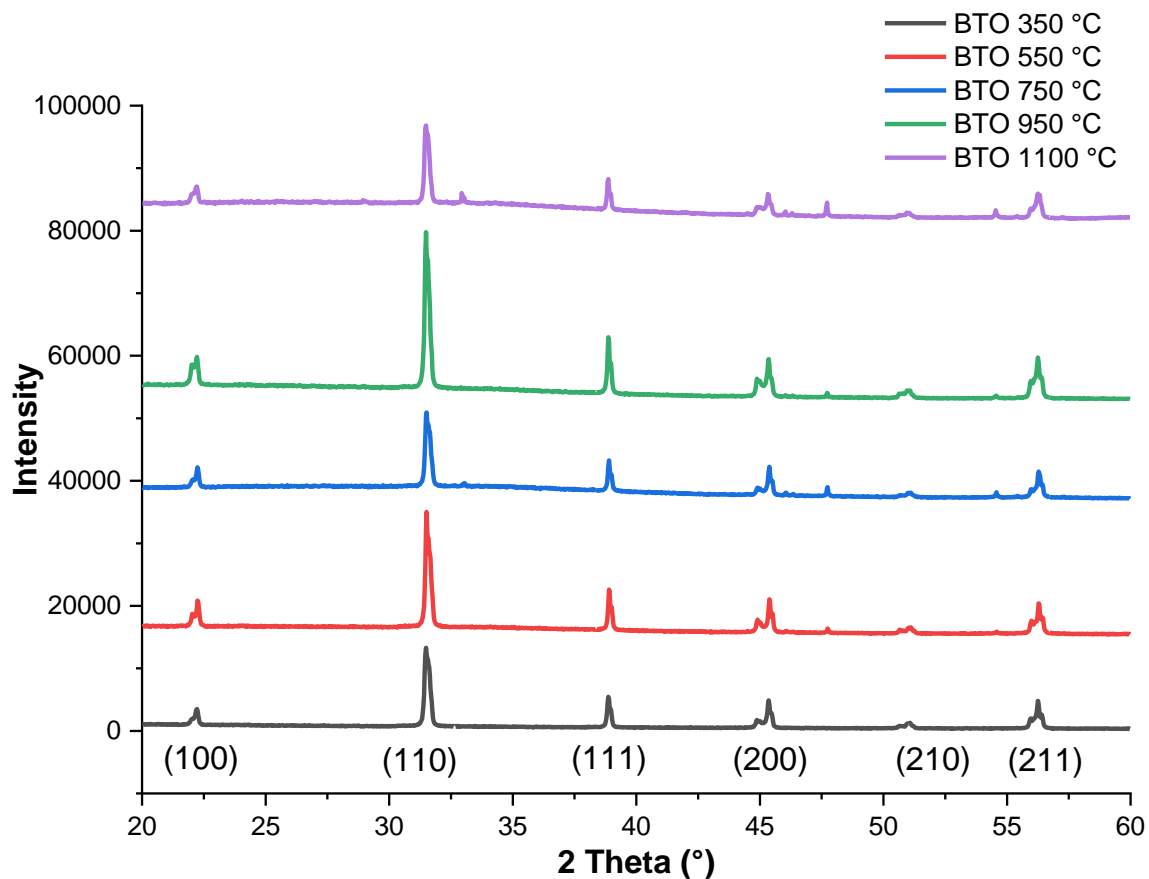


Figure S 20. XRD of 200 nm BTO printed layer cured at 150 degree and sintered at 350 °C, 550 °C, 750 °C, or 1100 °C.

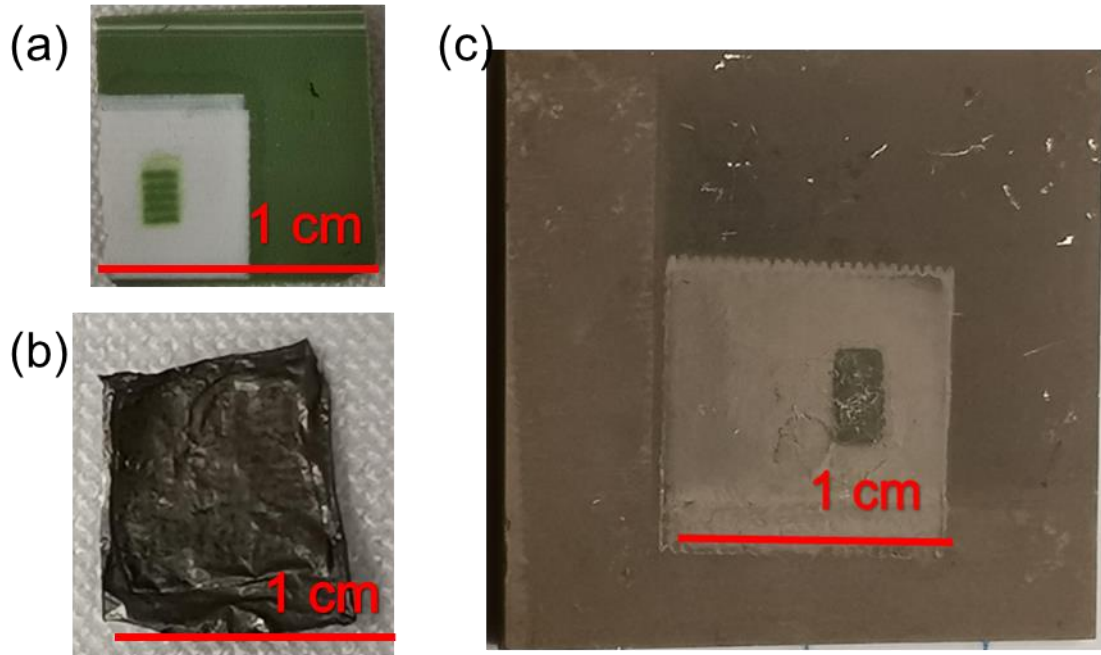


Figure S 21. Peeled off inkjet printed Ni capacitor on green BTO substrate sintered (a) 1100 °C in air condition, (b) 1300°C in reducing atmosphere. (c) Inkjet-printed Ni capacitor on fired BTO substrate sintered in 1300°C reducing atmosphere.

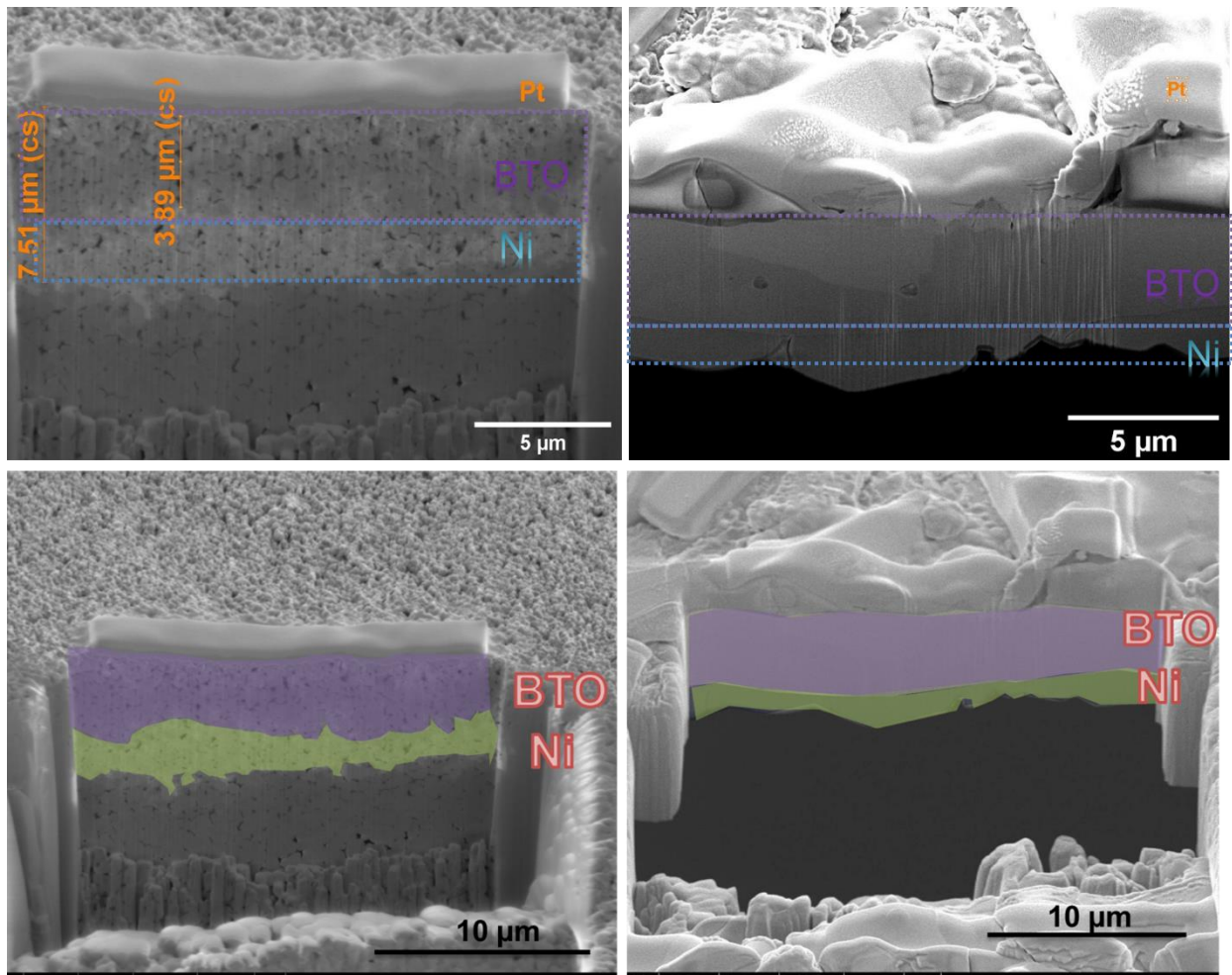


Figure S 22. (a) Inkjet-printed Ni/BTO layer and (b) Sintered printed Ni/BTO layer.

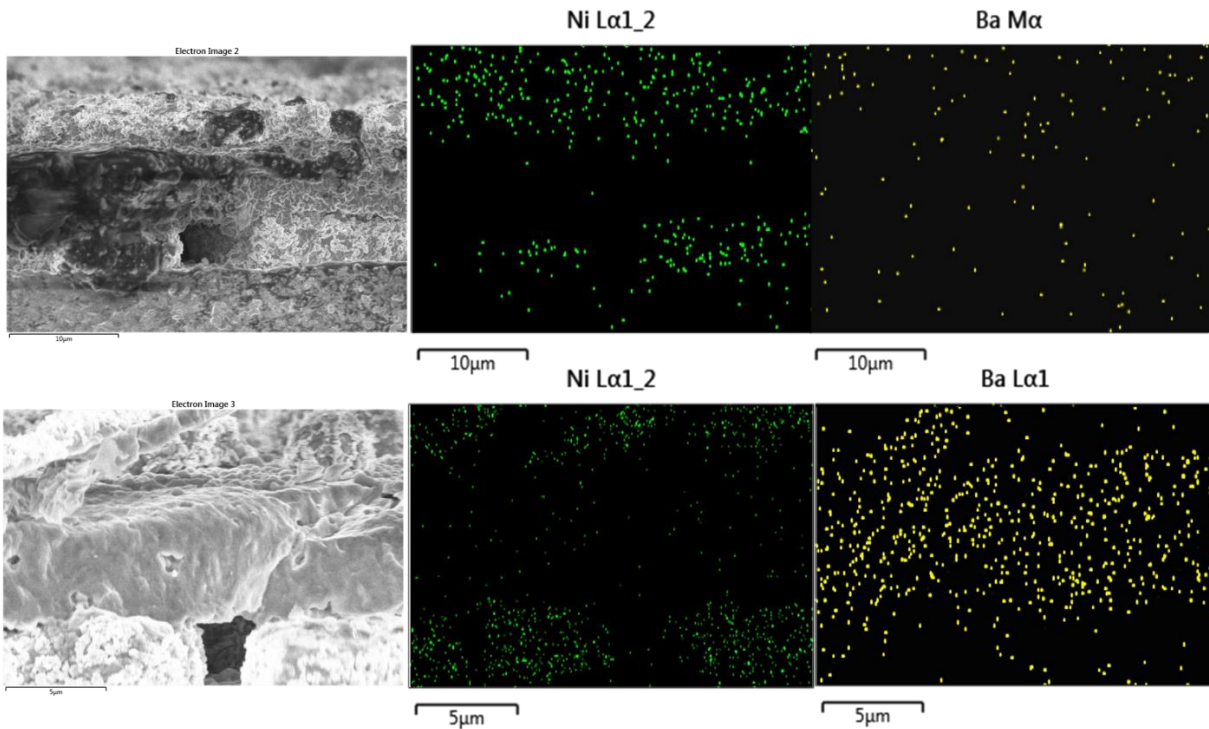


Figure S 23. Ni capacitor SEM with EDS

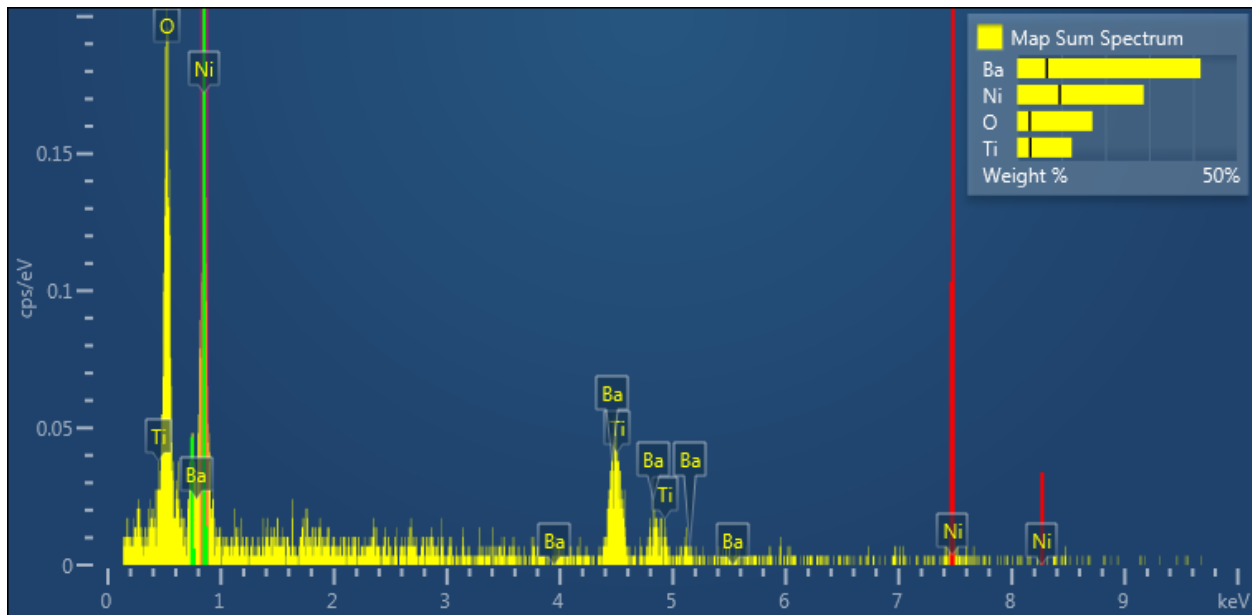


Figure S 24. Sintered inkjet-printed Ni capacitor SEM with EDS

Appendix-5: Supporting Information for Chapter 8

Supporting Information for Chapter 8

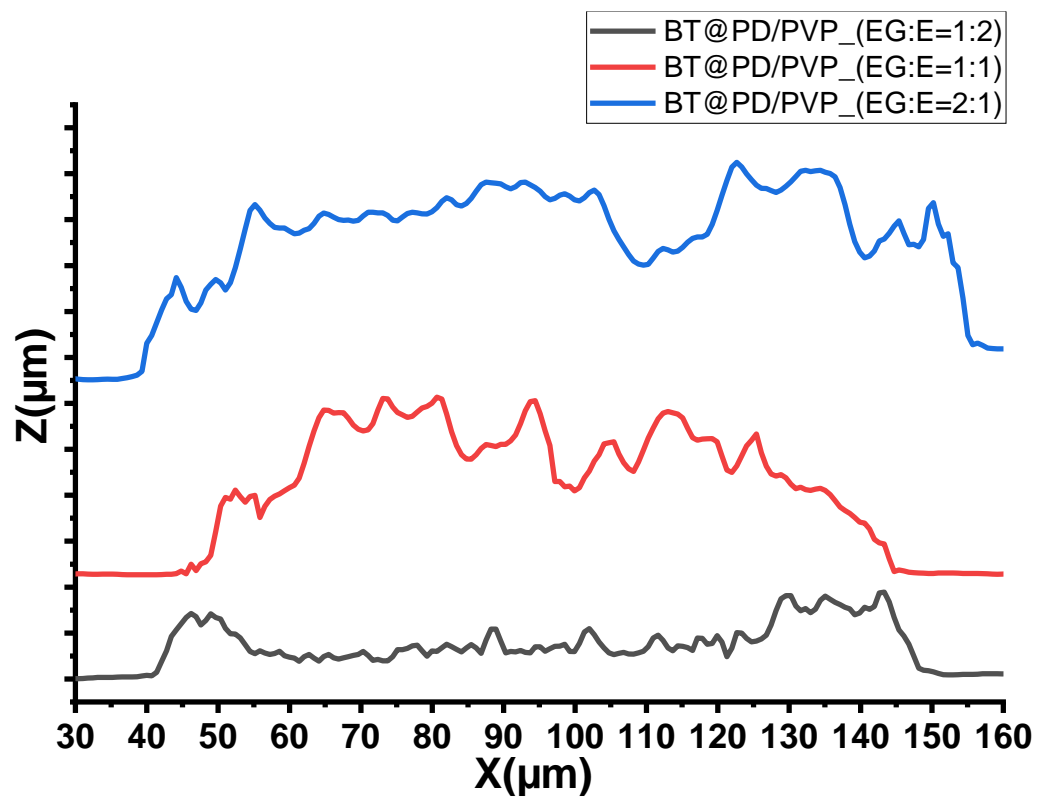


Figure S 25. The height profile of the single droplets at different ratio in horizontal direction.